1993

Metal And Ring Oxidation In Metallophthalocyanines

Edward A. Ough

METAL AND RING OXIDATION IN METALLOPHTHALOCYANINES

by

Edward A. Ough

Department of Chemistry

Submitted in partial fulfillment

of the requirements for the degree of

Doctor of Philosophy

Faculty of Graduate Studies

The University of Western Ontario

London, Ontario

November 1992

ISBN 0-315-81324-5

ABSTRACT

Absorption and magnetic circular dichroism (MCD) spectra of neutral and oxidized magnesium and iron phthalocyanine (MgPc and FePc) are reported. Chemical, electrochemical and photochemical methods are employed in the generation of the stable π-cation radical of magnesium phthalocyanine. The broad absorption band at 500 nm is a "marker" band that verifies oxidation of the phthalocyanine ring. Variable temperature absorption and EPR spectra indicate that oxidized MgPc(-1) exists in solution as a mixture of monomer ($[MgPc(-1)]^{\cdot +}$) and dimer ($[MgPc(-1)]_2^{++}$). Least squares and Simplex calculations were performed on the absorption and MCD spectra of MgPc(-2) and MgPc(-1) to determine the band centre energies for $\pi \rightarrow \pi^*$ (Q, B1, B2, N and L) and $\pi \rightarrow \pi$ (in the radical cation) transitions. Deconvolution yielded band centres of 670 (Q), 361 (B1), 338 (B2), 282 (N) and 246 nm (L) for $(im)_2MgPc(-2)$; 828 (Q), 507 ($\pi \rightarrow \pi$), 411 ($\pi \rightarrow \pi$), 387 (B1), 330 (B2), 277 (N), and 247 nm (L) for $[(im)_nMgPc(-1)]^{\cdot +}$; and 712 (Q), 505 ($\pi \rightarrow \pi$), 420 ($\pi \rightarrow \pi$), 368 (B1), 320 (B2), 278 (N), and 249 nm (L) for $[(H_2O)MgPc(-1)]_2^{++}$.

Absorption and MCD spectra for $L_2Fe(II)Pc(-2)$ (L = im, meim, py, mepy, pip, CN, CO, NH_3), $L(X)Fe(III)Pc(-2)$ (L = im, CN; X = Br, CN), $(X)Fe(III)Pc(-2)$ (X = Cl, Fo), and $Cl_2Fe(III)Pc(-1)$ complexes are reported. Low temperature MCD and electron paramagnetic resonance (EPR) spectra were used to assign the above complexes ground states as $^1A_{1g}$, ^2E_g, $^4A_{2g}$, and ^3E_u, respectively. The low and intermediate spin states in iron(III) phthalocyanine are directly related to the coordination number of the ferric ion, where octahedral L(X)Fe(III)Pc(-2) is low spin (S=1/2) and square pyramidal (X)Fe(III)Pc(-2) is intermediate spin (S=3/2). The triplet (S=1) nature of the EPR spectrum of $Cl_2Fe(III)Pc(-1)$ demonstrates that this ring oxidized π-cation radical exists in solution as a pure monomer. The orbital degeneracy in L(X)Fe(III)Pc(-2) and $Cl_2Fe(III)Pc(-1)$ and the spin degeneracy in

(X)Fe(III)Pc(−2) results in their MCD spectra being dominated by temperature dependent C terms. The above series of neutral and oxidized iron phthalocyanine complexes were subjected to spectral deconvolution in order to isolate xy polarized $\pi \rightarrow \pi^*$ (Q, B1, B2, N and L), $\pi \rightarrow \pi$ (into the half filled $1a_{1u}(\pi)$ MO of the π−cation radical), MLCT ($e_g(d\pi) \rightarrow 1b_{1u}(\pi^*)$, $1b_{2u}(\pi^*)$; present in the ferrous and ferric spectra), and LMCT (into the 3/4 filled $e_g(d\pi)$ MO of the ferric complexes) transitions. From the series of spectral fits for $L_2Fe(II)Pc(-2)$, the $e_g(d\pi)$ orbitals act as electron conduits between the axial and equatorial π−systems. The energy of the B1 band decreases with good π donor ligands (cyanide) and increases with good π acceptor ligands (carbon monoxide). The variation in the B1 band energy demonstrates that the ferrous to ferric oxidation increases the π−acceptor strength of the central metal.

ACKNOWLEDGEMENTS

At this time, I would like to express my sincere gratitude to all the people, without whose help and support, this work would not have been possible.

I would first like to thank my supervisor, Dr. Martin Stillman, for his guidance, support and encouragement during this study. Since the task of undertaking a doctoral degree is impossible without financial support, I also thank NSERC and Imperial Oil for their financial support.

I thank the members of my advisory committee, Dr. R.J. Puddephatt and Dr. R.G. Kidd for the time and attention they have invested during this study.

I am grateful to Drs. T. Nyokong, Z. Gasyna, K. Creber, W. Browett and S. Radzki for their help and discussions over the past six years. I also appreciate the support and help of past and present lab-mates: Wuhua Lu, Scott Kirkby, John Mack, Sharbari Lahiri, Qiwei Zhu and Bill Yuan. Special thanks go out to Dr. Creber, for her donation of the metallophthalocyanine-N-isologs used in this study, to John Mack, for his help setting up the MCD equipment and his work on the CDSCAN program, and to Bill Yuan, for the computer program to convert EPR data.

Thanks go out to my parents and sisters, for their encouragement during my years at university. Last, but far from least, I thank my wife Anna Rae, not only for her love and support, but also for her help proof reading this thesis.

TABLE OF CONTENTS

often makes it difficult to determine band centre energies directly from the absorption spectra. Unlike absorption spectra, MCD spectra provide state to state transition polarization information that, for these highly symmetric porphyrinic systems, is otherwise only available from crystal studies. MCD also provides direct information about the magnetic moments of degenerate ground and excited states. When MCD spectra are used in conjunction with absorption spectra, they are very useful in discerning band centre energies.

Magnetic optical activity was discovered by Faraday in 1854, but MCD spectroscopy did not obtain interest from chemists and physicists until the 1960's. The advances in MCD spectroscopy may be attributed to the development of compact magnets, with high magnetic fields, that allowed researchers to analyse their data in both qualitative and quantitative manners. The development of instrumentation for the rapid measurement of MCD spectra [24] and the development of theory [25] to explain the data have led to the growth of this experimental technique

1.4.1 MCD Theory

MCD spectroscopy can be thought of as a magnetically induced chirality (CD effect) in a molecule. When a molecule is subjected to an external magnetic field, electronic transitions within the molecule will display a preference for either right or left circularly polarized light. The MCD spectral intensity is represented either as the absorbance difference $\Delta A = A_L - A_R$, where L and R represent left and right circularly polarized light, or as the molar ellipticity $[\theta]_M$. Three spectral band types can arise in a MCD spectrum and the absorbance difference can be represented as the sum of the three terms:

$$\frac{\Delta A}{E} = \frac{\Delta \epsilon c' \ell}{E} = \gamma \beta B \left[A_1 \left[- \frac{\delta f(E)}{\delta E} \right] + \left[B_0 + \frac{C_0}{kT} \right] \times f(\Sigma) \right] \qquad (1.1)$$

This follows the notation suggested by Piepho and Schatz [25] where E is the

LIST OF TABLES

LIST OF FIGURES

ABBREVIATIONS

MCD	Magnetic Circular Dichroism
LMCT	Ligand to Metal Charge Transfer
MLCT	Metal to Ligand Charge Transfer
CT	Charge Transfer
EPR	Electron Paramagnetic Resonance
DPPH	α,α'-Diphenyl-β-picryl hydrazyl
CV	Cyclic Voltammetry
DPV	Differential Pulse Voltammetry
CPC	Controlled Potential Coulometry
SCE	Saturated Calomel Electrode
DCM	1,1-Dichloromethane
CB	2-Chlorobutane
DCE	1,2-Dichoroethane
DCB	1,4-Dichlorobutane
o-DCB	1,2-Dichorobenzene
DMF	N,N-Dimethylformamide
DMA	N,N-Dimethylacetamide
TPAP	Tetrapropylammonium Perchlorate
CO	Carbon Monoxide
NH_3	Ammonia
CN^-	Cyanide
im	Imidazole
meim	N-Methylimidazole
py	Pyridine
mepy	4-Methylpyridine
pip	Piperidine
Ac	Acetate
Fo	Formate
Pr	Propionate
La	Lactate
MPc	Metallophthalocyanine
$MPcN_4$, $MPcN_8$	Metallophthalocyanine-N-Isologs

CHAPTER 1

INTRODUCTION

1.1 GENERAL INTRODUCTION

Since its discovery fifty years ago, the phthalocyanine molecule and its metal complexes have been the focus of many studies [1,2]. The considerable chemistry, electrochemistry and photochemistry of this macrocycle make it of interest to industrial and research chemists. Their high thermal and chemical stability, limited solubility in a wide variety of solvents, and the deep blue-green pigmentation make phthalocyanines a very important class of commercial dyes. In The United States of America, twelve million pounds of phthalocyanine blue and three million pounds of phthalocyanine green are produced annually [3]. Active areas of research, that are focusing on the phthalocyanine molecule, are: the conversion of solar energy to chemical energy (ie. the photo-reduction of water to molecular hydrogen [4,5]), the photodynamic treatment of cancer [6] and the development of one-dimensional molecular metals [7-9]. Currently irradiation of the photo-sensitizers in the ultraviolet region is required for the photochemical generation of hydrogen from water [4,5]. The viability of this type of technology is dependent upon the development of photo-sensitizers, that are able to absorb incident sunlight that lies above the ultraviolet region. Metallophthalocyanines are suitable candidates because they are intense absorbers of light in the visible and near infrared regions of the electromagnetic spectrum. Water soluble tetrasulfonated phthalocyanines (TsPc) are being studied as potential sensitizers in the photodynamic treatment (PDT) of cancer [6]. In this treatment, the photochemically excited tetrasulfonated phthalocyanine molecules are used to convert triplet oxygen to highly reactive singlet oxygen, which reacts with and destroys the cancer cells. Crystals of partially oxidized phthalocyanines are being studied as model systems in the development of molecular electronic devices [10,11]. These crystals behave like

one-dimensional molecular metals and have optical and electrical conductivities that approach those of metals [7-9]. The metallophthalocyanine molecules arrange in longitudinal stacks and the conductivities along the stacking axis range from 500 to 2000 $\Omega^{-1}cm^{-1}$.

1.2 HISTORY OF THE PHTHALOCYANINES

Like many important scientific discoveries, phthalocyanines were discovered by accident. In 1907, the heating of an alcoholic solution of ortho-cyanobenzamide produced a blue product, which turned out to be metal free phthalocyanine (H_2Pc) [12]. The word phthalocyanine is derived from the Greek words, naptha (rock oil) and cyanide (dark blue). In 1927 copper phthalocyanine, the first metallophthalocyanine, was prepared when attempts were made to produce ortho-xylene dicyanide from ortho-dibromobenzene and cuprous cyanide [12]. Iron phthalocyanine was accidently prepared in 1928 at the Grangemouth works of Scottish Dyes Limited when workers attempted to prepare phthalamide from phthalic anhydride and ammonia in a glass lined iron kettle that had a crack in the glass lining. The first patent for phthalocyanines was issued to Dandridge, Drescher and Thomas of Scottish Dyes Ltd [13].

The first scientific papers to focus on the phthalocyanine molecule were reported by Linstead et al. [14,15] in the 1930's. Linstead's group reported that the molecular structure of metal free phthalocyanine (Figure 1-1) included a ring system of four isoindole units linked by four aza-bridging nitrogens. Aside from the aza-bridging nitrogens, the phthalocyanine molecule closely resembles naturally occurring porphyrins. With the aid of his coworkers, Linstead was able to prepare the first row transition metal phthalocyanines ranging from manganese to zinc.

Linstead's proposed structures of metal and metal-free phthalocyanine were verified by single crystal x-ray analysis. In a series of papers by Robertson [16-19],

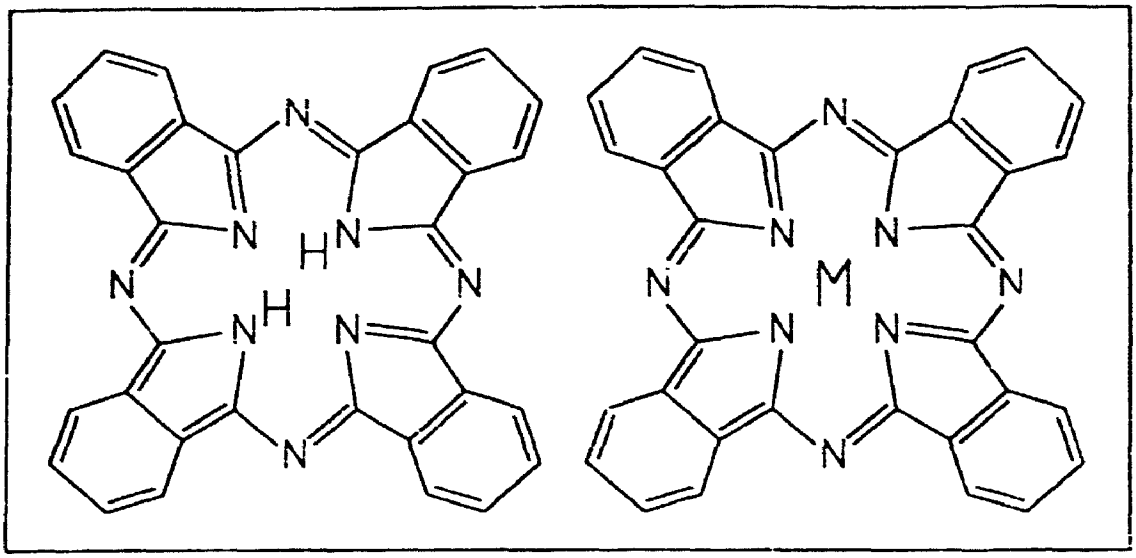

Figure 1–1 Molecular structure of metal and metal–free phthalocyanines.

H																	
Li	Be																
Na	Mg											Al	Si				
K	Ca	Sc	Ti	V	Cr	Mn	Fe	Co	Ni	Cu	Zn	Ga	Ge	As			
		Y	Zr	Nb	Mo	Tc	Ru	Rh	Pd	Ag	Cd	In	Sn	Sb			
		La	Hf		W	Re	Os	Ir	Pt	Au	Hg	Tl	Pb				
		Ac															

Lanthanides		Pr	Nd		Sm	Eu	Gd		Dy	Ho	Er	Tm	Yb	Lu
Actinides	Th	Pa	U	Np										

Figure 1–2 Elements in the periodic table that have been used to prepare stable metallophthalocyanine complexes.

it was shown that the central metal exists in a square planar environment. Unlike the porphyrins, the phthalocyanine macrocycle is essentially planar.

From 1907 to 1963 46 different unsubstituted metallophthalocyanines have been prepared and from 1963 to date an additional 17 unsubstituted metallophthalocyanines have been synthesized. The periodic table in Figure 1-2 contains the elements that have been used to prepare stable metallophthalocyanine complexes [20].

1.3 THE ELECTRONIC SPECTRA OF PHTHALOCYANINES

The spectral properties of t..e phthalocyanines and porphyrins can been explained in terms of the Gouterman "four-orbital" model [21]. In this model, the assumption is made that the inner cyclic-16-member ring of these macrocycles acts as a relatively independent, aromatic annulene dianion. Peripheral groups, such as the fused benzene rings in the phthalocyanine molecule, act as minor perturbations of the core 18-π-electron system. A "descent in symmetry" model uses the molecular orbitals of the D_{16h} annulene to approximate the molecular orbitals of the D_{4h} metalloporphyrins and metallophthalocyanines. Figure 1-3 illustrates how the descent from D_{16h} to D_{4h} symmetry causes the degenerate e_u orbitals to split into pairs of nondegenerate orbitals while the e_g orbitals retain their degeneracy. Under D_{4h} symmetry, the four orbitals of Gouterman's model are the two highest occupied $1a_{1u}(\pi)$ and $1a_{2u}(\pi)$ orbitals and the lowest unoccupied $1e_g(\pi^*)$ orbital. The electronic transitions, within these orbitals, are used to divide the electronic spectra into two distinct spectral regions: the intense narrow absorption in the region between 600 and 700 nm is known as the Q band region, and the broad and less intense absorption in the region between 300 and 400 nm is known as the B or Soret band region. The one electron $1a_{1u}(\pi) \rightarrow 1e_g(\pi^*)$ and $1a_{2u}(\pi) \rightarrow 1e_g(\pi^*)$ transitions give rise to the Q and B (Soret) bands, respectively. In the porphyrins, the $1a_{1u}(\pi)$ and $1a_{2u}(\pi)$ orbitals are accidentally degenerate. The porphyrin Q band is formally forbidden, but gains

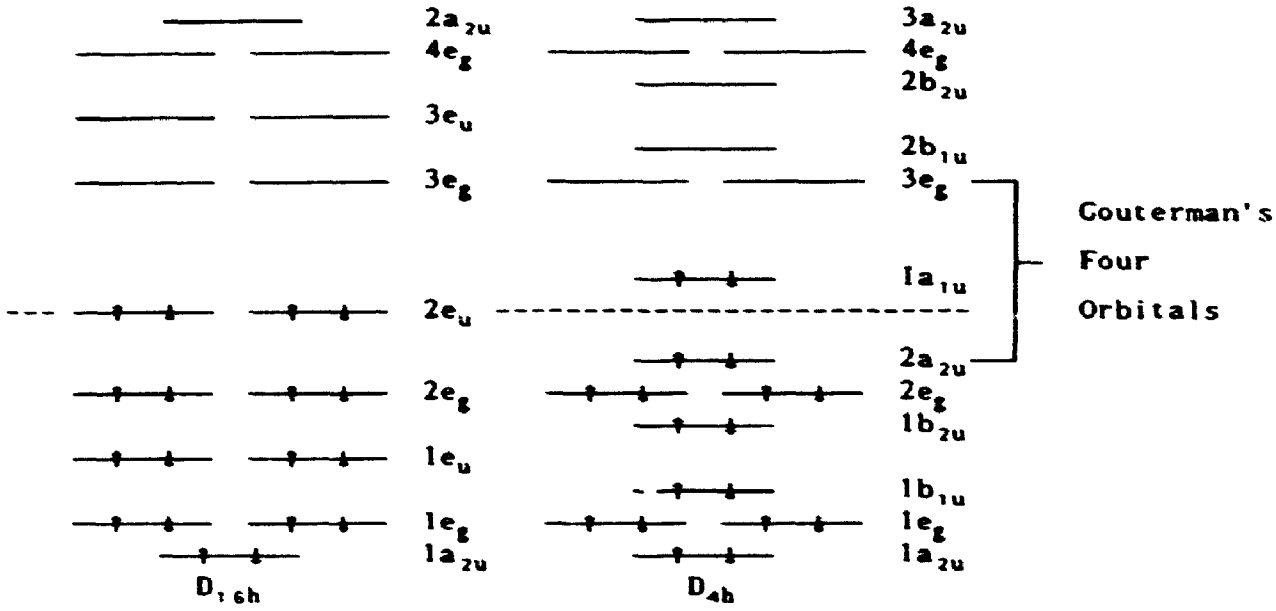

Figure 1–3 An energy level diagram for the molecular orbitals of the 18–π–electron system in an ideal 16–member cyclic annulene and the symmetry reduced D_{4h} metallophthalocyanine.

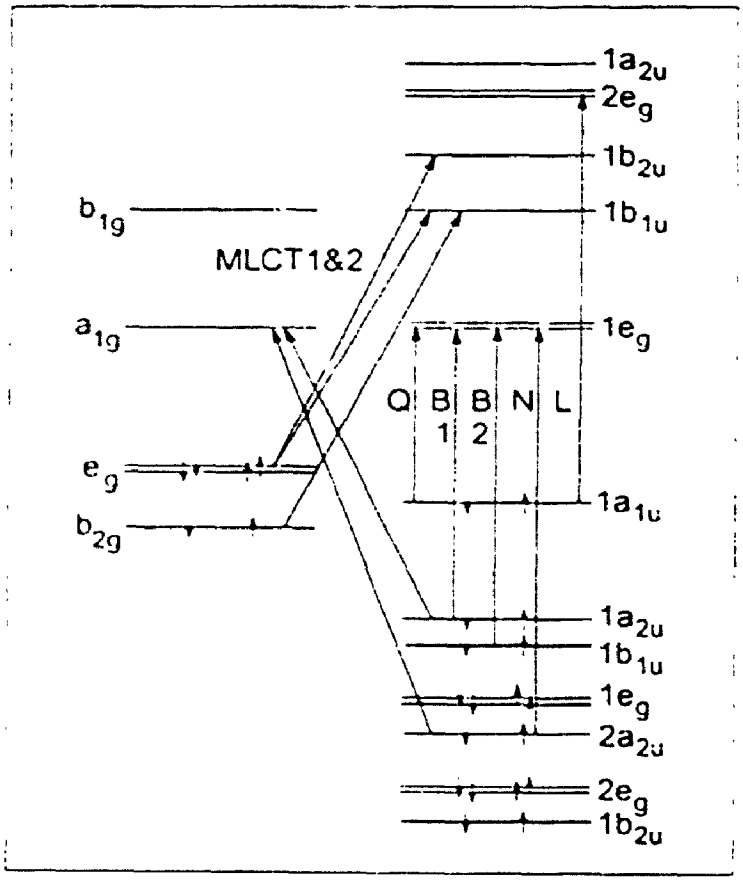

Figure 1–4 Selected molecular orbitals and electronic transition in a transition metal phthalocyanine, with an A_{1g} ground state. The order of the orbitals has been adapted from reference [21].

intensity through configuration interaction with the allowed B band. The aza-bridging nitrogens in the phthalocyanine molecule lifts the accidental degeneracy in the $1a_{1u}(\pi)$ and $1a_{2u}(\pi)$ orbitals. As the two orbitals pull apart in energy, the phthalocyanine Q band gains intensity and becomes the dominant band with extinction coeffients (ε) reaching values of 10^5 $Lmol^{-1}cm^{-1}$.

Gouterman's theory predicts that three additional xy polarized transitions, the N, L and C bands, will occur in the 200 to 400 nm region. These bands arise from other transitions within the molecular orbital system of the 18-π-electron core. Recent studies by our group [1,2] have demonstrated that two degenerate transitions comprise the B band and the Q, B1, B2, N and L ordering, which is shown in Figure 1-4, is now employed in the assignment of the metallophthalocyanine spectra.

The electronic spectra between 200 and 1000 nm, for transition metal phthalocyanines, is further complicated by the presence of charge transfer (CT) bands. Figure 1-4 illustrates that when the energies of the metal 3d orbitals are comparable to the energies of the molecular orbitals of the phthalocyanine ring, then metal to ligand (ML) and ligand to metal (LM) charge transfer (CT) transitions arise in this region of the electronic spectra. Both MLCT and LMCT bands have been identified in the electronic spectra of transition metal phthalocyanines [22,23]. The charge transfer bands, in Figure 1-4, are those expected for a low spin d^6 transition metal phthalocyanine.

1.4 MAGNETIC CIRCULAR DICHROISM SPECTROSCOPY

The studies of metalloporphyrins and metallophthalocyanines have been aided by the development of magnetic circular dichroism (MCD) spectroscopy. When compared to MCD spectroscopy, the more conventional technique of absorption spectroscopy conveys very limited information about the ground and excited states of these macrocycles. Spectral overlap and band broadening due to configuration interaction

often makes it difficult to determine band centre energies directly from the absorption spectra. Unlike absorption spectra, MCD spectra provide state to state transition polarization information that, for these highly symmetric porphyrinic systems, is otherwise only available from crystal studies. MCD also provides direct information about the magnetic moments of degenerate ground and excited states. When MCD spectra are used in conjunction with absorption spectra, they are very useful in discerning band centre energies.

Magnetic optical activity was discovered by Faraday in 1854, but MCD spectroscopy did not obtain interest from chemists and physicists until the 1960's. The advances in MCD spectroscopy may be attributed to the development of compact magnets, with high magnetic fields, that allowed researchers to analyse their data in both qualitative and quantitative manners. The development of instrumentation for the rapid measurement of MCD spectra [24] and the development of theory [25] to explain the data have led to the growth of this experimental technique

1.4.1 MCD Theory

MCD spectroscopy can be thought of as a magnetically induced chirality (CD effect) in a molecule. When a molecule is subjected to an external magnetic field, electronic transitions within the molecule will display a preference for either right or left circularly polarized light. The MCD spectral intensity is represented either as the absorbance difference $\Delta A = A_L - A_R$, where L and R represent left and right circularly polarized light, or as the molar ellipticity $[\theta]_M$. Three spectral band types can arise in a MCD spectrum and the absorbance difference can be represented as the sum of the three terms:

$$\frac{\Delta A}{E} = \frac{\Delta \epsilon c' \ell}{E} = \gamma\beta B \left[A_1 \left[- \frac{\delta f(E)}{\delta E} \right] + \left[B_0 + \frac{C_0}{kT} \right] \times f(E) \right] \qquad (1.1)$$

This follows the notation suggested by Piepho and Schatz [25] where E is the

photon energy, c' is the sample concentration, ℓ is the path length, B is the magnetic field, β is the Bohr magneton, $f(E)$ is the band shape and γ is defined as:

$$\gamma = \frac{2N_0\pi^3\alpha^2c'\ell\log(e)}{250hcn} \tag{1.2}$$

where h is Plancks constant and c is the speed of light.

For an allowed electronic transition A → J, the three MCD terms (A_1, B_0, and C_0) in equation 1.1 and the dipole strength (D_0) are given by:

$$A_1 = \frac{1}{|A|}\left[\langle J\lambda|L_z+2S_z|J\lambda\rangle^0-\langle A\alpha|L_z+2S_z|A\alpha\rangle\right]\left[\langle A\alpha|m_-|J\lambda\rangle^0-\langle A\alpha|m_+|J\lambda\rangle^0\right] \tag{1.3}$$

$$B_0 = \frac{2}{|A|}\,Re\sum_{\alpha\lambda}\left[\sum_{K\kappa(K\neq J)}\frac{\langle J\lambda|L_z+2S_z|K\kappa\rangle^0}{W_K{}^0-W_J{}^0}\times\right.$$

$$\left[\langle A\alpha|m_-|J\lambda\rangle^0\langle K\kappa|m_+|A\alpha\rangle^0-\langle A\alpha|m_+|J\lambda\rangle^0\langle K\kappa|m_-|A\alpha\rangle^0\right]+$$

$$\left.\sum_{K\kappa(K\neq A)}\frac{\langle K\kappa|L_z+2S_z|A\alpha\rangle^0}{W_K{}^0-W_A{}^0}\left[\langle A\alpha|m_-|J\lambda\rangle^0\langle J\lambda|m_+|K\kappa\rangle^0\langle A\alpha|m_+|J\lambda\rangle^0\langle K\kappa|m_-|K\kappa\rangle^0\right]\right] \tag{1.4}$$

$$C_0 = \frac{1}{|A|}\sum_{\alpha\lambda}\langle A\alpha|L_z+2S_z|A\alpha\rangle^0\left[\left|\langle A\alpha|m_-|J\lambda\rangle^0\right|^2-\left|\langle A\alpha|m_+|J\lambda\rangle^0\right|^2\right] \tag{1.5}$$

$$D_0 = \frac{1}{2|A|}\sum_{\alpha\lambda}\left[\left|\langle A\alpha|m_-|J\lambda\rangle^0\right|^2-\left|\langle A\alpha|m_+|J\lambda\rangle^0\right|^2\right] \tag{1.6}$$

In equations 1.3–1.6, A is the electronic degeneracy of state A; K is the state into which A and J are mixed; α, λ, κ are components of the electronic states A, J and K; L_z is the orbital angular momentum; S_z is the spin angular momentum; $W_K{}^0$, $W_J{}^0$ and $W_A{}^0$ are the energies of states K, J and A; and *Re* are the real part of the equations. The electric dipole operators ($m_\pm$) can be represented by:

$$m_\pm = \frac{1}{\sqrt{2}}\left[m_x \pm m_y\right] = \mp\, m_\pm \tag{1.7}$$

The magnetic moment operator (μ_z) is related to the z component of spin and orbital

angular momentum by:

$$\mu_z = -\beta(L_z + 2S_z) \qquad (1.8)$$

The Bohr magneton (β) has a constant value of 0.4669 $cm^{-1}T^{-1}$. Substituting for β and γ, equation 1.1 can be rewritten as:

$$\frac{\Delta A}{E} = \frac{\Delta \epsilon c' \ell}{E} = 152.5 c' \ell \left[A_1 \left[-\frac{\delta f(E)}{\delta E} \right] + \left[B_0 + \frac{C_0}{kT} \right] \times f(E) \right] \qquad (1.9)$$

In equations 1.1 to 1.5, the rigid shift approximation is employed, which means that the absorption band shape is independent of the magnetic field. The Born–Oppenheimer approximation, which assumes that the atomic nuclei stay stationary during electronic transition since they are more massive than electrons, is also utilized in the derivation of equations 1.1 to 1.6. The three terms A_1, B_0 and C_0 are known as the MCD A, B and C terms, respectively.

1.4.2 The MCD A Term

Figure 1–5A demonstrates how the MCD A term arises from a transition from a nondegenerate ground state to a degenerate excited state which has its degeneracy removed by the applied magnetic field. The splitting in the excited states is exactly equal to $g\beta B$, where g is the Lande g factor, β is the Bohr magneton and B is the strength of the applied external magnetic field. The splitting of the excited state and the intensity of the MCD signal are directly related to the strength of the applied magnetic field. The selection rule for the absorption of right circularly polarized (RCP) light is $\Delta M_J = -1$ and for left circularly polarized (LCP) light is $\Delta M_J = +1$. The line shape ($\delta f / \delta E$) of an MCD A term can be considered to be the sum of two oppositely signed bands which are separated from each other by the excited state splitting ($g\beta B$). By convention, absorption of LCP light is taken as positive and absorption of RCP light as negative.

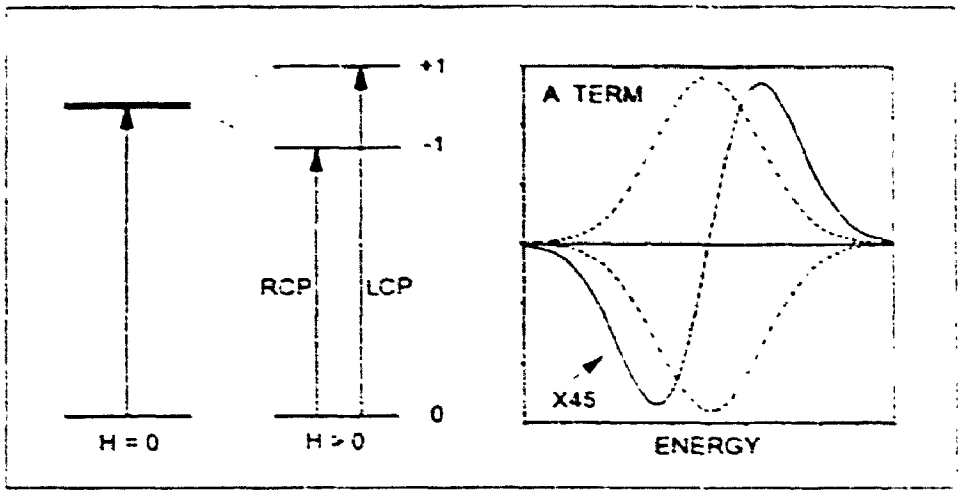

Figure 1-5A The origin and shape of the MCD A term (the A term has been expanded 45 times). The dotted lines represent the positive (ΔM_J=-1) and negative (ΔM_J=+1) intensity transitions that give rise to the A term.

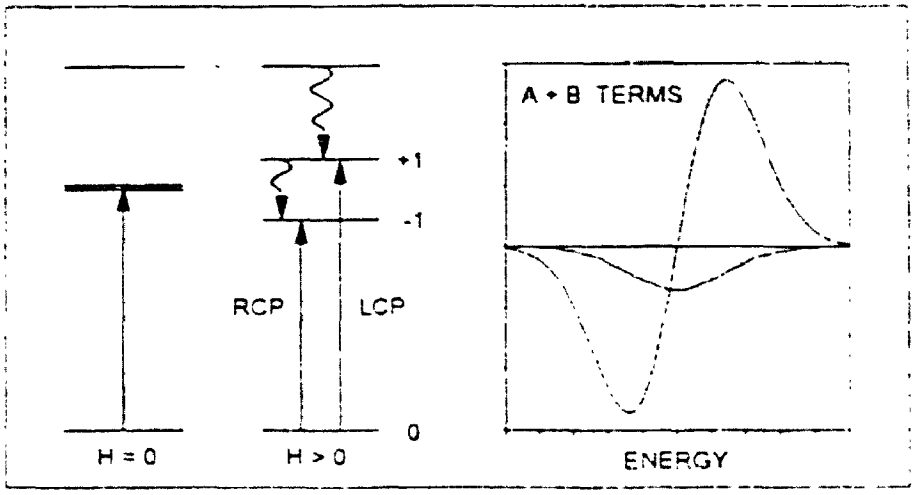

Figure 1-5B The origin and shape of the MCD B term.

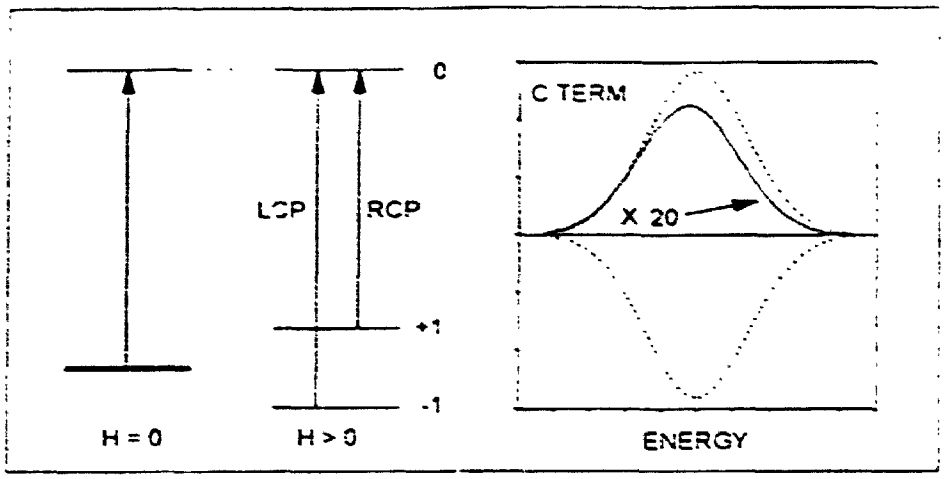

Figure 1-5C The origin and shape of the MCD C term (the C term has been expanded 20 times). The dotted lines represent the positive (ΔM_J=-1) and negative (ΔM_J=+1) intensity transitions that give rise to the C term.

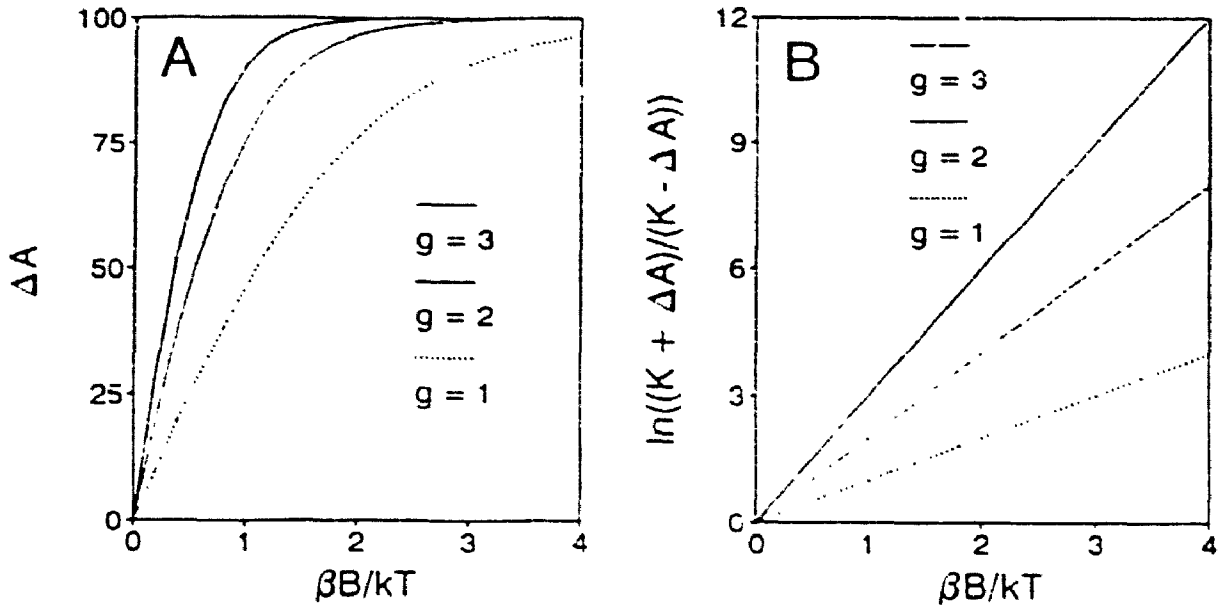

Figure 1-6 Computer simulated plots of **A.** ΔA versus $\beta B/kT$ and **B.** $\ln[(K+\Delta A)/(K-\Delta A)]$ versus $\beta B/kT$, for MCD C terms with orbital g factors of 1, 2 and 3, respectively.

1.4.3 The MCD B Term

The B term shown in Figure 1-5B arises from field induced mixing of states. Under the influence of an applied magnetic field, upper states mix with lower states to impart non-zero ΔM_J values to transitions between nondegenerate states. The degree of field induced mixing of states is inversely proportional to the energy separation between the states. The spectral intensity due to B terms sums to zero across the entire MCD spectrum.

1.4.4 The MCD C Term

MCD C terms arise from degenerate to nondegenerate state to state transitions (Figure 1-5C). The selection rules are the same as those that govern MCD A terms. The shape of the MCD C term is the same as the B term, but unlike the temperature independent B term the C term intensity is temperature dependent. The relative population of the two levels within the degenerate ground states which is governed by the Boltzman distribution functions, determines the intensity of the C term. Variable temperature MCD studies can be used to determine the ground state splitting (ΔE) and the Lande g factor.

1.4.5 MCD Moments

The calculation of absorption and MCD spectra can be used to determine the magnetic moments of degenerate ground and excited states. The zeroth and first moments of the MCD spectrum are defined as [25]:

$$\langle \Delta\epsilon_M \rangle_0 = 152.5 \left[B_0 + \frac{C_0}{kT} \right] = \int \frac{\Delta\epsilon}{E} \, dE \qquad (1.10)$$

$$\langle \Delta\epsilon_M \rangle_1 = 152.5 \, A_1 = \int \frac{\Delta\epsilon}{E} (E - E^0)^1 dE \qquad (1.11)$$

where E^0, for the first moment is the band centre. The zeroth moment of the

absorption spectra is defined as:

$$\langle \epsilon_M \rangle_0 = 326.6\ D_0 = \int \epsilon\, dE \qquad (1.12)$$

$A_1(\beta)/D_0$ and $C_0(\beta)/D_0$ are ratios of that involve magnetic moments of the ground and excited states respectively.

1.5 SPECTRAL ANALYSIS

1.5.1 Band Deconvolution

When high quality absorption and MCD spectra are available, spectral band deconvolution calculations can be employed to determine the location of the electronic transitions that contribute to the spectral envelopes. The deconvolution results can then be used to determine the magnetic moments of the ground and excited states. The difficulty with band deconvolution is the choice of an appropriate band shape function to fit the spectral data. Fitting data with a set of Gaussian and Gaussian-like bands has been shown to be a suitable method for obtaining a set of parameters for the number and position of bands in a set of spectra [1,2,26-28].

The Gaussian line shape functions, as described by Piepho and Schatz [25] are:

$$f_G(E) = \frac{1}{\Delta\sqrt{\pi}} \exp\left[\frac{-(E-E^0)^2}{\Delta^2}\right] \qquad (1.13)$$

for absorption bands, and MCD B and C terms and:

$$\frac{\delta f_G(E)}{\delta E} = \frac{-2(E-E^0)}{\Delta^3\sqrt{\pi}} \exp\left[\frac{-(E-E^0)^2}{\Delta^2}\right] \qquad (1.14)$$

for the derivative shaped MCD A term data. E^0 is the energy of the Gaussian band maximum, Δ is the bandwidth parameter for Gaussian line shapes and is related to the experimental full bandwidth at half height (Γ) by:

$$\Gamma = 2\Delta\sqrt{\ln 2} \qquad (1.15)$$

Substituting equations 1.13 and 1.14 into 1.1 yields:

$$\frac{\Delta A}{E} = \gamma\beta B\left[A_1\left\{\frac{2(E-E^0)}{\Delta^3/\pi}\exp\left[\frac{-(E-E^0)^2}{\Delta^2}\right]\right\}+\left[B_0+\frac{C_0}{kT}\right]\left\{\frac{1}{\Delta/\pi}\exp\left[\frac{-(E-E^0)^2}{\Delta^2}\right]\right\}\right] \tag{1.16}$$

When $E = E^0$, equation 1.16 breaks down and B_0, C_0 can be solved from:

$$\left[\frac{\Delta A}{E}\right]_0 = \gamma\left[B_0+\frac{C_0}{kT}\right]\left[\frac{1}{\Delta/\pi}\right]\beta B \tag{1.17}$$

and D_0 can be solved from:

$$\left[\frac{A}{E}\right] = \gamma D_0\left[\frac{1}{\Delta/\pi}\right] \tag{1.18}$$

The maxima for MCD A terms corresponds to $E=\Delta/2$ and A_1 can be obtained from:

$$\left[\frac{\Delta A}{E}\right]_{\Delta/\pi} = \gamma A_1\beta B\left[\frac{-2e}{\Delta/\pi}\right]+\left[\frac{\Delta A}{E}\right]_0\exp\left[\frac{-(\Delta/2-E^0)^2}{\Delta^2}\right] \tag{1.19}$$

A non-linear least squares fitting procedure is used to fit the absorption data while a Simplex procedure is used to fit the MCD data.

1.5.2 Determination of the g Factor for Degenerate Ground States

When a molecule has a degenerate (E) ground state (Figure 1-5C), the relative population of the two energy levels within the Zeeman split ($B\neq0$) Kramers doublet is governed by the Boltzman distribution function:

$$\frac{N_-}{N_+} = \exp\left[-\Delta E/kT\right] \tag{1.20}$$

where N_- represents the relative population of the upper state, N_+ represents the relative population of the lower state, ΔE is the energy difference between the two states, k is the Boltzman constant and T is the temperature of the sample. Substituting $g\beta B$ for ΔE and $(1-N_+)$ for N_-, equation 1.20 is rewritten as:

$$N_+ = \frac{1}{1+\exp\left[-g\beta B/kT\right]} \tag{1.21}$$

In the MCD spectrum, if the spectral band width (Γ) is much larger than the Zeeman splitting (ΔE), then the observed MCD C term spectral intensity can be approximated by:

$$\Delta A \simeq K(N_+ - N_-) \tag{1.22}$$

where ΔA is the MCD spectral intensity and K is the saturated MCD spectral intensity constant that represents ΔA, when the MCD spectral intensity is saturated. Since the population of the two levels comprising the ground Kramers doublet sums to unity, N_- can be replaced by $(1-N_+)$ to give:

$$\Delta A = K(2N_+ - 1) \tag{1.23}$$

Substituting equation 1.21 into equation 1.23 and multiplying both sides of the resulting equation by exp $[g\beta B/kT]$ yields:

$$\Delta A = K \frac{\exp\,[g\beta B/kT] - 1}{\exp\,[g\beta B/kT] + 1} \tag{1.24}$$

Equation 1.24 relates the MCD spectral intensity (ΔA) to the applied magnetic field (B) and to the sample temperature (T). The plot of ΔA versus $\beta B/kT$ in Figure 1-6A is a computer simulation of MCD C terms with Lande g factors of 1, 2 and 3, respectively. The value of the Lande g factor can be determined by isolating the exponential in equation 1.24 to give:

$$\exp\,[g\beta B/kT] = \frac{K + \Delta A}{K - \Delta A} \tag{1.25}$$

and then taking the natural log of equation 1.25 to yield

$$\frac{g\beta B}{kT} = \ln\left[\frac{K + \Delta A}{K - \Delta A}\right] \tag{1.26}$$

The plot of $\ln[(K+\Delta A)/(K-\Delta A)]$ versus $\beta B/kT$ is linear and the slope of the line is the average Lande g factor. Equation 1.26 is used to generate the natural log plots in Figure 1-6B for Lande g factors of 1, 2 and 3, respectively.

1.6 SCOPE OF THESIS

Although metallophthalocyanines have been extensively studied there is a poor understanding of the electronic arrangement within these molecules. In several instances experimental assignments of spectral data [26,27] disagree with theoretical assignments [21,29-30] of the energies of electronic transitions within the molecule. In order to understand the electronic arrangement within individual metallophthalocyanine molecules, absorption and MCD spectra have been used in the determination of the energies of specific state to state transitions in neutral and ring oxidized metallophthalocyanines. Chemical, electrochemical and photochemical oxidation methods are employed in the generation of stable, long lived phthalocyanine π-cation radicals. The spectral results for the phthalocyanine π-cation radical complexes are especially important because they contribute to the limited spectral database for phthalocyanine π-anion and π-cation radicals [26,28,31,32].

The peripherally substituted phthalocyanines, studied in Chapter 3, are used to determine the effect of asymmetric substitution on the zero field splitting of the degenerate excited states. The asymmetric arrangement of the peripheral groups reduces the total molecular symmetry from D_{4h} to D_{2h} and, depending on the strength of this perturbation, it may remove the degeneracy from the e_g orbitals. Absorption and MCD spectra probe the degeneracy of the molecular orbitals within the 18-π-electron system of the metallophthalocyanine-N-isologs: $MgPcN_4(-2)$, $ZnPcN_4(-2)$ and $ZnPcN_8(-2)$.

The absorption and MCD spectra of neutral and ring oxidized magnesium phthalocyanine (MgPc) are presented in Chapters 4 and 5, respectively. Since magnesium is chromophorically silent, the electronic transitions that contribute to the spectral intensity are pure ring transitions. Spectral deconvolution results are used to locate and to determine the energy of the Q, B1, B2, N and L bands. The spectra of MgPc can then be used in Chapters 6 to 9, where we attempt to separate LMCT

and MLCT bands from the ring transitions.

In Chapters 6 to 9, absorption, electron paramagnetic resonance (EPR), and MCD spectroscopy are employed in our study of the ligand and the redox chemistry of iron phthalocyanine (FePc). In these four chapters, we study complexes of low spin (S=0) iron(II) phthalocyanine (L_2Fe(II)Pc(−2)), low spin (S=1/2) iron(III) phthalocyanine (L(X)Fe(III)Pc(−2)), intermediate spin (S=3/2) iron(III) phthalocyanine ((X)Fe(III)Pc(−2)) and low spin (S=1) iron(III) phthalocyanine π−cation radical (X_2Fe(III)Pc(−1)). Analysis of the spectral results focuses on: the orbital and spin degeneracies of the ground states; the site (metal and/or ligand) of oxidation; the effect of axial ligands on band energies; the location, in the absorption and MCD spectra, of MLCT, LMCT, and ring transitions; and the effect of the redox chemistry on the axial ligands.

CHAPTER 2

EXPERIMENTAL

2.1 MATERIALS

Magnesium phthalocyanine (MgPc) was prepared according to literature methods [33]. MgPc and iron phthalocyanine (FePc; Kodak) were purified by repeated vacuum sublimation at 550°C. The fragmentation patterns in the mass spectra of purified samples of MgPc and FePc were used to verify that there was no peripheral substitution at the fused benzene rings and to verify the purity of the samples. Purified samples of the magnesium and zinc 3,4-pyridinoporphrazine ($MgPcN_4$ and $ZnPcN_4$) and zinc 3,4-pyridazinoporphrazine ($ZnPcN_8$) were provided by Dr. K.A.M. Creber (Royal Military College, Kingston, Ontario). The purity of these samples was checked by mass spectroscopy. Additional chemicals essential to this study are: imidazole (im; Aldrich), sodium cyanide (NaCN; Fisher), tetrabutylammonium cyanide (TBACN; Aldrich), pyridine (py; BDH), 4-methylpyridine (mepy; BDH), piperidine (pip; BDH), 1-methylimidazole (meim; Aldrich), ammonia (NH_3; Union Carbide), carbon monoxide (CO; Union Carbide), formic acid (HFo; Fisher), acetic acid (HAc; Fisher), proprionic acid (HPr; Fisher), lactic acid (HLa; Fisher), hydrobromic acid (HBr; Nichols), hydrochloric acid (HCl; BDH), 1,1-dichloromethane (DCM; BDH), 1,2-dichloroethane (DCE; BDH), 1,4-dichlorobutane (DCB; Aldrich), ortho-dichlorobenzene (*o*-DCB; Kodak), 2-chlorobutane (CB; BDH), N,N-Dimethylformamide (DMF; BDH), N,N-Dimethylacetamide (DMA; BDH), Dimethylsulfoxide (DMSO; BDH), methanol (MeOH; BDH), isopropanol (iPrOH; BDH), bromine (Br_2; Fisher), iodine (I_2; Baker), chlorine (Cl_2; Linde), nitric acid (HNO_3; BDH) tetrapropylammonium perchlorate (TPAP; Kodak), carbon tetrabromide (CBr_4; Kodak), magnesium metal (Mg; BDH), urea (Fisher) and phthalonitrile (Kodak). DMF, DMA and CB were distilled prior to use. TPAP was recrystallized twice from

aqueous acetone and CBr_4 was recrystallized twice from 95% ethanol.

2.2 PREPARATION OF L_nMPc COMPLEXES

Three samples of each L_nMPc complex were prepared. The absorption spectra measured for the three samples were compared to each other and to literature spectra (when available), in order to verify the purity of the prepared complex.

TBA[(CN)Zn(II)PcN$_4$(−2) was prepared by refluxing 1 mg of Zn(II)PcN$_4$(−2) in 25 mL of iPrOH containing 0.001 M of TBACN for 1 hour.

L$_2$M(II)Pc(−2) (L = im, meim, py, mepy, pip, CN^-; M = Mg, Fe) was prepared according to literature methods [34,35].

(NH$_3$)$_2$Fe(II)Pc(−2) was prepared by bubbling ammonia gas (NH_3) through a suspension of 1.0 mg Fe(II)Pc(−2) in 25 mL DCM for 30 minutes. The solution was filtered to remove solid Fe(II)Pc(−2).

(NH$_3$)(CO)Fe(II)Pc(−2) was prepared by bubbling carbon monoxide (CO) through a DCM solution of (NH$_3$)$_2$Fe(II)Pc(−2) for 1 hour. Absorption spectra were measured every 5 minutes, in order to follow the conversion from (NH$_3$)$_2$Fe(II)Pc(−2) to (NH$_3$)(CO)Fe(II)Pc(−2).

(S)(CO)Fe(II)Pc(−2) (S = DMA, DMF) was prepared by bubbling carbon monoxide (CO) through a suspension of Fe(II)Pc(−2) (1 mg) in a 95:5 DCE:S mixture for 1 to 2 hours.

2.3 CHEMICAL OXIDATION

0.001 M solutions of the oxidizing agents (Cl_2, Br_2, I_2 and HNO_3) were prepared in DCM. The oxidizing agent was titrated stepwise into a solution of the appropriate MPc complex, with absorption spectroscopy used to monitor the extent of oxidation. The titrations were repeated on three different MPc samples to ensure that the oxidations were reproducable and to verify the purity of the oxidation product.

2.4 PREPARATION OF OXIDIZED MPc COMPLEXES

$[L_nMg(II)Pc(-1)]^+$ (n=1,2) was prepared by titrating either HNO_3 or Br_2 into either DCM or DCE solutions of $L_2Mg(II)Pc(-2)$ (L = H_2O, im, meim, py, mepy, pip, CN−).

L(X)Fe(III)Pc(−2) (X = Cl, Br, I) was prepared by titrating either Cl_2, Br_2, I_2 or HNO_3 into DCM solutions of $L_2Fe(II)Pc(-2)$ (L = im, meim).

$Na[(CN)_2Fe(III)Pc(-2)]$ was prepared by titrating Br_2 into 98:2 DCM:DMF solutions of $Na_2[(CN)_2Fe(II)Pc(-2)]$.

Na[(Cl)(CN)Fe(III)Pc(−2)] was prepared by titrating HCl into a 98:2 DCM:DMF solution of $Na[(CN)_2Fe(III)Pc(-2)]$.

$Cl_2Fe(III)Pc(-1)$ was prepared by titrating Cl_2 into a DCM solution of (meim)(Cl)Fe(III)Pc(−2).

(X)Fe(III)Pc(−2) (X = Cl, Br, Fo, Ac, La, Pr) was prepared by titrating the appropriate acid (HCl, HBr, HFo, HAc, HLa or HPr) into boiling DCB or o-DCB solutions of Fe(II)Pc(−2).

2.5 ELECTROCHEMISTRY

Cyclic voltammetry (CV), differential pulse voltammetry (DPV) and controlled potential coulometry (CPC) measurements were carried out using a Princeton Applied Research model 273 electrochemical system controlled by an IBM instruments S9001 computer, using the computer program ELECTRA [36], essentially as previously described. [35,37]

2.5.1 Cyclic and Differential Pulse Voltammetry

CV and DPV measurements on the $L_2Mg(II)Pc(-2)$ complexes were carried out in freshly distilled DMA in the presence of 0.05 M TPAP. All solutions were deoxygenated with dry nitrogen. A platinum bead was used as the working electrode

and a platinum wire as the auxiliary electrode. Silver wire and ferrocene were used as internal standards [37].

2.5.2 Controlled Potential Coulometry (Electrochemical Oxidation)

Electrochemical oxidation of $(pip)_2Mg(II)Pc(-2)$ was carried out in DCM in the presence of 0.05 M (TPAP) using an oxidation potential of +0.7 V. All solutions were saturated with dry, deoxygenated nitrogen. For oxidations, a platinum mesh was used as the working electrode, while platinum foil was used as the auxiliary electrode. Silver wire was used as an internal standard [37].

2.6 PHOTOCHEMICAL OXIDATION

For photochemical oxidation, $(meim)_2Mg(II)Pc(-2)$ was dissolved in nitrogen-saturated DCM made up to 0.01 M in CBr_4. The solution was irradiated with light from a 300 W tungsten-halogen Kodak projector lamp. Irradiation into the Q band of the phthalocyanine was ensured by the use of a Corning CS 2-73 high energy (580 nm) cut-off filter.

2.7 SPECTROSCOPIC METHODS

2.7.1 Absorption and MCD Spectra

All solutions were saturated with nitrogen gas prior to the measurement of their absorption and MCD spectra. Spectra of MgPc and FePc complexes were recorded in either DCM, DCE or DCB solutions while spectra of $MgPcN_4$, $ZnPcN_4$ and $ZnPcN_4$ were recorded in either iPrOH, DMA or DMSO solutions. Low temperature ($T<150$ K) spectra of MgPc and FePc complexes were recorded on glassed samples. The glasses were prepared from solutions of 70:30 DCM:CB or 50:50 DCB:DCE.

Absorption spectra were recorded using Cary model 219 and 2200 spectrophotometers. Low temperature absorption spectra were recorded from samples

placed in an Oxford Instruments CF-204 cryostat. MCD spectra were recorded at room temperature using a Jasco J500C spectropolarimeter controlled by a IBM S9001 computer using the computer program CDSCANS [38,39], with a field of 5.5 tesla provided by an Oxford Instruments SM2 superconducting magnet. Calibration of the MCD signal intensity was performed using an aqueous solution of cobalt(II) sulphate, with the negative band intensity at 510 nm, as $\Delta\epsilon_M$=-1.9x10^{-2} L mol^{-1} cm^{-1} T^{-1}. Low temperature MCD spectra were measured from samples placed in an Oxford instruments SM4 superconducting magnet which has a maximum field strength of 4.9 tesla.

2.7.2 Electron Paramagnetic Resonance (EPR) Spectra

Room and low temperature EPR spectra were recorded on a Bruker ESP 300 spectrometer with solution samples being placed in 4 mm o.d. quartz tubes. The absolute values of the g factors were calculated from the signal of either a carbon black or a DPPH standard. Low temperature (T<10 K) EPR measurements on oxidized FePc complexes were recorded from samples placed in an Oxford instruments ESR-900 continuous flow cryostat. Variable temperature (200 - 300 K) EPR spectra of [(meim)Mg(II)Pc(-1)]$^{\cdot+}$ were measured using the Bruker ER-4111-VT variable temperature unit.

2.7.3 Data Analysis

Gaussian band shapes were used to fit the absorption and MCD spectra. Fitting was performed using the program SIMPFIT [40], which utilizes a Simplex routine, to fit the MCD spectra, and a least squares minimisation routine based on second derivatives, to fit the absorption data. The database management program Spectra Manager [41] was used to manipulate the spectral data.

CHAPTER 3

NITROGEN HOMOLOGUES OF MAGNESIUM AND ZINC PHTHALOCYANINE

3.1 INTRODUCTION

In recent years there has been a considerable effort to modify the periphery of the phthalocyanine molecule in order to increase its solubility [42–44]. While the studies of the chemical and physical properties of porphyrins have been aided by their high solubility in a wide variety of solvents, similar studies of phthalocyanines have been hindered by their limited solubility. The solubility of phthalocyanines is enhanced by the choice of the central metal, by the addition of axial ligands to form soluble five and six coordinate MPc complexes, and by chemical modification of the peripherally fused benzene rings. Group I and II metallophthalocyanines exhibit high solubilities in a wide range of spectroscopic and electrochemically useful solvents. Axial ligands do enhance the solubility of many metallophthalocyanines, but the presence of excess ligand in solution or even the bound ligands themselves, reduces the transparency in the 200 to 300 nm region. In tetrasulphonated phthalocyanines, the presence of sulphate groups enhances the solubility of the phthalocyanine, but aggregation makes interpretation of the spectroscopic data difficult [1].

While the absorption and magnetic circular dichroism (MCD) spectra of symmetric phthalocyanines are well known [1,2], very little data are available for phthalocyanines with unsymmetric peripheral substitution. The symmetry reduced free base phthalocyanine (H_2Pc) is characterized by two major bands in the Q region (or Q band region) at 650 and 697 nm [1,34,45]. The reduction from D_{4h} to D_{2h} symmetry breaks the degeneracy of the e_g orbitals and the MCD spectra clearly identify the split Q_x and Q_y components [1,34,45]. In heme porphyrins, the effect of unsymmetric peripheral substitution is to remove the degeneracy of the E_g excited states through rhombic distortion of the molecule [46]. The zero field splitting

parameters for metalloporphyrins can be measured from the MCD and absorption spectral data, but the compression of the electronic transitions into a narrow spectral range makes accurate determination of these parameters difficult. Although the effects of unsymmetric peripheral substitution are not well known for phthalocyanines, the intense, narrow and relatively isolated Q_{00} transition can be used to study rhombic distortions and to determine the zero field splitting parameters. The MCD technique provides the unambiguous assignment criteria which may be used to calculate the extent of the splitting induced by the reduction in symmetry. Figure 3-1 shows the

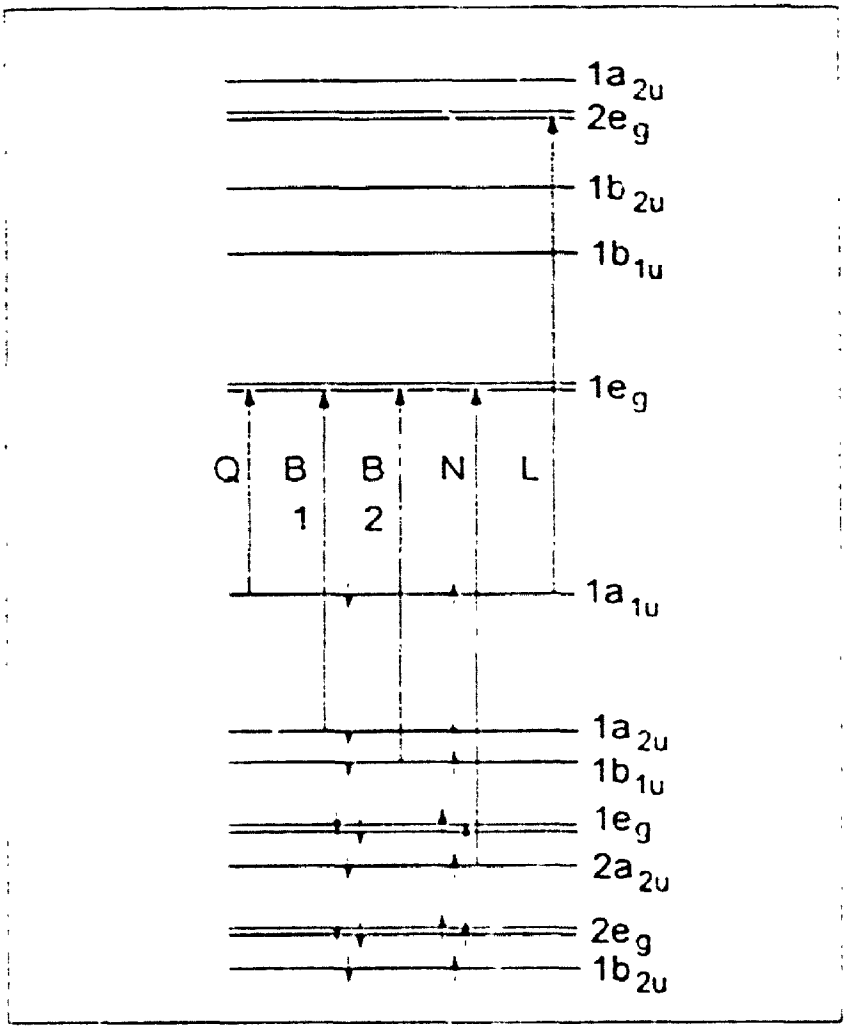

Figure 3-1 Selected molecular orbitals and allowed ring transitions for a metallophthalocyanine with D_{4h} symmetry.

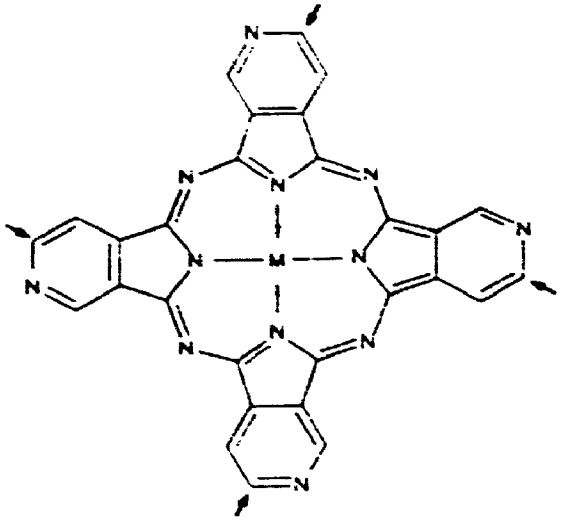

I (C_{4h} . 1/8)

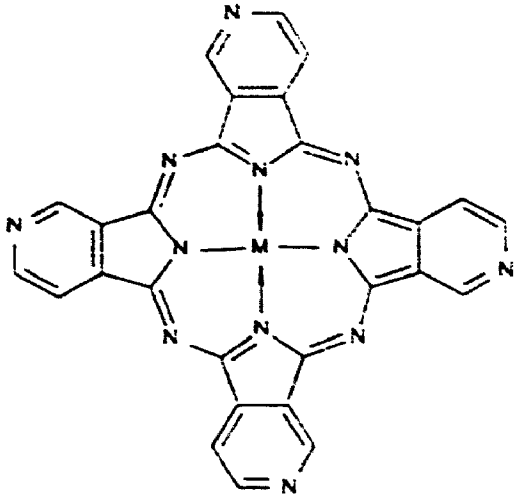

II (D_{2h} . 1/8)

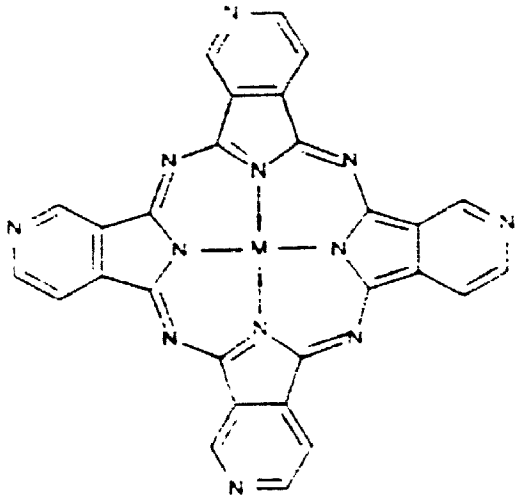

III (C_{2v} . 2/8)

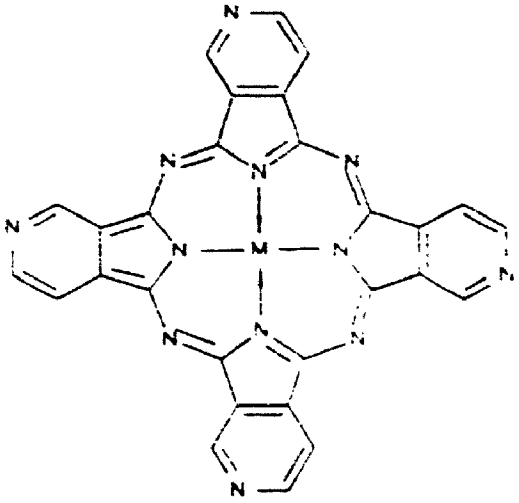

IV (C_s . 4/8)

Figure 3-2 The four structural isomers of $MPcN_8(-2)$. The symmetry group and the statistical probability of formation for each isomer is listed below the isomer. The arrows pointing towards isomer I are directed towards the carbon atoms that are replaced by nitrogen atoms in $MPcN_8(-2)$.

simplified molecular orbital diagram, based on Gouterman's four-orbital calculations [21], that identifies the one-electron transitions which give rise to the first 5 allowed transitions in symmetric, closed-shell metallophthalocyanines [26,27]. Each of the resulting states will be orbitally degenerate, and positive A terms will be observed in the MCD spectrum.

In the late 1950's and early 1960's, cobalt and nickel salts were reacted in a urea melt with cinchomeronic acid (3,4-dicarboxypyridine) to form phthalocyanine derivatives where the peripherally fused benzene rings were replaced with fused pyridines [47-51]. Absorption spectra of various metal-3,4-pyridinoporphrazines (metallophthalocyanine-N-isologs; $MPcN_4$) indicated the presence of two overlapping bands where a single degenerate Q band was normally situated [47,49]. During its synthesis, $MPcN_4$ can be formed as one or more of the four possible structural isomers displayed in Figure 3-2. Since three isomers have reduced symmetries, it is reasonable to assume that the two overlapping bands occur either from a mixture of structural isomers or from a single structural isomer exhibiting significant rhombic distortion.

In this chapter, we report absorption and MCD spectra for $MgPcN_4(-2)$, $ZnPcN_4(-2)$ and the symmetric D_{4h} zinc-3,4-pyridazinoporphrazine ($ZnPcN_8(-2)$) (Figure 3-2). Deconvolution calculations are used to obtain band centre energies and to obtain the magnetic moments of the transitions that contribute to the observed spectral envelopes, especially the in Q region between 500 and 700 nm.

3.2 RESULTS

3.2.1 Spectral Data

A common feature in the absorption spectra of symmetric metallophthalocyanines is the intense narrow band near 670 nm which is associated with a positive MCD A term [1]. Figure 3-3 shows the absorption and MCD spectra of $MgPcN_4(-2)$ in

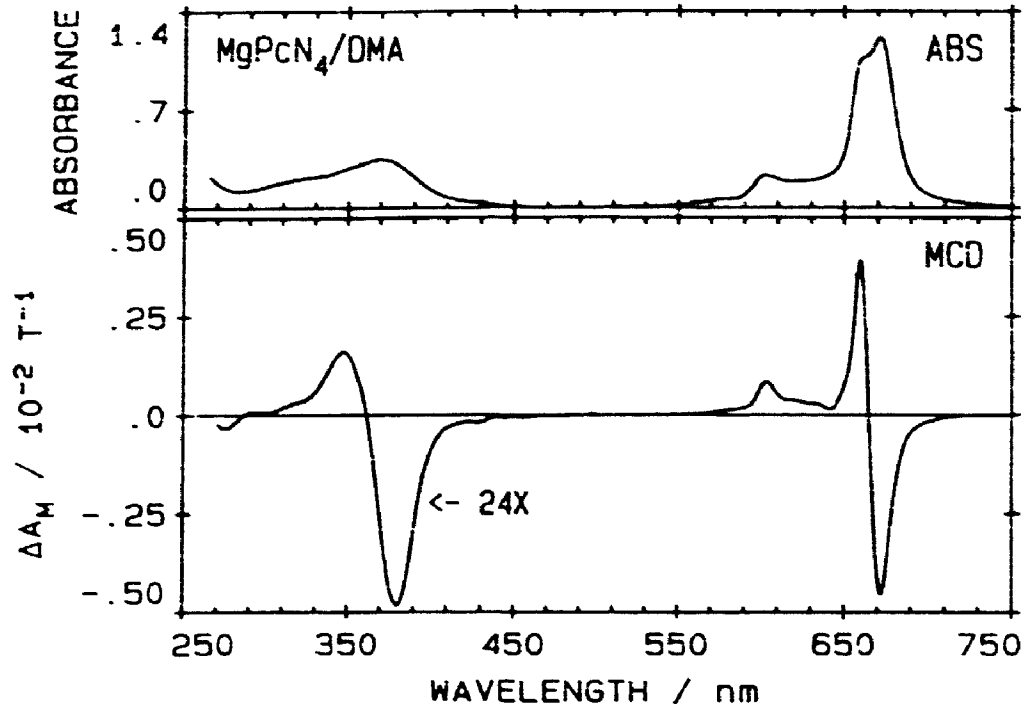

Figure 3–3 Absorption (ABS) and MCD spectra for $MgPcN_4$(–2) in DMA.

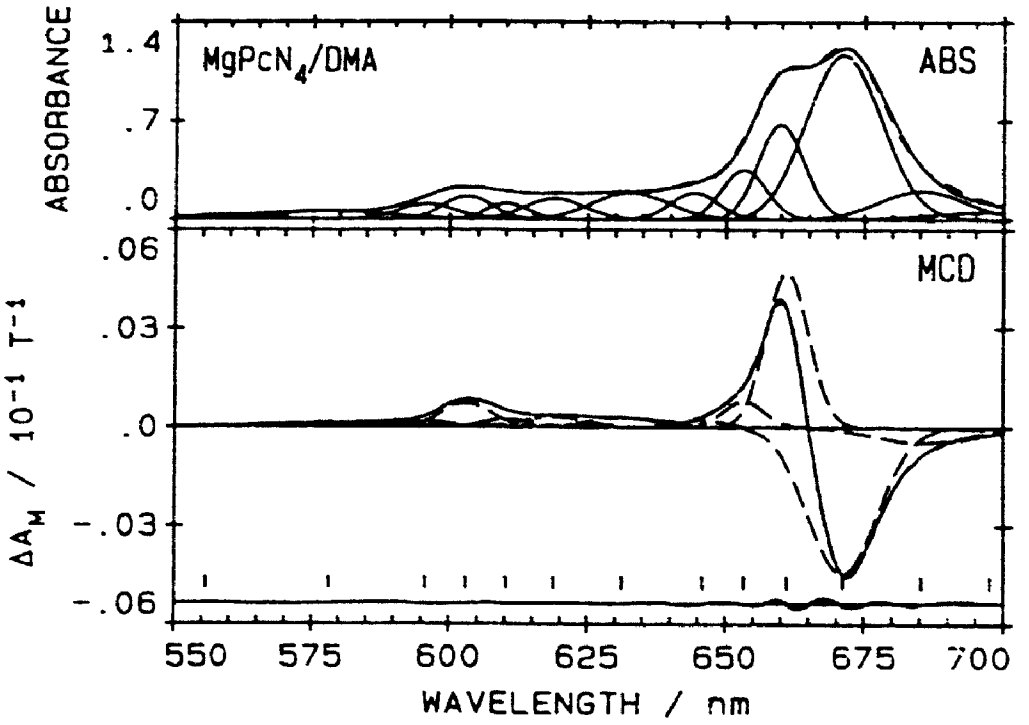

Figure 3–4 Results of a band analysis for $MgPcN_4$(–2) in DMA in the visible region (bands 1–13). (a) Absorption: (———) experimental data; (– – – –) fitted data; (———) individual bands. (b) MCD (———) experimental data; (– – –) fitted data; (– – –) B terms.

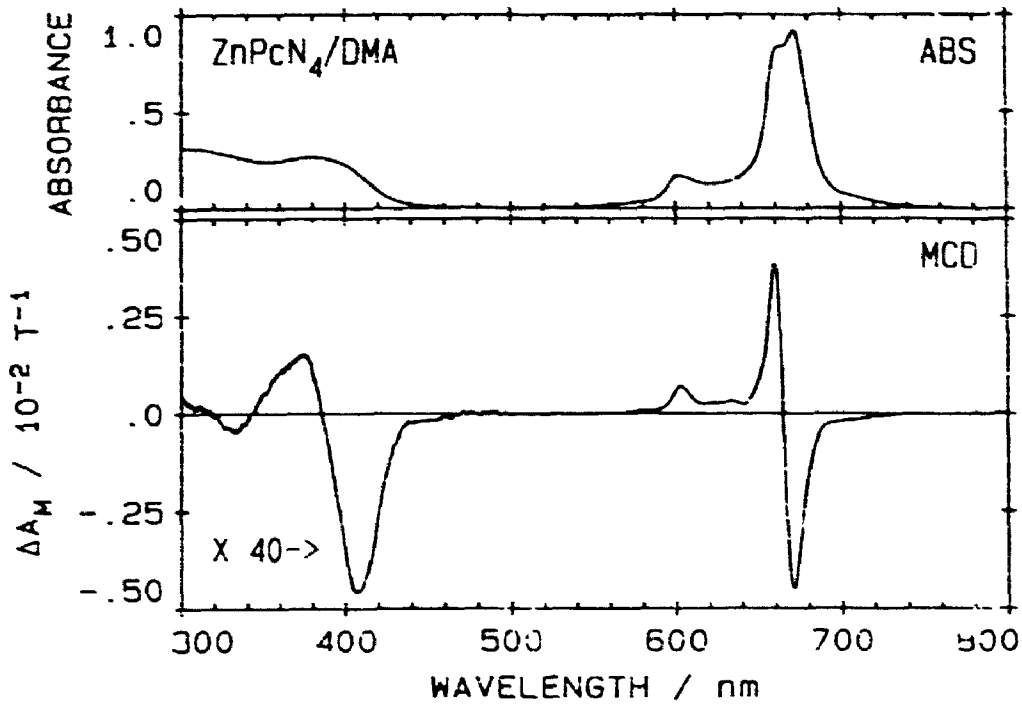

Figure 3-5 Absorption (ABS) and MCD spectra for $ZnPcN_4(-2)$ in DMA.

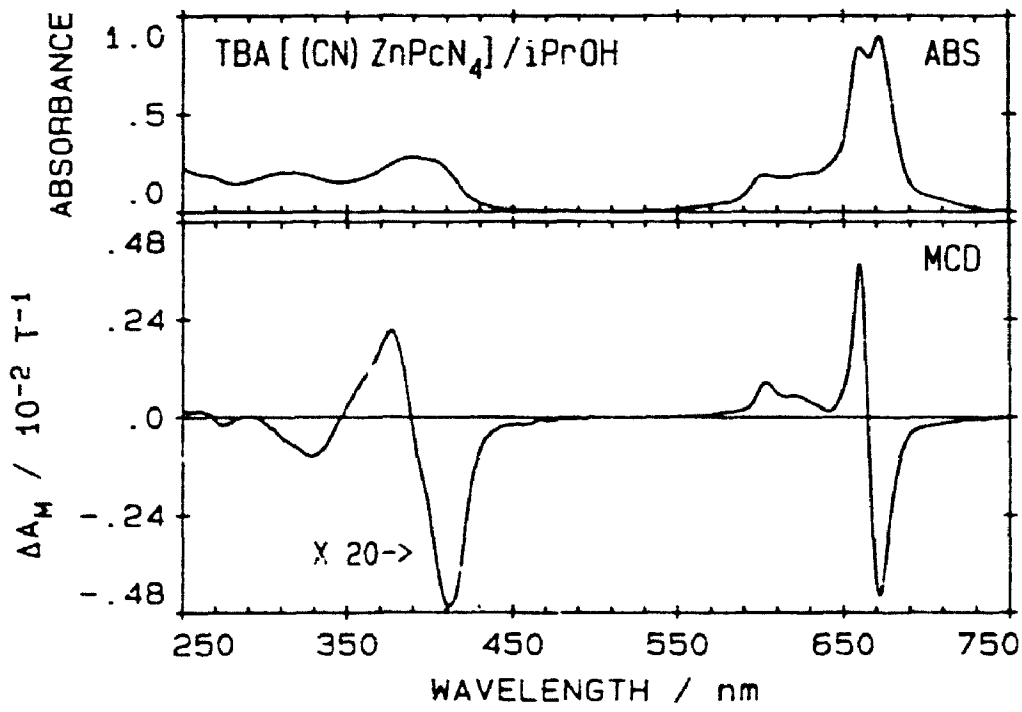

Figure 3-6 Absorption (ABS) and MCD spectra for $TBA[(CN)ZnPcN_4(-2)]$ in iPrOH.

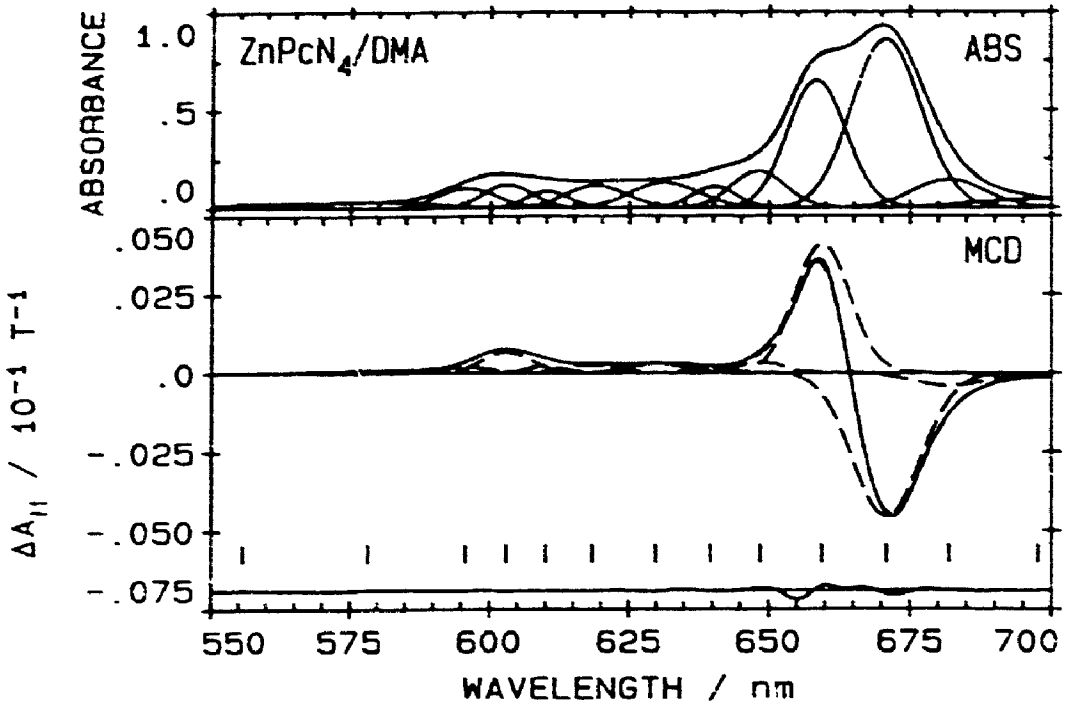

Figure 3–7 Results of a band analysis for $ZnPcN_4$(–2) in DMA in the visible region (bands 1–13). (a) Absorption: (———) experimental data; (– – – –) fitted data; (———) individual bands. (b) MCD (———) experimental data; (– – –) fitted data; (– – –) B terms.

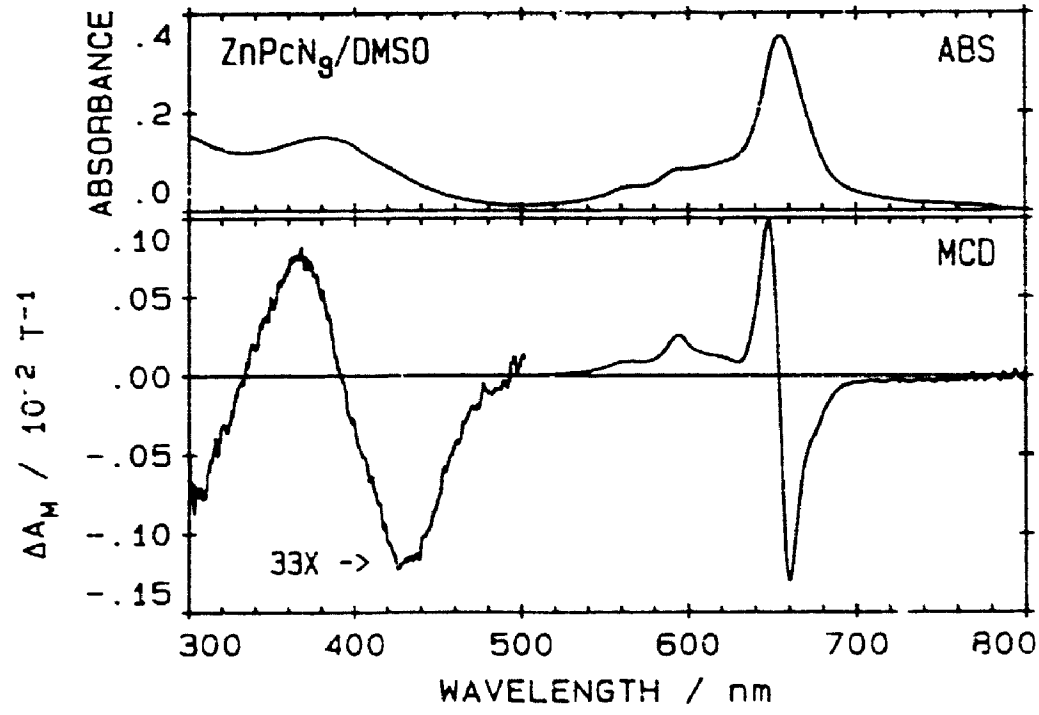

Figure 3–8 Absorption (ABS) and MCD spectra for $ZnPcN_8$(–2) in DMSO.

DMA. The predominant feature in the absorption spectrum (Figure 3-3) is the zero field split Q band between 650 and 680 nm. Molecular aggregation is ruled out as the cause of this splitting, since aggregation would cause extensive broadening in the Q region. The MCD spectral envelope between 625 and 700 nm appears to have the degenerate band shape that is typical of an MCD A term. The band deconvolution results in Figure 3-4 show that the MCD feature arises from two overlapping, oppositely signed, nondegenerate transitions; MCD B terms. Aside from the split Q bands, the absorption and MCD spectra bear a close resemblance to those of simple, unsubstituted phthalocyanines with the series of Q_{vib} bands, the spectral window between 450 and 550 nm and the series of overlapping transitions in the 300 to 500 nm region.

The Q region absorption and MCD spectra of $ZnPcN_4(-2)$ (Figure 3-5), recorded in DMA, and TBA[$(CN)ZnPcN_4(-2)$] (Figure 3-6), recorded in iPrOH, closely resemble the spectra of $MgPcN_4(-2)$ (Figure 3-3). Both sets of spectra have the two absorbance bands where the single Q band is expected and the MCD spectra exhibits an asymmetric degenerate band shape. Deconvolution of the Q region of $ZnPcN_4(-2)$ (Figure 3-7) also indicates that the derivative shape arises from two overlapping,

Table 3-1

Observed Maxima in the Absorption Spectra of the $MPcN_{4,8}(-2)$ Complexes

$MPcN_{4,8}$	λ/nm					
$ZnPcN_8$/DMSO	655	594		569	381	
$MgPcN_4$/DMA	671	662†		603	369	
$ZnPcN_4$/DMA	672	664†		602	380	
$[(CN)ZnPcN_4]^-$/iPrOH	671	660	627	601	389	312

† shoulder

oppositely signed MCD B terms. The B region (500 - 250 nm) of TBA[(CN)ZnPcN$_4$(-2)] (Figure 3-6) has the spectral envelope expected when cyanide is used as an axial ligand [1,35,52]. In addition, the overlapping bands in the 650 to 700 nm region are split further apart when cyanide is the axial ligand.

The absorption and MCD spectra of ZnPcN$_8$(-2), recorded in DMSO are displayed in Figure 3-8. The predominant feature is the single intense absorbance band in the 625 to 700 nm region of the spectrum. The MCD spectral envelope in this region has the symmetric derivative shape expected for a nondegenerate to degenerate state to state transition. The Q region spectral deconvolution in Figure 3-9 demonstrates that this feature can be fitted with an MCD A term. The absorption band maxima recorded from the absorption spectra (Figures 3-3, 3-5, 3-6 and 3-8) are listed in Table 3-1.

3.2.2 Spectral Envelope Deconvolution Calculations

The fits of the absorption and MCD spectra of MgPcN$_4$(-2), ZnPcN$_4$(-2) and ZnPcN$_8$(-2) were split into the 500 - 800 nm (Q band) and 250 - 500 nm (B band) regions (Figures 3-4, 3-7, and 3-9 to 3-12). Deconvolution of the Q region for MgPcN$_4$(-2) (Figure 3-4) and ZnPcN$_4$(-2) (Figure 3-7), required 13 bands to fill the absorption and the MCD spectral envelopes. The electronic transitions are nondegenerate, since all the bands correspond to B terms in the MCD spectra. Included in the MCD plots is the residual, which is the difference in the experiment and fitted envelopes. The randomness of the residual plots indicates that there is little systematic error in fitting the MCD envelope. The greatest noise occurs in the 650 to 700 nm region where two B terms were fit to the two overlapping absorption bands. Attempts to fit one or two MCD A terms in this region did not significantly reduce the residual noise or enhance the quality of the spectral fit. The bands at 671 nm (14 902 cm^{-1}) and 661 nm (15 126 cm^{-1}), for MgPcN$_4$(-2) and at 671 nm

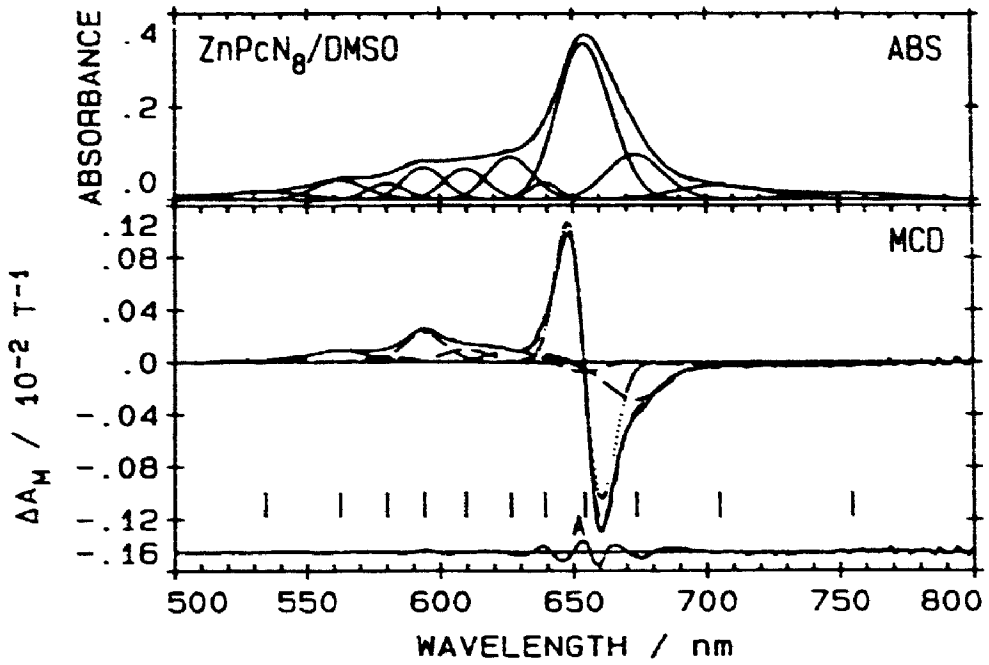

Figure 3-9 Results of a band analysis for $ZnPcN_8(-2)$ in DMA in the visible region (bands 1-11). (a) Absorption: (———) experimental data; (- - - -) fitted data; (———) individual bands. (b) MCD (———) experimental data; (- - -) fitted data; (.....) A terms; (– – –) B terms. The band centre of the MCD A term is labelled.

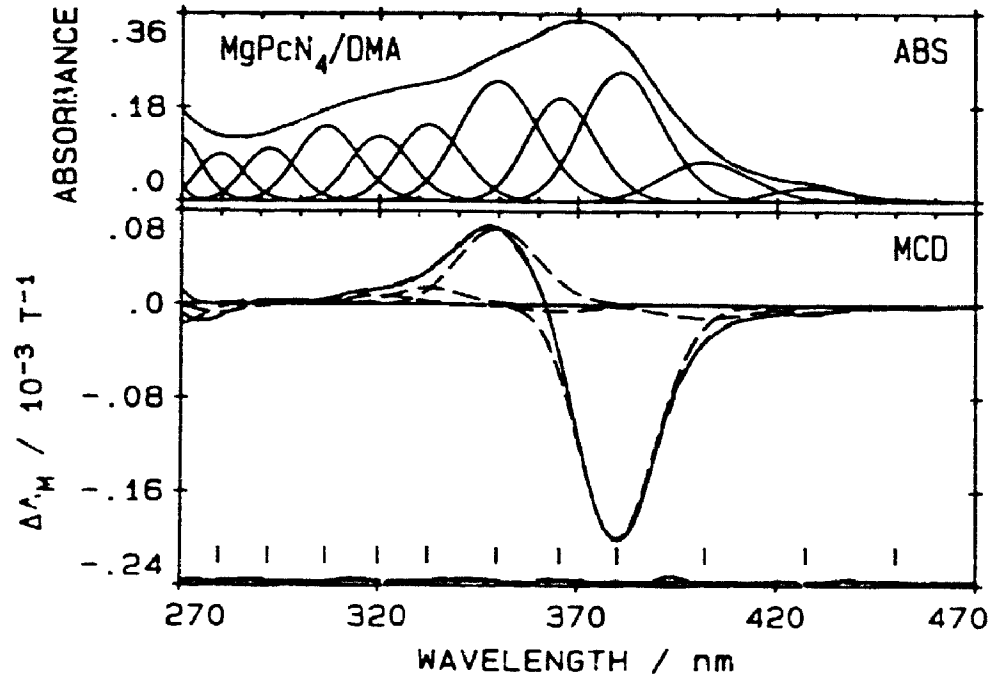

Figure 3-10 Results of a band analysis for $MgPcN_4(-2)$ in DMA in the ultraviolet region (bands 14-24). (a) Absorption: (———) experimental data; (- - - -) fitted data; (———) individual bands. (b) MCD (———) experimental data; (- - -) fitted data; (– – –) B terms.

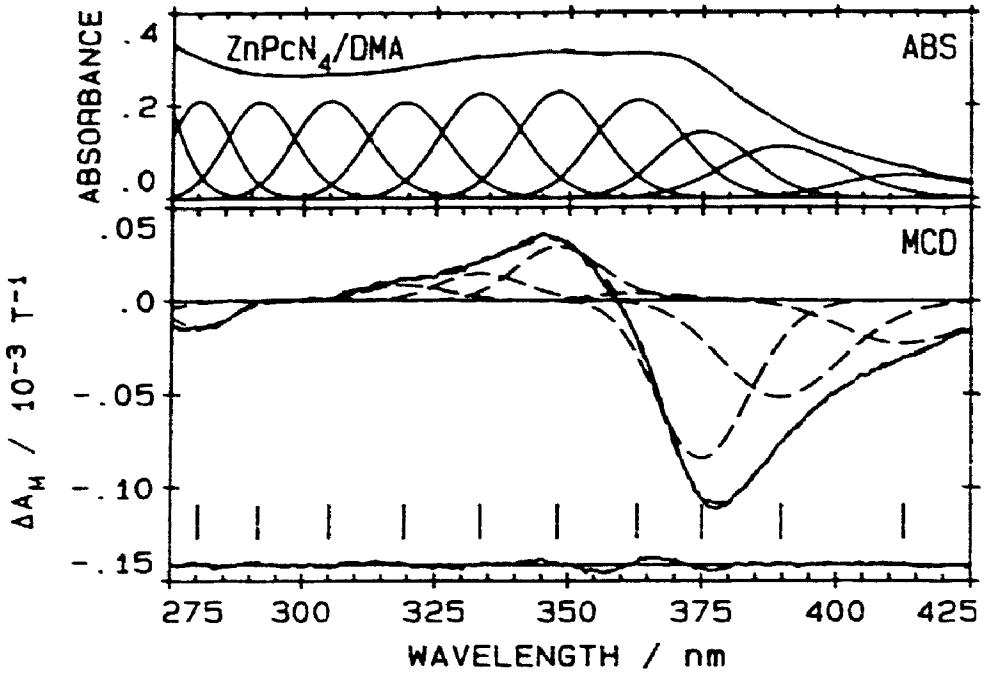

Figure 3-11 Results of a band analysis for $ZnPcN_4(-2)$ in DMA in the ultraviolet region (bands 14-23). (a) Absorption: (———) experimental data; (– – – –) fitted data; (———) individual bands. (b) MCD (———) experimental data; (– – –) fitted data; (– – –) B terms.

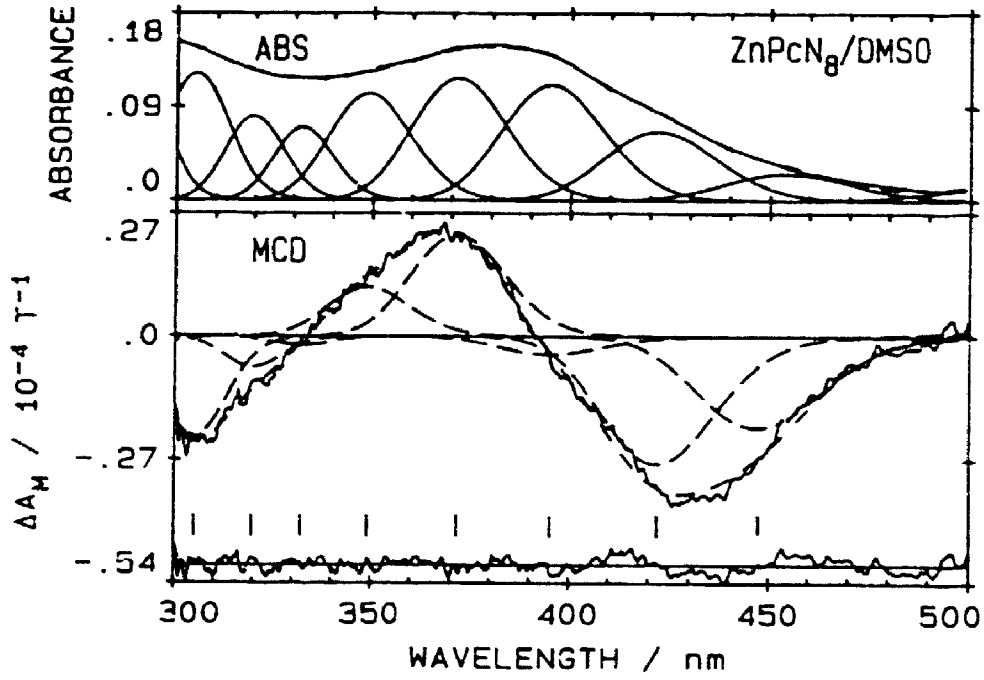

Figure 3-12 Results of a band analysis for $ZnPcN_8(-2)$ in DMA in the ultraviolet region (bands 12-19). (a) Absorption: (———) experimental data; (– – – –) fitted data; (———) individual bands. (b) MCD (———) experimental data; (– – –) fitted data; (– – –) B terms.

(14 910 cm^{-1}) and 658 nm (15 189 cm^{-1}), for $ZnPcN_4(-2)$ have been assigned as the zero field split x and y components of the Q band.

The B region of the phthalocyanine-N-isologs is complicated by the presence of several overlapping and relatively equal intensity transitions. In Figures 3-10 and 3-11, twelve and eleven bands are required to fit this spectral region for $MgPcN_4(-2)$ and $ZnPcN_4(-2)$, respectively. When the absorption spectrum has the complexity that the B region displays, the MCD spectrum provides the necessary and critical information that allows sensible fits to be obtained. Since the absorption band in Figures 3-10 and 3-11 were fit to MCD B terms, the B region spectral envelope is dominated by nondegenerate transitions. The residuals show little systematic noise, a result which indicates a satisfactory fit of the MCD spectra. The fitting parameters for $MgPcN_4(-2)$ and $ZnPcN_4(-2)$ are summarized in Tables 3-2 and 3-3.

Deconvolution results for the Q (500 - 800 nm) and the B (290 - 500 nm) regions of $ZnPcN_8(-2)$ are presented in Figures 3-9 and 3-12. The Q region is fit to eleven bands. All but one of absorption bands were fit to MCD B terms. The band at 654 nm (15 282 cm^{-1}) was fit to linked MCD A and B terms. The A term is indicative of a transition from a nondegenerate ground state into a degenerate excited state and is assigned as the Q band. The quality of the MCD spectrum between 300 and 500 nm is low because of the low solubility of $ZnPcN_8(-2)$ in DMSO. The poor quality makes the fit of this region (Figure 3-12) highly questionable. The 9 bands required to fit the absorption spectrum correspond to B terms in the MCD spectrum, but the MCD residual suggest that there is very little validity to this fit. The fitting parameters for $ZnPcN_8(-2)$ are summarized in Table 3-4.

Table 3-2
Band Fitting Parameters[a] for $MgPcN_4(-2)$ in DMA[c].

band no.	ν cm^{-1}	λ nm	$\Delta\nu$ cm^{-1}	D_0/C^b (10^{-5})	band type	$\langle\Delta A_M\rangle_0{}^c$ (10^{-5})	B_0/C^d (10^{-7})	B_0/D_0 (10^{-3})
1	14334	698	522	1.83	B	-2.74	-1.80	-9.84
2	14593	685	414	4.07	B	-15.48	-10.15	-24 94
3	14902	671	323	17.01	B	-112.9	-74.07	-43.54
4	15126	661	204	6.69	B	74.59	48.91	73.11
5	15308	653	200	3.35	B	12.12	7.95	23.73
6	15483	646	200	2.00	B	3.32	2.17	10.85
7	15843	631	358	3.29	B	7.14	4.68	14.22
8	16162	619	333	2.03	B	7.33	4.81	23.69
9	16389	610	243	1.14	B	4.17	2.74	24.04
10	16585	603	282	1.82	B	14.51	9.51	52.25
11	16788	596	344	1.49	B	3.58	2.35	15.77
12	17295	578	754	1.71	B	5.96	3.91	22.87
13	17997	556	699	0.56	B	0.352	0.231	4.13
14	22214	450	1861	0.17	B	-0.139	-0.091	-5.35
15	23395	427	1255	0.97	B	-0.332	-0.218	-2.25
16	24867	402	1637	3.28	B	-0.868	-0.569	-1.73
17	26311	380	1568	10.07	B	-13.93	-9.13	-9.07
18	27359	366	1511	7.16	B	-0.335	-0.220	-0.307
19	28595	350	1912	10.07	B	5.11	3.35	3.33
20	30084	332	1761	5.61	B	0.985	0.646	1.15
21	31254	320	1728	4.51	B	0.524	0.343	0.761
22	32613	307	1970	5.70	B	0.226	0.148	0.260
23	34233	292	1786	3.46	B	0.201	0.132	0.382
24	35761	280	1762	2.92	B	-0.416	-0.273	-0.935
25	37107	270	1708	3.59	B	-0.940	-0.616	-1.72
26	38138	262	1391	4.36	B	-3.81	2.50	5.73

[a]Statistics are as follows. B-band region: $\lambda_{360-500nm}$, $\chi^2=1.37\times10^{-3}$, $\Sigma(\Delta A)^2=4.09\times10^{-7}$. Q-band region: $\lambda_{500-700nm}$, $\chi^2=4.51\times10^{-4}$, $\Sigma(\Delta A)^2=2.38\times10^{-4}$. [b]$D_0 = \langle A\rangle_0/326.6$ where the units of D_0 (dipole strength) are D^2 (D: Debye units); Nyokong, T. N., Ph.D. Thesis, The University of Western Ontario, London, Canada, 1986, p 537. [c]$\langle\Delta A_M\rangle_0$ is the zeroth moment of the MCD. When fitting with a B term, the program calculates $\langle\Delta A_M\rangle_0$. The Faraday term value of B_0 is calculated directly from the moments as follows: $B_0 = \langle\Delta A_M\rangle_0/152.5$. [d]The units of B_0 are D^2/cm^{-2}; see TNN Thesis, p 537. [e]The concentration (C) of $MgPcN_4(-2)$ is not known.

Table 3-3
Band Fitting Parameters[a] for $ZnPcN_4(-2)$ in DMA[e].

band no.	ν cm^{-1}	λ nm	$\Delta\nu$ cm^{-1}	D_0/C^b (10^{-5})	band type	$\langle\Delta A_M\rangle_0{}^c$ (10^{-5})	B_0/C^d (10^{-7})	B_0/D_0 (10^{-3})
1	14334	698	521	0.54	B	-2.55	-1.67	-30.93
2	14667	682	323	1.04	B	-5.30	-1.62	-15.58
3	14910	671	318	5.98	B	-55 82	-17.09	-28.58
4	15189	658	278	3.88	B	41.42	12.68	32.68
5	15433	648	266	1.06	B	2.88	0.883	8.33
6	15621	640	229	0.52	B	1.22	0.372	7.15
7	15843	631	358	0.97	B	3.24	0.991	10.22
8	16162	619	333	0.78	B	2.60	0.797	10.22
9	16389	610	243	0.41	B	1.82	0.558	13.61
10	16585	603	281	0.66	B	6.66	2.04	30.91
11	16788	596	344	0.68	B	2.24	0.685	10.07
12	17294	578	754	0.48	B	2.48	0.759	15.81
13	17997	556	699	0.26	B	0.200	0.061	2.35
14	24242	413	1638	1.12	B	-0.917	-0.601	-5.37
15	25660	390	1744	2.46	B	-2.07	-1.36	-5.53
16	26662	375	1449	2.54	B	-2.69	-1.76	-6.93
17	27547	363	1549	3.87	B	0.133	0.087	0.225
18	28738	348	1564	4.07	B	0.923	0.605	1.49
19	29990	333	1655	4.06	B	0.475	0.311	0.766
20	31314	319	1736	3.74	B	0.272	0.178	0.476
21	32769	305	1837	3.83	B	0.032	0.021	0.055
22	34288	292	1814	3.58	B	0.002	0.002	0.006
23	35686	280	1663	3.19	B	-0.385	-0.253	-0.793
24	37112	269	1774	4.93	B	-0.183	-0.120	-0.243
25	38352	261	1267	5.13	B	0.123	0.085	0.166

[a]Statistics are as follows. B-band region: $\lambda_{260-500nm}$, $\chi^2=8.09\times10^{-6}$, $\Sigma(\Delta A)^2=5.66\times10^{-8}$. Q-band region: $\lambda_{500-700nm}$, $\chi^2=2.89\times10^{-4}$, $\Sigma(\Delta A)^2=5.31\times10^{-5}$. [b]$D_0 = \langle A\rangle_0/326.6$ where the units of D_0 (dipole strength) are D^2 (D: Debye units); Nyokong, T. N., Ph.D. Thesis, The University of Western Ontario, London, Canada, 1986, p 537. [c]$\langle\Delta A_M\rangle_0$ is the zeroth moment of the MCD. When fitting with a B term, the program calculates $\langle\Delta A_M\rangle_0$. The Faraday term value of B_0 is calculated directly from the moments as follows: $B_0 = \langle\Delta A_M\rangle_0/152.5$. [d]The units of B_0 are D^2/cm^{-2}; see TNN Thesis, p 537. [e]The concentration (C) of $ZnPcN_4(-2)$ is not known.

Table 3-4
Band Fitting Parameters[a] for $ZnPcN_8(-2)$ in DMSO[f].

band no.	ν cm^{-1}	λ nm	$\Delta\nu$ cm^{-1}	D_0/C^b (10^{-5})	band type	$\langle\Delta A_M\rangle_n{}^c$ (10^{-5})	$B_0(A_1)/C^d$ (10^{-7})	$B_0(A_1)/D_0$ (10^{-3})	μ^e
1	13253	755	759	0.25	B	-0.879	-0.576	-23.04	
2	14190	705	782	0.57	B	-0.893	-0.586	-10.28	
3	14850	673	546	1.17	B	-6.33	-4.15	-35.47	
4	15282	654	350	3.94	A	3469.	2275.	5774.	5.39
					B	-1.05	-0.686	-1.74	
5	15648	639	307	0.24	B	0.648	0.425	17.71	
6	15964	626	507	0.96	B	1.67	1.09	11.35	
7	16405	610	491	0.66	B	1.73	1.13	17.12	
8	16836	594	507	0.69	B	3.91	2.56	37.10	
9	17244	580	503	0.34	B	0.765	0.501	14.74	
10	17784	562	754	0.60	B	2.21	1.45	24.17	
11	18718	534	1198	0.39	B	0.707	0.464	11.90	
12	20003	500	1247	0.19	B	-0.084	-0.055	-9.00	
13	22350	447	1786	0.71	B	-0.965	-0.633	-8.92	
14	23687	422	1823	1.71	B	-1.29	-0.844	-4.94	
15	25306	395	1946	2.78	B	-0.178	-0.117	-0.421	
16	26909	372	2028	2.89	B	0.977	0.640	2.21	
17	28649	349	2012	2.35	B	0.446	0.293	1.25	
18	30110	332	1610	1.24	B	-0.076	-0.050	-0.403	
19	31287	320	1718	1.46	B	-0.192	-0.126	-0.863	
20	32781	305	2014	2.46	B	-0.852	-0.558	-2.27	
21	34325	291	1780	1.98	B	0.117	0.077	0.389	
22	35626	281	1659	1.73	B	0.367	0.241	1.39	
23	36937	271	1785	1.74	B	-4.04	-2.65	-15.23	

[a]Statistics are as follows. B-band region: $\lambda_{260-500nm}$, $\chi^2=1.33\times10^{-5}$, $\Sigma(\Delta A)^2=9.22\times10^{-9}$. Q-band region: $\lambda_{500-800nm}$, $\chi^2=1.34\times10^{-4}$, $\Sigma(\Delta A)^2=3.22\times10^{-6}$. [b]$D_0 = \langle A\rangle_0/326.6$ where the units of D_0 (dipole strength) are D^2 (D: Debye units); Nyokong, T. N., Ph.D. Thesis, The University of Western Ontario, London, Canada, 1986, p 537. [c]$\langle\Delta A_M\rangle_1$ is the first moment and $\langle\Delta A_M\rangle_0$ is the zeroth moment of the MCD. When fitting with an A term, the program calculates $\langle\Delta A_M\rangle_1$; therefore n=1 in the table. When fitting with a B term, the program calculates $\langle\Delta A_M\rangle_0$; therefore n=0 in the table. The Faraday term values A_1 and B_0 are calculated directly from the moments as follows: $A_1 = \langle\Delta A_M\rangle_1/152.5$ and $B_0 = \langle\Delta A_M\rangle_0/152.5$. [d]The units of A_1 are D^2, and the units of B_0 are D^2/cm^{-2}; see TNN Thesis, p 537. A_1 data are printed above B_0 data when both A and B terms are used. [e]μ=magnetic moments in units of Bohr magnetons, μ_β, calculated as $2(\langle A_1/D_0\rangle \times 0.4669)$ [f]The concentration (C) of $ZnPcN_8(-2)$ is not known.

3.2.3 Moment Analysis of the Q Region

Table 3-5 lists the results of a moments analysis for the Q region (500-750 nm) of $MgPcN_4(-2)$, $ZnPcN_4(-2)$ and $ZnPcN_8(-2)$ and the previously reported results for (im)ZnPc(-2) [26,35] and $(im)_2MgPc(-2)$ [27]. The moments calculations were carried out using the program TNMOMET4 [53] with only the well resolved and isolated Q band being analysed in this manner. The moment calculations provide a value for the magnetic moment of the Q band excited state [54] with the A_1/D_0 parameter factoring out any errors that might occur in the calculation of the solution concentration because the same solution is used for both absorption and MCD measurements.

Table 3-5

Moment Analysis of the Q Region ABS and MCD spectra of the $MPcN_n(-2)$ (n=0,4,8) complexes

$MPcN_n(-2)^d$	ν cm^{-1}	D_0/C^a 10^{-4}	$\langle\Delta A_M\rangle_1$ 10^{-4}	A_1/C^b 10^{-4}	A_1/D_0	$\mu_\beta{}^c$	$\langle\Delta A_M\rangle_0$ 10^{-4}	$\langle B_0/D_0\rangle$ 10^{-4}
$ZnPcN_4$(DMA)	15271	2.48	1780	11.7	3.65	3.41	.3596	8.36
$[(CN)ZnPcN_4]^-$	15378	1.95	1070	7.04	3.60	3.36	.1479	4.95
$MgPcN_4$(DMA)	15343	2.72	1270	8.30	3.06	2.86	.0592	1.43
$ZnPcN_8$(DMSO)	15682	0.97	446	2.93	3.01	2.81	.0610	4.11
$(im)_2MgPc$[27]	15173				2.54	2.37		2.37
(im)ZnPc [35]	15289				1.51	1.40		2.79

[a]The units of the dipole strength, D_0 are D^2 (D=Debye units). [b]A_1 has the units of D^2, and B_0 has the units of D^2/cm^{-2}. [c]Magnetic moment in units of μ_β, calculated from $2(\langle A_1/D_0\rangle \times 0.4669)$. [d]The concentration (C) of the $MPcN_{4,8}(-2)$ complexes is not known.

3.3 DISCUSSION

The majority of the theoretical and experimental studies of phthalocyanines have been performed on phthalocyanine molecules with metal centred, D_{4h} and free base, D_{2h} symmetry [1]. The rich visible-ultraviolet spectra are presumed to originate from molecular orbitals within the aromatic 18-π-electron system and from overlapping orbitals on the central metal, while virtually ignoring the fused peripheral rings. Reported absorption maxima for the Q_{00} transition in octasubstituted phthalocyanines [1,55,56] indicate a distinct perturbation of the core π system. Since peripheral substitution has been shown to influence the transition energies and the redox potentials of the 18-π-electron system, then asymmetric peripheral substitution is expected to influence the total symmetry of the π system. With the current interest in the spectral and the redox properties of substituted phthalocyanines, we decided to investigate the effect of introducing one and two nitrogen atoms into the fused benzene rings on the energies of the ground and excited states and on the symmetry of the central π system. Reduction of the tetragonal (D_{4h}) symmetry by the introduction of fused pyridine rings and its restoration through the introduction of fused pyridazine rings was monitored by absorption and MCD spectroscopy.

3.3.1 Assignment of the Q Band in $MgPcN_4$ and $ZnPcN_4$

Used alone, absorption spectroscopy is not sufficient to probe the electronic structure of porphyrins and phthalocyanines. MCD spectroscopy has proven invaluable in the studies of phthalocyanines [1] and porphyrins [46,57,58]. This technique is sensitive to the symmetry, spin degeneracy and orbital degeneracy within a molecule [1,25,46,58]. The power of MCD spectroscopy can be seen in the published deconvolution results for the B region of ZnPc(-2) [26,35] and MgPc(-2) [27] which placed two degenerate transitions where only the theoretically predicted B band was expected.

The spectral envelopes of $MgPcN_4(-2)$ (Figure 3-3) and $ZnPcN_4(-2)$ (Figures 3-5 and 3-6) display significant zero field splitting of the Q band. The absorption spectra do not provide sufficient evidence to assign these bands as the symmetry split x and y components of the Q_{00} transition. It is not uncommon to encounter incorrect assignments that have been based solely on the analysis of the absorption spectra. Visual inspection of the MCD spectra in Figures 3-3, 3-5 and 3-6, would assign the spectral intensity between 650 and 680 nm to an A term, but deconvolution of the Q region placed two MCD B terms here instead of an A term. This result suggests that the asymmetry of the peripheral groups imparts a definite rhombic distortion on the inner 18-π-electron system. Before definitely assigning these two bands as the x and y components of the zero field split Q band, the possibility that these bands arise from different structural isomers needs to be addressed.

3.3.2 The Structural Isomers of $MPcN_4$

The four structural isomers of the $MPcN_4$ molecule are plotted in Figure 3-2. The symmetry group that each isomer belongs to is written below the isomer's structure. Character tables indicate that only the isomer with C_{4h} symmetry will have degenerate excited states [59]. If the synthesis of $MPcN_4(-2)$ is unaffected by the arrangement of the precursor molecules, then statistics can be employed to determine the relative abundance of the four isomers. The relative abundance is calculated to be 1:1:2:4 for isomers I, II, III and IV, respectively. If the four isomers are synthesized in the predicted ratio, then the observed absorption and MCD spectra represent the weighted sum of the individual isomers spectra. Assuming that all four isomers are present in solution, we can use the electronic spectra to determine whether the isomers have similar or different transition energies. When the isomers have different transition energies, the bands in the Q region should be broadened and the spectral envelope should be less resolved than the same region in MgPc(-2) [27]

and ZnPc(−2) [1,35,52]. Aside from the split bands in the region of the Q_{00} transition, the Q region of $MgPcN_4(-2)$ and $ZnPcN_4(-2)$ displays the spectral sharpness and clarity seen in the unsubstituted phthalocyanines. This result indicates that if all four isomers are present, then they cannot have different transition energies.

When the four isomers are assumed to have similar transition energies, it is possible to focus on whether or not the asymmetric peripheral subsititution distorts the D_{4h} symmetry of the inner 18−π−electron system. If the D_{4h} symmetry is maintained, then the shape of the Q band spectral envelope should mimic the same spectral region in the unsubstituted metallophthalocyanines. The split Q bands of $MgPcN_4(-2)$ and $ZnPcN_4(-2)$ are not encountered in the absorption spectra of the unsubstituted metallophthalocyanines. If there is a lowering of the D_{4h} symmetry, the degeneracy of the Q_{0c} transition will be removed in three of the four isomers and the spectral envelope, in the region of the Q_{00} transition, is expected to be broadened and to contain high and low energy shoulders. The sharpness of the split Q bands in the absorption spectra $MPcN_4(-2)$ is not consistent with the presence of high and low energy shoulders on these bands. The above spectral analysis indicates that our initial assumption is incorrect and that only one of the four structural isomers is present in solution.

Although there is limited information on the mechanism for the formation of phthalocyanines and their derivatives [60], analysis of the absorption and MCD spectra of $MPcN_4$ indicates that the pyridine rings in 3,4−pyridocarboxylic acid have a pronounced effect on the template synthesis of $MPcN_4(-2)$. Since the absorption and MCD spectral fits of $MgPcN_4(-2)$ and $ZnPcN_4(-2)$ were unable to place a MCD A term under the Q band (Figures 3−4 and 3−7), isomer I cannot be the product. Using the assumption that the precursor molecules are required to align in an ordered arrangement, isomer IV is also ruled out as the product. With the limited understanding of the mechanism for the synthesis of phthalocyanines, it is difficult to

determine the product from isomers II and III. The synthesis of both isomers can be explained by mechanisms that require the precursor molecules to arrange in a specific orientation. There is however a distinct difference between the mechanism of formation for the two isomers. The mechanism for the formation of isomer III is most likely a two step reaction, where two precursor molecules react to form an intermediate complex and then two intermediate complexes react to form isomer III. The mechanism for the formation of isomer II is a template reaction of four ordered precursor molecules. Since phthalocyanines are known to form by template reactions and since the proposed mechanism for the formation of isomer III is not a true template reaction, we tentatively assign isomer II as the synthesis product.

3.3.3 Zero Field Splitting of the Excited States in $MPcN_4$

The absorption spectrum for the 1:1 binding of HCl to FePc displayed the split Q bands that are observed in the spectra of $MgPcN_4(-2)$ and $ZnPcN_4(-2)$. The authors suggest that the chloride ion binds axially to iron, while the acidic proton binds equatorially to an aza bridging nitrogen. Protonation of the phthalocyanine ring will lower the molecular symmetry from D_{4h} to C_s in FePc·HCl. The split Q bands in the absorption spectra of FePc·HCl supports the lowering of the D_{4h} symmetry within the 18-π-electron system of $MPcN_4(-2)$. The titration of strong acids and strong bases into solutions of $MPcN_4(-2)$ affects the solubility of the molecules, but not the shapes of their spectral envelopes. These titration results indicate that the asymmetric arrangement of the fused pyridine rings, rather than protonation of aza-bridging nitrogens, is responsible for the lower symmetry of the core π-system. The loss of the split Q bands in $MPcN_4(-2)$ and the restoration of the degenerate Q band in the symmetric D_{4h} $ZnPcN_8(-2)$ molecule verifies the rhombic distortion of the inner 18-π-electron system and the zero field splitting of the E_g states in $MPcN_4$.

3.3.4 Comparison of the Deconvolution Data for ZnPc, $ZnPcN_4$, $ZnPcN_8$, MgPc and $MgPcN_4$

Figures 3-13 and 3-14 are energy level diagrams that compare the spectral fits of: (i) (im)ZnPc(-2) [26], $ZnPcN_4$(-2) and $ZnPcN_8$(-2), and (ii) $(im)_2$MgPc(-2) [27] and $MgPcN_4$(-2), respectively, across the 12 000 to 40 000 cm^{-1} spectral region. The energy level diagram in Figure 3-15 focuses on the fitted Q region (10 000 - 20 000 cm^{-1}) for (im)ZnPc(-2) [26], $ZnPcN_4$(-2), $ZnPcN_8$(-2), $(im)_2$MgPc(-2) [27] and $MgPcN_4$(-2). In comparing the energies of the degenerate or zero field split Q bands, there is a blue shift in band centre energies as the nitrogen content of the peripherally-fused rings is increased. There is a shift from 14 906 cm^{-1}, in (im)ZnPc(-2), to 15 050 cm^{-1}, in $ZnPcN_4$ [this is the midpoint between the 14 910 cm^{-1} (-) and 15 189 cm^{-1} (+) MCD bands], to 15 282 cm^{-1}, in $ZnPcN_8$(-2), and from 14 874 cm^{-1}, in $(im)_2$MgPc(-2), to 15 014 cm^{-1}, in $MgPcN_4$(-2) [midpoint between the (14 902 cm^{-1} (-) and 15 126 cm^{-1} (+)

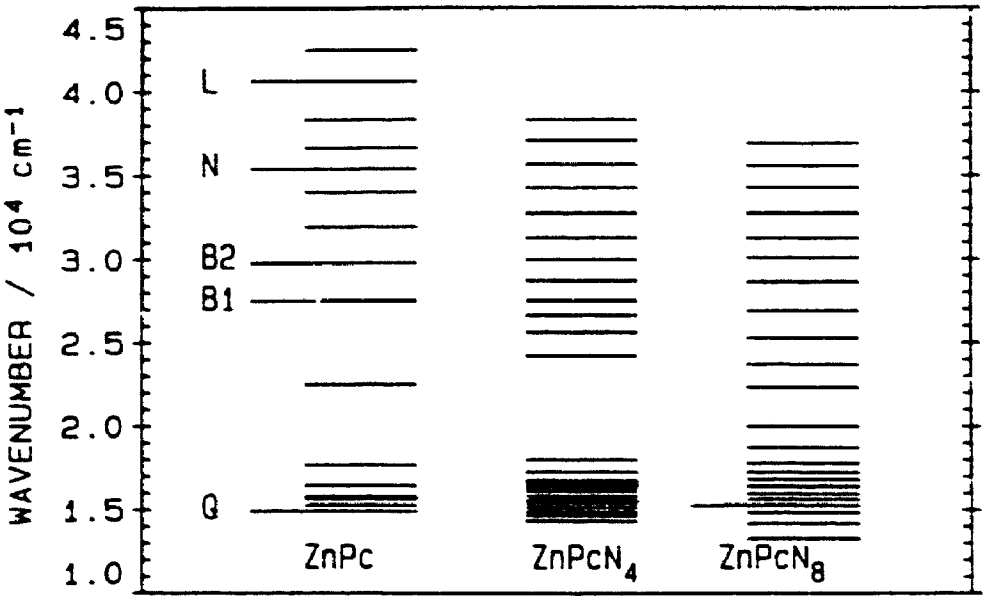

Figure 3-13 Comparison of the energy levels, between 12 000 cm^{-1} and 40 000 cm^{-1}, for (im)ZnPc(-2) [26], $ZnPcN_4$(-2) and $ZnPcN_8$(-2) calculated by band deconvolution of the absorption and MCD spectra.

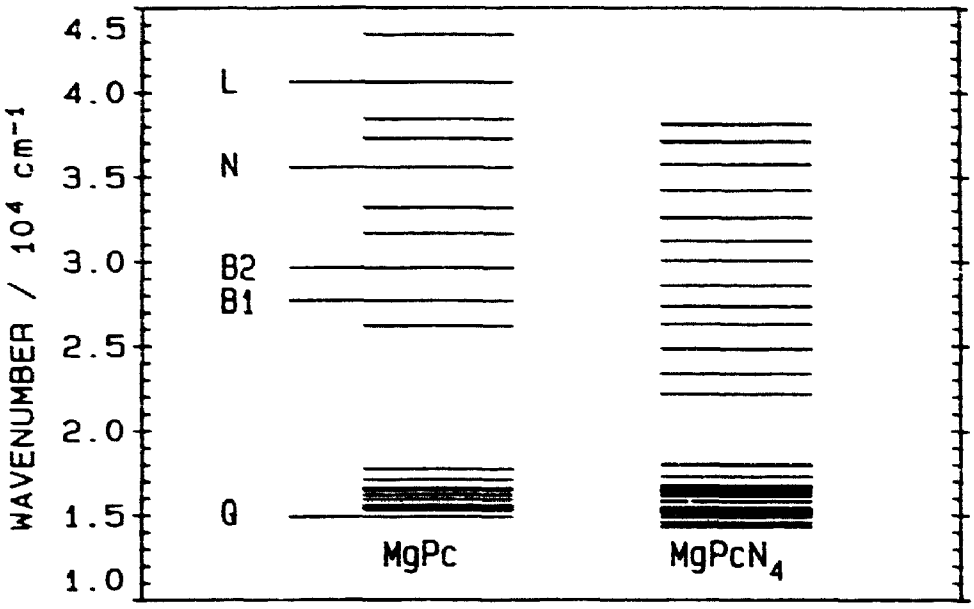

Figure 3–14 Comparison of the energy levels, between 12 000 cm^{-1} and 40 000 cm^{-1}, for $(im)_2MgPc(-2)$ [27] and $MgPcN_4(-2)$ calculated by band deconvolution of the absorption and MCD spectra.

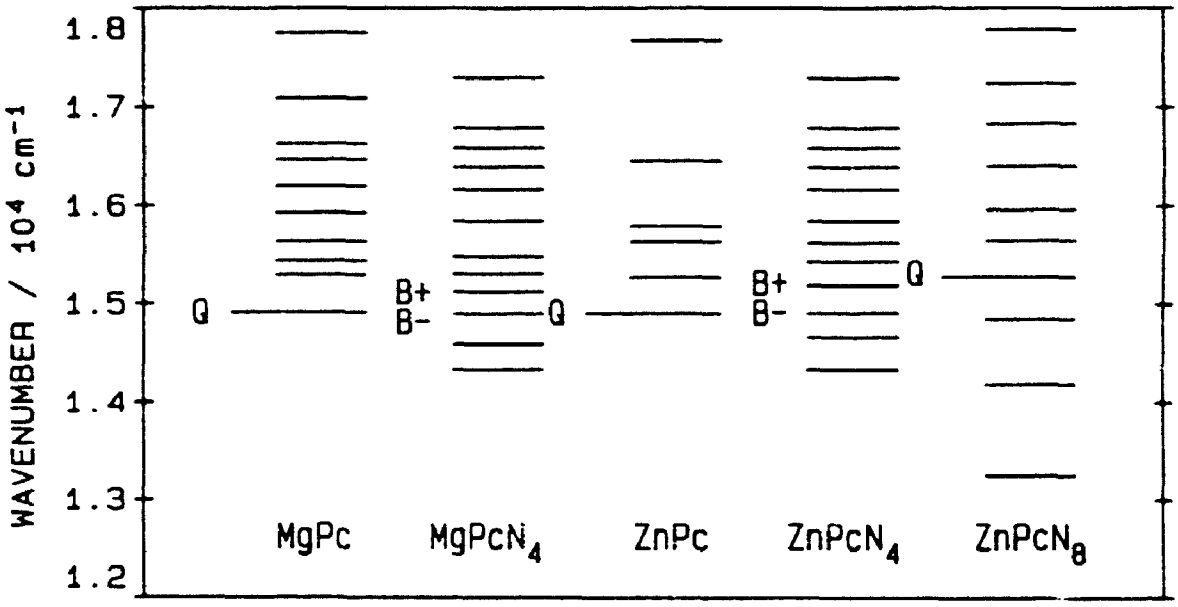

Figure 3–15 Comparison of the energy levels, between 12 000 cm^{-1} and 18 000 cm^{-1}, for $(im)_2MgPc(-2)$ [27], $MgPcN_4(-2)$, $(im)ZnPc(-2)$ [26], $ZnPcN_4(-2)$ and $ZnPcN_8(-2)$ calculated by band deconvolution of the absorption and MCD spectra.

bands]. If the blue shift is related to the number of the nitrogens atoms incorporated into the fused rings, then the energy of the Q_{00} transition, or the average energy for the split x and y components for $ZnPcN_4(-2)$, should be midway between the band centre energies for ZnPc(-2) [26] and for $ZnPcN_8(-2)$. The midpoint between the Q bands for (im)ZnPc(-2) and for $ZnPcN_8(-2)$ occurs at 15 094 cm^{-1}. This position is very close to the midpoint (15 050 cm^{-1}) of the Q_x and Q_y bands for $ZnPcN_4(-2)$. The zero field splitting of the Q band in $ZnPcN_4(-2)$ is 279 cm^{-1} and in $MgPcN_4(-2)$ it is 224 cm^{-1}. The larger rhombic distortion in $ZnPcN_4(-2)$ may be due to a small displacement of the zinc ion out of the plane of the $PcN_4(-2)$ ring.

3.3.5 Moment Analysis

The isolation of the Q band (Q_{00} + Q_{vib} transitions) from other ring transitions in $MPcN_{4,8}(-2)$ complexes allows the use of the MCD spectral results to determine the angular momentum of the excited state. Since the Q band is generally isolated from the charge transfer bands of transition metal phthalocyanines, it is possible to compare the magnetic moments of a wide range of substituted and unsubstituted metallophthalocyanines. The A_1/D_0 values for $MgPcN_4(-2)$ (3.06) and $ZnPcN_4(-2)$ (3.60 and 3.65) (following the conventions of Schatz [62] and Stephens [63,64]), obtained by integration over the whole band envelope in the 500 to 750 nm region of the absorption and MCD spectra, are consistently above the values of: 1.3 - 3.55 for LZnPc(-2) [35]; 2.49 - 2.78 for $L_2MgPc(-2)$ [27]; 2.7 - 3.11 for $L_2Fe(II)Pc(-2)$ (Chapter 6) and 3.01 for $ZnPcN_8(-2)$. Because of the large zero field splittings, 279 cm^{-1} in $ZnPcN_4(-2)$ and 224 cm^{-1} in $MgPcN_4(-2)$, the A_1/D_0 values for the $MPcN_4(-2)$ complexes are predicted to be below those for the D_{4h} MPc complexes which have small zero field splitting values. The above prediction is based on the inverse relationship between the MCD intensity and the energy separation between the zero field split excited states. Assuming that the zero field splitting parameters

obtained fr .n the deconvolution results are valid, then the method of moments fails under large zero field splittings

3.4 CONCLUSIONS

Absorption and MCD spectra are reported for the metallophthalocyanine-N-isologs: $ZnPcN_4(-2)$, $MgPcN_4(-2)$ and $ZnPcN_8(-2)$. Qualitative analysis of the spectra of $ZnPcN_4(-2)$ and $MgPcN_4(-2)$ indicated that only one of the four structural isomers of $MPcN_4(-2)$ is formed during synthesis. The isomer with D_{2h} symmetry is assigned as the synthesis product. Quantitative analysis of the spectral results for $ZnPcN_4(-2)$ and $MgPcN_4(-2)$ yielded zero field splitting parameters of 279 and 224 cm^{-1}, repectively, and band centre energies (midpoint between the Q_x and Q_y bands) of 664 nm (15 050 cm^{-1}) and 666 nm (15 014 cm^{-1}), respectively. No zero field splitting was observed in the spectra of $ZnPcN_8(-2)$. Spectral deconvolution placed the degenerate Q band of $ZnPcN_8(-2)$ at 654 nm (15 282 cm^{-1}). Analysis of the deconvolution results indicated that the Q band energy was blue shifted as the nitrogen content of the fused rings was increased.

CHAPTER 4

MAGNESIUM PHTHALOCYANINE

4.1 INTRODUCTION

Many optical spectra of metallophthalocyanine (MPc) complexes have been reported, but very few attempts have been made to assign the electronic transitions that give rise to these spectra [23,26,34,35,65,66]. In particular, with exception of previous studies on ZnPc [26,35] and α-phase thin films [67], no deconvolution calculations have been reported that identify the individual bands that make up a significant fraction of the absorption envelope between 220 and 1000 nm. With envelopes that extend over wide spectral range, as observed for MPc complexes, and where the possibilities for photochemistry involving the MPc excited states are so extensive, analysis of the origin of the major spectral intensity is important. As a minimum, an estimation of the number of bands that can contribute to the envelope is necessary before either an assignment of the orbital or state to state origin can be attempted. The situation for both the phthalocyanines and porphyrins is complicated because some of the most interesting chemistry takes place with complexes metallated with transition metals [1,68,69], where charge transfer transitions overlap the ring $\pi \rightarrow \pi^*$ transitions or with oxidized or reduced complexes, where new bands are observed that can arise from internal, ring-based ($\pi \rightarrow \pi$) transitions [2,32]. Although many absorption spectra of oxidized MPc complexes have been reported [2,35,37,68,70-72], it is only very recently that detailed attempts have been made at assigning any of the bands that are observed [26,35]. These studies on the π-cation species have identified a need for a full assignment of the $\pi \rightarrow \pi^*$ spectral envelope in neutral MPc(-2) species.

In this chapter, the spectral and electrochemical properties of a range of highly soluble $L_2MgPc(-2)$ complexes are described. MgPc(-2) is chemically [72],

electrochemically [73] and photochemically [33,74] a very interesting molecule, and the reported data can act as a model for the spectral properties of many other MPc species. Deconvolution calculations are used to obtain the energies, band widths and magnetic moments of the transitions that contribute to the observed spectral envelope between 230 and 800 nm.

4.2 RESULTS

4.2.1 Electrochemistry

The cyclic voltammetry (CV) and differential pulse voltammetry (DPV) response curves for $(H_2O)_2MgPc(-2)$ are shown in Figure 4-1. The results are displayed in Table 4-1 together with those for $L_2MgPc(-2)$ (L = im, meim, py, mepy). The CV and DPV results were obtained in DMA, which makes the use of water based electrodes such as the saturated calomel electrode (SCE) and normal hydrogen electrodes (NHE) impractical. In nonaqueous electrochemistry a liquid-junction potential would occur at the solution interface causing significant unwanted errors in the recorded potentials. As in previous studies [35,37] this problem was overcome by utilizing a silver wire as an internal reference electrode. The ferrocene/ferrocenium (fc/fc+) couple was used to provide internal calibration [75]. The voltages of the CV and DPV results plotted in Figure 4-1 are referenced to the silver wire electrode [35,37]. The half wave potentials recorded in Table 4-1 are shown versus the fc/fc+ couple and versus the SCE. The values with respect to the SCE were calculated by taking the value for $E_{\frac{1}{2}}$ (fc/fc+) as +0.47 V in DMA; these corrected values versus the SCE are used throughout the text.

Figure 4-1 shows typical, full voltage range CV and DPV curves obtained for $(H_2O)_2MgPc(-2)$ in DMA. Both scans can be used to calculate half-wave potentials. The half-wave potentials (Table 4-1) were calculated using the DPV data because superior resolution is obtained in this type of experiment. The peak to trough

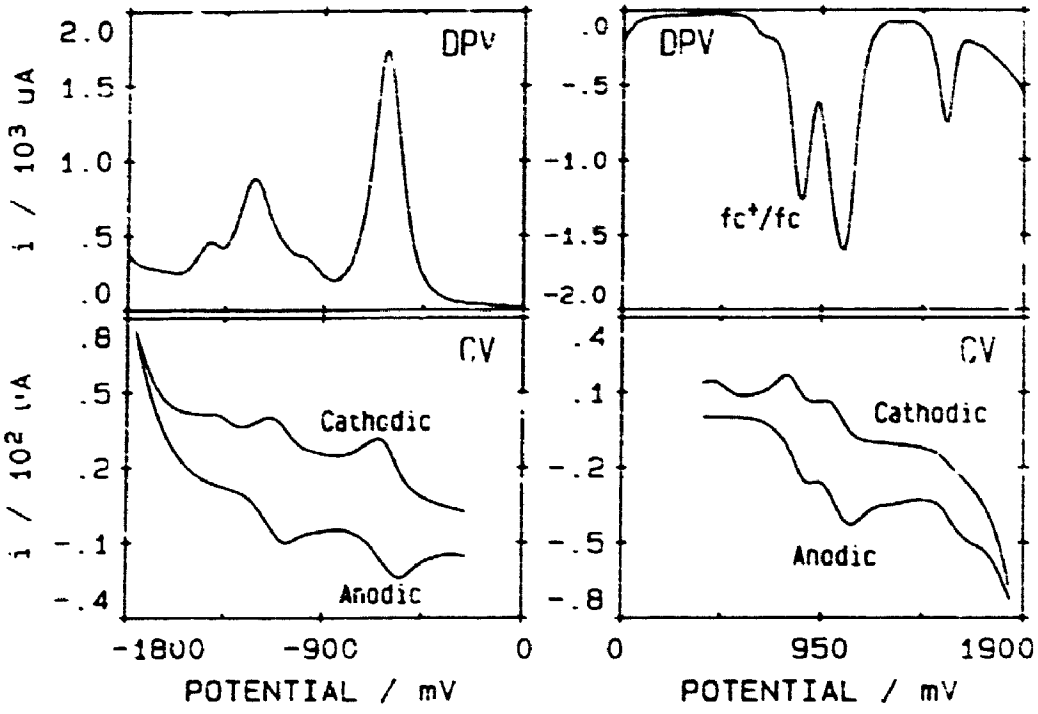

Figure 4-1 The CV and DPV of $(H_2O)_2MgPc(-2)$ dissolved in DMA containing 0.10 M TPAP.

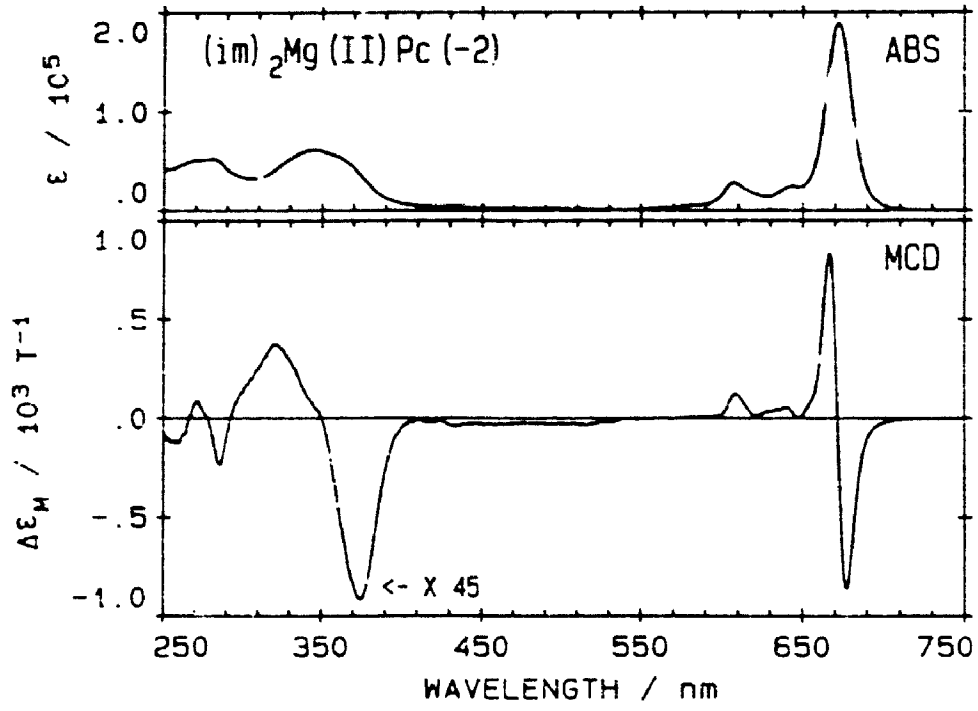

Figure 4-2 Absorption (ABS) and MCD spectra for $(im)_2MgPc(-2)$ in DCM.

separations indicate truly reversible electron transfer is taking place [76]. The solutions could be cycled continuously with no loss of peak position, which indicates that no chemical changes were taking place. The data for all the complexes studied exhibited the same, overall electrochemical properties with, typically, reduction to $[MgPc(-3)]^{\cdot -}$ at −0.88 V, to $[MgPc(-4)]^{\cdot --}$ at −1.43 V, and oxidation to the π−cation radical species $[MgPc(-1)]^{\cdot +}$ at 0.65 V and the dication at 1.11 V, all values corrected to be referenced against the SCE, (where the nomenclature used to indicate electron distribution between the metal and the π ring follows previous style [35,37,77]). Clearly, the lack of metal oxidation results in very clean electrochemical behaviour. We can compare these reduction and oxidation potentials with (im)ZnPc(−2) [35,37] where $E_{\frac{1}{2}}$ = −1.43, −0.98 and 0.71 V versus the SCE and with MgTPP(−2) [78] where E = −1.80, −1.35 and 0.54 V versus the SCE. The more positive oxidation potentials from the M(II)Pc(−2) species (0.65 V for $(H_2O)_2MgPc(-2)$ and 0.71 V for (im)ZnPc(−2)), requires the use in photooxidation reactions [68,35,37] of electron acceptors that have greater oxidizing power than is needed for the comparable porphyrin complex. Thus carbon tetrabromide has to be used with MgPc(−2) and ZnPc(−2), while carbon tetrachloride can be used quite successfully with the porphyrins [68].

4.2.2 Absorption and MCD Spectra

Figure 4−2 shoes the absorption and magnetic circular dichroism (MCD) spectra of $(im)_2MgPc(-2)$ in 1,1−dichloromethane (DCM). There is little change in the absorption band maxima and spectral envelope for the various $L_2MgPc(-2)$ complexes. The absorption band maxima for all the $L_2MgPc(-2)$ complexes are listed in Table 4−2. The spectral data for all the $L_2MgPc(-2)$ complexes resemble that of the simplest phthalocyanines [1,34,35,45,65] (no charge transfer between metal and ligand), with a well resolved Q band, a spectral window at 500 nm and a series of

Table 4-1
The half-wave potentials of the $L_2MgPc(-2)$ species dissolved in DMA containing 0.10 M TPAP

$L_2MgPc(-2)$	$E_{\frac{1}{2}}$ (fc+/fc)	$E_{\frac{1}{2}}$ (V) (SCE)
$(H_2O)_2MgPc(-2)$	0.64	1.11
	0.18	0.65
	-1.37	-0.90
	-1.86	-1.39
$(im)_2MgPc(-2)$	0.63	1.10
	0.17	0.64
	-1.40	-0.93
	-1.94	-1.47
$(meim)_2MgPc(-2)$	0.74	1.21
	0.17	0.64
	-1.39	-0.92
	-1.86	-1.39
$(py)_2MgPc(-2)$	0.69	1.16
	0.20	0.67
	-1.38	-0.91
	-1.92	-1.45
$(mepy)_2MgPc(-2)$	0.66	1.13
	0.20	0.67
	-1.29	-0.82
	-1.76	-1.29
Ferrocene	0.00	0.47

Table 4-2
Observed maxima in the absorption spectra of the $L_2MgPc(-2)$ species in DCM.

$L_2MgPc(-2)$	λ_{max} (nm)[a]				
L = H_2O	670	642	606	345	282
L = im	672	643	607	345	281
L = meim	672	643	607	345	282
L = py	671	642	605	345	282
L = mepy	671	642	607	345	282
L = CN^-	671	642	606	345	282

[a] λ_{max} is measured directly from the absorption spectrum.

overlapping bands extending from 400 to well below 250 nm. As in the study of ZnPc(−2) [26,35,37], we are interested in the number of transitions that arise in the region from 230 to 400 nm. From the MCD, it appears that several degenerate transitions lie in this spectral region [26,35]. The MCD data provides transition polarization data directly from the spectra because the ground state is nondegenerate, so only Faraday A and B terms will be observed. The MCD spectrum closely resembles the spectra reported for ZnPc(−2) [26,35,37] and Li_2Pc(−2) [34,45,79]. The enhanced solubility of MgPc(−2) (with respect to other metallophthalocyanines) in a solvent as transparent in the UV as DCM means that bands below 300 nm are well defined in all the spectral data, allowing deconvolution analysis to be carried out down to 230 nm. This is considerably lower than previous MCD measurements and provides a significant improvement in the spectral quality above 230 nm.

4.2.3 Spectral Band Deconvolution Calculations

The deconvolution "fitting" calculations were performed on pairs of associated absorption and MCD spectra which were separated into the 700 − 500 nm Q (band) and 230 − 500 nm B (band) regions [26,35,40].

The visible region absorption bands are quite isolated from the other degenerate bands and therefore represent a straightforward fitting problem. However, in order to assess the reliability of the Gaussian bands chosen for fitting, Figure 4-3 is included and shows the results of a single calculation for the Q band of $(im)_2$MgPc(−2). The absorption and MCD fits use the same band numbers, band centres and band widths, in order to provide severe restrictions on the calculations. In this fit the absorption spectral envelope is filled with 10 Gaussian bands. The 672 nm (14 878 cm^{-1}) band corresponds to both A and B terms in the MCD spectrum. The A term indicates that the transition giving rise to the band has a degenerate excited state [25]. This band is assigned as the Q band [21]. The additional B term arises from field induced

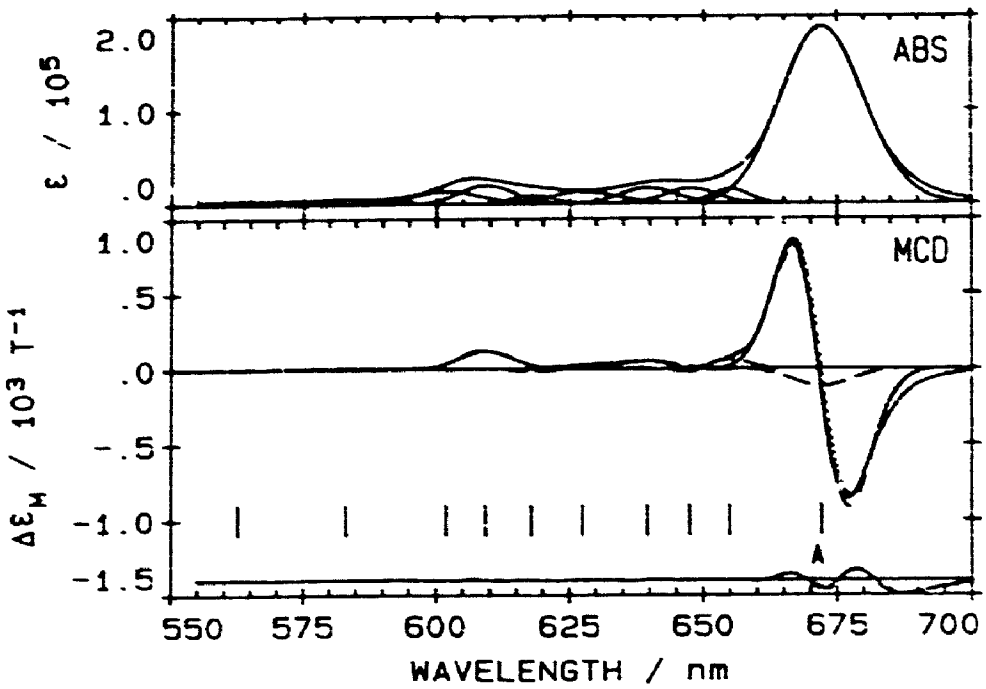

Figure 4-3 Results of band analysis for $(im)_2MgPc(-2)$ in DCM: The visible region (bands 1 to 10). (a) absorption: (———) experimental data; (– – –) fitted data; (———) individual bands. (b) MCD: (———) experimental data; (– – –) fitted data; (.....) A terms; (– – –) B terms. The band centre of the MCD A term is labelled "A".

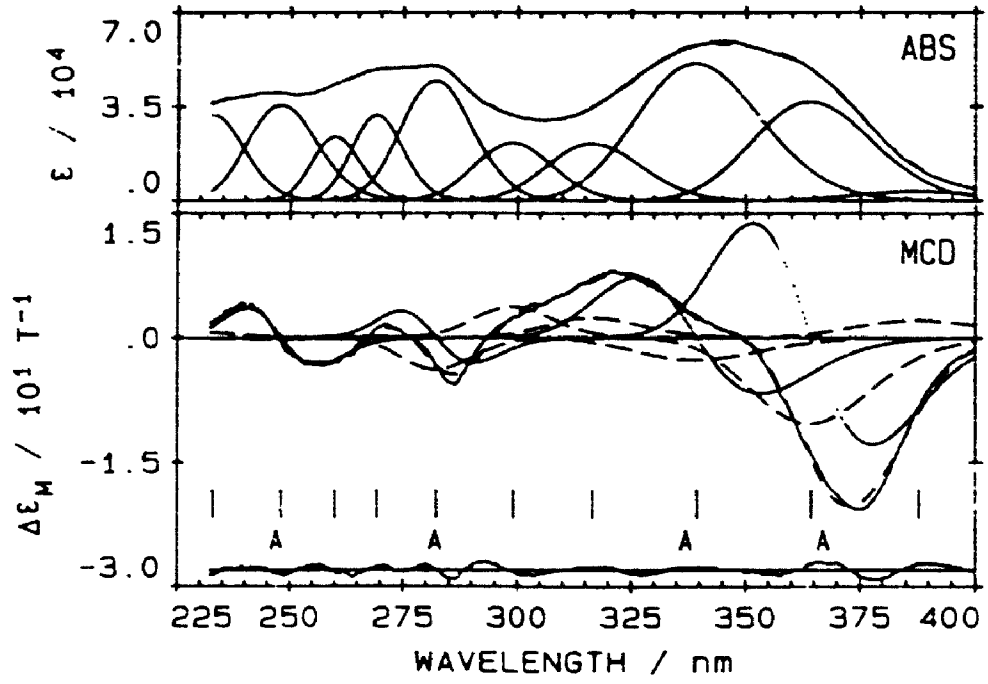

Figure 4-4 Results of band analysis for $(im)_2MgPc(-2)$ in DCM: The ultraviolet region (bands 11 to 20). (a) absorption: (———) experimental data; (– – –) fitted data; (———) individual bands. (b) MCD: (———) experimental data; (– – –) fitted data; (.....) A terms; (– – –) B terms. The band centres of MCD A terms are labelled "A".

mixing of states [25]. Deconvolution yields a series of weak B terms in the MCD spectrum for the vibrational bands that lie to the high energy side of the Q band. Although many different band shapes and combination of band shapes could be used in these calculations, the Gaussian band shape used here satisfactorily fills the observed envelopes without introducing additional variable parameters that the SIMPFIT [40] program would use to compensate for incorrect band numbers. Clearly this approach is a compromise, however, visual inspection of the band maxima in each absorption spectra reveals that the deconvolution calculations placed bands where visual inspection would expect them.

The absorption and MCD spectra in the B region (230 to 400 nm) of the $(im)_2MgPc(-2)$ is shown in Figure 4-4. The spectral envelope is very complicated and several overlapping bands of relatively equal intensity are observed in the absorption spectrum. Deconvolution calculations required 10 bands to fill the spectral envelope. In this region it is the MCD spectrum that provides the necessary and critical information that allows sensible fits to be obtained. Two degenerate transitions, indicated by A terms, overlap between 300 and 400 nm. This overlap is a common feature in all $L_2MgPc(-2)$ complexes and arises in several other MPc(-2) complexes [26,35,68,52]. The results of the calculations carried out on the MCD spectrum for $(im)_2MgPc(-2)$ indicate that there are four degenerate electronic transitions (four linked A and B terms). The band centres for these transitions were calculated to be 364 nm (27 451 cm^{-1}), 339 nm (29 463 cm^{-1}), 282 nm (35 440 cm^{-1}) and 248 nm (40 319 cm^{-1}). The fitting parameters are summarized in Table 4-3.

Since the other $L_2MgPc(-2)$ complexes exhibit similar absorption and MCD spectral envelope, as well as similar deconvolution results to those obtained for $(im)_2MgPc(-2)$, all band analysis results have been summarized in the energy level diagram represented as Figure 4-5. The dashed lines in Figure 4-5 represent the

fitted band centres. The long lines represent degenerate electronic transitions, while the short lines are nondegenerate electronic transitions.

Table 4-3
The band fitting parameters[a] for $(im)_2MgPc(-2)$ in DCM.

band #	ν /cm^{-1}	λ /nm	$\Delta\nu$ /cm^{-1}	D_0[b]	Band type	$\langle\Delta\epsilon_M\rangle_n$[c]	A_1, B_0[d] /10^{-3}	B_0/D_0 /10^{-3}	A_1/D_0	μ[e]
1	14874	672	280	16.8	A	3340.	21900.		1.30	1.21
					B	-2.42	-15.8	-0.94		
2	15270	655	188	0.60	B	0.81	5.29	8.81		
3	15445	647	265	0.89	B	-0.32	-2.08	-2.34		
4	15637	640	295	1.04	B	1.05	6.85	6.59		
5	15939	627	385	1.02	B	0.61	4.02	3.94		
6	16185	618	232	0.44	B	-0.20	-1.29	-2.93		
7	16414	609	321	1.27	B	2.50	16.4	12.9		
8	16617	602	402	1.10	B	0.06	0.40	0.36		
9	17150	583	536	0.57	B	0.29	1.89	3.32		
10	17750	563	511	0.34	B	-0.05	-0.30	-0.88		
11	25785	388	2246	1.02	B	0.20	1.28	1.25		
12	27451	364	2322	10.1	A	1958.	12840.		1.27	1.18
					B	-0.93	-6.12	-0.61		
13	29463	339	2770	15.6	A	1361.	8925.		0.57	0.53
					B	-0.27	-1.78	-0.11		
14	31584	317	2424	5.31	B	0.20	1.31	0.25		
15	33449	299	2255	4.72	B	0.27	1.77	0.38		
16	35440	282	2313	9.48	A	352.0	2308.		0.24	0.22
					B	-0.27	-1.77	-0.19		
17	37153	269	1831	5.09	B	0.008	0.05	0.01		
18	38465	260	1845	3.71	B	-0.009	-0.06	-0.02		
19	40319	248	2957	8.51	A	561.0	3676.		0.43	0.40
					B	-0.02	-0.12	-0.01		
20	42953	233	2926	7.03	B	0.05	0.30	0.04		

[a]Statistics. B region: $\lambda_{230-500\ nm}$, χ^2=0.50, $\Sigma(\Delta\epsilon)^2$=53.9. Q region: $\lambda_{500-800\ nm}$, χ^2=31.1, $\Sigma(\Delta\epsilon)^2$=86 880 [b]$D_0 = \langle\epsilon\rangle_0/326.6$, where the units of D_0 (dipole strength) are D^2 (Debye units) [25]. [c]$\langle\Delta\epsilon_M\rangle_1$ is the first moment and $\langle\Delta\epsilon_M\rangle_0$ is the zeroth moment of the MCD; when fitting with an A term, the program calculates $\langle\Delta\epsilon_M\rangle_1$, and when fitting with an B term the program calculates $\langle\Delta\epsilon_M\rangle_0$. The Faraday term values, A_1 and B_0, are calculated directly from the moments as follows: $A=\langle\Delta\epsilon_M\rangle_1/152.5$ and $B=\langle\Delta\epsilon_M\rangle_0$. [d]$A_1$ data are printed above B_0 data when both an A term and an B term are used. [e]μ=magnetic moment, calculated as $2((A_1/D_0)\times 0.4669)$.

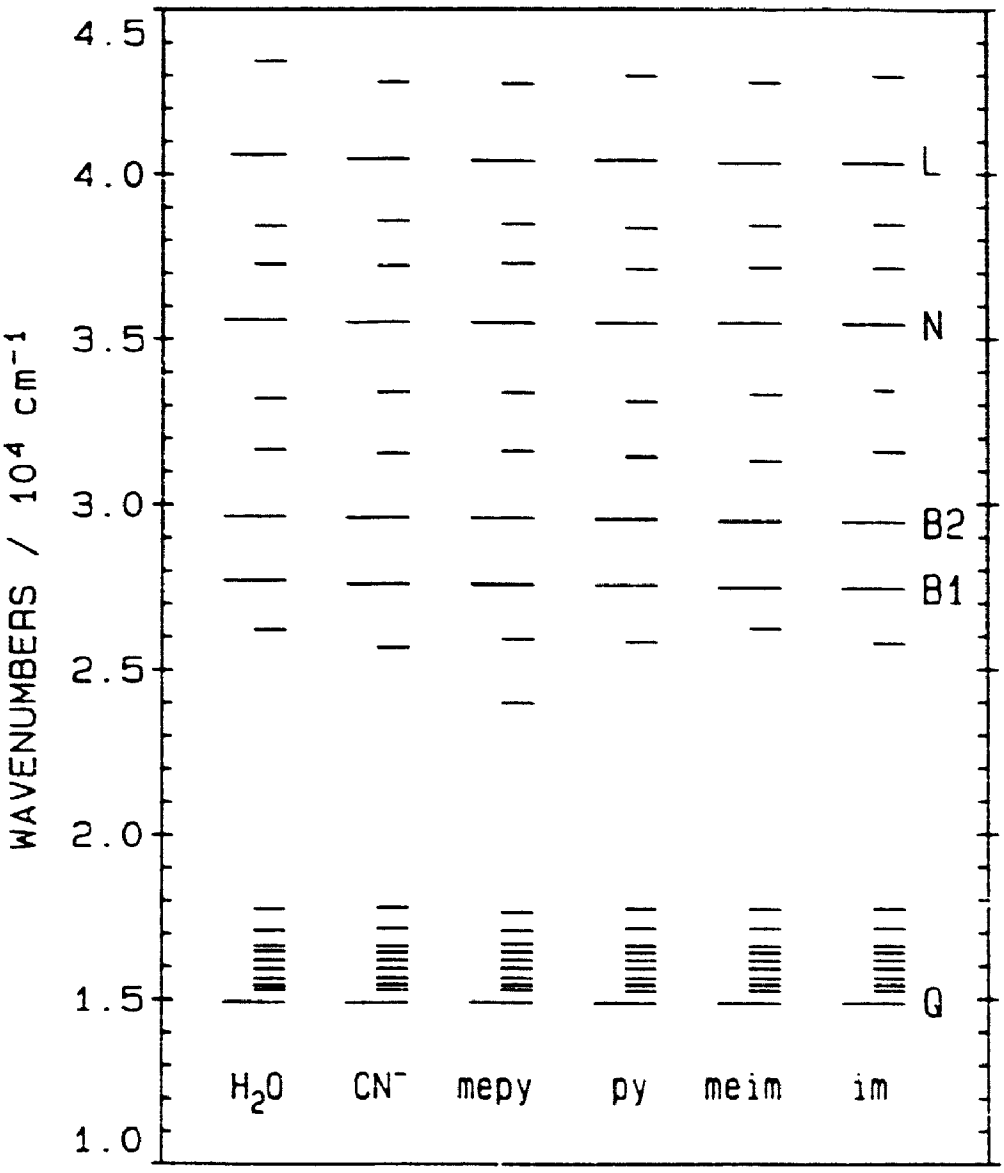

Figure 4-5 Comparison of the energy levels of $L_2MgPc(-2)$ (L = H_2O, im, meim, py, mepy and CN^-) calculated by band deconvolution of the absorption and MCD spectra of these complexes.

4.2.4 Moments Analysis of the Q Region

Table 4-4 lists the results of a moments analysis for the Q band in each $L_2MgPc(-2)$ complex. The moments calculation was carried out using the same program as described previously [25]. Since the program can only be used to analyse well resolved bands, the analysis was limited to the Q band. The moment calculations provide a value for the magnetic moment of the entire Q band excited state [54] (the high energy vibrational bands are included in the calculations). The A_1/D_0 parameter factors out any error in the estimation of the concentration for each solution because the same solution is used for both absorption and MCD measurements.

4.3 DISCUSSION

Despite the interest in the physical properties of MPc(-2) complexes, a general assignment of the absorption bands observed for many MPc(-2) species is not available. The problem in the analysis of the spectra of MPc(-2) complexes rests with the extensive overlap of transitions associated with the π ring in the 200 to 500 nm region of the neutral species [26,35]. The absorption spectrum becomes significantly more difficult to assign when extra bands due to charge transfer between the central metal and the ring are also present or when oxidation or reduction of the ring adds in new transitions that arise from the partially filled π orbitals [26,35,68,80].

Recently, in an extension of the pioneering studies of MPc(-2) spectra by Goutermans group, Nyokong et al. [26,35] have analysed the absorption and MCD spectra of neutral (im)ZnPc(-2) The results obtained in this first full deconvolution calculation carried out over the entire visible-UV range of a monomeric phthalocyanine, provide evidence that the absorption maximum near 350 nm comprised two bands, the B1 and B2 bands, both arising from degenerate transition. While Cd(II)Pc(-2) could also serve as a model MPc, its limited solubility in UV transparent solvents make it a poor model. As a result, we have carried out this study of the

absorption and MCD spectra of highly soluble $L_2MgPc(-2)$ complexes to establish the generality of the results reported for (im)ZnPc(−2).

4.3.1 Band Assignments

The molecular orbitals that are responsible for the bands observed between 250 and 800 nm are shown in Figure 4–6. For the porphyrins, the accidental degeneracy of the two highest occupied molecular orbitals ($1a_{1u}(\pi)$ and $1a_{2u}(\pi)$) leads to extensive configuration interaction, resulting in an allowed band, the B or Soret, and a forbidden band, the Q or α/β set [21]. Absorption and MCD spectra of a wide range of substituted metalloporphyrin complexes confirm that the Q band intensity is highly sensitive to vibronic coupling, yet has a high magnetic moment, of about 5 B.M., associated with it [21,81]. The Q transition can be readily identified from the MCD spectrum by the presence of its distinctive positive A term signature, even when the absorption intensity is so low that the band is obscured by the Q_{vib} progression. On the other hand, the Soret band is clearly allowed, and is found to have a magnetic moment of about 0.8 B.M. [21].

For phthalocyanines the situation is quite different. The Q band is clearly the most prominent feature in the spectrum of an "average" MPc complex. MCD spectra show that the magnetic moment is still about six times the magnitude of the B band (Table 4–3). Significant vibronic effects on the Q band appear to be restricted to the vibrational envelope observed to the blue of Q. Unlike the case for the porphyrins, the B band is difficult to find. In the 350 nm region, several broad bands overlap. In addition, charge transfer bands may overlay this region as well, further complication the assignment problem [68,52].

Gouterman and coworkers [65], have reported a wide range of MPc(−2) spectra using gas phase studies in order to overcome the notorious insolubility properties of phthalocyanines. In absorption and MCD studies of a series of MPc(−2) complexes in

DMSO solutions, Stillman and Thomson [52] reported that the second excited state (the B1 band) was probably located near 370 nm, rather than the 300 nm that would be normally determined from the absorption maximum. MCD spectra [34,45,79] suggested that for Li_2Pc and ZnPc in DMSO, two degenerate transitions lie close enough that in many instances the resultant bands would completely overlap. Nyokong et al. [26,35] confirmed this observation for a series of LZnPc(−2) complexes whose spectra were recorded in DCM. Full band envelope deconvolution was shown to be essential in determining the exact band centres from a series of six or seven that overlapped between 240 and 450 nm. The data presented here for $L_2MgPc(-2)$ confirmed the earlier observation that the B region comprises a series of broad, overlapping bands.

The absorption maxima measured directly from the absorption spectra (Table 4–2) are useful in the identification of phthalocyanines from recorded spectra. However, care should be exercised when these maxima are used to assign band centres. Direct assignment works when the band is either well removed from other bands or its intensity is significantly larger than any overlapping bands. Deconvolution of the B region of $(im)_2MgPc(-2)$ (Figure 4–4) emphasizes inadequacies in assigning these spectra directly from band maxima. The results clearly indicate that there are two overlapping bands in this region (with centres near 338 and 362 nm). Deconvolution of the MCD spectra indicate that the two overlapping bands are A terms, which are assigned as the B1 and B2 bands of the revised model [1,28]. The deconvolution yielded two additional A terms which are assigned as the higher energy N and L bands [26,35].

4.3.2 Comparison Between the Deconvolution Data for MgPc and ZnPc

Reproduction of data for one series of complexes by fitting bands to a series of related spectra greatly enhances the reliability of the calculation. An energy level

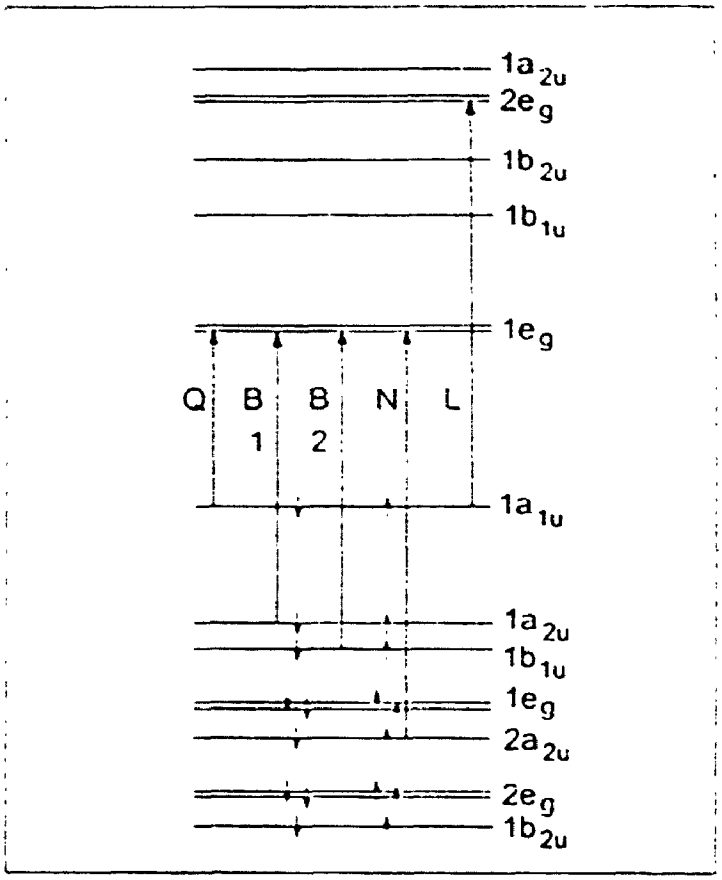

Figure 4-6 Selected molecular orbitals and allowed ring transitions for the $^1A_{1g}$ ground state of MgPc(-2).

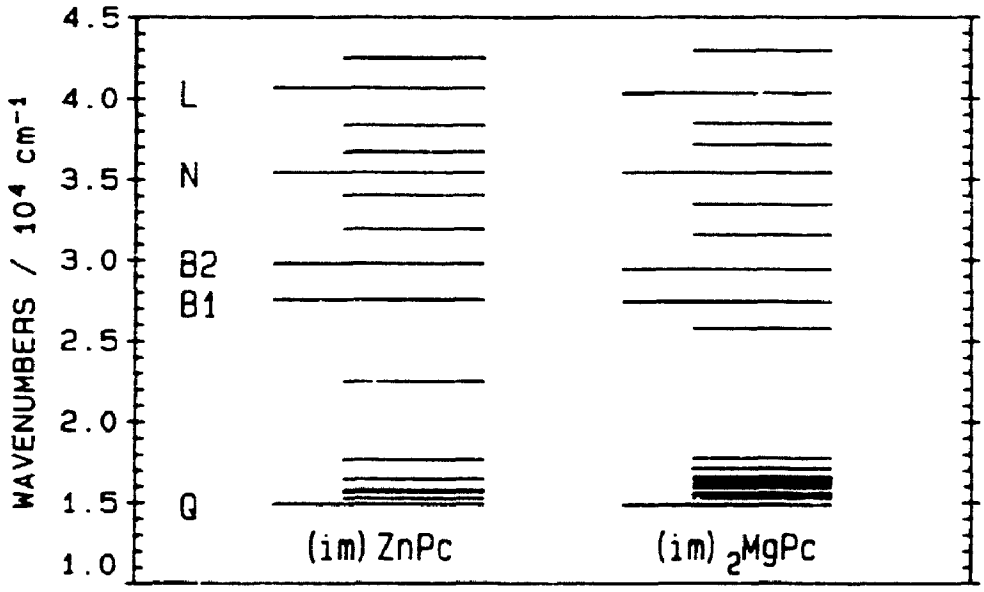

Figure 4-7 Comparison of the energy levels of $(im)_2MgPc(-2)$ and (im)ZnPc(-2) [26] calculated by band deconvolution of the absorption and MCD spectra for these two complexes.

diagram comparing (im)ZnPc(−2) and $(im)_2$MgPc(−2) compounds is shown in Figure 4–7. Focusing on the degenerate transitions, one can see that the results are comparable between zinc and magnesium. In this study, we also examined a variety of L_2MgPc(−2) complexes. An energy level diagram for the six L_2MgPc(−2) complexes studied is shown in Figure 4–6. Aside from an additional band (a nondegenerate transition) required for $(mepy)_2$MgPc(−2), all six species required the same number of bands to fit the spectral envelopes. The energies of the bands vary little as a function of the ligand attached to the magnesium. The deconvolution results (Figure 4–5) illustrate the similarities in band energies and transition polarizations across the different sets of data. Table 4–5 lists the band centres for the degenerate transitions obtained from the deconvolution calculations, rather than directly from the band maxima in the absorption spectra, and assignments based on the modified Gouterman model (the Q, B1, B2, N and L bands) are associated with each of these bands.

In Figure 4–8, the energy difference $[\nu_{max}(L_2MgPc)-\nu_{max}(H_2O)_2MgPc]$ for each of the degenerate bands (Q, B1, B2, N and L) is plotted for the six different L_2MgPc(−2) species. The plot shows that the energies of the degenerate bands decreases across the ligand series: H_2O > CN^- > mepy > py > meim > im. The series shows that all the ligand species have band maxima that are red–shifted to varying extents from the hydrated MgPc(−2) species dissolved in DCM. The Q band energy is affected the least by the change in the ligand attached to magnesium. The shift in the band centre energy for the B1 and B2, and the N and L bands, is approximately equal for each pair of bands.

Since magnesium is a hard metal, the ligands attached to it should not exert a large effect. Figure 4–5 shows that this is the case as there is little difference in the band centres for the six complexes. The data in Figure 4–8 indicates that the band centre energies decrease (red shift) in a sequence that follows a decrease in the σ

Table 4-4

Moment analysis of the Q region absorption and MCD spectra of the $L_2MgPc(-2)$ complexes.

L[a]	ν/cm^{-1}	D_0[b]	$\langle\Delta\epsilon_M\rangle$	A_1[c]	A_1/D_0	A_1/D_0 ZnPc[26]	magnetic moment[d]	$\langle\Delta\epsilon_M\rangle$	B_0/D_0 /10^{-1}
H_2O	15232	18.8	7990	524	2.78		2.60	1.93	6.72
im	15173	23.8	9240	606	2.54	1.51	2.37	0.86	2.37
meim	15172	20.1	7610	499	2.49		2.33	0.98	3.20
py	15194	32.6	13200	862	2.65	2.62	2.48	3.35	6.75
mepy	15244	65.1	25800	1690	2.60		2.43	1.35	1.36
CN^-	15205	18.6	7480	491	2.64	3.55	2.47	1.33	4.69

[a]In DCM. [b]The units of the dipole strength, D_0 are D^2 (D=Debye units) [25]. [c]A_1 has the units of D^2 and B_0 has the units of D^2/cm^{-2}. [d]Magnetic moment in units of μ_β, calculated from $2((A_1/D_0)\times 0.4669)$.

Table 4-5

Band centres for the degenerate transitions of $L_2MgPc(-2)$, obtained by the deconvolution of the absorption and MCD spectra.

$L_2MgPc(-2)$	Q	B	B	N	L
$(H_2O)_2MgPc(-2)$	670	361	338	281	246
$(im)_2MgPc(-2)$	672	364	339	282	248
$(meim)_2MgPc(-2)$	672	364	339	282	248
$(py)_2MgPc(-2)$	671	363	338	282	247
$(mepy)_2MgPc(-2)$	671	363	338	282	248
$[(CN)_2MgPc(-2)]^{-2}$	671	363	338	282	247

donor and π acceptor strength of the ligand [34,37]. The data in Figure 4-8 also shows that the B1 and B2 lines roughly follow the same slope. The effect is also apparent, but not so obvious for the N and L bands. It is believed that the effect seen for the data for the two sets of bands arise either from a coupling between the two pairs of energy levels or the use of a common molecular orbital in the construction of the excited states [21].

Deconvolution calculations carried out for complexes of $L_2MgPc(-2)$ and $LZnPc(-2)$ [26,35], readily verify the presence of five degenerate electronic transitions which correspond to the Q, B1, B2, N and L bands. The adjustment to the B1 and B2 nomenclature allows one to correlate the experimental band energies with theoretical calculations. Of the limited number of theoretical calculations, those of Gouterman and coworkers, who calculate energy levels and later magnetic properties, are the most useful. Without adjustments, the Q and B bands correlates well between experiment and theory, but the N, L and C bands do not correlate. The adjustment

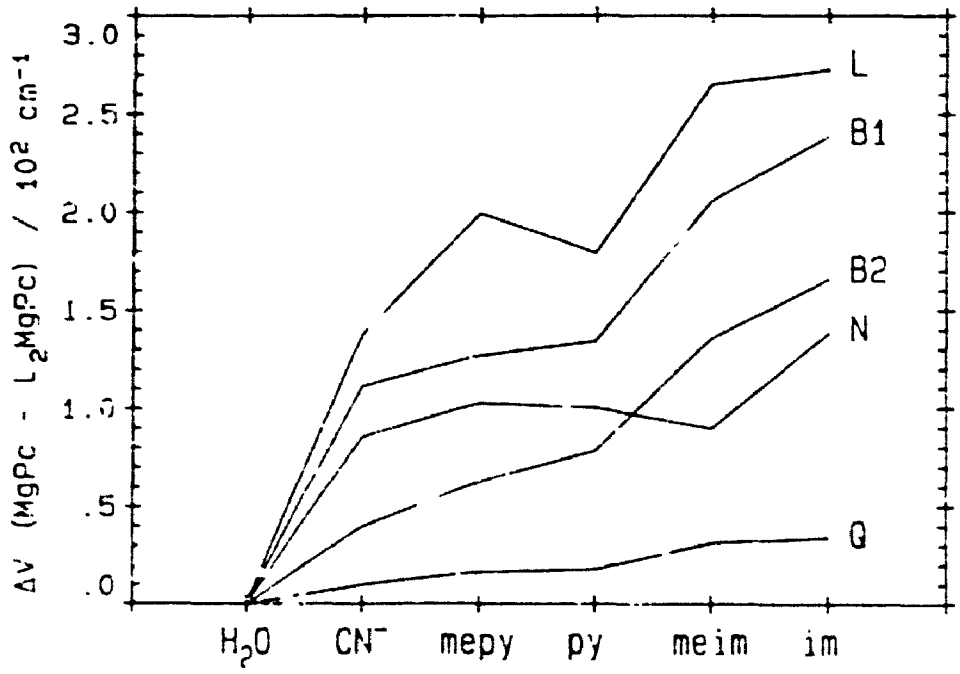

Figure 4-8 Plot of differences in band centres for each of the five degenerate transitions (Q, B1, B2, N and L) of the $L_2MgPc(-2)$ complexes. The energies for the five degenerate bands are subtracted from the reference $(H_2O)_2MgPc(-2)$ compound. This standardizes the $\Delta\nu$ (cm^{-1}) values for the five degenerate bands in $(H_2O)_2MgPc(-2)$ to zero.

of the theory to include a second B term shifts the experimental N and L band energies (the C band is further in the UV) to positions that correlate well with the theoretical predictions.

4.3.3 Moment Analysis

In addition to providing more detail in the spectrum, the MCD technique can also be used to provide angular momentum data for excited states as long as the transition is part of an isolated band system [26,35,52] For phthalocyanines, the Q band is usually completely isolated from other bands, including charge transfer bands. This property means that it is possible to compare the magnetic moments of the excited singlet of a wide range of different MPc complexes. Only Stillman and Thomson [52] and Nyokong et al. [26,35], have previously published data for a range of phthalocyanines. The MCD technique makes the determination of these values reasonably straightforward, and with a sufficient range available, interpretation of ring–metal orbital interaction should be more reliable than basing such discussion on either band centres or on Q–B splitting energies.

A_1/D_0 values (following the conventions of Schatz [62] and Stephens [63,64]) calculated from the first and zeroth moments of the absorpton and MCD spectra which were obtained by integrating over the whole band envelope in the 500 to 750 nm region, fall into the range reported previously for ZnPc [26,35]. The trend in values depends on the axial ligand as noted previously for a wider range of metals. For L_2MgPc(−2) compounds (Table 4–4) we find that the magnetic moment of the S_1 state (which gives rise to the Q band) is remarkably constant at about 2.6 (expressed in terms of A_1/D_0). This compares with a range of 1.5 to 3.55 for LZnPc(−2) compiexes [26,35,52]. This variation is interpreted as a difference in response by the two metals to axial ligation, with interaction between the filled d orbitals and the ligand's σ and π orbitals being possible with the zinc, but absent with the magnesium.

4.4 CONCLUSIONS

Quantitative analysis of the absorption and MCD spectra of various liganded species of MgPc(−2) indicate the presence of five degenerate transitions. Band deconvolution calculations placed the band centres for these transitions at: 670 (Q), 362 (B1), 338 (B2), 282 (N) and 247 nm (L). The agreement of these results with those for ZnPc(−2) [26,35], suggests that the difference in coordination geometry, covalent radii and the presence of a filled d shell in zinc do not significantly affect the $\pi \rightarrow \pi^*$ spectra.

CHAPTER 5

MAGNESIUM PHTHALOCYANINE π-CATION RADICAL

5.1 INTRODUCTION

Studies of the electrochemical and photochemical properties of porphyrins are facilitated by their high solubility in a wide range of solvents. Similar studies with phthalocyanines have been hindered by their limited solubility. Group 1 and 2 metal-substituted phthalocyanines are very much more soluble in spectroscopically transparent and electrochemically useful solvents. Magnesium phthalocyanine (MgPc) exhibits no bands due to charge transfer between 200 nm and 1000 nm in its absorption spectrum [27]. Because MgPc(-2) is highly soluble in chlorinated solvents such as dichloromethane (DCM), formation of concentrated solutions of the radical cation by a variety of methods is also possible. Thus MgPc(-2) serves as an ideal model for the spectral properties of both neutral and oxidized phthalocyanines.

The two top filled molecular orbitals in metallophthalocyanines are assigned symmetry labels of $1a_{1u}$ and $1a_{2u}$, with $1a_{1u}$ highest in energy [7,21]. Oxidation of phthalocyanines yields $^2A_{1u}$ as the ground state for the ring. The MgPc(-1) species models the extreme situation of the electronic arrangement in many complexes of octaethylporphyrin (OEP) [82,83], and in the heme enzyme catalase [84], in which it is suggested the ground state is $^2A_{1u}$, rather than the $^2A_{2u}$ state. This contrasts the situation found for other porphyrin radical cation species, for example, ZnTPP(1) [82], where the ground state has been assigned as $^2A_{2u}$ One electron oxidation and reduction of the π ring in MgPc has been achieved chemically [72,85], electrochemically [85,86] and photochemically [87-88]. Although absorption spectra of MgPc(-1) have been previously reported [70], there remains considerable uncertainty as to the origin of the major absorption bands observed between 200 and 1000 nm [32].

In this chapter the photochemical, electrochemical and chemical methods used to

form monomeric and dimeric MgPc(−1) species are described. The first MCD spectra for these species, and deconvolution calculations for the absorption and the MCD spectra for several $L_nMgPc(-1)$ complexes are reported.

5.2 RESULTS

5.2.1 Ring Oxidation in MgPc(−2)

The oxidation of $L_2MgPc(-2)$ to form the ring oxidized species can be readily followed in the absorption spectrum. In DCM solutions oxidation can be carried out photochemically (Figure 5−1), electrochemically (Figure 5−2) and chemically by the addition of either Br_2 (Figure 5−3) or nitric acid (Figure 5−4). In Figures 5−1 to 5−4, the intensities of the spectral features characteristic of the neutral MgPc(−2) [27], the Q band at 670 nm and the B band at 345 nm, decrease as the oxidation proceeds. Intensities of the absorption and the MCD bands change with the axial ligand. The characteristic spectral features of phthalocyanine cation radicals at room temperature, bands centred near 825, 717, 507 and 422 nm, grow in intensity isosbestically as the oxidation proceeds with each of these methods.

Photochemical (Figure 5−1), electrochemical (Figure 5−2) and chemical oxidation using Br_2 (Figure 5−3), leads to incomplete oxidation of MgPc(−2). Figure 5−1 displays the absorption spectra obtained during photochemical oxidation of $(meim)_2MgPc(-2)$. Complete oxidation, which we associate with total loss of the 670 nm band, only takes place with considerable loss in intensity of the bands from the oxidized species. Continued irradiation in the Q region appears to cause disruption of the phthalocyanine ring. In Figure 5−1, the photolysis was stopped with about 5% of the neutral MgPc(−2) remaining.

During the electrochemical oxidation, Figure 5−2, new bands centred near 650 nm and 690 nm intensify at the end of the oxidation. The positions of these two absorption bands are those expected for the symmetry split Q band of metal free

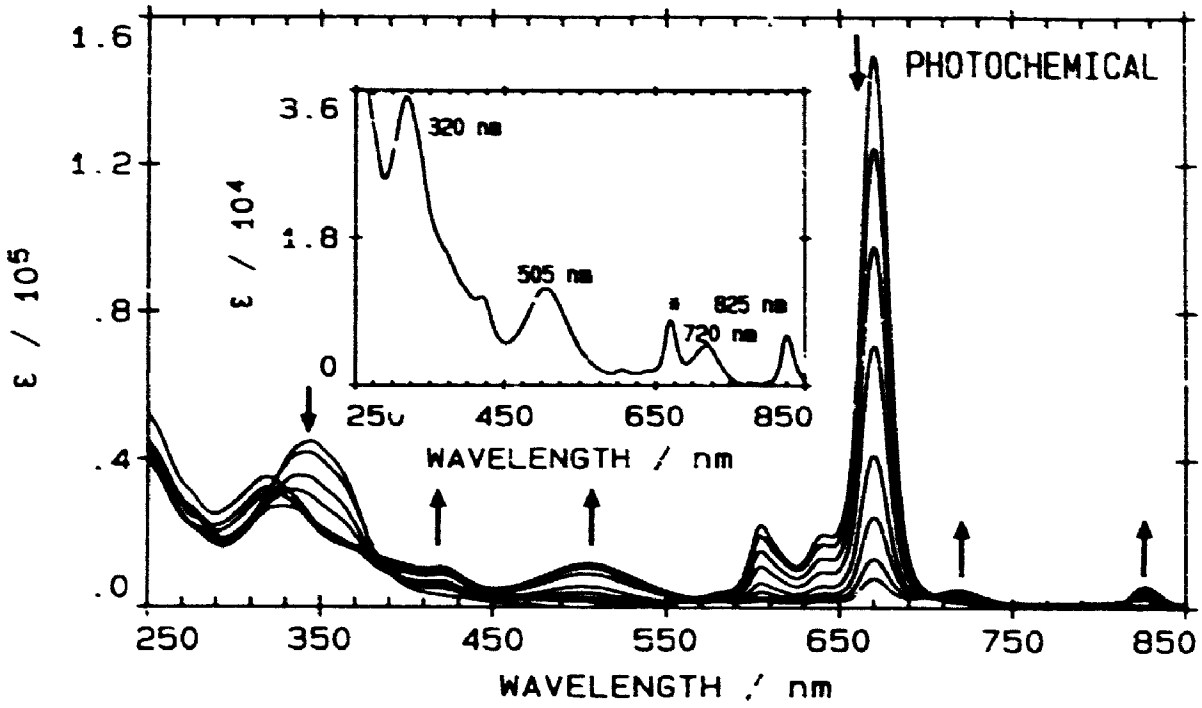

Figure 5-1 Absorption changes observed during the photochemical oxidation of $(H_2O)_2MgPc(-2)$ dissolved in DCM containing 10^{-2} M CBr_4. The inset displays the absorption spectrum of the radical with less than 5% unoxidized $(H_2O)_2MgPc(-2)$. The arrows represent the changes in spectral intensity upon oxidation.

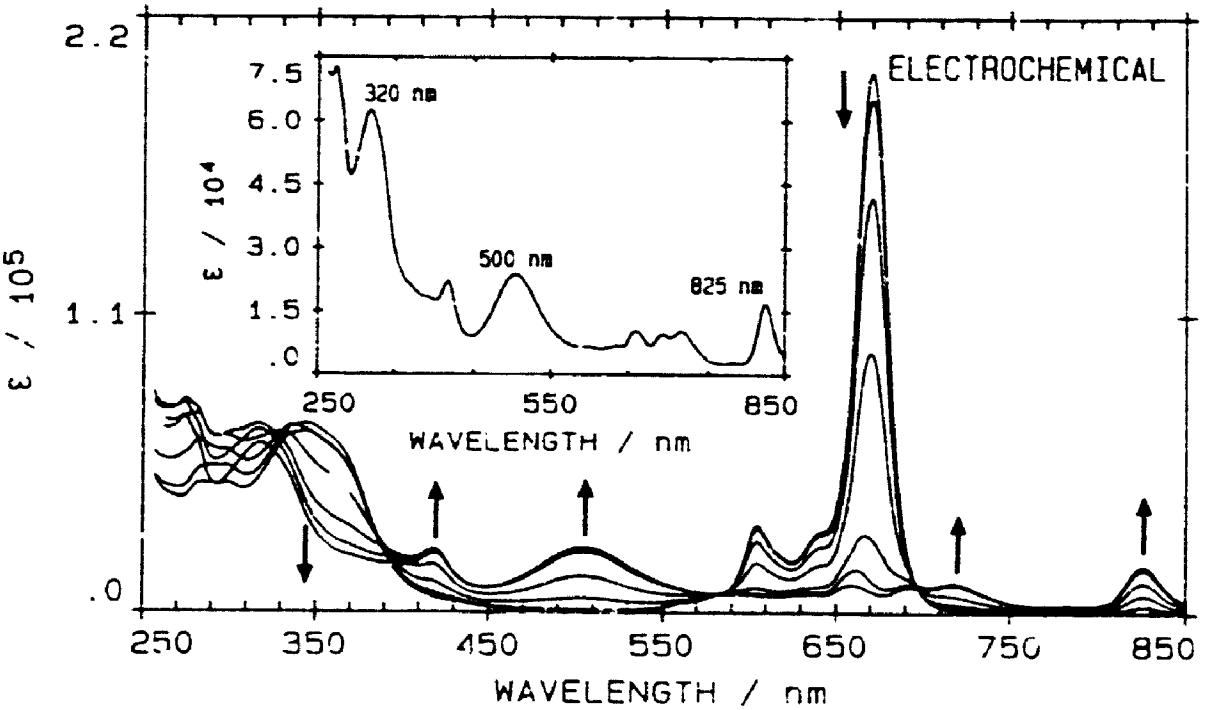

Figure 5-2 Absorption changes observed as CPC was performed at + 0.70 V vs. SCE on $(pip)_2MgPc(-2)$ dissolved in DCM containing 0.05 M TPAP. The inset displays the absorption spectrum with less than 5% unoxidized $(pip)_2MgPc(-2)$. The arrows represent the changes in spectral intensity upon oxidation.

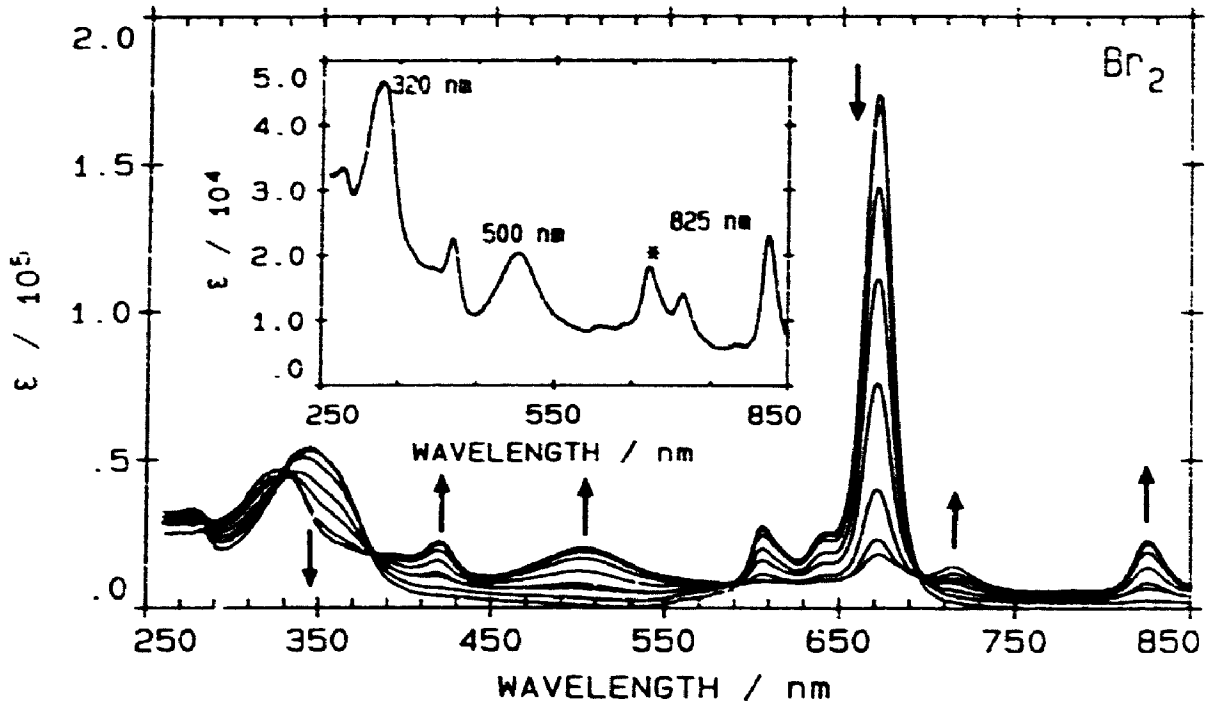

Figure 5-3 Absorption changes observed during the chemical oxidation of $(py)_2MgPc(-2)$ dissolved in DCM. Br_2 was used as the oxidizing agent. The inset displays the absorption spectrum of radical with less than 5% unoxidized $(py)_2MgPc(-2)$. The arrows represent the changes in spectral intensity upon oxidation.

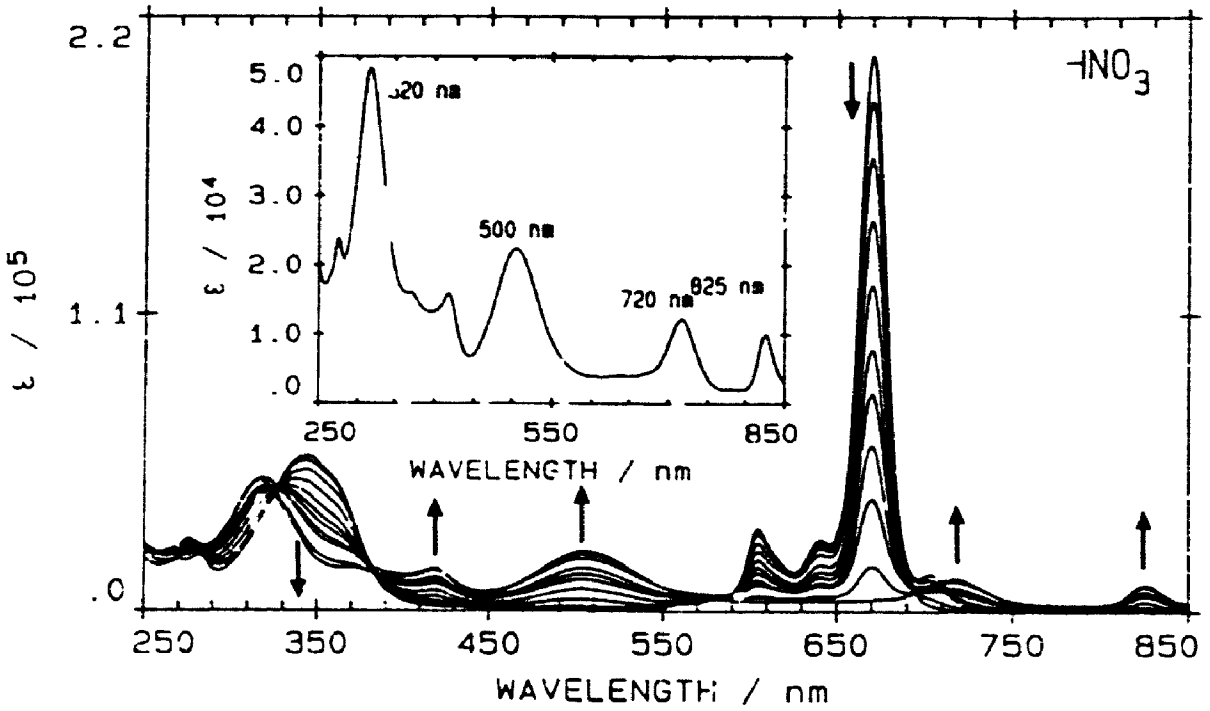

Figure 5-4 Absorption changes observed during the chemical oxidation of $(H_2O)_2MgPc(-2)$ dissolved in DCM. Nitric acid was used as the oxidizing agent. The inset displays the absorption spectrum for 100% $(H_2O)_nMgPc(-1)$. The arrows represent the changes in spectral intensity upon oxidation.

phthalocyanine ($H_2Pc(-2)$). With oxidation by Br_2, Figure 5-3, a shoulder on the low energy side of the 670 nm band appears when oxidation exceeds 95%.

Chemical oxidation using nitric acid (Figure 5-4) generates the cleanest solution of $L_nMgPc($;. Complete loss of the MgPc(-2) Q band at 670 nm and the retention of isosbestic points, indicates that quantitative oxidation has been achieved. The inset in Figure 5-4 shows a spectrum of MgPc(-1), which exhibits well resolved bands centred on 825, 717, 507 and 319 nm. With nitric acid, the initial oxidation products are characterized by a weak absorption band near 705 nm, which grows rapidly in intensity, but later disappears as the oxidation proceeds. This band is not related by isosbestic points to the 717 nm band that is characteristic of the oxidized product. As we will discuss below, the 717 nm band arises from the dimer, $[LMgPc(-1)]_2^{++}$, whereas the 825 nm band arises from monomeric $[L_nMgPc(-1)]^{+}$.

5.2.2 Absorption, MCD and EPR Spectral Results

Figure 5-5 shows the room temperature absorption and MCD spectra of $(im)_2MgPc(-2)$ and $(im)_nMgPc(-1)$ formed by adding Br_2 in DCM. Absorption band maxima for a range of $L_nMgPc(-1)$ species are listed in Table 5-1. The spectral data closely resemble the spectra obtained for ring oxidized ZnPc(-1) [26,35]. With the loss of the intense Q band in $(im)_nMgPc(-1)$ (Figure 5-5) three weak, but well-resolved, absorption bands appear in the window regions of the spectrum of the neutral species. These bands are centred near 825, 717, and 507 nm. The absorption band located near 507 nm is a characteristic feature of phthalocyanine π-cation radical species and is associated with a B term in the MCD spectra, which means that the transition is to a nondegenerate excited state. The 825 and 717 nm bands are relatively isolated from other absorption bands and appear as A terms in the MCD spectrum, although the band width of the 717 nm band (700 cm^{-1}) is considerably greater than that of the 825 nm band (200 cm^{-1}). The change in

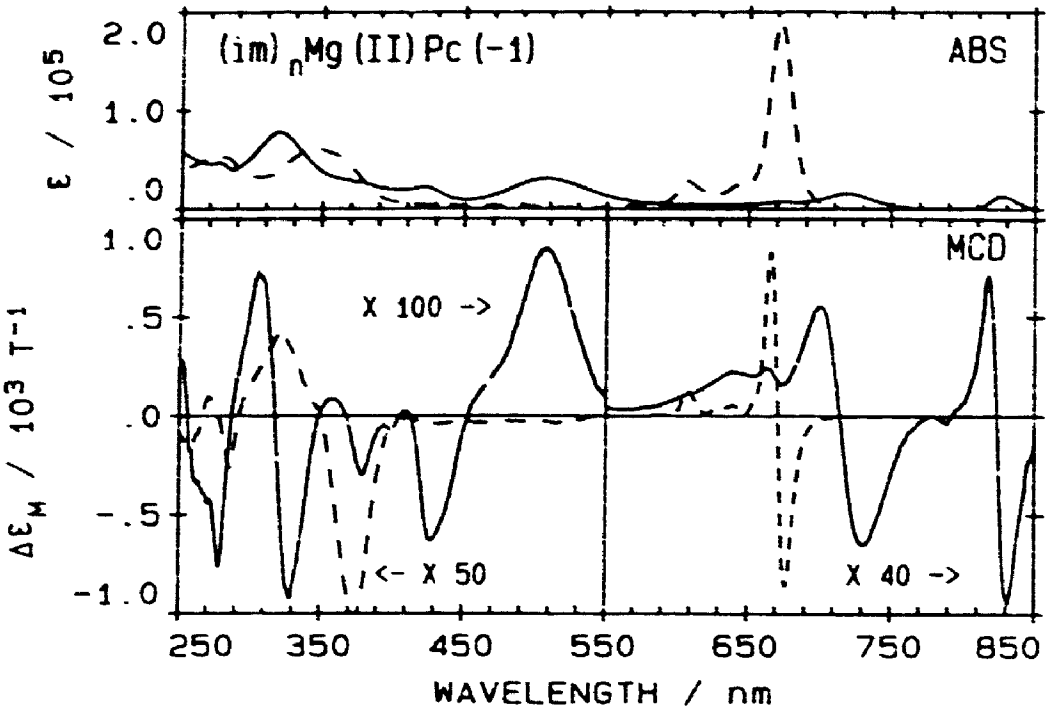

Figure 5-5 Absorption (ABS) and MCD spectra for neutral $(im)_2MgPc(-2)$ (dashed lines) and oxidized $(im)_nMgPc(-1)$ (solid lines) recorded in DCM. Note the changes in ordinate scales for the MCD traces.

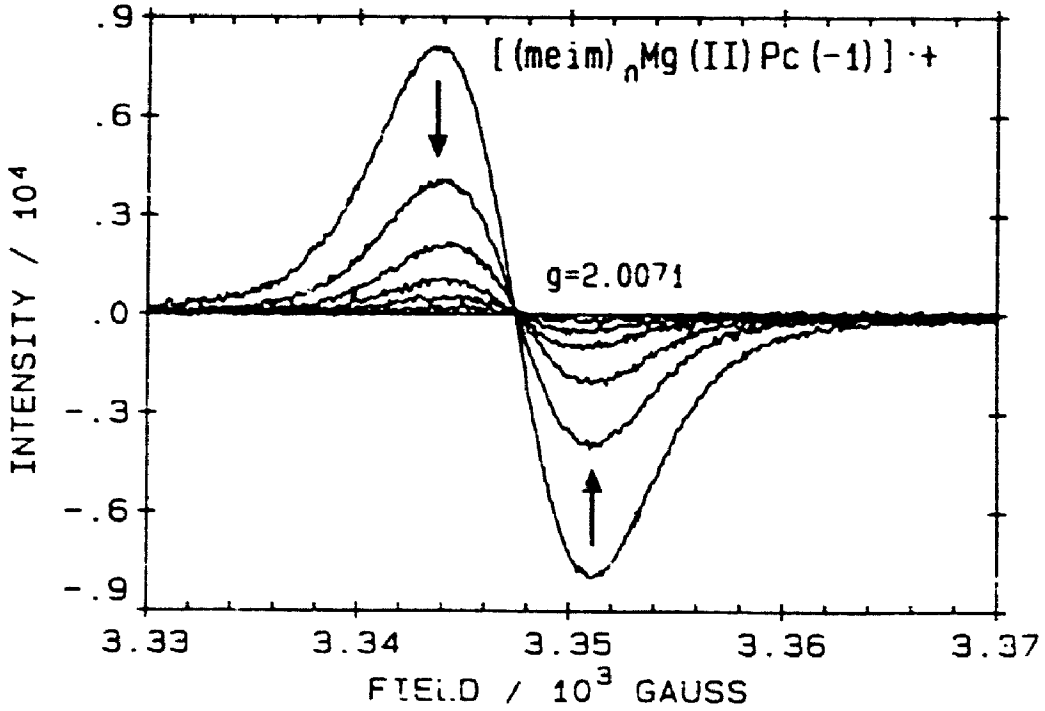

Figure 5-6 EPR spectral changes observed for $(meim)_nMgPc(-1)$ in DCM as the solution was cooled from 300 K to 200 K. The arrows represent intensity changes as the solution was cooled.

spectral properties between neutral and π–cation radical is not nearly as pronounced in the B region as in the Q region. Absorption band maxima are located at 422, 319 and 276 nm for the B region of the π–cation radical.

Figure 5–6 is a variable temperature (300 to 200 K) plot of the EPR spectral intensity for nitric acid oxidized $(meim)_nMgPc(-1)$. The EPR signal intensity for $(meim)_nMgPc(-1)$ decreases to zero at 200 K. The room temperature EPR g values and band widths (Gauss) for $L_nMgPc(-1)$ complexes, are listed in Table 5–2. The EPR g values calculated for the $L_nMgPc(-1)$ species are very close to the free electron value of 2.0023.

Figure 5–7 shows the absorption spectra of $(H_2O)_nMgPc(-1)$ in DCM, formed by oxidation with nitric acid, recorded between 300 and 200 K. Significant changes in band intensities are observed as the temperature is lowered (the arrows indicate changes in absorbance as the temperature falls from 300 K to 200 K). The effect is completely reversible, with recovery of the initial spectrum when the solution is warmed to room temperature. The major changes between 300 and 200 K are the loss of the 825 nm band, and the intensification of the 717 nm band. The absorption band intensity at 717 nm increases about 50% from 300 K down to 200 K. The loss of the EPR spectral intensity at 200 K, in Figure 5–6, aids the assignment of the 200 K absorption spectrum to dimeric $[(H_2O)MgPc(-1)]_2^{++}$. Figure 5–8 illustrates absorption and MCD spectra of the dimeric species recorded from a solution at 200 K.

Monomeric $[MgPc(-1)]^{\cdot +}$ is difficult to obtain. However, by reducing the fraction of dimer, it is possible to construct a spectrum of the pure monomeric species. Figure 5–9 displays the absorption and MCD spectra of monomeric $[MgPc(-1)]^{\cdot +}$ in DCE at 300 K obtained by subtracting residual dimer bands based on the absorption at 710 nm.

Table 5-1

Observed maxima in the absorption spectra of the bromine (Br_2) oxidized $L_2MgPc(-1)$ species in DCM.

$L_2MgPc(-1)$	λ_{max} (nm)[a]						
L = H_2O	826	714	506	423	—	320	278
L = im	827	720	507	422	—	319	276
L = meim	827	719	507	423	—	318	276
L = py	827	720	506	422	—	318	276
L = mepy	827	719	507	423	—	320	279
L = CN^-	826	718	507	416	—	310	—
L = im MONOMER AT 300 K[b]	827	—	505	411	387	328	275
L = H_2O DIMER AT 200 K	—	712	510	—	370	317	277

[a] λ_{max} is measured directly from the absorption spectrum. [b] Monomer spectra recorded in DCE.

Table 5-2

The EPR parameters for Br_2 oxidized $L_2MgFc(-1)$ in DCM.

COMPLEX	g value	band width (Gauss)
$(H_2O)_nMgPc(-1)$	2.0039	6.75
$(im)_nMgPc(-1)$	2.0032	6.75
$(meim)_nMgPc(-1)$	2.0071	6.75
$(py)_nMgPc(-1)$	2.0048	7.25
$(mepy)_nMgPc(-1)$	2.0065	5.25
$(CN^-)_nMgPc(-1)$	2.0076	1.50

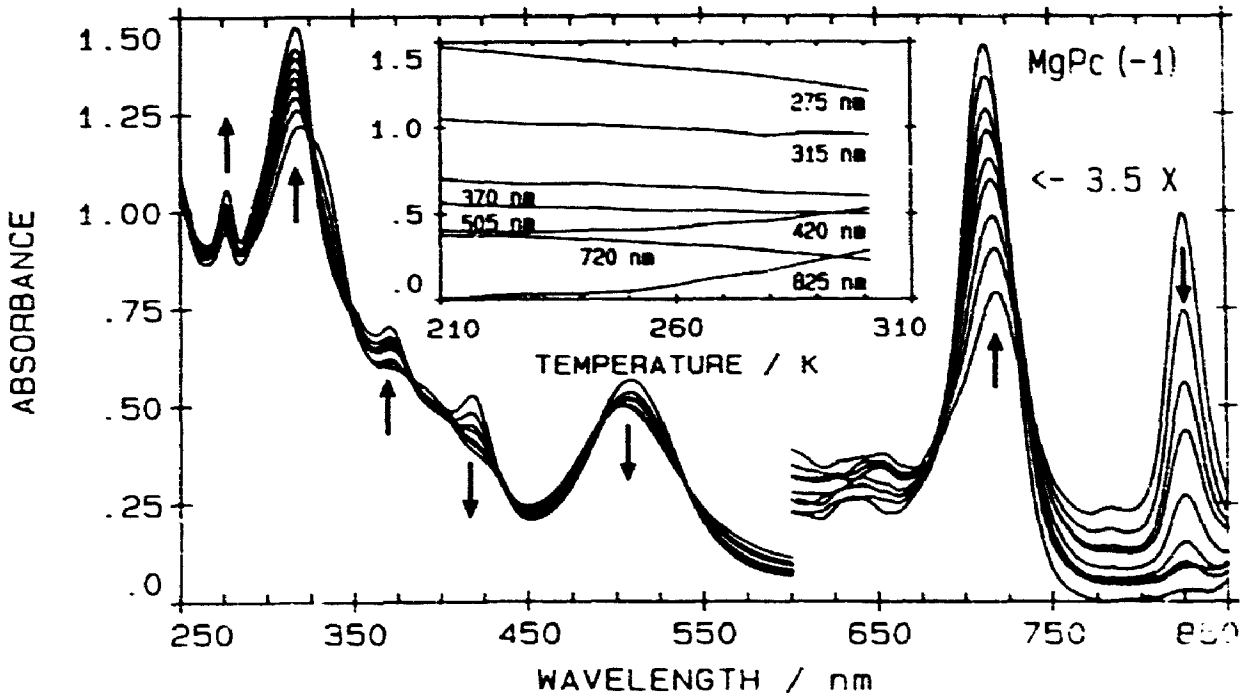

Figure 5-7 Absorption changes observed for $(H_2O)_nMgPc(-1)$ in DCM as the solution was cooled from 300 K to 200 K. The arrows represent intensity changes as the solution was cooled.

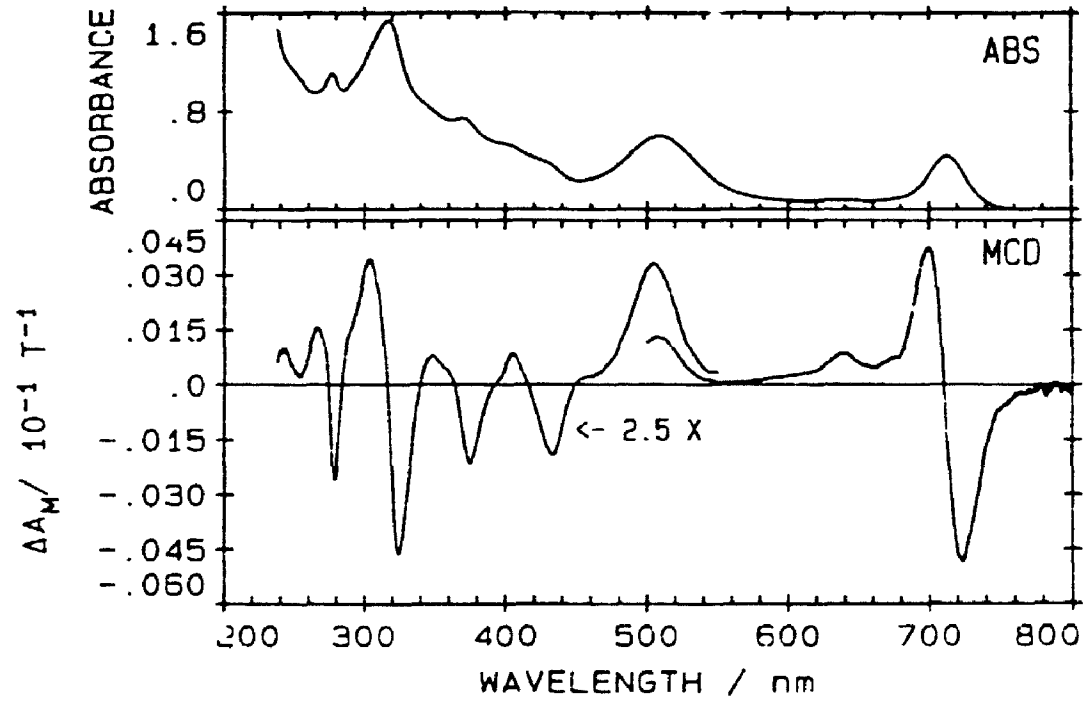

Figure 5-8 Low temperature (200 K) Absorption (ABS) and MCD spectra for dimeric $[(H_2O)MgPc(-1)]_2^{++}$ in DCM.

5.2.3 Deconvolution of the Q Region

The absorption and MCD spectral data presented in Figure 5–10, as the solid lines, represent the characteristic, room temperature spectral properties of $L_nMgPc(-1)$. As with the treatment of the spectral data for ZnPc(−2) [26,35], ZnPc(−1) [26,35] and MgPc(−2) [27], band positions can be accurately identified if band deconvolution techniques are employed. While the spectral data for $L_nMgPc(-1)$ are more complicated than the data for $L_2MgPc(-2)$, the Gaussian band shapes still yield reliable deconvolution results when used to fit the spectral data of the radical cation. MCD residuals are plotted below the MCD spectra in Figures 5–10 to 5–15. The randomness of the residual suggests little systematic error. The greatest amount of residual noise occurs in the near infrared region (800 – 870 nm) where resolution of the experimental spectra is the lowest due to a reduction of the signal to noise ratio of the spectrometer.

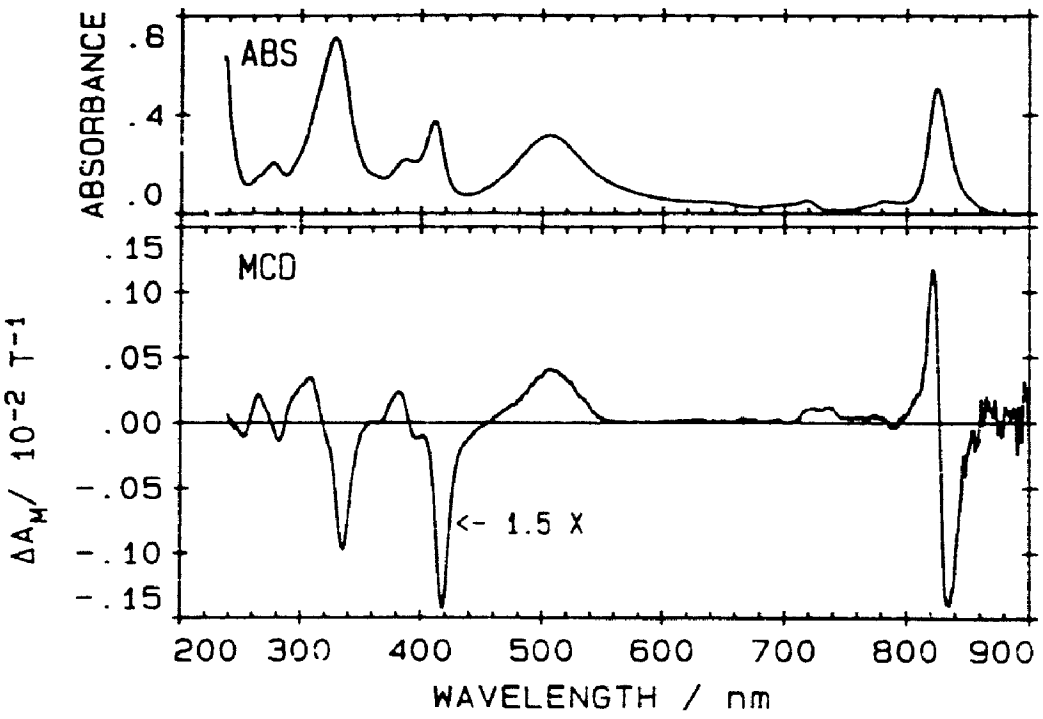

Figure 5–9 Room temperature (300 K) Absorption (ABS) and MCD spectra for monomeric $[(im)_nMgPc(-1)]^{\cdot+}$ in DCE. The spectral bands due to residual contribution by the dimer have been subtracted out.

While the intense Q band, and associated A term in the MCD spectrum of MgPc(−2) is absent for $L_nMgPc(-1)$, the MCD spectrum of $L_nMgPc(-1)$ shows that degenerate excited states are responsible for a significant fraction of the absorption intensity in the Q region. In the Q region (550 − 850 nm) of $(im)_nMgPc(-1)$ (Figure 5−10), 6 out of the 10 fitted bands have relatively equal intensities. In the absorption spectra, two well resolved bands, with maxima near 825 and 717 nm, are associated with A terms in the MCD spectra (the fitting links a B term with every A term).

5.2.4 Deconvolution of the B Region

The absorption and MCD spectra in the B region (250 − 550 nm) of $(im)_nMgPc(-1)$ (Figure 5−11) are considerably more complicated than the same region for $(im)_2MgPc(-2)$ [27]. From the absorption spectra of $(im)_nMgPc(-1)$ (Figure 5−11) we observe a series of overlapping bands, several of which appear in the spectral window (400 − 550 nm) of the neutral phthalocyanine. Deconvolution of the absorption spectra requires 18 overlapping bands to fill the envelope. This fit utilizes 8 more bands than was required to deconvolute the corresponding region of MgPc(−2) [27]. Six of the absorption bands result from degenerate electronic transitions, since these bands correspond to linked A and B terms in the MCD spectra. The additional 12 bands required to fill the absorption spectral envelope correspond to B terms in the MCD spectra. Table 5−3 summarizes the parameters used to fit the absorption and MCD spectra of the Q and B regions of $(im)_nMgPc(-1)$.

5.2.5 Monomer and Dimer Absorption and MCD Spectra

The absorption and MCD spectral data for monomeric $[(im)_nMgPc(-1)]^{\cdot +}$, Figures 5−12 and 5−13, were analysed in two sections, the 600 − 900 nm region encompassing the Q band and the 200 − 550 nm region which encompasses degenerate

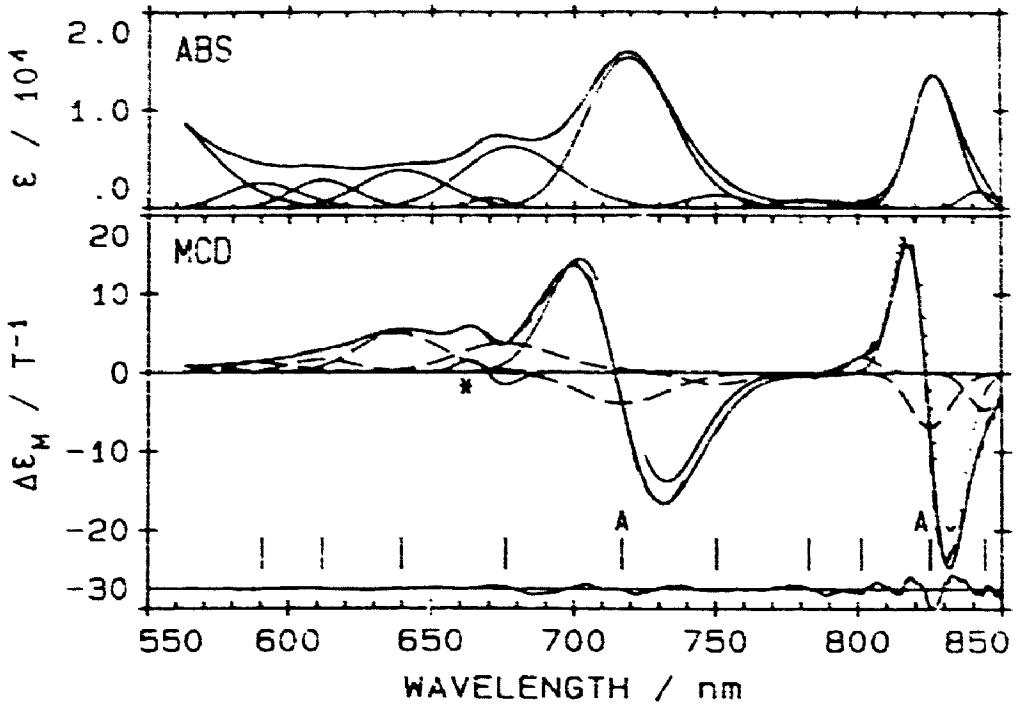

Figure 5-10 Results of a band analysis for $(im)_nMgPc(-1)$ in DCM: the visible region (bands 1 to 10). (a) absorption: (——) experimental data; (– –) fitted data; (——) individual bands. (b) MCD: (——) experimental data; (– –) fitted data; (····) A terms; (– –) B terms. The band centres of A terms are labelled "A".

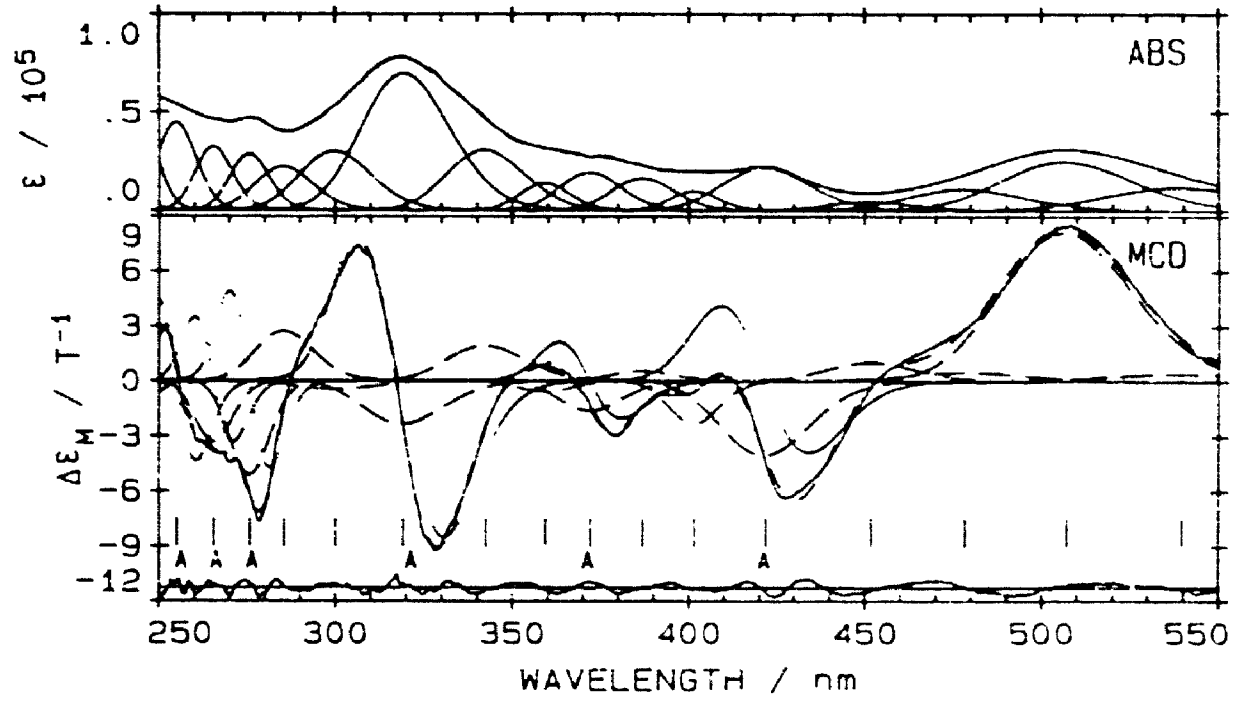

Figure 5-11 Results of a band analysis for $(im)_nMgPc(-1)$ in DCM: the ultraviolet region (bands 11 to 27). (a) absorption: (——) experimental data; (– –) fitted data; (— —) individual bands. (b) MCD: (——) experimental data; (– –) fitted data; (····) A terms; (– –) B terms. The band centres of A terms are labelled "A".

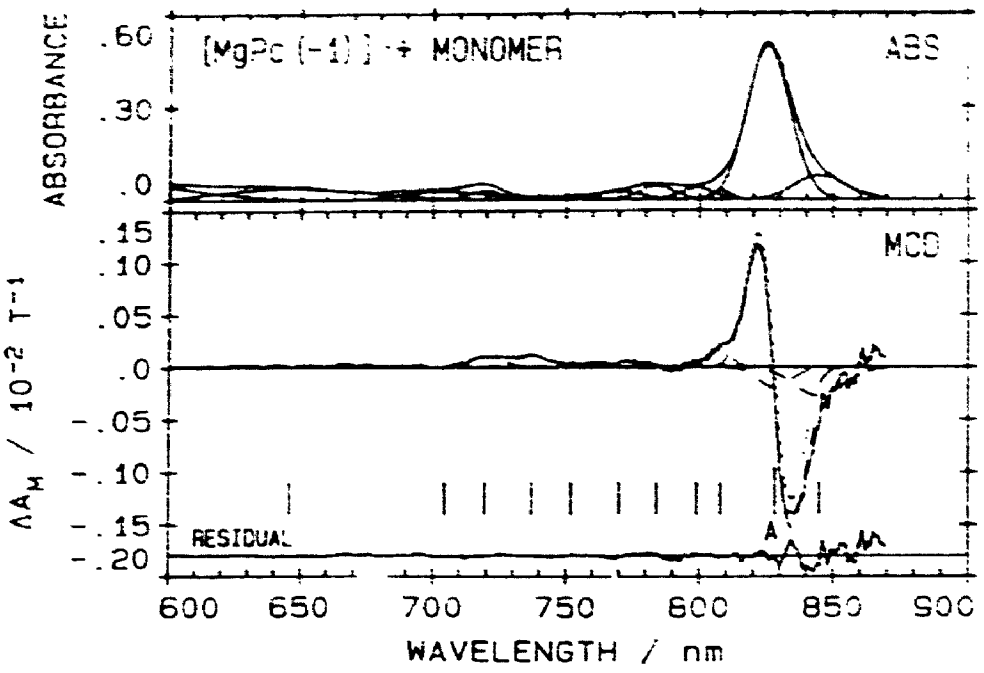

Figure 5-12 Results of a band analysis for the visible region of monomeric $[(im)_nMgPc(-1)]^+$ recorded in DCE at 300 K: the visible region (bands 1 to 11). (a) absorption: (——) experimental data; (– –) fitted data; (——–) individual bands. (b) MCD: (——) experimental data; (– –) fitted data; (····) A terms; (– –) B terms. The band centre of the A term is labelled "A".

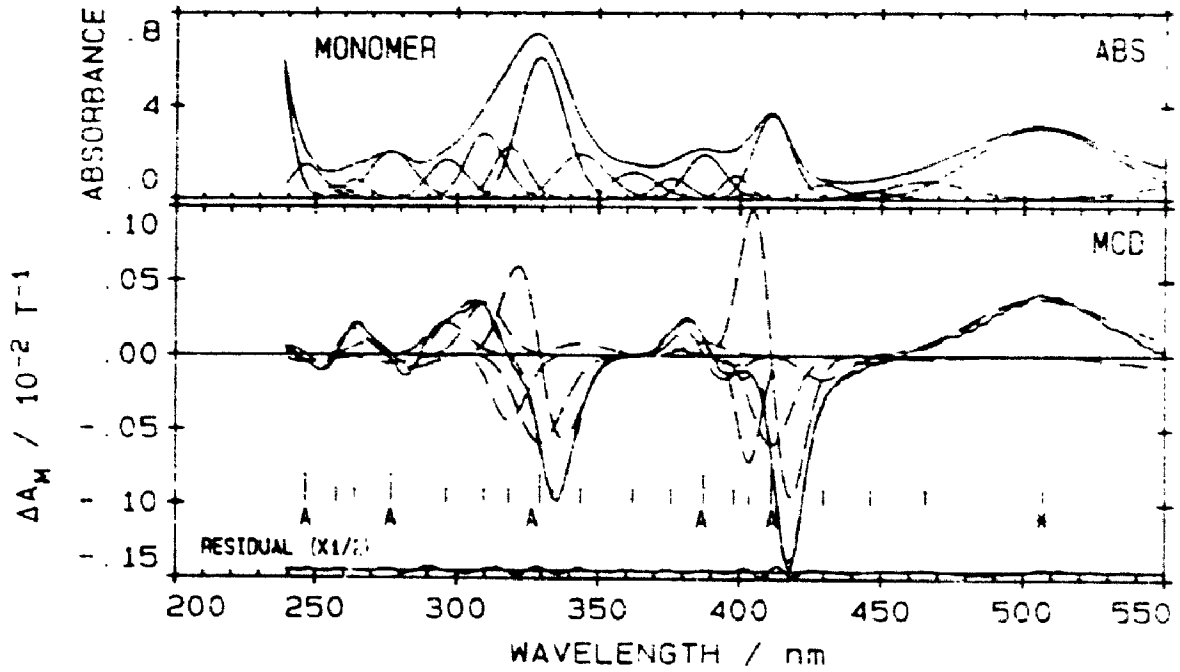

Figure 5-13 Results of a band analysis for the ultraviolet region of monomeric $[(im)_nMgPc(-1)]^+$ absorption spectra, recorded in DCE at 300 K: the ultraviolet region (bands 12 to 27). (a) absorption: (——) experimental data; (– –) fitted data; (——) individual bands. (b) MCD: (——) experimental data; (– –) fitted data; (–·–·–) A terms; (– –) B terms. The 5 band centres of A terms are labelled "A".

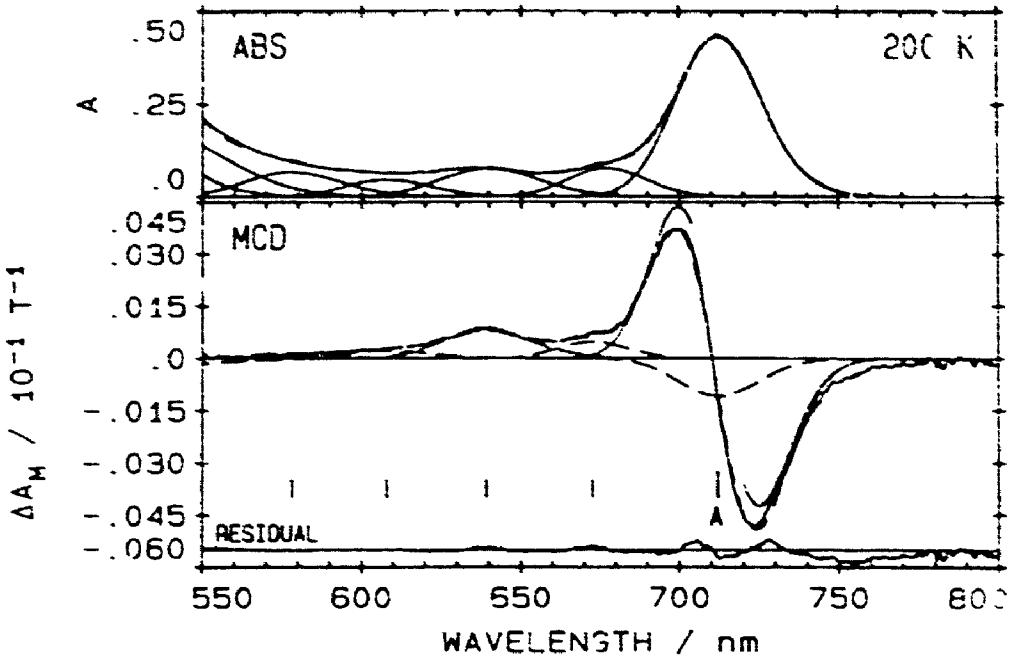

Figure 5-14 Results of a band analysis for the visible region of dimeric $[(H_2O)MgPc(-1)]_2^{++}$ recorded in DCM at 200 K: the visible region (bands 1 to 5). (a) absorption: (———) experimental data; (– – –) fitted data; (———) individual bands. (b) MCD: (———) experimental data; (– – –) fitted data; (.....) A terms; (– – –) B terms. The band centre of the A term is labelled "A".

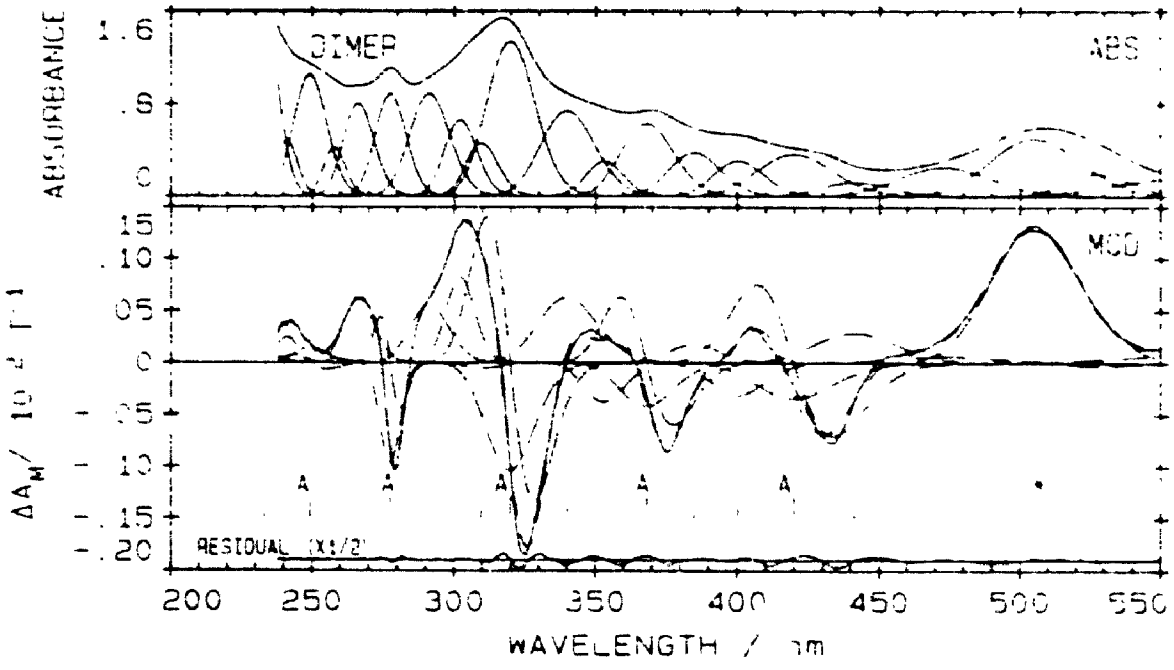

Figure 5-15 Results of a band analysis for the ultraviolet region of dimeric $[(H_2O)MgPc(-1)]_2^{++}$ recorded in DCM at 200 K: the ultraviolet region (bands 6 to 18). (a) absorption: (———) experimental data; (– – –) fitted data; (———) individual bands. (b) MCD: (———) experimental data; (– – –) fitted data; (–·–·–) A terms; (– – –) B terms. The band centres of A terms are labelled "A".

Table 5-3
The band fitting parameters[a] for $(im)_nMgPc(-1)$ in DCM.

band #	ν /cm^{-1}	λ /nm	$\Delta\nu$ /cm^{-1}	D_0[b]	Band type	$\langle\Delta\epsilon_M\rangle_n$[c]	A_1, B_0[d] /10^{-3}	B_0/D_0 /10^{-3}	A_1/D_0	μ[e]
1	11848	844	188	0.089	B	-0.076	-0.50	-5.62		
2	12121	825	245	1.01	A	74.2	486.7		0.48	0.45
					B	-0.15	-0.97	-0.96		
3	12482	801	202	0.023	B	0.037	0.24	10.4		
4	12776	783	484	0.085	B	-0.010	-0.067	-0.79		
5	13326	750	451	0.14	B	-0.048	-0.31	-2.21		
6	13949	717	703	2.52	A	375.4	2462.		0.98	0.91
					B	-0.21	-1.38	-0.55		
7	14800	676	900	1.23	B	0.24	1.60	1.30		
8	15633	640	850	0.68	B	0.30	1.97	2.90		
9	16347	612	701	0.40	B	0.091	0.60	1.50		
10	16932	591	857	0.42	B	0.064	0.42	1.00		
11	18531	540	1756	3.71	B	0.037	0.24	0.07		
12	19724	507	1702	7.05	B	0.74	4.88	0.69		
13	20907	478	1690	2.92	B	0.042	0.28	0.10		
14	22135	452	1430	3.95	B	0.071	0.46	0.48		
15	23712	422	1654	4.97	A	344.9	2261		0.45	0.42
					B	-0.30	-1.98	-0.40		
16	24905	402	1021	1.33	B	-0.10	-0.67	0.50		
17	25847	387	1400	2.93	B	0.033	0.21	0.07		
18	26879	372	1500	3.55	A	130.3	854.4		0.24	0.22
					B	-0.097	-0.64	-0.18		
19	27838	359	1294	2.13	B	-0.029	-0.19	-0.09		
20	29201	343	2200	7.59	B	0.16	1.03	0.14		
21	31337	319	2600	20.9	A	1417.	9291.		0.44	0.42
					B	-0.21	-1.37	-0.07		
22	33335	300	2661	7.88	B	-0.040	-0.26	-0.03		
23	35028	285	2399	5.03	B	0.20	1.31	0.26		
24	36271	276	1733	4.49	A	297.8	1953.		0.43	0.41
					B	-0.26	-1.71	-0.38		
25	37658	266	1790	5.07	A	216.7	1421.		0.28	0.26
					B	-0.17	-1.10	-0.22		
26	39219	255	2003	7.46	A	340.3	2232.		0.30	0.28
					B	-0.009	-0.057	-0.01		
27	40663	246	1703	4.97	B	-0.047	-0.31	-0.06		

[a]Statistics. B region: $\lambda_{230-550\ nm}$, χ^2=0.28, $\Sigma(\Delta\epsilon)^2$=18.5. Q region: $\lambda_{550-870\ nm}$, χ^2=0.51, $\Sigma(\Delta\epsilon)^2$=68.7. [b]$D_0=\langle\epsilon\rangle_0/326.6$, where the units of D_0 (dipole strength) are D^2 (Debye units) [25]. [c]$\langle\Delta\epsilon_M\rangle_1$ is the first moment and $\langle\Delta\epsilon_M\rangle_0$ is the zeroth moment of the MCD; when fitting with an A term, the program calculates $\langle\Delta\epsilon_M\rangle_1$ and when fitting with an B term the program calculates $\langle\Delta\epsilon_M\rangle_0$. The Faraday term values, A_1 and B_0, are calculated directly from the moments as follows: $A=\langle\Delta\epsilon_M\rangle_1/152.5$ and $B=\langle\Delta\epsilon_M\rangle_0$. [d]$A_1$ data are printed above B_0 data when both an A term and an B term are used. [e]μ=magnetic moment, calculated as $2((A_1/D_0)\times0.4669)$.

and nondegenerate $\pi \rightarrow \pi$ bands, and degenerate $\pi \rightarrow \pi^*$ B1, B2, N and L bands. The Q region, Figure 5-12, fits readily with a single MCD A term at 828 nm, followed to higher energy by a series of B terms that arise from the vibronic components of the Q band. The B region is fit to 5 MCD A terms and 14 MCD B terms, with the nondegenerate band at 510 nm the familiar marker band of ring oxidized metallophthalocyanines [2,35,37,70,71].

MgPc(-1) dimerizes in many solvents at room temperature. At 200 K in DCM, the complex is completely dimerized, Figure 5-8. Deconvolution analysis results for the absorption and MCD spectra of the $[(H_2O)MgPc(-1)]_2^{++}$ complex measured at 200 K are shown in Figures 5-14 and 5-15. As is the case with other phthalocyanines [89], we find that the 230 - 550 nm region does not exhibit significant marker bands to discriminate between the monomer and the dimer. The bands used in the final deconvolution calculation of the data measured at 200 K match closely many of the bands used when fitting the room temperature data (because of temperature-dependent shifts in wavelength and absorptivity we do not expect a 1:1 match). Six A terms and a single, strong B term at 510 nm, account fo. the most important absorption and MCD bands. As with the fits to the monomer data, the experimental and fitted lines of the absorption data superimpose, but the traces for the MCD data exhibit some errors which are not considered to be significant.

5.3 DISCUSSION

Oxidized metalloporphyrin species serve as vital intermediates in important biological pathways such as the catalytic site in the iron containing peroxidases and catalases [84,90-93]. Analysis of the optical spectral data of oxidized porphyrins and phthalocyanines has been complicated by the number of overlapping bands observed in the absorption spectrum. Only recently have detailed analyses of the spectral data of oxidized porphyrins been reported [83,94,95], even though the spectral properties of

both tetraphenyl and octaethyl porphyrin π-cation radical species have been known for many years [82,96-98]. The spectral data for phthalocyanine π-cation radicals appear not to be as complicated as those for the porphyrin species, which suggests that a reasonable band assignment may be more readily achieved.

MgPc(-2) is readily oxidized and reduced electrochemically [37,86,99,100] and photochemically [37,68,80,87,101], where the mechanism for the photooxidation of MgPc(-2) in the presence of an electron acceptor, with light of visible region wavelengths, is thought to be similar to that of porphyrins such as MgOEP(-2) and MgTPP(-2). The suggested mechanism for photochemical oxidation is through the lowest lying excited triplet state of the phthalocyanine [89,102].

Despite the general interest in the redox chemistry of the phthalocyanines, there have been few attempts at a quantitative assignment of the absorption spectrum. The problem in assigning the absorption spectra arises from the obvious complexity in the solution spectral data. Lack of high quality solution spectra makes it difficult to establish the effects of variables such as solvent, axial ligand and central metal on band energies and intensities. Published absorption spectra of ring oxidized metallophthalocyanines include: ZnPc(-1) [35,37,89], Ru(II)Pc(-1) [35,80,99], Co(II)Pc(-1) [68], Li_2Pc(-1) [71], H_2Pc(-1)] [70], Cu(II)Pc(-1) [70], MgPc(-1) [70] and Fe(III)Pc(-1) [68,103]. Comparison between these published MPc(-1) spectra and the data presented here for MgPc(-1) indicates that the spectra of MgPc(-1) most closely resembles the spectra obtained for the ZnPc(-1) and Ru(II)Pc(-1) species, where charge transfer bands do not lie in the same region.

5.3.1 Oxidation of Magnesium Phthalocyanine

Chemical oxidation using nitric acid is the cleanest method to form MgPc(-1). With photochemical oxidation there appears to be bleaching of the oxidized complex as oxidation approaches completion. Electrochemical oxidation appears to generate a

small amount of metal free phthalocyanine, while chemical oxidation using Br_2 either generates a small amount of metal free phthalocyanine or because of bromine's strong oxidizing power ($E_{\frac{1}{2}}$=1.09 V versus SCE in aqueous solutions), some of the π-cation radical is further oxidized to the dication.

A transient species is encountered during the chemical oxidation of MgPc(-2) with nitric acid (Figure 5-4). At the onset of the reaction an additional band at 705 nm appears, intensifies, then disappears as the oxidation reaches completion. Studies of the complexation of HCl to ZnPc(-2) [61] and Fe(II)Pc(-2) [61] indicate that this transient is a symmetry reduced MgPc(-2) complex, where the proton from nitric acid coordinates to an aza-bridging nitrogen of the phthalocyanine ring.

5.3.2 Variable Temperature Absorption and EPR Spectra

Experimental results indicate that MgPc(-1) exists as a mixture of monomeric and dimeric species at room temperature. Homborg [70] has suggested that the π-cation radical readily dimerizes in polar solvents existing mainly as the dicationic $[MgPc(-1)]_2^{++}$ species, while in nonpolar solvents the monomeric $[MgPc(-1)]^{\cdot +}$ π-cation radical species predominates. The presence of the two marker bands at 825 and 717 nm in the room temperature absorption spectra for $L_nMgPc(-1)$ in DCM, shows that a mixture of monomer and dimer exists. The variable temperature absorption (Figure 5-7) and EPR (Figure 5-6) spectra of MgPc(-1) confirm this conclusion.

The 825 nm band is assigned to monomeric $[MgPc(-1)]^{\cdot +}$ while the 720 nm band is assigned to the dimeric $[MgPc(-1)]_2^{++}$ species. The assignment of the 825 and 717 nm bands is consistent with previous studies of phthalocyanines which indicate a blue shifting of Q absorption band upon dimerization [1,89].

5.3.3 Comparison Between Bands Obtained from the Deconvolution Calculations and Bands Predicted by Theoretical Calculations

Although theoretical calculations of band energies for a variety of neutral metallophthalocyanines and metalloporphyrins are available and have been compared with experimental calculations for many years, it is only recently that attempts have been made to interpret the absorption spectra of the oxidized π-cation radical species. Minor et al. [104] reported a theoretical interpretation of data they recorded for cationic and anionic absorption spectra of a variety of metallophthalocyanines. The band assignments of Minor et al. [104] are complicated by the fact that many of the spectra were obtained from samples in the solid state, in which intermolecular effects, such as Davydov coupling, broaden, shift and duplicate many of the bands [105].

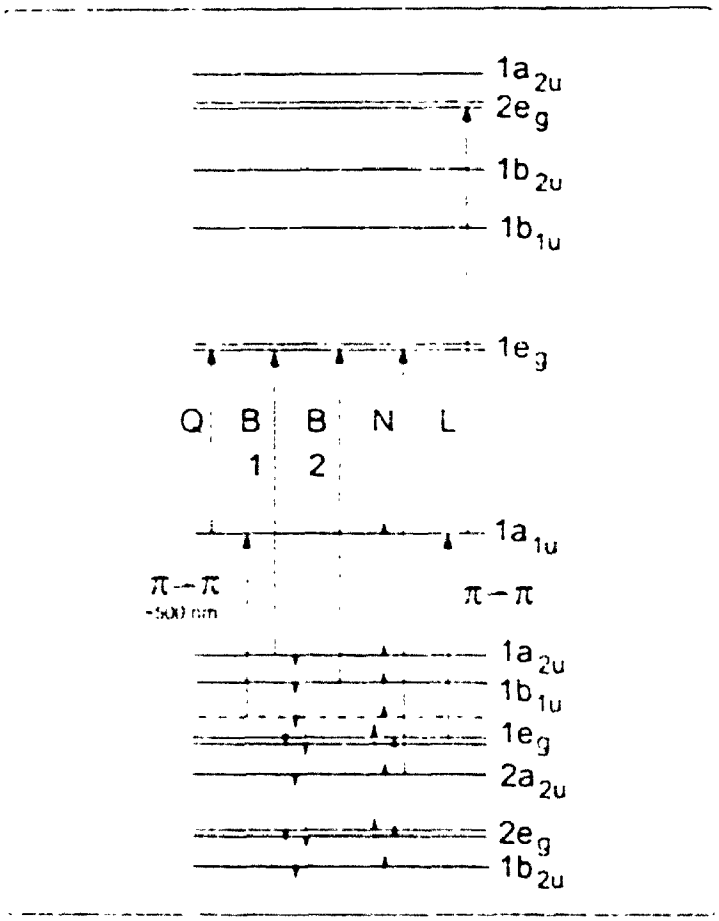

Figure 5-16 Selected molecular orbitals and allowed electronic transitions for the π-cation radical of magnesium phthalocyanine.

Figure 5-16 displays the molecular orbitals that give rise to states in the energy region 10 000 - 50 000 cm^{-1}. The removal of an electron from the highest filled orbital of MgPc(-2) does not change the orbital degeneracy of the ground or excited state. Selection rules for D_{4h} restrict us to transitions from $^2A_{1u} \rightarrow {}^2E_g$ and $^2A_{1u} \rightarrow {}^2A_{2g}$. The former will result in MCD A and B terms, the latter just B terms. In the absorption and MCD spectra the five ring based degenerate $\pi \rightarrow \pi^*$ electronic transitions assigned as the Q, B1, B2, N and L bands are expected. In addition, transitions into the half filled HOMO ($1a_{1u}(\pi)$) level of the π-cation radical are also allowed. These new transitions can extend from the near infrared (900 nm) to the spectral window (400 - 550 nm) region of the neutral MgPc(-2).

Band maxima, measured directly from absorption spectra, of various $L_nMgPc(-1)$ species (Table 5-1) are useful in the identification of MPc(-1) spectra, but because of the complexity of the spectral envelope, and in particular the presence of both monomers and dimers, these data are of little use in the assignment of band energies. Deconvolution of the Q band (Figure 5-10) and B band (Figure 5-11) regions of $(im)_nMgPc(-1)$ shows that band centres are not always positioned at the absorption maxima and that several transitions can overlap to give rise to an absorption band.

5.3.4 Deconvolution Results for Monomeric and Dimeric MgPc(-1)

The difference in energy between the Q band in the oxidized monomeric and dimeric MgPc(-1) can be used to estimate the energies of the B1, B2, N and L bands from the spectral data. The deconvolution results obtained for the absorption and MCD spectra of monomeric, dimeric and room temperature solutions of MgPc(-1) are shown in Figure 5-17. Using the assignments proposed in Figure 5-17, we can compare the composition of the spectral envelope of MgPc(-2) [27] with that of MgPc(-1), both recorded at room temperature in solution. The band centres of degenerate transitions are drawn as long lines, while nondegenerate transitions are

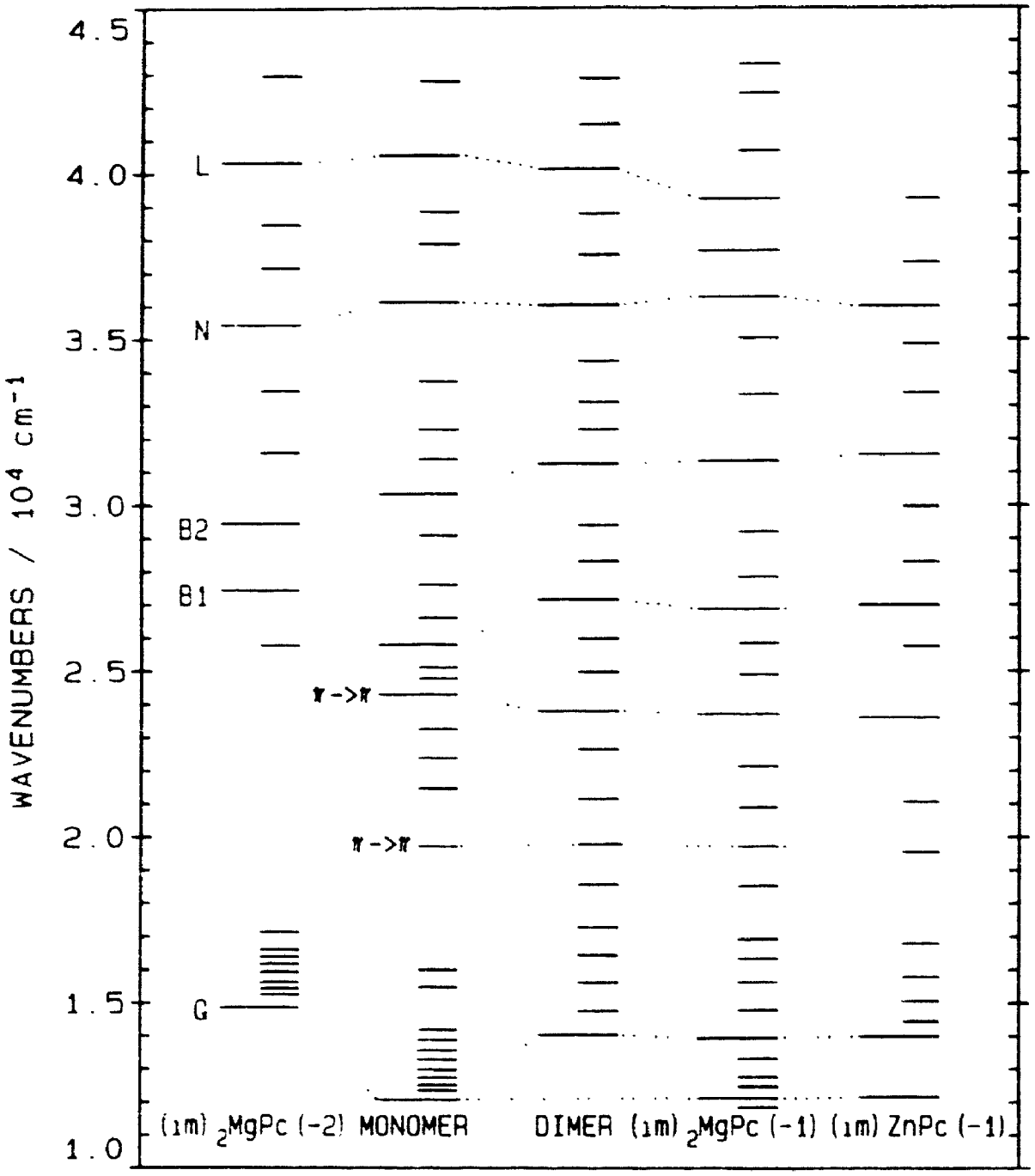

Figure 5-17 Comparison between the energy levels of $(im)_2MgPc(-2)$ [27], $[MgPc(-1)]^+$ (monomer), $[MgPc(-1)]_2^{++}$ (dimer), $(im)_2MgPc(-1)$ and (im)ZnPc(-1) [26] calculated by deconvolution of the absorption and MCD spectra.

represented as the short lines. The 828 nm (12 075 cm^{-1}) band in the monomer fit, Figure 5-12, and the 712 nm (14 041 cm^{-1}) band in the dimer fit, Figure 5-14, are assigned as the Q band. Clearly, the degenerate bands at 387 nm (25 808 cm^{-1}), 330 nm (30 342 cm^{-1}), 277 nm (36 113 cm^{-1}) and 247 nm (40 542 cm^{-1}), for the monomer fit in Figure 5-13, and at 368 nm (27 156 cm^{-1}), 320 nm (31 250 cm^{-1}), 278 nm (36 023 cm^{-1}) and 249 nm (40 115 cm^{-1}), for the dimer fit in Figure 5-15, line up closely enough with the B1, B2, N and L bands of the neutral species for us to suggest that these bands are those of the oxidized species. The blue shift, from monomer to dimer, in the energies of the assigned B1 and B2 bands is consistent with the shift in the Q band energy. The N and L bands energies appear to have small variation with respect to dimerization.

Adopting the above assignment implies that oxidation of the phthalocyanine ring reorganizes the molecular orbitals such that the energy difference between the ground state and the first two excited states is reduced and a red shift is observed. In a recent valence effective Hamiltonian calculation for Li(I)Pc(-1), Orti et al. [32] predicted the energies and polarizations of transitions between 800 and 306 nm. Transitions polarized x,y are predicted at 317, 316, 311 and 306 nm. It is not easy to associate any one of these with a specific band in the experimental spectra because the energy range is so small when compared with the range observed (370-255 nm). Their prediction of the $1a_{1u}(\pi) \rightarrow 1e_g(\pi^*)$ Q transition at 764 nm, is very close to the observed value of 828 nm.

5.3.5 Assignment of the $\pi \rightarrow \pi$ Transitions in MgPc(-1)

The nondegenerate transition (MCD B term) centred at 507 nm (19 729 cm^{-1}) in the monomer fit and at 505 nm (19 791 cm^{-1}) in the dimer fit is relatively isolated from other bands being located in the "window region" of many neutral phthalocyanines. This band is one of the most intense in the absorption spectrum and

it is often used as a "fingerprint" marker for formation of the π-cation radical [37,68,104]. While it has been suggested that this band has $\pi \rightarrow \pi^*$ origins, possibly the displaced Q band [1,70,104], the nondegenerate nature of the transition strongly suggests that it is neither the Q band nor the B1 band, but a low lying $\pi \rightarrow \pi$ transition. Because a similar band is observed for each of the MPc(-1) species we have studied previously [35,37,68], we conclude that the band does not arise from axial ligand to phthalocyanine ring charge transfer or from any metal related transitions.

The degenerate transition (MCD A term) centred at 411 nm (24 304 cm^{-1}) in the monomer fit and at 420 nm (23 799 cm^{-1}) in the dimer fit was previously assigned as the B1 band [2,28]. The red shift from monomer to dimer in this transition's energy is opposite to the blue shift experienced by the Q band and expected for the B1 band. This spectral result has facilitated the reassignment of this band to the $1e_g(\pi) \rightarrow 1a_{1u}(\pi)$ transition. The red shift in energy of this $\pi \rightarrow \pi$ transition from the monomer to dimer can be explained empirically by focusing on the energy of the HOMO ($1a_{1u}(\pi)$) upon dimerization. If the energy of the HOMO is responsible for the blue shifts in the energy of the two $\pi \rightarrow \pi^*$ transitions, then $\pi \rightarrow \pi$ transitions into the HOMO are expected to display the observed red shift from monomer to dimer.

In the Orti et al. [32] calculation for Li(I)Pc(-1), it is predicted that bands near 411 and 512 nm are $\pi \rightarrow \pi$ in character. However, this proposed assignment requires x,y degeneracy for the 512 nm transition. Clearly, this important band in the radical cation spectrum of both monomers and dimers is nondegenerate.

5.3.6 Comparison Between the Deconvolution Data For MgPc(-1) and ZnPc(-1)

While the deconvolution calculations are very complicated, the plots of the residuals for the MCD spectra (Figures 5-10 to 5-15) do indicate the accuracy of the

fits, however, reproduction in a series of spectra for related complexes enhances the reliability of the calculations. Figure 5-17 compares the results of independent calculations from spectra measured at room temperature for $(im)_nMgPc(-1)$ with those obtained for (im)ZnPc(−1) [26]. It is apparent that the major calculated bands are at the same energies in both species. Figure 5-17 shows that $(im)_nMgPc(-1)$ required many more bands to completely fit the spectral envelopes (Figures 5-10 and 5-11) than were required for (im)ZnPc(−1). These additional bands are the result of better spectral resolution in the near infrared region and extended range into the ultraviolet region.

A discrepancy in band types required for deconvolution occurs in the two bands that arise at slightly higher energy than the C band. For $(im)_nMgPc(-1)$, the best fit used linked MCD A and B terms, which indicates degenerate transitions in contrast to our findings for (im)ZnPc(−1) where nondegenerate transitions were suggested. Since the $(im)_nMgPc(-1)$ spectra extend farther into the ultraviolet region, it appears that the enhanced range between 35 000 and 41 000 cm^{-1} has isolated these two additional degenerate electronic transitions. The higher energy transition represents the L band, which is beyond the spectral cutoff in ZnPc(−1), while the lower energy transition is an artifact resulting from overlapping bands of the monomer and dimer.

Figure 5-17 also compares the energies of transitions to degenerate states (identified by MCD A terms) for the neutral MgPc(−2) [27], and momomeric and dimeric MgPc(−1). The energies of bands in both neutral and oxidized MgPc at room temperature show little dependence on axial ligand. The increase in the energy gap between the B1 and B2 bands upon ring oxidation in MgPc is comparable to the increase observed when imidazole is replaced by cyanide in (im)ZnPc(−2) [26] and $(im)_2Fe(II)Pc(-2)$ (Chapter 6) and is due to the removal of electron density from the phthalocyanine ring. The figure illustrates clearly the overall red shift in the energies of the Q and B1 transitions in the radical spectrum.

5.4 CONCLUSIONS

Absorption and EPR spectra recorded for oxidized MgPc(−1), at various temperatures, indicate that the room temperature solution consists of a mixture of monomer and dimer. For $(im)_nMgPc(-1)$ five degenerate transitions are centred near 717, 372, 319, 276 and 255 nm, and are assigned from low to high energy as: the Q, $\pi \rightarrow \pi$, B1, B2 and N bands of the dimeric $[LMgPc(-1)]_2^{++}$ species. In room temperature solutions, a band is also observed at 825 nm and is assigned as the Q ban f monomeric $[L_nMgPc(-1)]^{\cdot +}$. The nondegenerate 507 nm band is assigned as a $\pi \rightarrow \pi$ transition. Deconvolution analysis assigned band centres at: 828 (Q), 411 ($\pi \rightarrow \pi$), 387 (B1), 330 (B2), 277 (N) and 247 nm (L) for $[(im)_nMgPc(-1)]^{\cdot +}$ and 712 (Q), 420 ($\pi \rightarrow \pi$), 368 (B1), 320 (B2), 278 (N), and 249 nm (L) for $[(H_2O)MgPc(-1)]_2^{++}$. The MCD data allow unambiguous assignment of the Q band for both monomeric and dimeric species.

CHAPTER 6

LOW SPIN IRON(II) PHTHALOCYANINE

6.1 INTRODUCTION

Spectral studies of "simple" metallophthalocyanines, such as magnesium phthalocyanine (MgPc) [1,2,27,28,70] and zinc phthalocyanine (ZnPc) [1,2,26,35,37,56], are invaluable in advancing our understanding of the spectral properties of the phthalocyanine ring. In these complexes the metal is chromophorically silent, with the spectral band intensity arising entirely from phthalocyanine ring based electronic transitions. Band analysis of the absorption and magnetic circular dichroism (MCD) spectra of MgPc and ZnPc provides invaluable information on the energies and polarization properties of state to state transitions in the phthalocyanine ring; however the limited metal chemistry makes MgPc and ZnPc poor models of complex systems such as the hemes (iron porphyrins) where charge transfer transitions between iron and the porphyrin ligand comprise a significant portion of the spectral envelope between 200 and 1000 nm [46,58]. Iron phthalocyanine (FePc) is useful in modelling studies of naturally occurring iron porphyrins [106–112]. The presence of iron, with its partially filled 3d shell, in the metallophthalocyanine molecule introduces charge transfer transitions into the electronic spectra.

In this chapter, the spectral properties of a variety of low spin $L_2Fe(II)Pc(-2)$ complexes are discussed. The axial ligands included in the study are: carbon monoxide (CO), imidazole (im), N-methylimidazole (meim), pyridine (py), 4-methylpyridine (mepy), ammonia (NH_3), piperidine (pip) and cyanide (CN^-). Spectral deconvolution is used to assign the energies, band widths and magnetic moments of the transitions that contribute to the spectral envelope. Results from previous studies of MgPc [27] and ZnPc [26,35] are used to isolate charge transfer bands from the "pure" phthalocyanine ring based transitions.

6.2 RESULTS

6.2.1 Absorption and MCD Spectra

Figure 6-1 displays the absorption and MCD spectra of $(NH_3)_2$Fe(II)Pc(-2) dissolved in dichloromethane (DCM). Absorption band maxima for $(NH_3)_2$Fe(II)Pc(-2) and the other L_2Fe(II)Pc(-2) complexes are listed in Table 6-1. The spectral data for $(NH_3)_2$Fe(II)Pc(-2) are quite distinct from the data acquired for main group metallophthalocyanines [1,27,34,35,37]. In Figure 6-1 the spectrum exhibits: (i) a well resolved Q band at 661 nm, (ii) a set of overlapping bands extending from 400 nm to well below 250 nm and (iii) the presence of spectral intensity in the 500 - 600 nm region, which is a spectral window in the "simple" phthalocyanines [1,27,34,35,37]. The latter region of the spectral envelope is known as the charge transfer region and the spectral bands observed here arise from transitions between the phthalocyanine π system and 3d orbitals on the iron [1]. The derivative shape in the MCD spectra indicates that at least one degenerate transition arises in this region. The charge transfer transitions can extend into the B region (250 - 400 nm), which further complicates the assignment of the ring transitions that occur in the B region of the spectrum.

Significant changes in the absorption spectral envelope of $(NH_3)_2$Fe(II)Pc(-2)

Table 6-1
Observed maxima in the absorption spectra of the L_2Fe(II)Pc(-2) species in DCM.

L_2Fe(II)Pc(-2)	λ_{max} (nm)					
$Na_2[(CN)_2$Fe(II)Pc(-2)]	664	602	371	313	273	236
$(py)_2$Fe(II)Pc(-2)651	591	412		328		
$(mepy)_2$Fe(II)Pc(-2)	652	592	413	331		
$(im)_2$Fe(II)Pc(-2)	657	596	423	339		
$(meim)_2$Fe(II)Pc(-2)	658	597	423	338		
$(pip)_2$Fe(II)Pc(-2)	659	598	425	340		
$(NH_3)_2$Fe(II)Pc(-2)	661	601	425	332		
(DMF)(CO)Fe(II)Pc(-2)	658	595	353	312	282	
(NH_3)(CO)Fe(II)PC(-2)	659	596	363	317	288	

occur when carbon monoxide (CO) is bubbled into a solution of $(NH_3)_2$Fe(II)Pc(−2) (Figure 6−2). The observed changes are: (i) a blue shift (661 to 659 nm) and increased intensity of the Q band; (ii) the reappearance of the spectral window between 400 and 500 nm and (iii) a blue shift of the bands between 250 and 450 nm. The presence of sharp isosbestic points near 485, 385, 370 and 335 nm indicate the formation of a single new Fe(II)Pc(−2) complex. Studies of the complexation of CO to Fe(II)Pc(−2) [108−112] indicate that under normal conditions CO binds *trans* to a basic (σ donor) ligand. The complex formed by the substitution of an axial ammonia (NH_3) ligand in $(NH_3)_2$Fe(II)Pc(−2) with a CO ligand is (NH_3)(CO)Fe(II)Pc(−2).

The absorption and MCD spectra of (NH_3)(CO)Fe(II)Pc(−2) are shown in Figure 6−3. The MCD spectrum lacks the derivative band shape at 430 nm that is observed in the spectrum of $(NH_3)_2$Fe(II)Pc(−2). With the reappearance of the spectral window between 400 and 500 nm, the absorption spectrum of (NH_3)(CO)Fe(II)Pc(−2) resembles the absorption spectra of MgPc(−2) [1,27] and ZnPc(−2) [1,35,37]. Inspection of the MCD spectra indicates that the spectral envelope between 350 and 250 nm is similar to the 250 to 400 nm spectral envelopes of $(im)_2$MgPc(−2) [1,27] and (im)ZnPc(−2)[1,35,37]. The absorption and MCD spectral intensity in the 350 to 400 nm region for (NH_3)(CO)Fe(II)Pc(−2) can be assigned to charge transfer bands which have been blue shifted from their normal region near 450 nm.

Titration of sodium cyanide (NaCN) into $(NH_3)_2$Fe(II)Pc(−2) (Figure 6−4) also leads to appreciable changes in the absorption spectrum. Unlike the addition of CO to $(NH_3)_2$Fe(II)Pc(−2), there are two distinct phases in the titration of NaCN into solutions of $(NH_3)_2$Fe(II)Pc(−2). The sharp jump in intensity of the Q band at 661 nm and the slight blue shift in the 425 nm charge transfer band before isosbestic changes take place indicate the initial formation of Na[(NH_3)(CN)Fe(II)Pc(−2)].

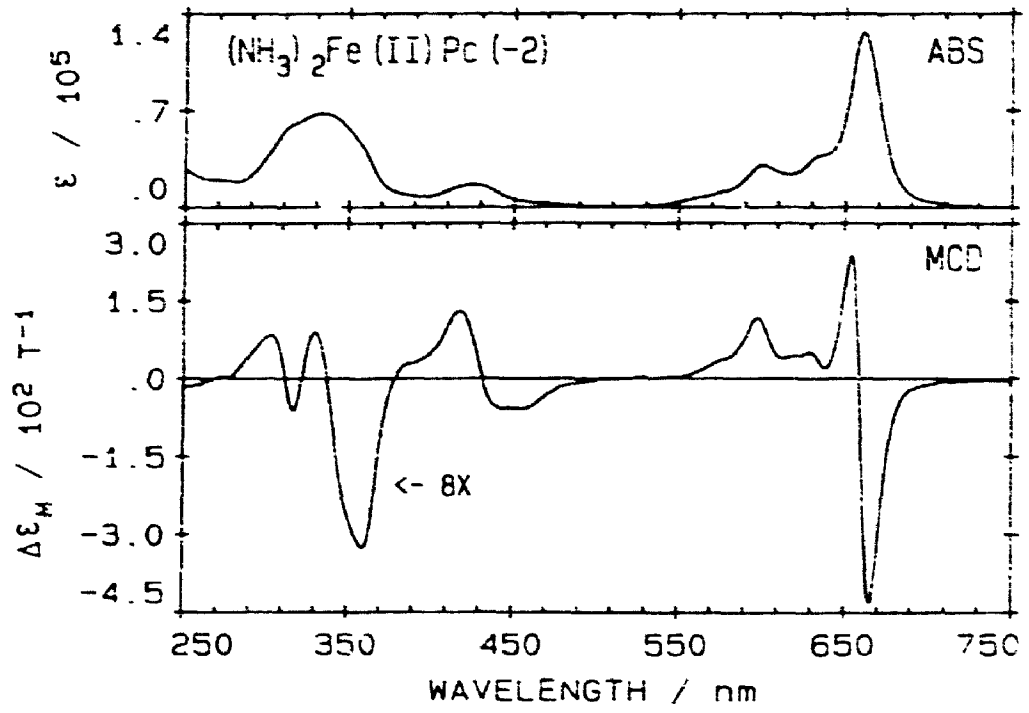

Figure 6-1 Absorption (ABS) and MCD spectra for $(NH_3)_2Fe(II)Pc(-2)$ recorded in DCM.

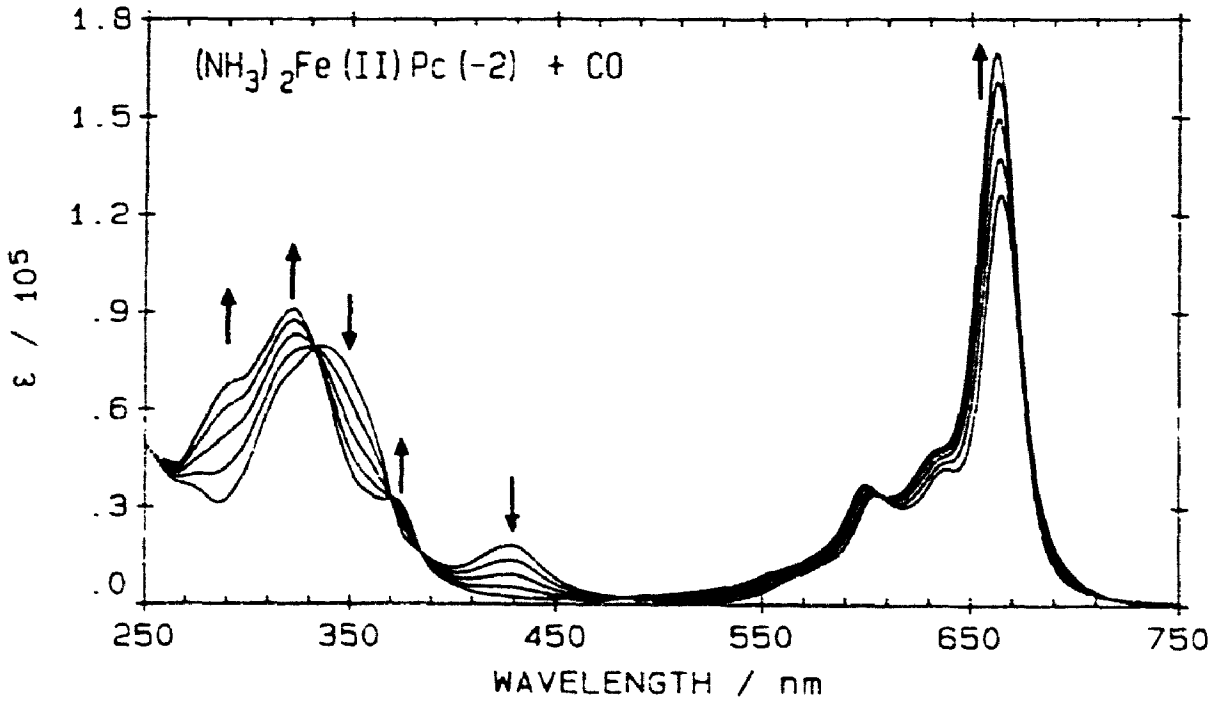

Figure 6-2 Absorption changes observed during the bubbling of carbon monoxide (CO) through a DCM solution of $(NH_3)_2Fe(II)Pc(-2)$. The arrows represent the spectral changes as CO was bubbled through the solution.

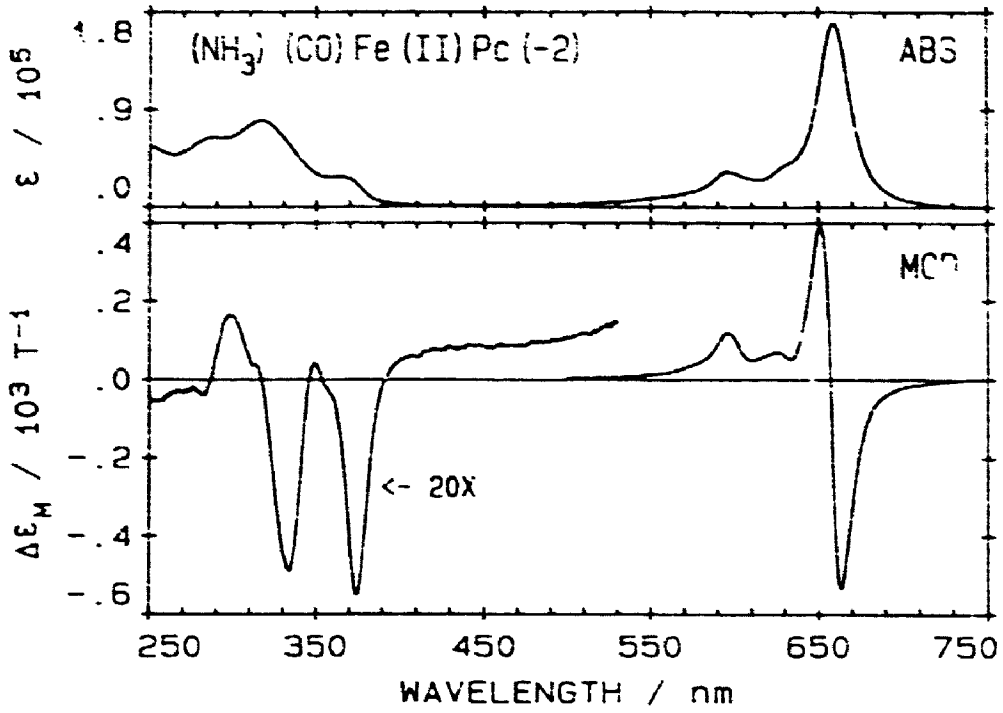

Figure 6–3 Absorption (ABS) and MCD spectra for $(NH_3)(CO)Fe(II)Pc(-2)$ recorded in DCM.

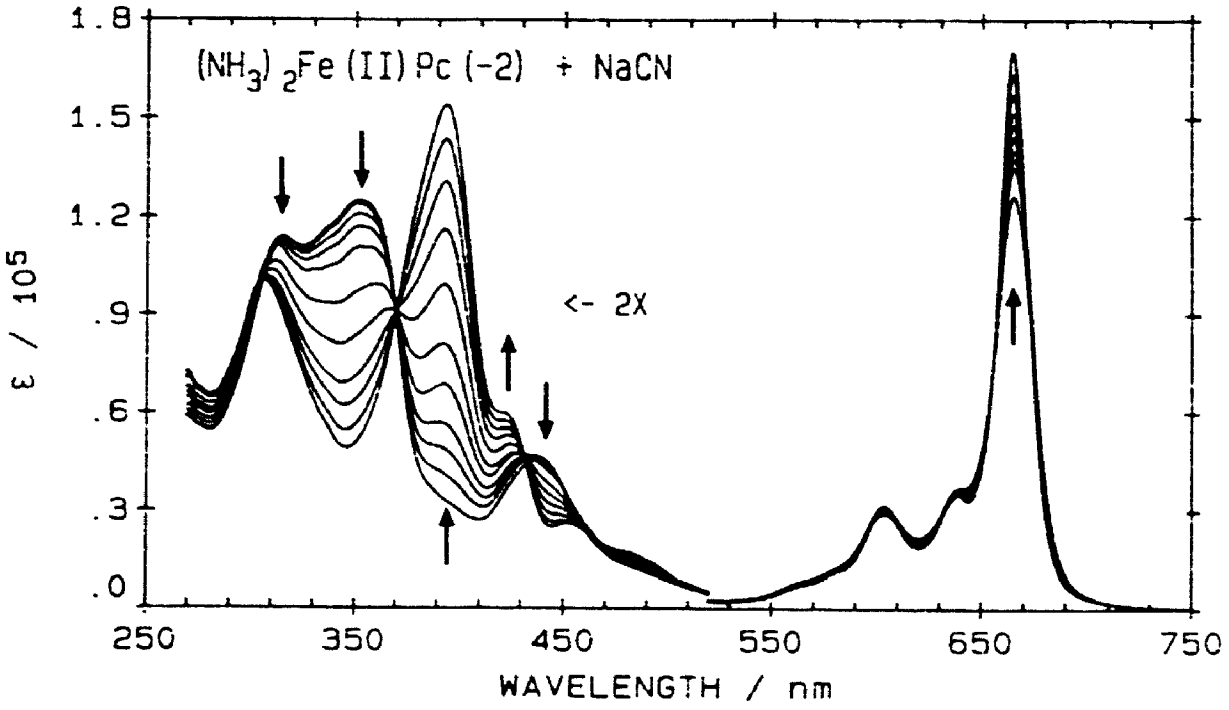

Figure 6–4 Absorption changes observed during the titration of sodium cyanide (NaCN) into a DMF solution of $(NH_3)_2Fe(II)Pc(-2)$. The arrows represent the spectral changes as NaCN was titrated into the solution.

Isobestic points at 430 and 370 nm follow in the second phase of the titration where $Na[(NH_3)(CN)Fe(II)Pc(-2)]$ is converted to $Na_2[(CN)_2Fe(II)Pc(-2)]$. Several distinct changes are observed as $Na_2[(CN)_2Fe(II)Pc(-2)]$ forms. The Q band spectral intensity increases and the band maxima red shifts from 661 to 664 nm. The splitting of the two bands that comprise the majority of the spectral intensity between 300 and 350 nm is a common feature of CN^- complexation to metallophthalocyanines [1,35,52]. The charge transfer bands in the 400 to 500 nm region also pull apart as the second CN^- ligand binds to form $Na_2[(CN)_2Fe(II)Pc(-2)]$.

The absorption and MCD spectra of ($Na_2[(CN)_2Fe(II)Pc(-2)]$) are shown in Figure 6-5. The spectra are remarkably similar to the those reported for $Na[(CN)ZnPc(-2)]$ [1,35,52] and $Na[(CN)_2Co(III)Pc(-2)]$ [1,52]. The 250 to 500 nm region in the MCD spectra exhibits the two split degenerate bands observed when CN^- is axially bound to ZnPc [1,35,52] and CoPc [1,52].

6.2.2 Spectral Band Deconvolution Calculations

Deconvolution results for the absorption and MCD spectra of the Q region (500 - 750 nm) of $L_2Fe(II)PC(-2)$ (L = NH_3, NH_3/CO and CN^-) are shown in Figures 6-6 to 6-8. Thirteen bands were required to fit the Q region for $(NH_3)_2Fe(II)Pc(-2)$, 13 for $(NH_3)(CO)Fe(II)Pc(-2)$ and 12 for $Na_2[(CN)_2Fe(II)Pc(-2)$. The MCD residual (the difference between the experimental and fitted spectral envelopes) is plotted at the bottom of the MCD fits. The lack of systematic noise in the residual plot verifies the reliability of the fits. In the Q region, all but one of the absorption bands were fit to B terms in the MCD spectrum. The absorption bands centred at 660 nm (15 147 cm^{-1}) for $(NH_3)_2Fe(II)Pc(-2)$, at 658 nm (15 207 cm^{-1}) for $(NH_3)(CO)Fe(II)Pc(-2)$ and at 661 nm (15 136 cm^{-1}) for $Na_2[(CN)_2Fe(II)Pc(-2)$ were fitted with pairs of A and B terms in the MCD spectra. Assignment of this transition as the Q band is consistent with the assignment of the Q

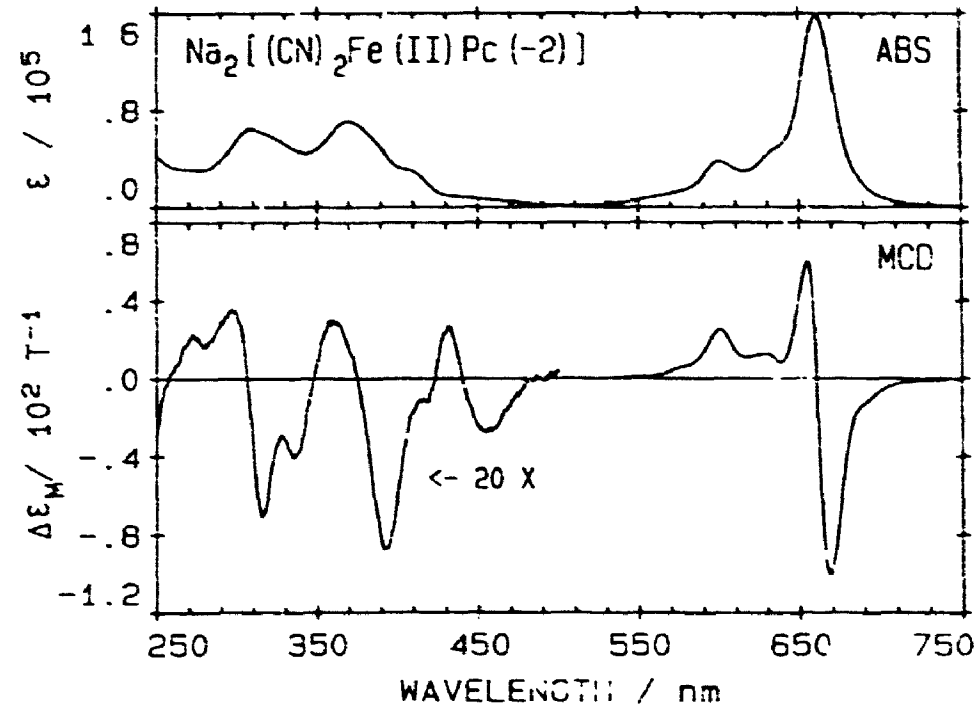

Figure 6-5 Absorption (ABS) and MCD spectra for $Na_2[(CN)_2Fe(II)Pc(-2)]$ recorded in 98:2 (V/V) DCM:DMF.

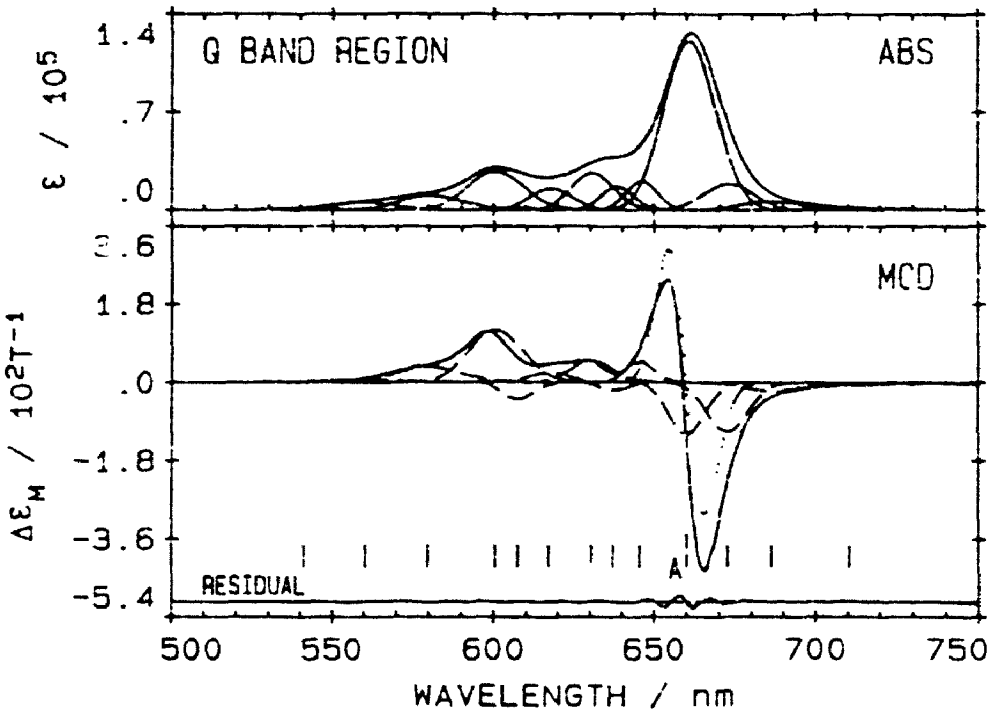

Figure 6-6 Results of a band analysis of the absorption and MCD spectra for $(NH_3)_2Fe(II)Pc(-2)$ in DCM in the visible region (bands 13-30). (a) Absorption: (———) experimental data; (- - -) fitted data; (———) individual bands. (b) MCD: (———) experimental data; (- - -) fitted data; (.....) A terms; (- - -) B terms. The band centre of the A term is labelled "A".

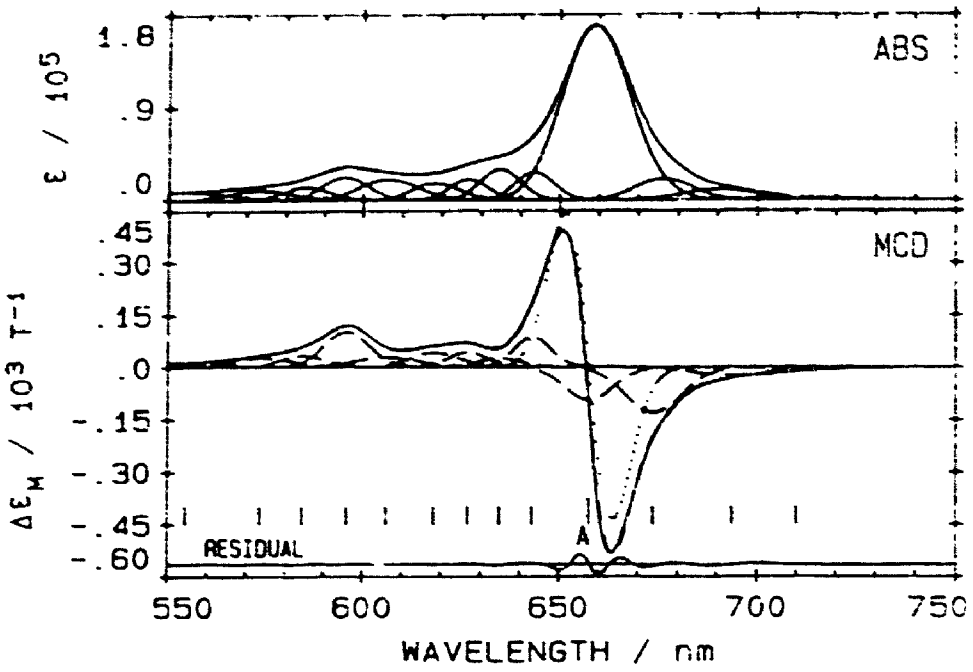

Figure 6-7 Results of a band analysis of the absorption and MCD spectra for $(NH_3)(CO)Fe(II)Pc(-2)$ in DCM in the visible region (bands 14-27). (a) Absorption: (———) experimental data; (- - -) fitted data; (———) individual bands. (b) MCD: (———) experimental data; (- - -) fitted data; (.....) A terms; (- - -) B terms. The band centre of the A term is labelled "A".

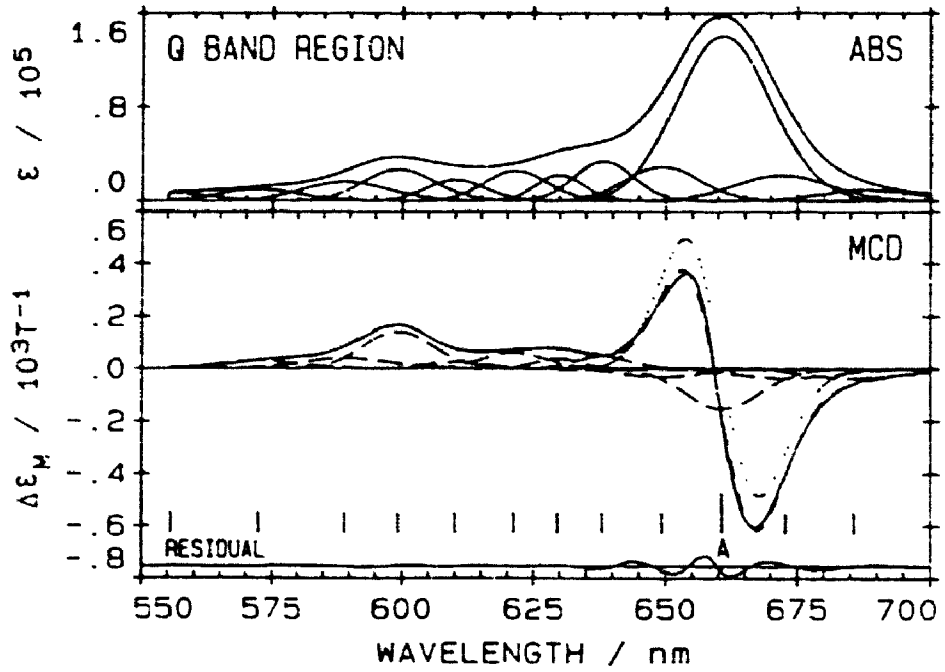

Figure 6-8 Results of a band analysis of the absorption and MCD spectra for $Na_2[(CN)_2Fe(II)Pc(-2)]$ in 98:2 DCM:DMF in the visible region (bands 13-30). (a) Absorption: (———) experimental data; (- - -) fitted data; (———) individual bands. (b) MCD: (———) experimental data; (- - -) fitted data; (.....) A terms; (- - -) B terms. The band centre of the A term is labelled "A".

band in $L_2MgPc(-2)$ [27] and in $LZnPc(-2)$ [26,35]. The B term that is associated with the A term is larger in the $L_2Fe(II)Pc(-2)$ complexes than the fits for the "simple" phthalocyanines [26,27,35]. It is probable that field induced mixing of the charge transfer states into the Q band states accounts for the increased intensity of the B term.

The absorption and MCD spectra in the B region (230 - 500 nm) of $L_2Fe(II)Pc(-2)$ are more complicated than the spectra recorded in the same region for $L_2MgPc(-2)$ [27] and $LZnPc(-2)$ [26,35]. With the increase in the number of electronic transitions occupying the same spectral range, it becomes more difficult to obtain a unique fit. The results of the fits in the B region for ring oxidized $MgPc(-1)$ (Chapter 6) and $ZnPc(-1)$ [26,35] indicate that the SIMPFIT program is able to provide unique results when a large number of relatively equal intensity bands occupy a narrow spectral region. Fits in the B region for $L_2Fe(II)Pc(-2)$ used 17 bands for $(NH_3)_2Fe(II)Pc(-2)$ (Figure 6-9), 14 bands for $(NH_3)(CO)Fe(II)Pc(-2)$

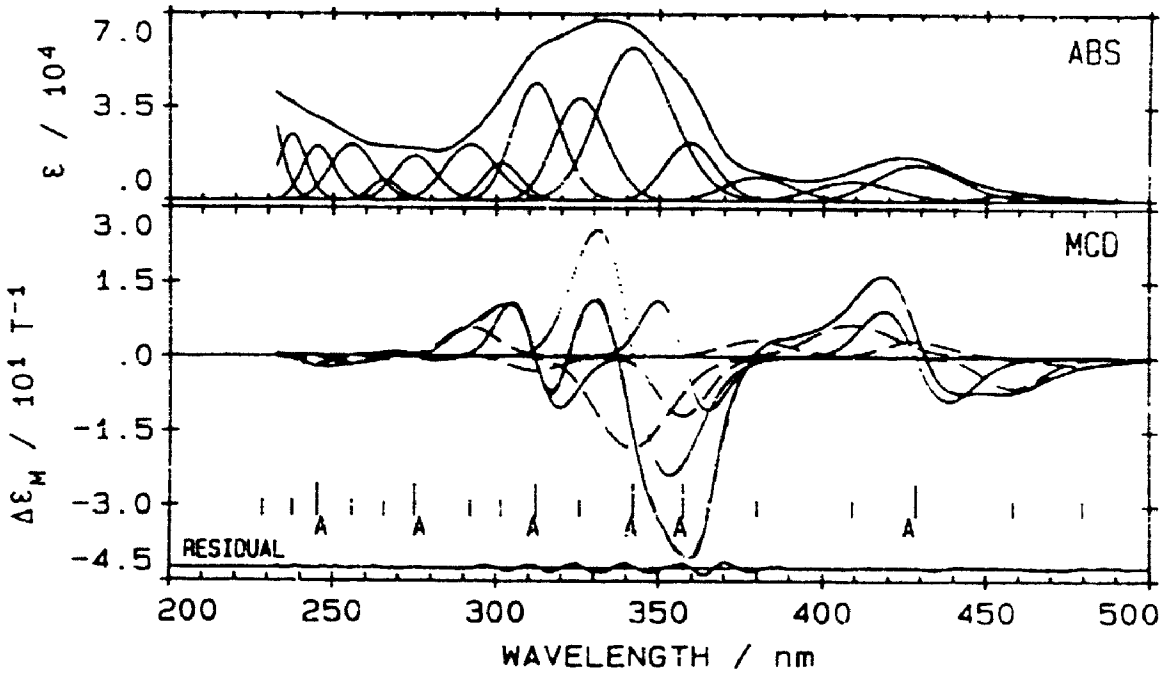

Figure 6-9 Results of a band analysis of the absorption and MCD spectra for $(NH_3)_2Fe(II)Pc(-2)$ in DCM in the ultraviolet region (bands 14-30). (a) Absorption: (———) experimental data; (- - -) fitted data; (———) individual bands. (b) MCD: (———) experimental data; (- - -) fitted data; (.....) A terms; (- - -) B terms. The 6 band centres of A terms are labelled "A".

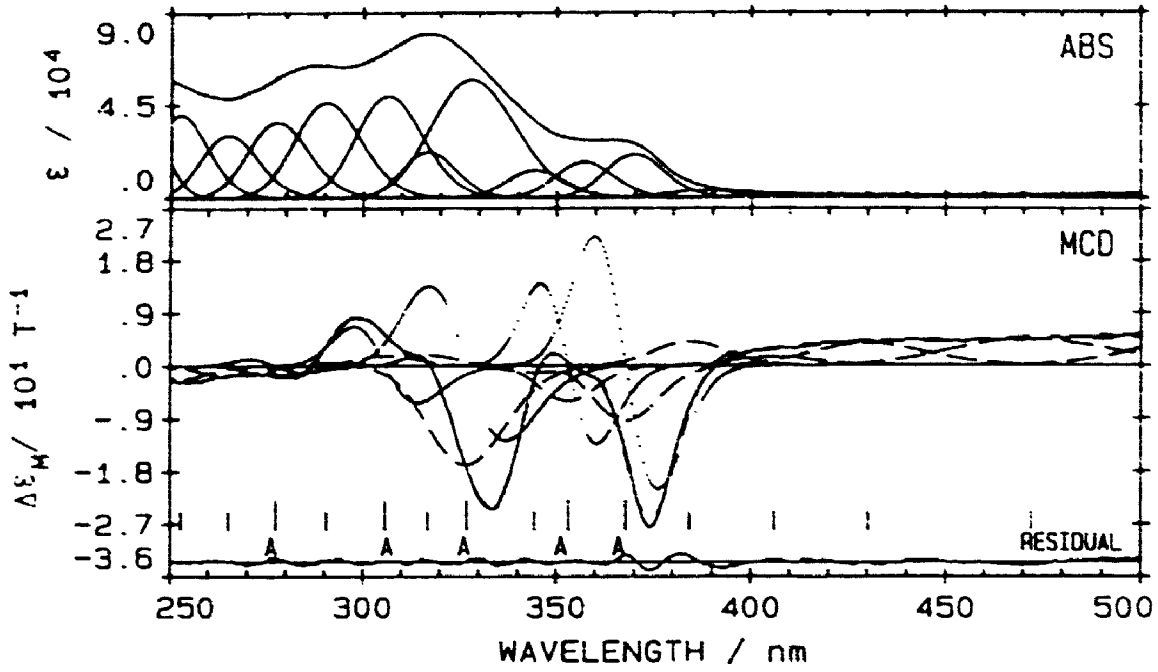

Figure 6–10 Results of a band analysis of the absorption and MCD spectra for $(NH_3)(CO)Fe(II)Pc(-2)$ in DCM in the ultraviolet region (bands 14–27). (a) Absorption: (———) experimental data; (– – –) fitted data; (———) individual bands. (b) MCD: (———) experimental data; (– – –) fitted data; (.....) A terms; (– – –) B terms. The 5 band centres of A terms are labelled "A".

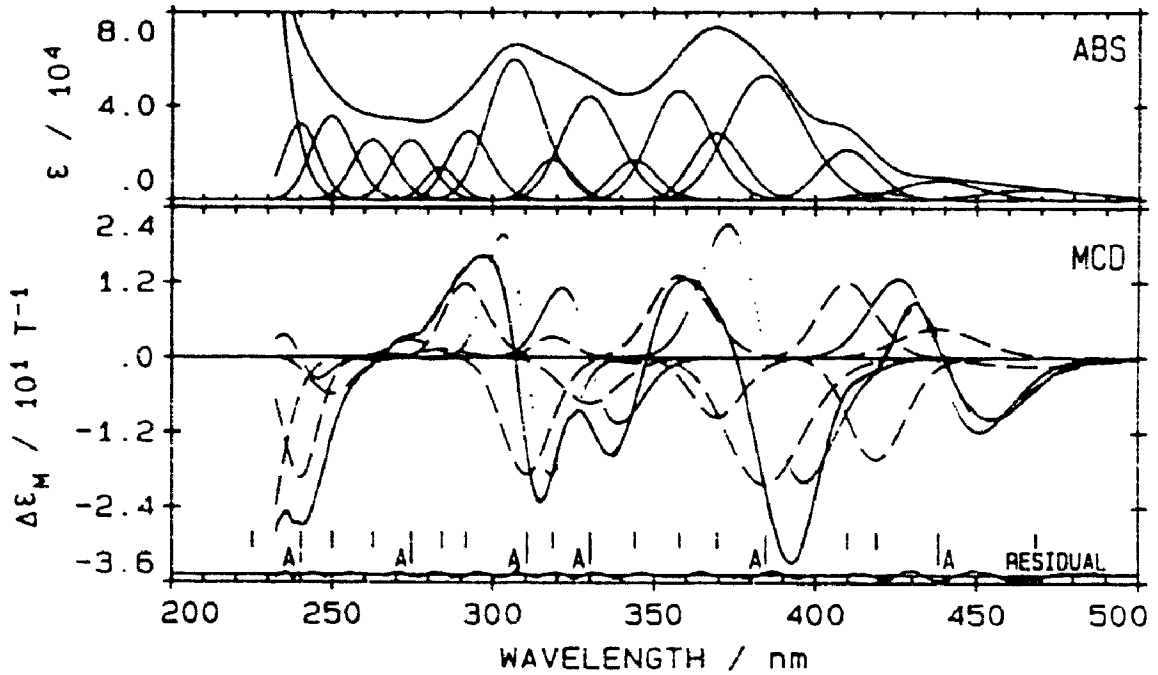

Figure 6–11 Results of a band analysis of the absorption and MCD spectra for $Na_2[(CN)_2Fe(II)Pc(-2)]$ in 98:2 DCM:DMF in the ultraviolet region (bands 13–30). (a) Absorption: (———) experimental data; (– – –) fitted data; (———) individual bands. (b) MCD: (———) experimental data; (– – –) fitted data; (.....) A terms; (– – –) B terms. The 6 band centres of A terms are labelled "A".

Table 6-2
The band fitting parameters[a] for$(NH_3)_2$Fe(II)Pc(-2) in DCM.

band #	ν /cm^{-1}	λ /nm	$\Delta\nu$ /cm^{-1}	D_0[b]	band type	$\langle\Delta\epsilon_M\rangle_n$[c]	A_1, B_0[d] /10^{-3}	B_0/D_0 /10^{-3}	A_1/D_0	μ[e]
1	14075	710	555	0.27	B	-0.23	-1.52	-5.63		
2	14569	686	436	0.70	B	-0.61	-3.99	-5.70		
3	14865	673	322	1.67	B	-2.63	-17.2	-10.3		
4	15147	660	297	10.1	A	1321.	8660.		0.86	0.80
					B	-2.50	-16.4	-1.62		
5	15492	645	259	1.21	B	0.82	5.39	4.45		
6	15693	637	264	1.03	B	-0.32	-2.10	-2.04		
7	15862	630	390	2.17	B	1.32	8.62	3.97		
8	16203	617	387	1.29	B	0.58	3.78	2.93		
9	16463	607	309	0.12	B	-0.78	-5.10	-42.5		
10	16653	601	544	3.10	B	4.19	27.5	8.87		
11	17249	580	670	1.38	B	1.50	9.83	7.12		
12	17843	560	661	0.69	B	0.27	1.82	2.64		
13	20847	480	1091	0.20	B	-0.08	-0.53	-2.65		
14	21814	458	1004	0.44	B	-0.30	-2.00	-4.55		
15	23326	429	1291	3.17	A	483.	3169.		1.00	0.93
					B	0.20	1.28	0.40		
16	24438	409	1781	1.72	B	0.52	3.38	1.97		
17	26317	380	1679	1.95	B	0.23	1.48	0.76		
18	27979	357	1414	3.61	A	587.	3848.		1.07	1.00
					B	-0.64	-4.22	-1.16		
19	29228	342	2242	14.3	A	3171.	20800.		1.45	1.35
					B	-1.51	-9.88	-0.69		
20	30701	326	1776	7.26	B	-0.02	-0.11	-0.01		
21	32028	312	1770	7.95	A	769.	5042.		0.63	0.59
					B	-0.17	-1.11	-0.14		
22	33160	302	1456	1.99	B	-0.01	-0.01	-0.01		
23	34235	292	2173	4.35	B	0.41	2.66	0.61		
24	36366	275	1971	2.96	A	69.9	458.3		0.15	0.14
					B	0.01	0.04	0.01		
25	37637	266	1436	0.93	B	-0.03	-0.18	0.19		
26	39112	256	2423	4.23	B	-0.09	-0.57	-0.13		
27	40774	245	1914	3.11	A	9.10	5.96		0.02	0.02
					B	-0.08	-0.49	-0.16		
28	42137	237	1769	3.39	B	-0.02	-0.12	-0.04		

[a]Statistics. B region: $\lambda_{230-500nm}$, χ^2=0.40, $\Sigma(\Delta\epsilon)^2$=14.8. Q region: $\lambda_{500-800nm}$, χ^2=3.14, $\Sigma(\Delta\epsilon)^2$=1058. [b]$D=\langle\epsilon\rangle_0/326.6$, where the units of D_0 (dipole strength) are D^2 (D=Debye units). [c]$\langle\Delta\epsilon_M\rangle_1$ is the first moment and $\langle\Delta\epsilon_M\rangle_0$ is the zeroth moment of the MCD; when fitting with an A term, the program calculates $\langle\Delta\epsilon_M\rangle_1$ and when fitting with a B term the program calculates $\langle\Delta\epsilon_M\rangle_0$. The Faraday term values, A_1 and B_0, are calculated directly from the moments as follows: $A=\langle\Delta\epsilon_M\rangle_1/152.5$ and $B=\langle\Delta\epsilon_M\rangle_0/152.5$. [d]$A_1$ data are printed above B_0 data when both an A and B term are used. [e]μ=magnetic moment, calculated as $2((A_1/D_0) \times 0.4669)$.

Table 6-3
The band fitting parameters[a] for $(NH_3)(CO)Fe(II)Pc(-2)$ in DCM.

band #	ν /cm^{-1}	λ /nm	$\Delta\nu$ /cm^{-1}	D_0[b]	band type	$\langle\Delta\epsilon_M\rangle_n$[c]	A_1, B_0[d] /10^{-3}	B_0/D_0 /10^{-3}	A_1/D_0	μ[e]
1	14085	710	573	0.27	B	-0.26	-1.67	-6.19		
2	14416	694	472	1.08	B	-0.83	-5.43	-5.03		
3	14840	674	370	1.69	B	-3.47	-22.8	13.4		
4	15207	658	333	16.8	A	2392.	15690.		0.93	0.87
					B	-2.22	-14.6	-0.89		
5	15500	643	260	1.59	B	1.55	10.2	6.42		
6	15755	635	299	1.83	B	0.54	3.52	1.92		
7	15959	627	286	1.19	B	0.83	5.46	4.59		
8	16177	618	368	1.23	B	1.04	6.83	5.55		
9	16502	606	493	1.94	B	0.93	6.10	3.14		
10	16784	596	384	1.73	B	2.51	1.65	0.95		
11	17110	584	391	1.01	B	0.82	5.39	5.33		
12	17438	573	571	1.07	B	0.95	6.22	5.81		
13	18035	554	787	1.23	B	0.61	4.03	3.28		
14	18847	531	2024	1.40	B	0.80	5.24	3.74		
15	21189	472	2178	0.50	B	0.49	3.24	6.48		
16	23245	430	1872	0.33	B	0.32	2.10	6.36		
17	24628	406	1485	0.23	B	0.09	0.62	2.70		
18	26022	384	1477	0.65	B	0.25	1.62	2.49		
19	27279	368	1434	3.29	A	1218.	7985.		2.43	2.27
					B	-0.53	-3.48	-1.06		
20	28321	353	1374	2.75	A	678.	4446.		1.62	1.51
					B	-0.31	-2.07	-0.75		
21	29034	344	1462	2.18	B	-0.06	-0.41	-0.19		
22	30592	327	2203	14.4	A	1563.	10250.		0.71	0.66
					B	-1.30	-8.52	-0.59		
23	31556	317	1601	3.68	B	0.10	0.67	0.18		
24	32704	306	2085	10.6	A	649.	4255.		0.40	0.37
					B	0.12	0.78	0.07		
25	34423	291	2188	10.4	B	0.04	0.28	0.03		
26	36050	277	2108	7.95	A	103.	675.		0.08	0.07
					B	-0.10	-0.63	-0.08		
27	37706	265	2463	6.47	B	-0.11	-0.71	-0.11		
28	39575	253	2549	8.44	B	-0.15	-0.99	-0.12		

[a]Statistics. B region: $\lambda_{230-500nm}$, χ^2=0.38, $\Sigma(\Delta\epsilon)^2$=161.8. Q region: $\lambda_{500-800nm}$, χ^2=1.05, $\Sigma(\Delta\epsilon)^2$=3376. [b]D=$\langle\epsilon\rangle_0$/326.6, where the units of D_0 (dipole strength) are D^2 (D=Debye units). [c]$\langle\Delta\epsilon_M\rangle_1$ is the first moment and $\langle\Delta\epsilon_M\rangle_0$ is the zeroth moment of the MCD; when fitting with an A term, the program calculates $\langle\Delta\epsilon_M\rangle_1$ and when fitting with a B term the program calculates $\langle\Delta\epsilon_M\rangle_0$. The Faraday term values, A_1 and B_0, are calculated directly from the moments as follows: $A=\langle\Delta\epsilon_M\rangle_1/152.5$ and $B=\langle\Delta\epsilon_M\rangle_0/152.5$. [d]$A_1$ data are printed above B_0 data when both an A and B term are used. [e]μ=magnetic moment, calculated as $2((A_1/D_0) \times 0.4669)$.

Table 6-4
The band fitting parameters[a] for $Na_2[(CN)_2Fe(II)Pc(-2)$ in DCM.

band #	ν /cm^{-1}	λ /nm	$\Delta\nu$ /cm^{-1}	D_0[b]	band type	$\langle\Delta\epsilon_M\rangle_n$[c]	A_1, B_0[d] /10^{-3}	B_0/D_0 /10^{-3}	A_1/D_0	μ[e]
1	14012	714	416	0.47	B	-0.25	-1.62	-3.45		
2	14586	686	422	0.91	B	-1.13	-7.40	-8.13		
3	14865	673	466	2.27	B	-1.21	-7.93	-3.49		
4	15136	661	380	14.5	A	3488.	22870.		1.58	1.48
					B	-4.14	-27.1	1.87		
5	15402	649	383	2.39	B	-0.83	-5.45	2.28		
6	15673	638	300	2.26	B	0.97	6.37	2.82		
7	15884	630	250	1.22	B	0.67	4.37	3.58		
8	16098	621	362	1.90	B	1.50	9.83	5.17		
9	16394	610	357	1.27	B	0.57	3.72	2.93		
10	16690	599	437	2.33	B	3.94	25.1	10.8		
11	16977	589	559	1.76	B	1.42	9.32	5.30		
12	17471	572	567	1.05	B	0.98	6.42	6.11		
13	17999	556	567	0.67	B	-0.01	-0.01	-0.01		
14	21344	469	1783	1.29	B	-0.12	-0.77	-0.60		
15	22822	438	1554	1.87	A	962.	6306.		3.37	3.15
					B	0.34	2.24	1.20		
16	23867	419	1163	0.55	B	-0.85	-5.55	-10.1		
17	24399	410	1205	3.46	B	0.63	4.15	1.20		
18	26003	385	1880	12.5	A	2092.	13710.		1.10	1.03
					B	-1.57	-10.3	-0.82		
19	27061	370	1349	4.64	B	-0.50	-3.31	-0.71		
20	27934	358	1714	9.33	B	0.85	5.58	0.60		
21	29071	344	1380	2.63	B	-0.04	-0.26	-0.10		
22	30285	330	1913	9.09	A	972.	6376.		0.70	0.65
					B	-0.49	-3.21	-0.35		
23	31387	319	1384	2.52	B	0.16	1.03	0.41		
24	32203	311	1811	12.8	A	1456.	9546.		0.75	0.70
					B	-1.12	-7.37	-0.58		
25	34296	292	1894	5.05	B	0.70	4.56	0.90		
26	35195	284	2092	1.89	B	0.08	0.55	0.29		
27	36410	275	1985	4.58	A	29.8	195.		0.04	0.04
					B	0.16	1.07	0.23		
28	38066	263	2193	4.85	B	-0.03	-0.22	-0.05		
29	40004	250	2466	7.18	B	-0.39	-2.54	-0.35		
30	41638	240	2188	5.59	A	302.	1983.		0.35	0.33
					B	-1.08	-7.09	-1.27		

[a]Statistics. B region: $\lambda_{230-500nm}$, χ^2=0.43, $\Sigma(\Delta\epsilon)^2$=66.4 Q region: $\lambda_{500-800nm}$, χ^2=5.45, $\Sigma(\Delta\epsilon)^2$=1859. [b]D=$\langle\epsilon\rangle_0$/326.6, where the units of D_0 (dipole strength) are D^2 (D=Debye units). [c]$\langle\Delta\epsilon_M\rangle_1$ is the first moment and $\langle\Delta\epsilon_M\rangle_0$ is the zeroth moment of the MCD; when fitting with an A term, the program calculates $\langle\Delta\epsilon_M\rangle_1$ and when fitting with a B term the program calculates $\langle\Delta\epsilon_M\rangle_0$. The Faraday term values, A_1 and B_0, are calculated directly from the moments as follows: $A=\langle\Delta\epsilon_M\rangle_1/152.5$ and $B=\langle\Delta\epsilon_M\rangle_0/152.5$. [d]$A_1$ data are printed above B_0 data when both an A and B term are used. [e]μ=magnetic moment, calculated as $2((A_1/D_0) \times 0.4669)$.

(Figure 6–10) and 18 bands for $Na_2[(CN)_2Fe(II)Pc(-2)$ (Figure 6–11). The parameters used to fit the absorption and MCD spectra of the Q and B regions for the three $L_2Fe(II)Pc(-2)$ complexes are listed in Tables 6–2 to 6–4. In the B region of the MCD spectra of $(NH_3)_2Fe(II)Pc(-2)$ (Figure 6–9) and $Na_2[(CN)_2Fe(II)Pc(-2)$ (Figure 6–11) six of the absorption bands were fit with linked MCD A and B terms, while the additional bands were fit to MCD B terms. Five of the 14 absorption bands in $(NH_3)(CO)Fe(II)Pc(-2)$ (Figure 6–10) were fit with linked A and B terms in the MCD spectrum with the other 9 bands fit with B terms. Table 6–5 lists the band centres of the degenerate transitions for the $L_2Fe(II)Pc(-2)$ complexes.

6.2.3 Moment Analysis of the Q Region

Table 6–6 lists the results of a moments analysis of the Q for $L_2Fe(II)Pc(-2)$. The moments calculation was carried out using the same program as described previously [35]. Since the program can only analyse well resolved bands, the analysis was limited to the Q band. The moments calculations provide values for the magnetic moment of the entire Q band excited state [54] (the high energy vibrational bands are included in the calculations). The A_1/D_0 parameter factors out any error in the estimation of the concentration for each solution because the same solution is used for both absorption and MCD measurements.

6.3 DISCUSSION

The "simple" phthalocyanines, such as MgPc and ZnPc, provide unique opportunities to probe the electronic structure of the phthalocyanine macrocycle. Although these phthalocyanines do act as model systems of the naturally occurring porphyrins, the lack of chemistry at the metal site limits their usefulness in the development of artificial systems that mimic the processes that take place in heme proteins and cytochromes. Studies of iron phthalocyanine show that the central iron

Table 6-5
Band centres for the degenerate transitions of $L_2Fe(II)Pc(-2)$ species obtained by the deconvolution of the absorption and MCD spectra.

$L_2Fe(II)Pc(-2)$	BAND CENTRE (nm)						
$Na_2[(CN)_2Fe(II)Pc(-2)$	661	438	385	330	311	275	240
$(py)_2Fe(II)Pc(-2)$	652	418	354	336	311	277	—
$(mepy)_2Fe(II)Pc(-2)$	652	418	356	336	311	277	—
$(im)_2Fe(II)Pc(-2)$	657	426	361	345	312	270	248
$(meim)_2Fe(II)Pc(-2)$	659	428	361	345	312	271	248
$(pip)_2Fe(II)Pc(-2)$	657	428	358	343	315	—	—
$(NH_3)_2Fe(II)Pc(-2)$	660	429	360	339	313	275	245
$(CO)(NH_3)Fe(II)PC(-2)$	658	368	353	326	306	277	

Table 6-6
Moment analysis of the Q region absorption and MCD spectra of the $L_2Fe(II)Pc(-2)$ complexes

L	ν/cm^{-1}	D_0[a]	$\langle\Delta\epsilon_M\rangle_1$	A_1[b]	A_1/D_0	magnetic moment[c]	$\langle\Delta\epsilon_M\rangle_0$	B_0/D_0 /10^{-1}
im	15 771	24.8	12 200	80.2	3.23	3.02	3.16	8.36
meim	15 788	27.7	12 600	82.6	2.99	2.79	1.90	4.49
py	15 844	24.6	11 800	77.5	3.15	2.94	1.56	4.16
mepy	15 850	26.1	11 800	77.6	2.98	2.78	2.00	5.03
pip	15 822	19.2	9 160	60.1	3.13	2.92	1.33	4.56
NH_3	15 653	24.9	12 600	82.8	3.32	3.10	1.53	4.02
NH_3/CO	15 709	33.5	17 000	112.	3.33	3.11	3.25	6.35
DMF/CO	15 756	34.4	16 400	108.	3.13	2.92	3.11	5.92
CN^-	15 580	25.1	12 500	82.2	3.27	3.05	0.38	0.99

[a]The units of the dipole strength D_0 are D^2 (D=Debye units) [25]. [b]A_1 has the units of D^2 and B_0 has the units of D^2/cm^{-2}. [c]Magnetic moment in units of μ_β, calculated from $2(A_1/D_0)\times 0.4669$.

atom exhibits a very diverse and interesting chemistry [1,2,42]. In a recent study of synthetic nitrogen fixation [113], nitrogen was electroreduced to ammonia in the presence of iron phthalocyanine. The photo and thermal dissociation of carbon monoxide (CO) and isocyanides (RCN) from iron phthalocyanine are suggested as model systems for the binding of oxygen to myoglobin and hemoglobin [108,114,115]. The photochemical dissociation of RNC from $(RNC)_2Fe(II)Pc(-2)$ [114] is a reaction with potential to be applied in the storage of solar energy.

Like the iron porphyrins [46,58], iron phthalocyanine can bind a wide variety of inorganic ligands [1,2]. A dissociative mechanism is suggested for the binding of axial ligands in iron porphyrins and iron phthalocyanine [108]. Although iron phthalocyanine can reversibly bind isocyanides and carbon monoxide [108,114,115], it is unable, at room temperatures and pressures, to reversibly bind oxygen [106,107]. The only reported $(O_2)FePc$ complex was isolated in a low temperature (15 K) matrix [107]. Infrared stretching frequencies indicated that K_D (dissociation constant) for oxygen is significantly larger for iron phthalocyanine than for hemoglobin. Kinetic studies on CO and the RCN binding indicate that the binding constants are 10^3 to 10^5 weaker in iron phthalocyanine than in iron porphyrins [108,115].

The discrepancy in K_D for axial ligands is attributed to the difference in the size of the central hole in the porphyrin and phthalocyanine rings [108]. The smaller hole size in iron phthalocyanine provides greater overlap of the π and π^* orbitals of the phthalocyanine ring with the $d\pi$ orbitals of iron and results in a greater crystal field splitting. The larger equatorial interaction results in iron phthalocyanine being a good π acceptor, while the iron porphyrins are weaker π acceptors.

Although iron phthalocyanine has been the subject of kinetic studies [103,114-118]; electrochemical measurements [42]; X-ray crystal structure determinations [109,119-121]; and Mossbauer [110,122-140], ultraviolet-visible [1,2] and MCD [1,2] spectroscopic studies, there have been few attempts to relate the

spectroscopic measurements to the molecule's chemical and physical properties. Spectral deconvolution provides the energies of specific transitions and the effect of axial ligation on these transition energies, which are invaluable to experimental and theoretical chemists.

6.3.1 Assignment of the Fitted Absorption and MCD Spectra

6.3.1.1 $(NH_3)_2$Fe(II)Pc(−2)

The spectral fits for $(NH_3)_2$Fe(II)Pc(−2) required seven degenerate transitions, two more than can be explained by assigning the Q, B1, B2, N and L transitions. The energy level diagram in Figure 6–12 outlines specific molecular orbitals and allowed transitions in low spin iron(II) phthalocyanine. Figure 6–13 illustrates the splitting of the iron(II) 3d orbitals, in iron(II) phthalocyanine, under octahedral ($10D_q$) and tetragonal (Δ_1,Δ_2) ligand fields. The stronger octahedral field, compared to the tetragonal field (Δ_1,Δ_2), is responsible for the L_2Fe(II)Pc(−2) complexes being low spin (S=0) in solution. Presented in Figure 6–12 are the two allowed degenerate MLCT transitions for the low spin (S=0) $^1A_{1g}$ ground state. The allowed charge transfer bands, the direction of charge transfer and the polarization of the transitions are listed in Table 6–7.

The assignment of the degenerate band at 660 nm (15 147 cm^{-1}) as the Q band is consistent with the spectral analysis of other M(II)Pc(−2) complexes [26,27,35]. Fitting the B region is not as simple because of the presence of the overlapping charge transfer bands. To analyse this region, one is required to compare the spectral fits obtained with other better understood systems. Low temperature absorption and MCD spectra of the ring reduced magnesium phthalocyanine π–anion radical ($[MgPc(-3)]^{\cdot-}$) [2,141] determined that the energy separation between the states arising from the electronic transitions $e_g(\pi^*) \rightarrow b_{1u}(\pi^*)$ and $e_g(\pi^*) \rightarrow b_{2u}(\pi^*)$ to be 2050 cm^{-1}. In Figure 6–12 and Table 6–7 the two degenerate MLCT transitions,

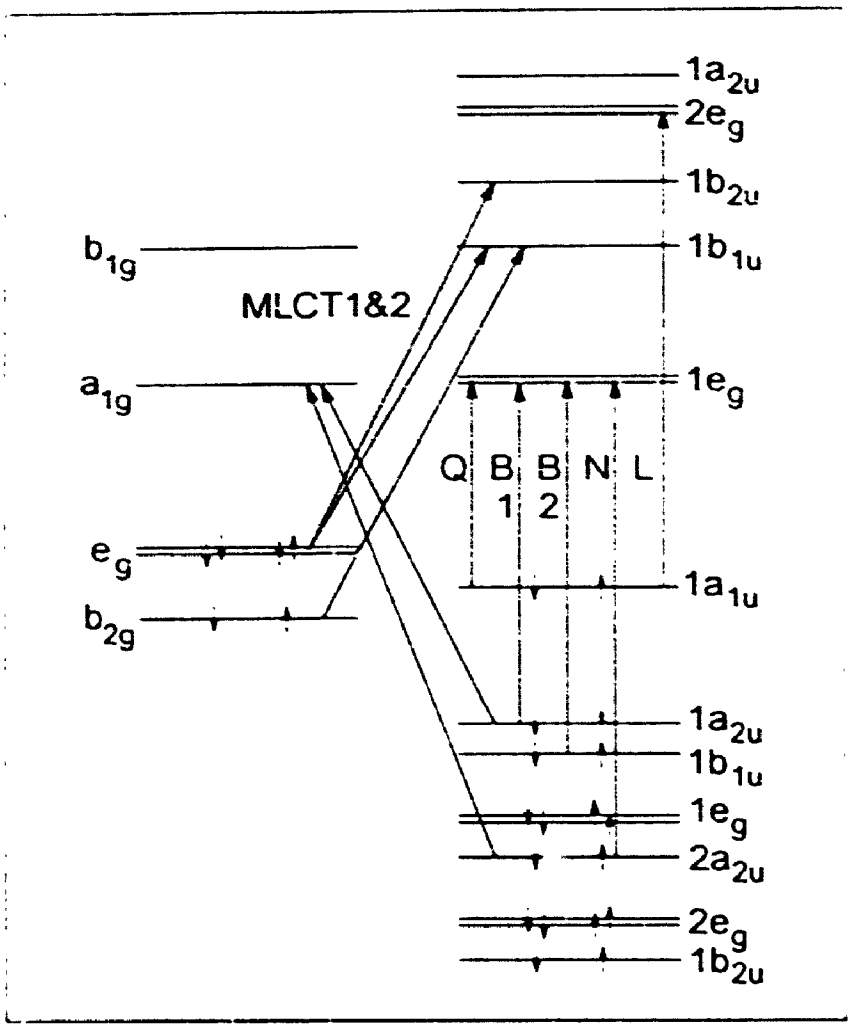

Figure 6–12 Selected molecular orbitals for the $^1A_{1g}$ ground state of $L_2Fe(II)Pc(-2)$

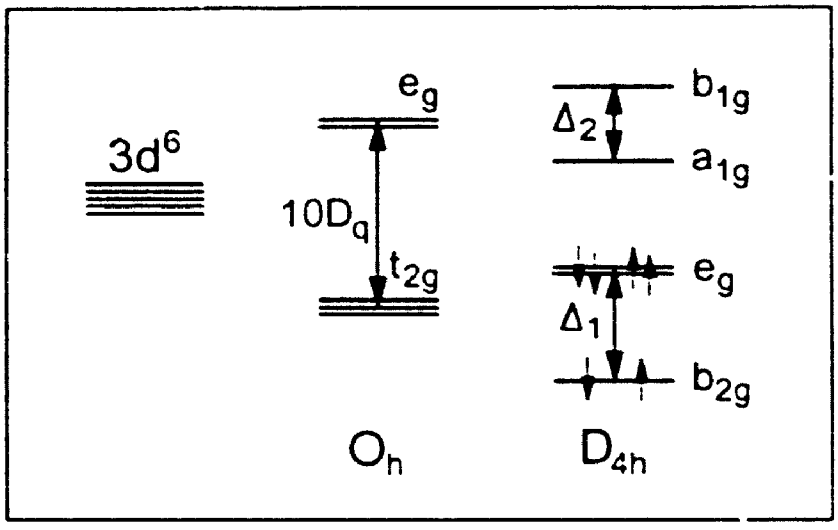

Figure 6–13 Energy level splitting for the 3d orbitals of the iron(II) ion in a ligand field with cubic ($10D_q$) and axial (Δ_1,Δ_2) distortions.

Table 6-7

Allowed charge transfer transition for low spin (S=0) Iron(II) Phthalocyanine[a].

One Electron Transition	Excited State	Charge Transfer	Polarization of Transition	MCD Term Expected
$a_{2u} \rightarrow a_{1g}$	$^1A_{2u}$	L → M	Z	B
$b_{2u} \rightarrow b_{1g}$	$^1A_{2u}$	L → M	Z	B
$b_{2g} \rightarrow b_{1u}$	$^1A_{2u}$	M → L	Z	B
$e_g \rightarrow b_{1u}, b_{2u}$	^1E_u	M → L	XY	A

[a]The ground state configuration of the iron 3d orbitals is $(b_{2g})^2(e_g)^4$ and the total symmetry of the ground state is $^1A_{1g}$.

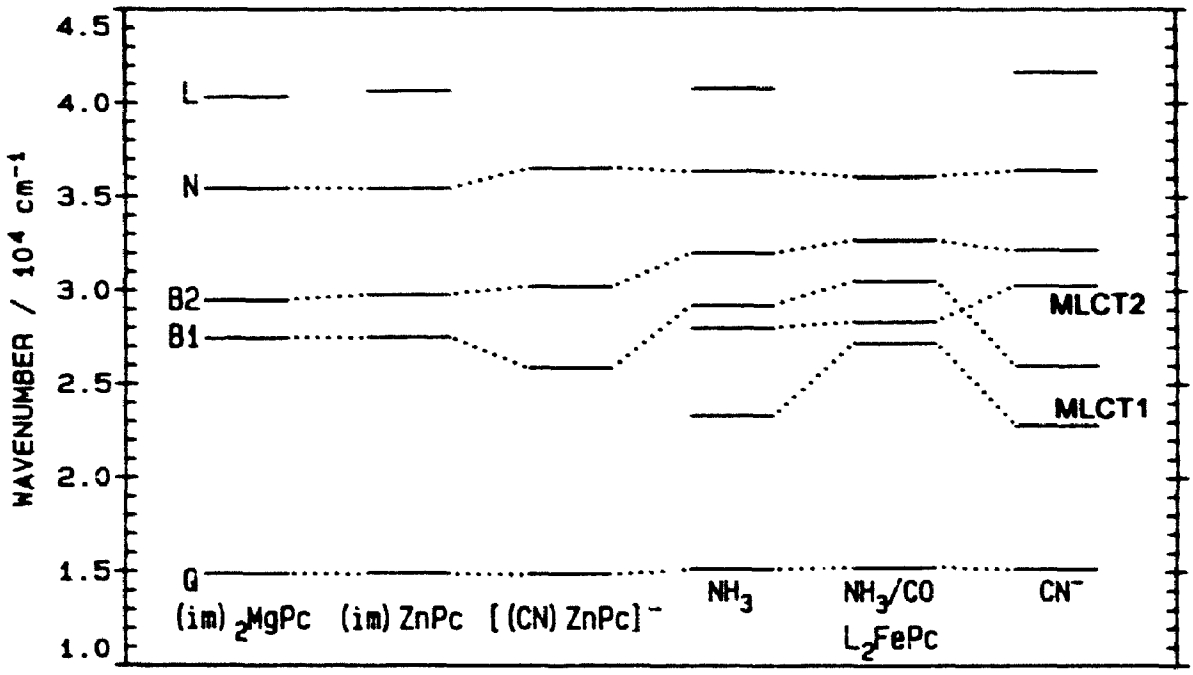

Figure 6-14 Comparison between the energies of the degenerate bands of $L_2Fe(II)Pc(-2)$ (L = NH_3, CO, CN^-), $LZnPc(-2)$ (L = im, CN^-) [26] and $(im)_2MgPc(-2)$ [27], calculated from deconvolution of the absorption and MCD spectra.

namely $e_g(d\pi) \rightarrow b_{1u}(\pi^*)$ and $e_g(d\pi) \rightarrow b_{2u}(\pi^*)$, are shown to have the same excited state molecular orbitals as the transitions for [MgPc(−3)]·−. The energy separation of the two radical anion transitions yields an approximate value for the energy separation of the two degenerate charge transfer transitions in L_2Fe(II)Pc(−2). This value is only an approximation because the negative charge on the phthalocyanine ring in [MgPc(−3)]·− and the 3d electrons in L_2Fe(II)Pc(−2) can have significant effects on the two sets of degenerate transitions and because configuration interaction will affect transition energies.

The fit of the B region (230 − 500 nm) of $(NH_3)_2$Fe(II)Pc(−2) (Figure 6–9) is an ideal starting point in the determination of the location of the two degenerate MLCT bands. It has been reported that charge transfer accounts for the spectral intensity between 400 and 500 nm in transition metal phthalocyanines [1]. The degenerate transition at 429 nm (23 326 cm^{-1}) is assigned as one of the two CT bands. The lack of additional degenerate bands between this band and the Q band (660 nm; 15 147 cm^{-1}) requires it to be the $e_g(d\pi) \rightarrow b_{1u}(\pi^*)$ orbital transition. This band is assigned as the MLCT1 band.

Locating the second degenerate MLCT band is more difficult since deconvolution places it under the 280 to 380 nm spectral envelope where the B1 and B2 bands are expected. Spectral deconvolution in this region isolated three degenerate transitions at 357 nm (27 979 cm^{-1}), 342 nm (29 228 cm^{-1}) and 312 nm (32 028 cm^{-1}). Taking into account configuration interaction, the 4453 cm^{-1} separation of the 357 nm and MLCT1 bands is close enough to the 2050 cm^{-1} separation of the $e_g(\pi^*) \rightarrow b_{1u}(\pi^*)$ and $e_g(\pi^*) \rightarrow b_{2u}(\pi^*)$ transitions in the MgPc(−3) π−anion radical. If the 357 nm band is MLCT2 ($e_g(d\pi) \rightarrow b_{2u}(\pi^*)$), then two fold difference in the energy separations is not unexpected considering the differences in the two systems. Since there is no quantitative measure of the differences between the two systems, then the bands at 342 nm and 312 nm cannot be ruled out as the MLCT2 band.

The deconvolution results for the absorption and MCD spectra of $L_2MgPc(-2)$ [27] and $LZnPc(-2)$ [26,35] are invaluable in separating the second MLCT band from the B1 and B2 bands. The fits of these "simple" phthalocyanines act as templates that can be superimposed on the spectra of $L_2Fe(II)Pc(-2)$ to isolate the $Pc(-2)$ $\pi \rightarrow \pi^*$ transitions. In Figure 6-14 the band centre energies of the degenerate transitions in $L_2Fe(II)Pc(-2)$ ($L = NH_3$, CO, CN^-), $LZnPc(-2)$ (L = im, CN^-) [26,35] and $(im)_2MgPc(-2)$ [27] are plotted. In this diagram there is a small blue shift in the energies of the Q, B1, B2, N and L bands and a small increase in the energy separation between the B1 and B2 bands as the central metal is changed from magnesium to zinc. This indicates that the filled d shell of Zn(II) does influence the energies of the $Pc(-2)$ ring orbitals. Extrapolating these effects to $(NH_3)_2Fe(II)Pc(-2)$, with its partially filled 3d shell, it is expected that the B1 and B2 bands will exhibit a larger energy separation and thus the bands at 342 and 312 nm are assigned as B1 and B2, respectively. The 357 nm band is accepted as the second charge transfer transition, the MLCT2 band. The moments obtained from spectral deconvolution of the Q and B1 bands in $(im)ZnPc(-2)$ (0.68 and 1.5 B.M.) [35] when compared to the moments of the tentatively assigned Q, MLCT2 and B1 bands in $(NH_3)_2Fe(II)Pc(-2)$ (0.80, 1.00 and 1.35 B.M.) support the current assignment. The complete assignment of the 300 to 500 nm region places the N and L bands at 275 nm (36 366 cm^{-1}) and 245 nm (40 774 cm^{-1}, respectively.

6.3.1.2 $Na_2[(CN)_2Fe(II)Pc(-2)]$

Of the seven degenerate transitions required to fit the Q and B regions of $Na_2[(CN)_2Fe(II)Pc(-2)]$, the bands at 661 nm (15 136 cm^{-1}), 275 nm (36 410 cm^{-1}) and 240 nm (41 368 cm^{-1}) are assigned as Q, N and L. The band centred at 438 nm (22 822 cm^{-1}) is in the CT region and is assigned as MLCT1. The B1 and B2 bands are known to split apart in $LZnPc(-2)$ [26,35]; therefore, the bands at

385 nm (26 003 cm^{-1}) and 311 nm (32 203 cm^{-1}) are assigned as B1 and B2. The magnetic moments reported [35] for the Q, B1 and B2 bands of Na[(CN)ZnPc(-2)] (1.57, 1.13 and 0.73 B.M.) compare very well to those for the assigned Q, B1 and B2 bands of $Na_2[(CN)_2Fe(II)Pc(-2)$ (1.48, 1.03 and 0.7 B.M.). Finally the band at 330 nm (30 285 cm^{-1}) is assigned as MLCT2.

6.3.1.3 $(NH_3)(CO)Fe(II)Pc(-2)$

Of the three $L_2Fe(II)Pc(-2)$ complexes, $(NH_3)(CO)Fe(II)Pc(-2)$ exhibits unique absorption and MCD spectra. Unlike the other two complexes, $(NH_3)(CO)Fe(II)Pc(-2)$ required six instead of seven degenerate transitions to fit the MCD spectral envelope between 250 and 800 nm. The Q band is located at 658 nm (15 207 cm^{-1}). The placement of 5 degenerate transitions in the 250 to 400 nm spectral region indicates a significant blue shift of the MLCT1 band. The large magnetic moment (2.27 B.M.) of the band at 368 nm (27 279 cm^{-1}) lies in the range for the MLCT1 band in $(NH_3)_2Fe(II)Pc(-2)$ (0.93 B.M.) and $Na_2[(CN)_2Fe(II)Pc(-2)]$ (3.15 B.M.) and this band is assigned as MLCT1. The compression of the next three degenerate bands (290 - 360 nm) into a narrow spectral region makes it difficult to separate the MLCT2 band from the B1 and B2 bands. Since the energy of the Q band blue shifts as a function of ligand, with: $CN^- < NH_3 < NH_3/CO$, the B1 and B2 bands are also expected to be blue shifted in $(NH_3)(CO)Fe(II)Pc(-2)$. The band at 353 nm (28 321 cm^{-1}) is at a higher wavelength than the B1 and B2 bands in $Na_2[(CN)_2Fe(II)Pc(-2)]$ and the high magnetic moment (1.51 B.M.) for this transition is consistent with its assignment as MLCT2. The final three bands centred at 327 nm (30 592 cm^{-1}), 306 nm (32 704 cm^{-1}) and 277 nm (36 050 cm^{-1}) are assigned as B1, B2 and N, respectively. The spectral cut off (250 nm) in $(NH_3)(CO)Fe(II)Pc(-2)$ makes it impossible to locate the L band.

6.3.2 The Effects of Axial Ligation on the Orbital Energies

The band energies obtained by spectral deconvolution for the three $L_2Fe(II)Pc(-2)$ complexes are plotted in Figure 6-15. The energy level diagram in Figure 6-16 shows the band energies for the degenerate transitions of these three complexes plus an additional five $L_2Fe(II)Pc(-2)$ complexes. The band centres from Figure 6-14 are listed in Table 6-5.

The band centre energies decrease across the ligand series: py > mepy > im > pip > CO/NH_3 > meim > NH_3 > CN^- for the Q band, and CO/NH_3 > mepy > py > im > pip > meim > NH_3 > CN^- for the MLCT1 band, and CO/NH_3 > py > mepy > NH_3 > pip > meim > im > CN^- for the B1 band. A general trend is observed when the above series are compared to the basicity (σ donor strength) of the axial ligands. As the basicity of the axial ligands increases across the series [34,129,142,143]: CO << py < mepy < im < meim < NH_3 ~ CN^- < pip, there is a general red shift in band centre energies. Axial σ donation may increase the electron density at the Fe(II) core and reduce equatorial σ donation, thus increasing the electron density at the Pc(-2) ring and decreasing the energy of the state to state transitions.

Figure 6-17A displays the overlap of specific orbitals in the axial and equatorial π systems in $L_2Fe(II)Pc(-2)$. The plot is useful in understanding the minor changes in the order of the ligand series for the Q, MLCT1 and B1 bands. Several of the axial ligands are weak π acceptors and from the spectral fits it is clear that back donation into axial π^* orbitals affects the energy separation (ΔE) between the B1/B2 and MLCT1/MLCT2 band pairs. The separation of the B1/B2 bands increases across the ligand series: CO/NH_3 < py < mepy < pip < NH_3 <im ~ meim < CN^-, while the separation of the MLCT2 and MLCT1 bands increases across the ligand series: CO/NH_3 < mepy < im < py < mepy < pip < NH_3 < CN^-. The location of CO, which is the strongest π acceptor ligand, at the start of the two

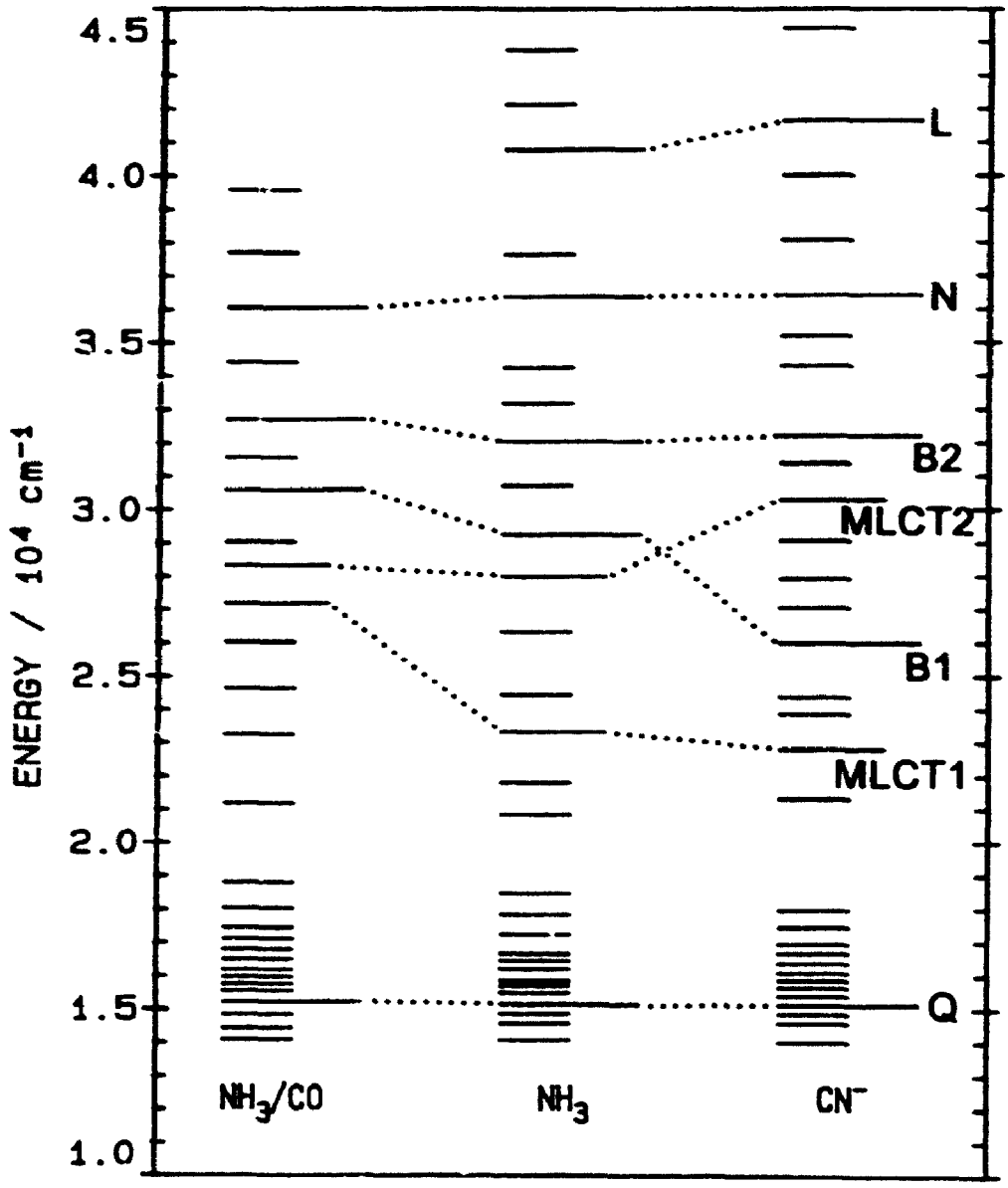

Figure 6-15 Comparison between the energies of the bands of $L_2Fe(II)Pc(-2)$ ($L = NH_3$, CO, CN^-), calculated from deconvolution of the absorption and MCD spectra.

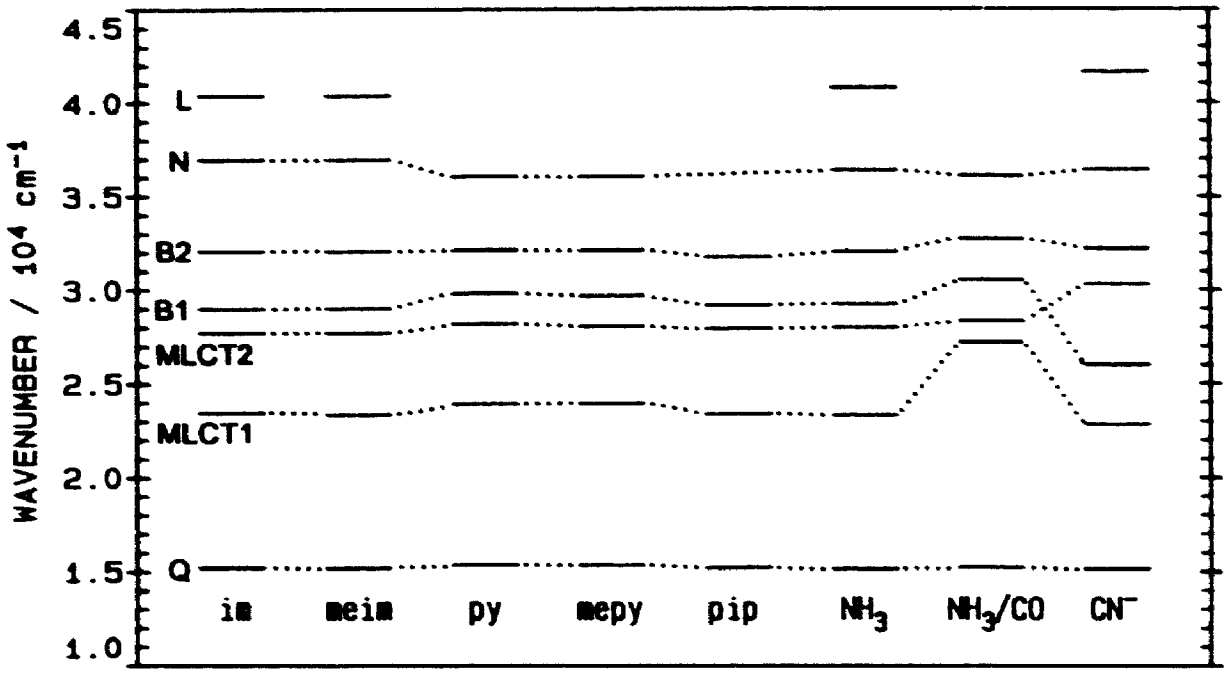

Figure 6-16 Comparison between the energies of the degenerate bands of L_2Fe(II)Pc(-2), calculated from deconvolution of the absorption and MCD spectra.

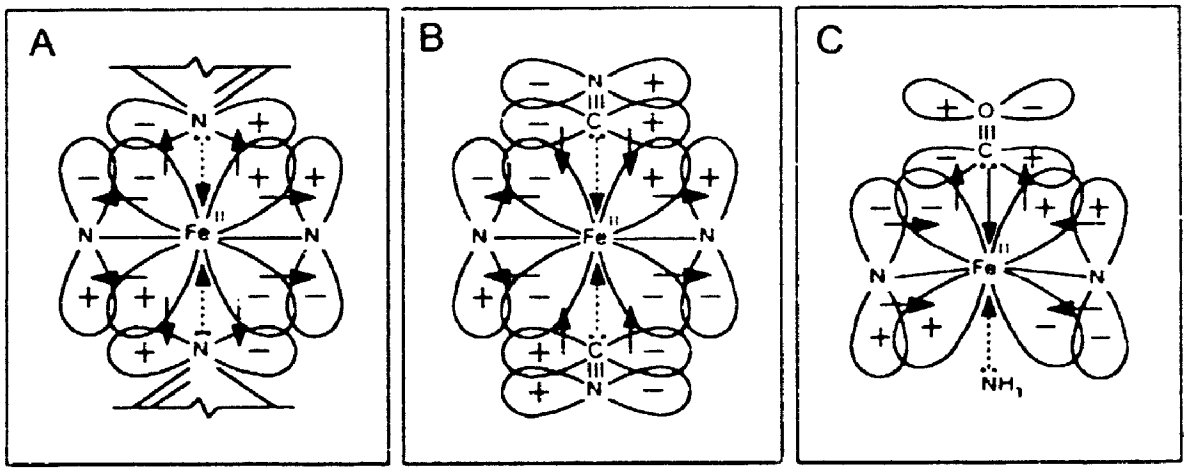

Figure 6-17 Selected overlapping axial and equatorial π and π^* orbitals in (A) L_2Fe(II)Pc(-2), (B) $Na_2[(CN)_2Fe(II)Pc(-2)]$ and (C) $(NH_3)(CO)Fe(II)Pc(-2)$. The arrows represent the direction of electron donation.

series suggests that the axial ligand π acceptor strength is inversely proportional to the energy separation. Excluding cyanide and carbon monoxide, the axial ligand π acceptor strengths are small when compared to σ donor strengths and are difficult to systematize across the ligand series. In the crystal structure of $(DMSO)_2Fe(II)Pc(-2)$ [120], the S=O bond length (1.474 Å) in the complexed DMSO is not significantly larger than the S=O bond length (1.443 Å) in free DMSO which, together with the relatively large Fe–S (2.308 Å) bond length, indicates only a small π backbonding effect in the DMSO ligand.

Although the spectral fits of $L_2Fe(II)Pc(-2)$ [L = py, mepy, im, meim, pip or NH_3] are explained according to the σ donor/π acceptor strengths of the axial ligands, the absorption and MCD results for $Na_2[(CN)_2Fe(II)Pc(-2)]$ and $(NH_3)(CO)Fe(II)Pc(-2)$ are difficult to interpret when compared to Mössbauer results [109,110,129,140]. Quadrupole splittings (ΔE_Q) recorded for intermediate spin iron(II) phthalocyanine complexes were shown to increase across the ligand series [109,110,129,140]: CN^- < CO < CO/NH_3 < im < py < mepy < pip. The value of ΔE_Q is sensitive to the electron density at the Fe(II) core and increases with π acceptor ligands and decreases with σ donor ligands [34,129,142,143]. The small ΔE_Q values for the axial CN^- and CO ligands [109,110,144] are inconsistent with the σ donor and π acceptor strengths of the ligands.

6.3.2.1 $Na_2[(CN)_2Fe(II)Pc(-2)]$

Cyanide and ammonia have similar basicities, but the absorption and MCD spectra for $(NH_3)_2Fe(II)Pc(-2)$, Figure 6-1, and $Na_2[(CN)_2Fe(III)Pc(-2)]$, Figure 6-3, exhibit drastically different B region spectral envelopes. The results of the spectral fits for these two complexes are shown in Figure 6-15. From Figure 6-15, it can be seen that in the B region the difference in the energies of the degenerate bands is considerable. The smaller ΔE_Q value of CN^- when compared to NH_3, which is a

weak π acceptor, is not consistent with the decrease in energy separation of the B1/B2 and MLCT1/MLCT2 band pairs when the two axial ligands are changed from CN^- to NH_3. The contradiction between the absorption and the Mössbauer spectra can be addressed by focusing on the π and π^* orbitals in $Na_2[(CN)_2Fe(II)Pc(-2)]$. Back donation into the π^* orbitals of CN^- will be inhibited by the negative charge on this ligand. This same negative charge may facilitate a removal of electron density from the filled $p\pi$ orbitals of CN^-, through the iron $d\pi$ orbitals, into the stronger π acceptor Pc(−2) ligand. This coupling results in an inductive effect, shown in Figure 6−17B, which increases the π electron density at the Pc(−2) ring, decreases the π electron density at the axial CN^- ligands, and maintains the $d\pi$ electron density at the iron core. The infusion of electron density into the π system of the Pc(−2) ring explains the increased separation of the B1/B2 and MLCT1/MLCT2 bands while the maintenance of the iron $e_g(d\pi)$ electron density explains the Mössbauer ΔE_Q parameter [109,110,129,140].

6.3.2.2 $(NH_3)(CO)Fe(II)Pc(-2)$

The CO ligand in $(NH_3)(CO)Fe(II)Pc(-2)$ is unique when compared to the other axial ligands since it is a weak σ donor and is a strong π acceptor. With the difference in donor/acceptor strengths, it is not unexpected that the absorption and MCD spectra of $(NH_3)(CO)Fe(II)Pc(-2)$ (Figure 6−2) are distinct from those for the other $L_2Fe(II)Pc(-2)$ complexes. Deconvolution results, shown in Figures 6−15 and 6−16, indicate that when CO is axially bound there is an appreciable blue shift in band centre energies. It is reasonable to assume that the shifts arise from metal to ligand π^* back donation as shown in Figure 6−17C. The placement of CO low in the Mössbauer ligand series imparts serious doubt on this assignment, since the small ΔE_Q values for L(CO)Fe(II)Pc(−2) [109,110] and $(CO)_2Fe(II)Pc(-2)$ [110] are unexpected for a weak σ donor and strong π acceptor ligand. The spectral results

can be explained using the inductive effect that was used to explain the results for cyanide. If the direction of the electron flow is reversed, π electron density will be removed from the Pc(−2) ring to the π^* orbitals of CO, with the $e_g(d\pi)$ orbitals of iron as the electron conduit. The loss of π density on the Pc(−2) ring results in the compression of the B1/B2 and MLCT1/MLCT2 band pairs and the blue shift of the spectral bands.

The crystal structure for (DMF)(CO)Fe(II)Pc(−2) [109] provides additional information to explain the spectral results. The analysis shows that there is a 0.04 Å displacement of Fe(II) out of the plane of the Pc ring. This results in a poorer overlap of the metal and Pc(−2) π orbitals, which may result in a readjustment of the orbital energies within the molecule.

6.3.3 Moment Analysis

The MCD technique can also provide angular momentum data for excited states as long as the transition is part of an isolated band system [26,35,52]. Stillman and Thomson [52], Ough et al. [27] and Nyokong et al. [26,35], have published Q band moments for a range of metallophthalocyanines. In iron(II) phthalocyanine, the Q band is completely isolated from charge transfer and other $\pi \rightarrow \pi^*$ transitions. This makes it possible to measure the magnetic moments for a variety of L_2Fe(II)Pc(−2) complexes. The magnetic moment of the S_1 state (which gives rise to the Q band) for the L_2Fe(II)Pc(−2) complexes (Table 6–6) is remarkably constant at 2.78 to 3.11 (expressed in terms of A_1/D_0). These values are comparable to the A_1/D_0 values of 1.5 to 3.55 for the LZnPc(−2) complexes [26,35,52], and of 2.43 to 2.60 for the L_2MgPc(−2) complexes [27]. The greater variation in the A_1/D_0 values for L_2Fe(II)Pc(−2) and LZnPc(−2), compared to those for L_2MgPc(−2), is interpreted as a difference in response by the three metals to axial ligation, with interaction between metal 3d orbitals and σ and π orbitals of the axial ligands possible for Zn(II) and

Fe(II), but impossible for Mg(II).

The difference in the range of magnetic moments for complexes of L_2Fe(II)Pc(−2) and LZnPc(−2), where the LZnPc(−2) complexes display a greater variability in their A_1/D_0 values, is not understood. The large number of magnetic moments reported here and the influence of axial ligands on the electronic spectra, for L_2Fe(II)Pc(−2) complexes, suggest that iron(II) phthalocyanine would be an ideal metallophthalocyanine to study the effect of axial ligation on the magnetic moments. Studying the magnetic moments of the various L_2Fe(II)Pc(−2) complexes listed in Table 6–6, we see that there is no direct correlation between A_1/D_0 values and the donor/acceptor properties of the axial ligands. Although the axial ligands do not appear to influence the magnetic moment of the entire Q band (Q_{00} + Q_{vib}), the A_1/D_0 values, for isolated Q_{00} bands, of 0.8 in $(NH_3)_2$Fe(II)Pc(−2), 0.87 in (NH_3)(CO)Fe(II)Pc(−2), and 1.48 in $Na_2[(CN)_2$Fe(II)Pc(−2)], which were obtained by deconvolution of the absorption and MCD spectra, indicate a considerable axial ligand effect on the distribution of the total magnetic moment between the Q_{00} and Q_{vib} bands. It appears that in L_2Fe(II)Pc(−2) complexes with π acceptor ligands (CO), a greater fraction of the the magnetic moment is distributed throughout the Q_{vib} bands, while in π donor ligands a larger portion of the magnetic moment is present in the Q_{00} band.

6.4 CONCLUSIONS

Three distinct types of absorption and MCD spectra are observed for low spin iron(II) phthalocyanine complexes. L_2Fe(II)Pc(−2) complexes can be sorted into three distinct groups according to the donor/acceptor strengths of the axial ligands. These are: (i) strong σ donors and weak π acceptors (L_2Fe(II)Pc(−2) (L = im, meim, py, mepy, pip and NH_3)); (ii) strong σ and weak π donors ($Na_2[(CN)_2$Fe(II)Pc(−2)]); and (iii) Weak σ donor and strong π acceptor (CO in (NH_3)(CO)Fe(II)Pc(−2)).

Deconvolution calculations identified degenerate bands at: 660 (Q), 429 (MLCT1), 357 (MLCT2), 342 (B1), 312 (B2), 275 (N) and 245 (L) for $(NH_3)_2Fe(II)Pc(-2)$; 661 (Q), 438 (MLCT1), 385 (B1), 311 (B2), 330 (MLCT2), 275 (N) and 240 nm (L) for $Na_2[(CN)_2Fe(II)Pc(-2)]$; and 658 (Q), 368 (MLCT1), 353 (MLCT2), 327 (B1), 306 (B2) and 277 (L) for $(NH_3)(CO)Fe(II)Pc(-2)$. Analysis of the spectral fits determined that the axial ligands effect the electronic spectra of Fe(II)Pc(−2) in three ways: (i) Increasing the σ donor strength of the axial ligands decreases the energy of the degenerate transitions; (ii) Increasing the π acceptor strength of the axial ligand decreases the separation between the B1/B2 and MLCT1/MLCT2 transitions; and (iii) Increasing the π donor strength of the axial ligands increases the separation between the B1/B2 and MLCT1/MLCT2 transitions.

CHAPTER 7

LOW SPIN IRON(III) PHTHALOCYANINE

7.1 INTRODUCTION

The large number of metal oxidation states (I to IV) available in iron phthalocyanine (FePc) [1,2,42] makes it an ideal molecule to use in the development of artificial systems that mimic biological molecules such as the cytochromes and the heme proteins. The ferrous/ferric oxidation couple, which is vital to electron transfer between cytochromes within the electron transfer pathway, ranges from - 0.20 to + 0.80 volts in a variety of axially ligated FePc complexes [42]. The "tunability" of this couple is ideal for tailoring electronic devices at the molecular level. The variability of this redox couple and the greater thermal and chemical stability of the phthalocyanines points out the promising potential of the FePc molecule.

In a paper by Lever et al. [23], the potential of the ferrous/ferric couple was related to the energy of charge transfer bands in the electronic spectra. Although this study did not take into account the effect of configuration interaction [21,145], it did provide a convenient starting point for groups attempting a more comprehensive analysis. Previous studies on closed shell metallophthalocyanines [1,26-28,35,37] demonstrate our ability to isolate and assign the transitions that comprise the absorption and magnetic circular dichroism (MCD) spectra. In this chapter, the low temperature absorption and MCD spectra of iron(III) phthalocyanine are subjected to spectral deconvolution. Low temperature MCD spectra are employed in the determination of the orbital g factor and the degeneracy of the ground state.

7.2 RESULTS

7.2.1 Chemical Oxidation of Iron(II) Phthalocyanine

The absorption spectral changes observed during the titration of bromine into a

solution of $Na_2[(CN)_2Fe(II)Pc(-2)]$ are plotted in Figure 7-1. The following spectral changes are observed during oxidation: (i) the Q band energy shifts from 660 to 685 nm and exhibits a 30% reduction in intensity, (ii) charge transfer (CT) bands appear to the low energy (700 - 850 nm) side of the Q band, (iii) CT bands overlap the vibrational components (Q_{vib}) of the Q band between 550 and 670 nm, and (iv) the band at 380 nm is lost. The sharp isosbestic points near 410, 585, 600 and 670 nm indicates that the oxidation proceeds cleanly, without any side reactions occurring. The lack of the 500 nm marker band indicative of ring oxidation, verifies the oxidation site is the metal. Based on the published spectra for iron(III) phthalocyanines [1,2,52], the oxidation product is $Na[(CN)_2Fe(III)Pc(-2)]$.

The addition of hydrochloric acid (HCl) to a solution of $Na[(CN)_2Fe(III)Pc(-2)]$ results in small changes to the absorption spectrum (Figure 7-1B). These changes are: (i) the loss of the two absorption bands between 370 and 450 nm, and (ii) small changes in the intensity and the position of the additional bands that comprise the spectral envelope. The final spectrum resembles those reported for iron(III) phthalocyanine complexes with axial pyridine [146] and imidazole [147,148] ligands. The presence of an isosbestic point at 380 nm, and the shape of the spectral envelope for the final absorption spectrum, indicate that the reaction is a ligand exchange between cyanide and chloride which results in the formation of $Na[(Cl)(CN)Fe(III)Pc(-2)]$.

The absorption spectral recorded during the oxidation of $(meim)_2Fe(II)Pc(-2)$ with bromine (Br_2) and with chlorine (Cl_2) are plotted in Figures 7-2A and 7-2B, respectively. Aside from slight differences in the positions and the intensities of absorption bands, the Cl_2 and Br_2 oxidized complexes exhibit remarkably similar spectra. The blue shift and reduction in the Q band intensity (this band is present at 691 nm for oxidation by Br_2 and at 685 nm for oxidation by Cl_2), the presence of CT bands between 700 and 850 nm, and the overlapping CT and Q_{vib} bands between

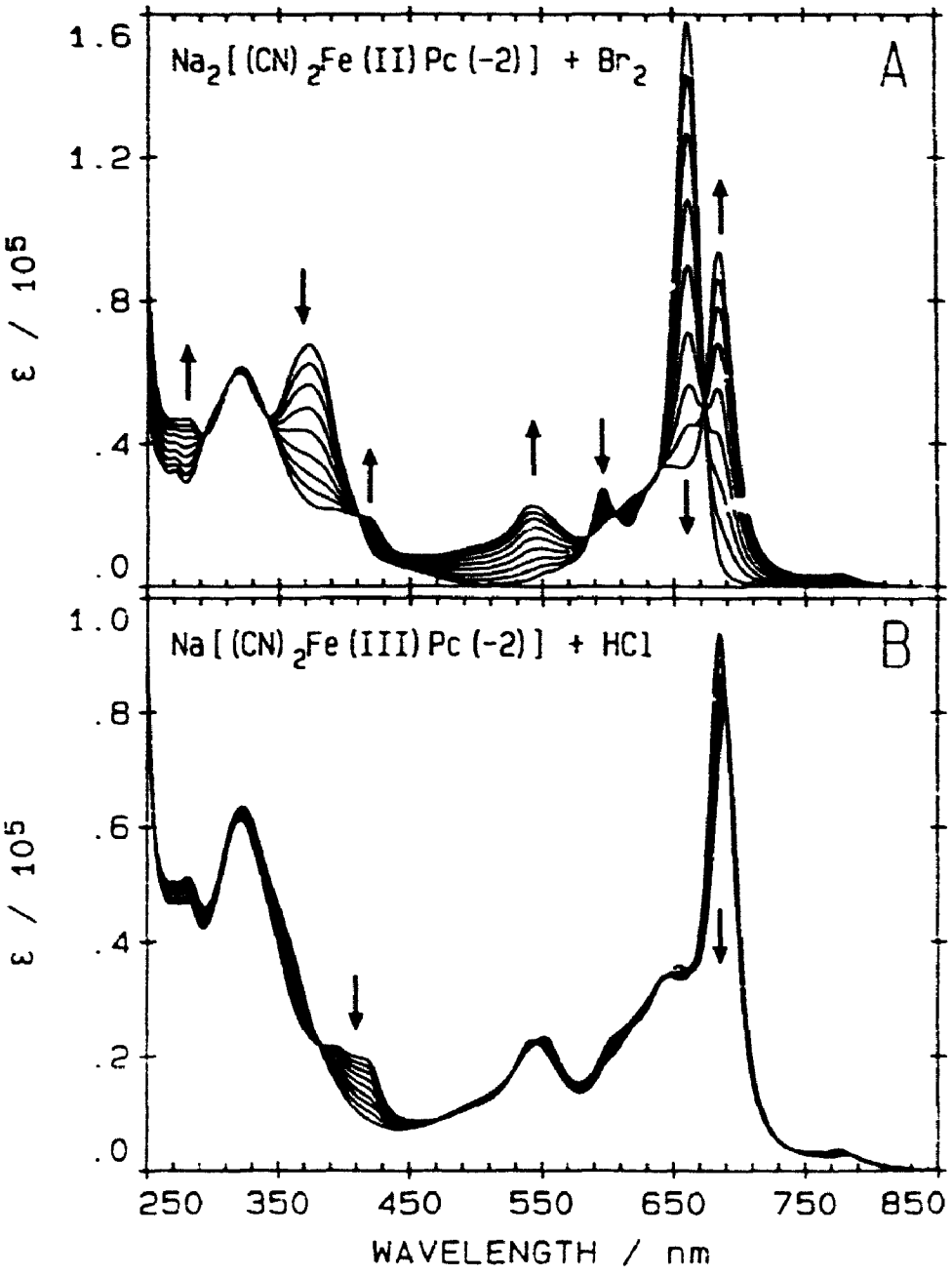

Figure 7-1 Absorption changes observed **(A)** during the chemical (Br_2) oxidation of $Na_2[(CN)_2Fe(II)Pc(-2)]$ dissolved in 98:2 DCM:DMF and **(B)** during the titration of HCl into metal oxidized $Na[(CN)_2Fe(III)Pc(-2)]$ dissolved in 98:2 DCM:DMF. The small arrows represent the spectral changes during the titrations.

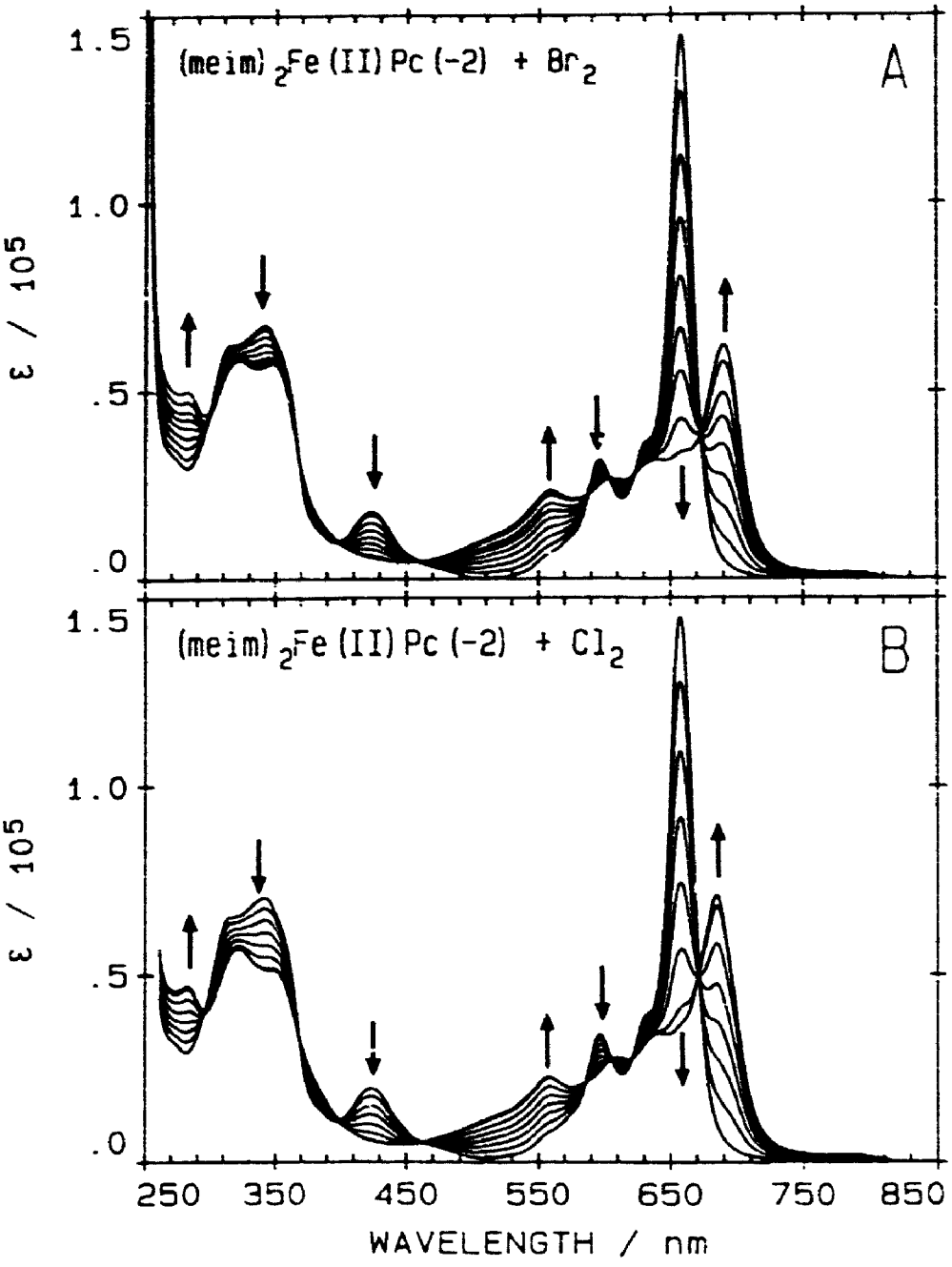

Figure 7-2 Absorption changes observed **(A)** during the chemical (Br_2) oxidation of $(meim)_2Fe(II)Pc(-2)$ dissolved in DCM and **(B)** during the chemical (Cl_2) oxidation of $(meim)_2Fe(II)Pc(-2)$ dissolved in DCM. The small arrows represent the spectral changes during the titrations.

460 and 680 nm are consistent with the spectrum of $Na[(CN)_2Fe(III)Pc(-2)]$. In addition to the above changes, the charge transfer band near 430 nm disappears and the bands in the 300 to 370 nm region exhibit a small reduction in spectral intensity. The presence of several sharp isosbestic points in Figures 7-2A and 7-2B is consistent with the formation of a single oxidation product. Previous electrochemical studies [42,149,150] indicate that metal oxidation is preceded by axial ligand exchange and the oxidation products are (meim)(Br)Fe(III)Pc(-2) and (meim)(Cl)Fe(III)Pc(-2). The absorption band maxima for the series of L(X)Fe(III)Pc(-2) [L = im, meim, py, mepy, CN, pip, NH_3; X = Cl, Br, I, CN, NO_3, ClO_4] complexes are listed in Table 7-1

Table 7-1
Observed maxima in the absorption spectra of L(X)Fe(III)Pc(-2) in chlorinated solvents.

L(X)Fe(III)Pc(-2)	λ_{max} (nm)							
$Na[(CN)_2Fe(III)Pc(-2)]^a$	774	684	645		542	391	320	280
$(im)(Cl)Fe(III)Pc(-2)^a$	774	690	606		558	349	323	284
$(im)(Br)Fe(III)Pc(-2)^a$	785	690	641	608	559	350	323	284
$(im)(NO_3)Fe(III)Pc(-2)^a$	785	690	643	609	559	351	322	284
$(im)(ClO_4)Fe(III)Pc(-2)^a$	787	685			557	322		283
$(meim)(Cl)Fe(III)Pc(-2)^a$	789	685	642	610	559	347	322	283
$(meim)(Br)Fe(III)Pc(-2)^a$	784	691	640	606	560	352	323	283
$(meim)(I)Fe(III)Pc(-2)^a$	779	691	645	612	562	353	323	283
$(meim)(NO_3)Fe(III)Pc(-2)^a$	796	689		613	561	349	327	283
$(meim)(ClO_4)Fe(III)Pc(-2)^a$	782	688			559		323	283
$(im)(Cl)Fe(III)Pc(-2)^b$	778	681		610	555		322	282
$(meim)(Cl)Fe(III)Pc(-2)^b$	779	682		610	555		323	282
$(py)(Cl)Fe(III)Pc(-2)^b$	791	688		615	562		324	
$(mepy)(Cl)Fe(III)Pc(-2)^b$	789	687		613	562		324	
$(pip)(Cl)Fe(III)Pc(-2)^b$		677		611	550		324	
$(NH_3)(Cl)Fe(III)Pc(-2)^b$	775	677		610	543		323	279

The spectra were recorded in: [a]DCM and [b]DCB.

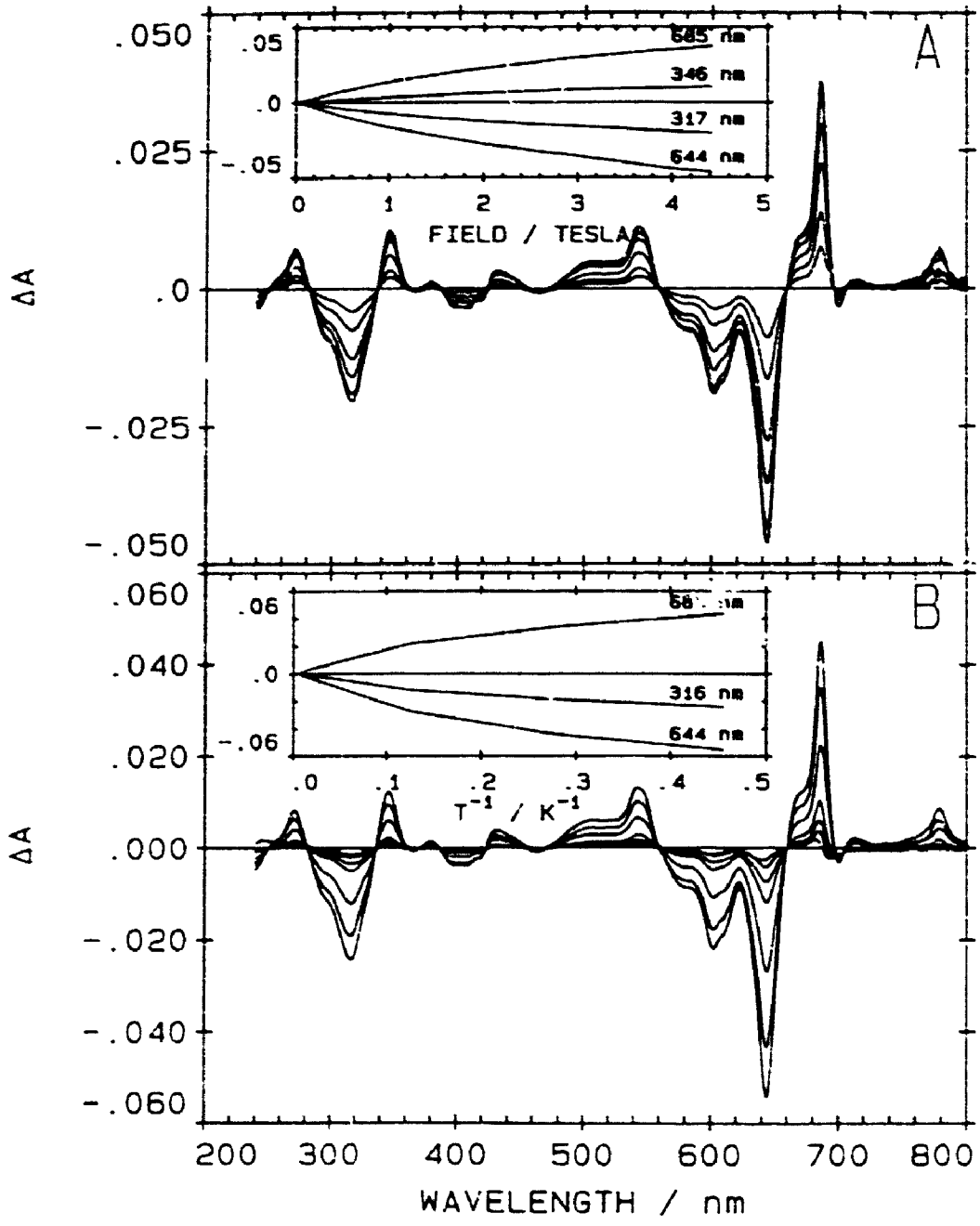

Figure 7-3 MCD changes observed for a 1 mm glass of $Na[(CN)_2Fe(III)Fe(-2)]$ **(A)** when the temperature is held constant at 3.8 K and the magnetic field is varied between 0 and 4 4 tesla (the inset displays the change in MCD intensity versus magnetic field at four wavelengths) and **(B)** when the temperature is varied between 3 and 120 K under a constant 3.92 T magnetic field (the inset displays the change in MCD intensity versus temperature at three wavelengths).

7.2.2 Low Temperature MCD Spectra of Iron(III) Phthalocyanine

The MCD spectrum of $Na[(CN)_2Fe(III)Pc(-2)]$ at 3.8 K is plotted in Figure 7-3A for magnetic flux densities between 0 and 4.4 tesla. Inspection of the (-) and (+) intensity bands at 644 and 685 nm indicates that ΔA is not linear with respect to the magnetic field intensity and saturates (approaches a local maximum or minimum value) at high applied magnetic fields. The inset in Figure 7-3A displays the saturation behaviour at 317, 346, 644 and 685 nm. The same behaviour occurs when the magnetic field is held constant at 3.92 tesla and the sample temperature varied between 3 and 120 K (Figure 7-3B). ΔA at the three wavelengths 316, 644 and 685 nm and approaches asymptotic values as the temperature falls below 4.2 K (the inset in Figure 7-3B). Saturation of the MCD signal in the temperature and field dependence plots for $Na[(CN)_2Fe(III)Pc(-2)]$ indicates that the ground state is orbitally degenerate.

The magnetic field dependence determined between 0 and 2.5 tesla for the 3.8 K MCD spectrum of (meim)(Br)Fe(III)Pc(-2) is illustrated in Figure 7-4. The inset in Figure 7-4 plots ΔA versus the magnetic field at five wavelengths. Although ΔA values at 305, 390, 550, 610 and 640 nm do not show saturation, the deviation from linearity verifies that the ground state in (meim)(Br)Fe(III)Pc(-2) is also orbitally degenerate.

7.2.3 Determination of the Lande g Factor

The field dependence plots for $Na[(CN)_2Fe(III)Pc(-2)]$ (Figure 7-3A) and (meim)(Br)Fe(III)Pc(-2) (Figure 7-4), can be used probe the orbitally degenerate ground state. The relative population of a Zeeman split Kramers doublet was shown in Chapter 1 to depend on the Boltzman distribution function ($N_A/N_B=\exp[-\Delta E/kT]$). The magnetic field strength (B), the Bohr magneton (β) and the averaged orbital g factor (g_{av}) determine the energy separation ($\Delta E=g_{av}\beta B$) between the two energy levels

within the doublet. If the MCD signal saturates (this occurs when there is 100% population of the lower energy level in the ground state Kramers doublet) then the spectral intensity (ΔA) at a specific wavelength can be plotted against $\beta B/kT$ and the equation $\Delta A = K\tanh(g_{av}\beta B/2kT)$ (adapted from [25]), where K represents ΔA at saturation, can be used to fit the experimental data and determine g_{av}.

The MCD signal for $Na[(CN)_2Fe(III)Pc(-2)]$ and (meim)(Br)Fe(III)Pc(−2) did not saturate under the lowest temperatures (<2 K) and the strongest magnetic fields (>4.5 tesla) available. Without a definite value for K, fitting the ΔA versus $\beta B/kT$ plot will yield an infinite number of values for g_{av}. The problem can be overcome by rearranging the tanh equation to the linear equation: $\ln[(K+\Delta A)/(K-\Delta A)] = g_{av}\beta B/kT$. A least squares routine can be employed to determine unique values for K and g_{av} from a $\ln[(K+\Delta A)/(K-\Delta A)]$ versus $\beta B/kT$ plot. The difference (χ^2) between the experimental data and a line of best fit was minimized in the determination of g_{av}.

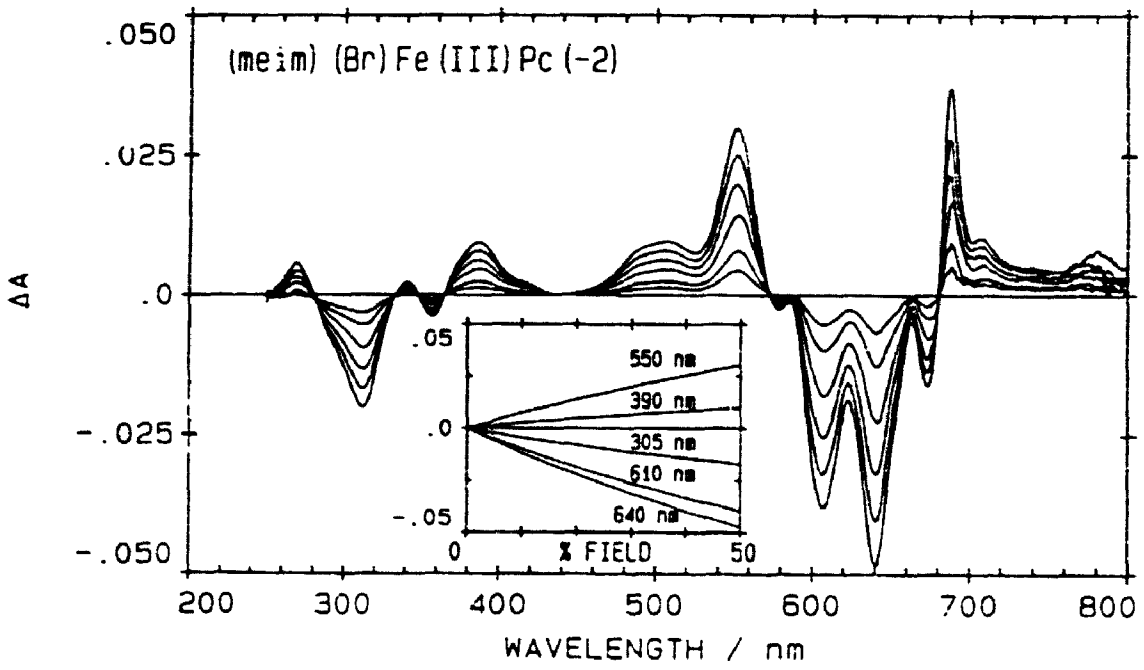

Figure 7-4 MCD changes observed for a 1 mm glass of (meim)(Br)Fe(III)Pc(−2) when the temperature is constant at 3.8 K and the magnetic field is varied between 0 and 2.5 tesla (the inset displays the change in MCD intensity versus magnetic field at four wavelengths).

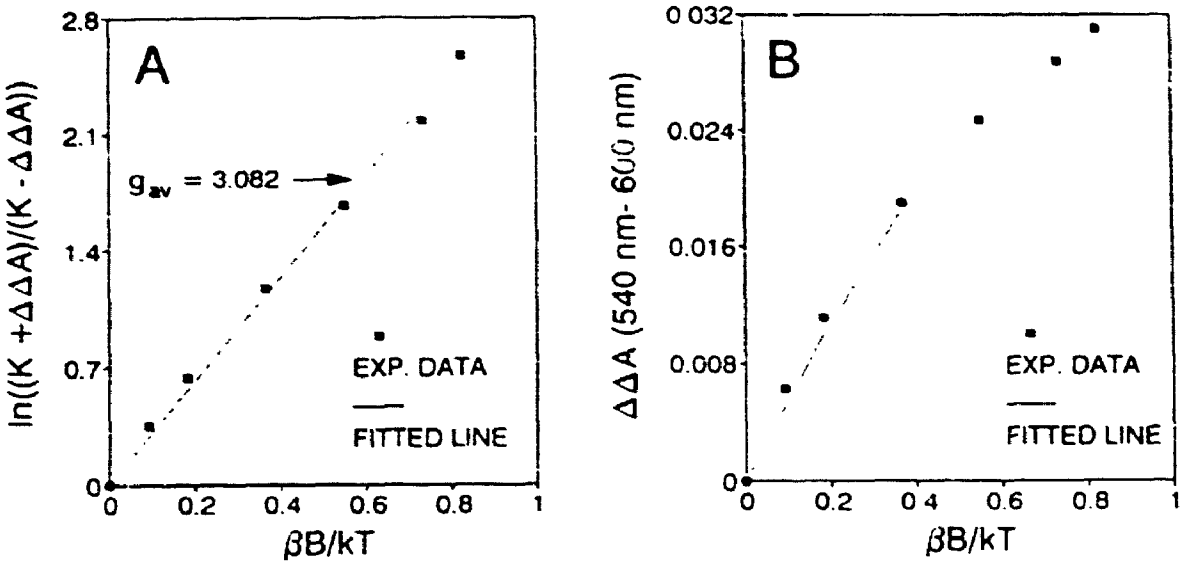

Figure 7-5 Plots of (A) $\ln[(K+\Delta\Delta A)/(K-\Delta\Delta A)]$ versus $\beta B/kT$ and (B) $\Delta\Delta A$ versus $\beta B/kT$, which present the experimental and fitted data obtained for a 3.6 K glassed sample of $Na[(CN)_2Fe(III)Pc(-2)]$. $\Delta\Delta A$ represents the MCD spectral intensity difference between the 540 and 600 nm MCD bands and K is the intensity of $\Delta\Delta A$ when the MCD signal is saturated.

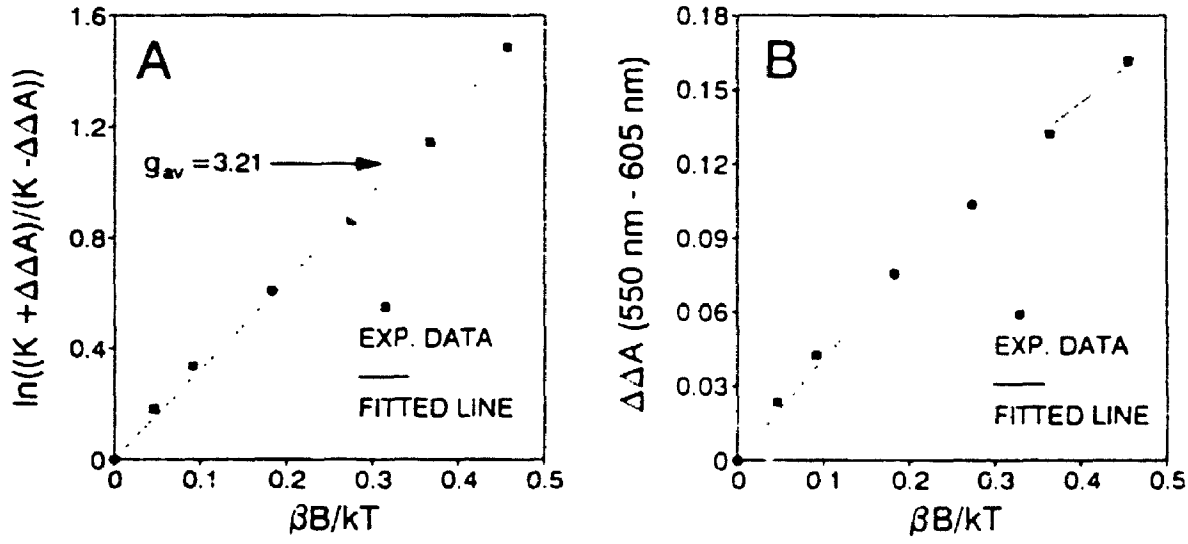

Figure 7-6 Plots of (A) $\ln[(K+\Delta\Delta A)/(K-\Delta\Delta A)]$ versus $\beta B/kT$ and (B) $\Delta\Delta A$ versus $\beta B/kT$, which present the experimental and fitted data obtained for a 3.6 K glassed sample of (meim)(Br)Fe(III)Pc(-2). $\Delta\Delta A$ represents the MCD spectral intensity difference between the 550 and 605 nm MCD bands and K is the intensity of $\Delta\Delta A$ when the MCD signal is saturated.

The $\ln[(K+\Delta\Delta A)/(K-\Delta\Delta A)]$ versus $\beta B/kT$ plot for $Na[(CN)_2Fe(III)Pc(-2)]$ in Figure 7–5A approaches linearity when $K=(3.61 \pm 0.06) \times 10^{-2}$ and $g_{av}=3.08 \pm 0.04$. $\Delta\Delta A$ is the difference in the MCD spectral intensity between the bands at 540 and 600 nm. Using the intensity difference between two close lying, oppositely signed MCD bands ensures that baseline distortion effects introduced by strains in the glass are minimized. The K and g_{av} values for $Na[(CN)_2Fe(III)Pc(-2)]$ are inserted into the hyperbolic tangent equation and the resulting curve is plotted in Figure 7–5B to demonstrate the accuracy of the K and g_{av} values.

The $\ln[(K+\Delta\Delta A)/(K-\Delta\Delta A)]$ versus $\beta B/kT$ and $\Delta\Delta A$ versus $\beta B/kT$ plots for (meim)(Br)Fe(III)Pc(–2) are presented in Figure 7–6. Here $\Delta\Delta A$ is the MCD spectral intensity difference between the 550 and 605 nm bands. The least squares routine obtained values for K of 0.256 ± 0.003 and g_{av} of 3.21 ± 0.04. The exponential plot in Figure 7–6B indicates that the calculated K and g_{av} values accurately fit the experimental data.

7.2.4 Room and Low Temperature Absorption and MCD Spectra of Iron(III) Phthalocyanine

The absorption and MCD spectra presented in Figure 7–7A represent low temperature measurements (4 K for the MCD and 77 K for the absorption) for $Na[(CN)_2Fe(III)Pc(-2)]$, while Figure 7–7B illustrates the room temperature absorption and MCD spectra for $Na[(CN)_2Fe(III)Pc(-2)]$. There is an absence of the derivative band shapes that are indicative of transitions from nondegenerate ground states into degenerate excited states, in the room temperature MCD spectrum. The (+) and (–) MCD bands that arise under the intense 680 nm absorbance band appear to belong to a MCD A term, but the bands actually represent two overlapping, oppositely signed MCD C terms.

The low temperature spectra of $Na[(CN)_2Fe(III)Pc(-2)$ are considerably different

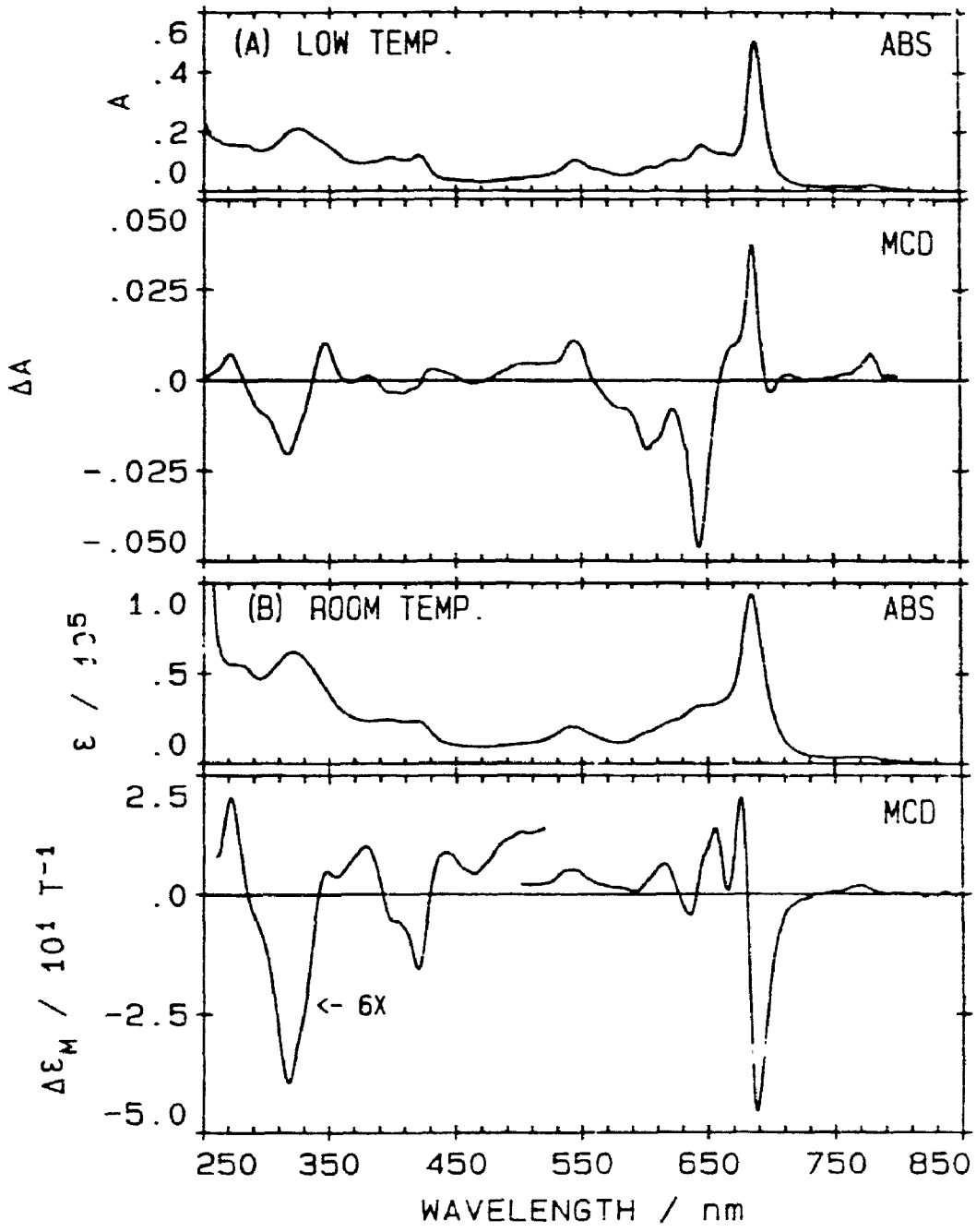

Figure 7-7 **(A)** The 77 K absorption (ABS) and 4 K MCD (4 K) spectra for a 1 mm glass of Na[$(CN)_2$Fe(III)Pc(-2)] and **(B)** the 300 K absorption ABS and MCD spectra for Na[$(CN)_2$Fe(III)Pc(-2)] recorded in DCM. ϵ for the Q_{00} transition (λ_{max}=684 nm) is 93 800 L mol^{-1} cm^{-1} at 300 K and 141 500 L mol^{-1} cm^{-1} at 77 K

from their room temperature counterparts. Cooling to 77 K (Figure 7–7A) results in a narrowing of band widths and a concurrent increase in the absorption spectral intensity. These effects are best seen for the Q band (centred near 680 nm) where the spectral intensity increased by 50% and the band width decreased about 30% upon cooling from 300 to 77 K. The temperature effects occur from the depopulation of thermally excited vibronic states that give rise to absorbance "hot" bands. The differences between the MCD at 300 K and at 4 K (Figure 7–7) are not limited to the narrowing of band widths and the small increases in spectral intensity. Lowering the temperature from 300 to 4 K results in the appearance of intense bands that were not present in the room temperature MCD. The 685 and 644 nm bands are examples of transitions that are not readily isolated from the 300 K MCD spectrum (Figure 7–7B), but dominate the 4 K spectrum (Figure 7–7A). This effect is commonly encountered in iron(III) porphyrins [46] where the MCD spectra are dominated by temperature dependent C terms.

The room and low temperature absorption and MCD spectra for (meim)(Br)Fe(III)Pc(−2) (Figure 7–8) are very similar to those obtained for $Na[(CN)_2Fe(III)Pc(-2)]$. Bands in the absorption and MCD intensify and sharpen upon cooling, with C terms dominating the 300 and 4 K MCD spectra.

7.2.5 Spectral Band Deconvolution Calculations

Since the ground state of L(X)Fe(III)Pc(−2) is orbitally degenerate, low temperature MCD spectra are required for spectral band deconvolution calculations. When a 4 K sample of $Na[(CN)_2Fe(III)Pc(-2)]$ is exposed to a 4.41 tesla magnetic field, the Zeeman split low energy component of the ground state Kramers doublet is 93% occupied. Depopulation of the higher energy component means that the nonderivative Gaussian band shapes provide reliable band widths and band centres for the electronic transitions contributing to the MCD spectrum. Because the fitting

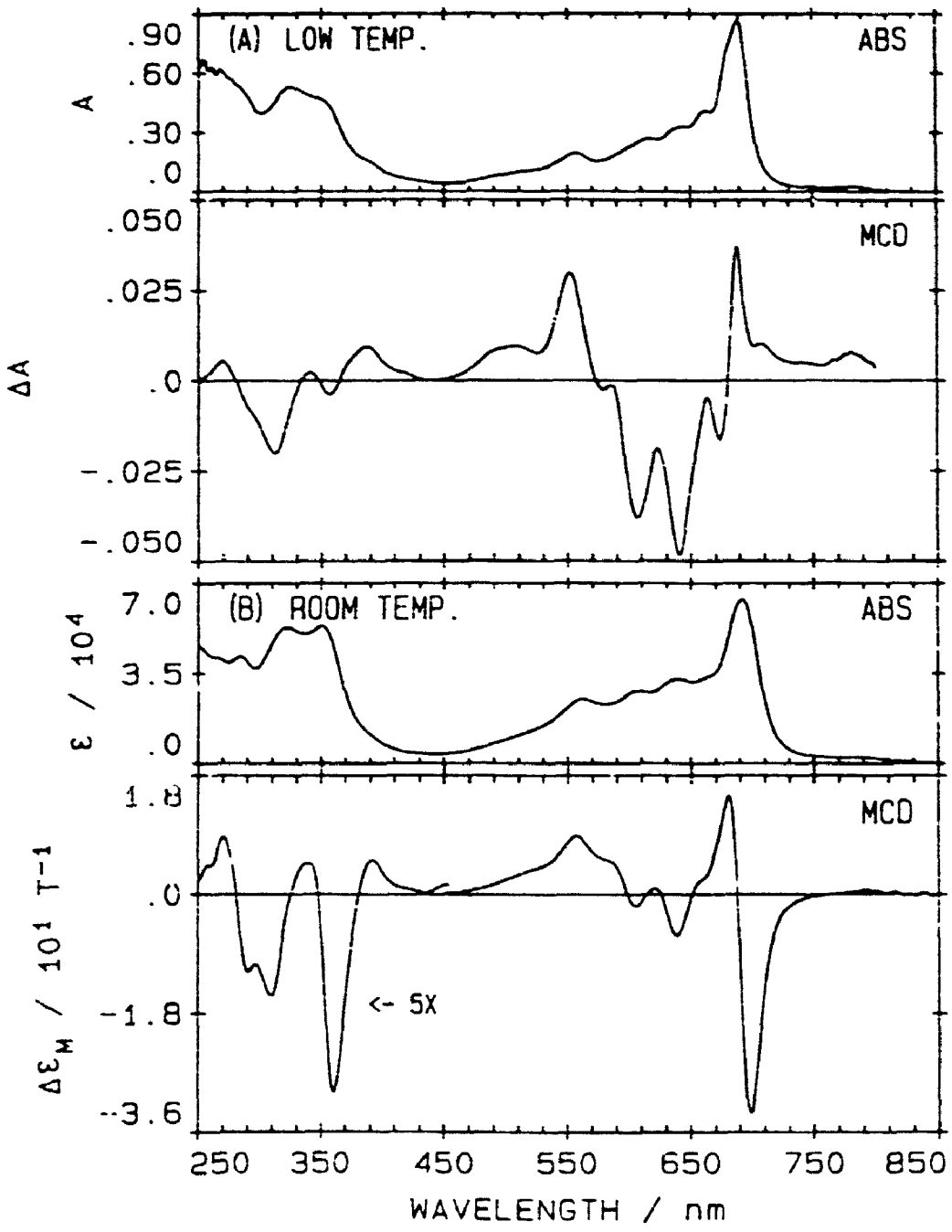

Figure 7-8 **(A)** The 77 K absorption (ABS) and 4 K MCD spectra for a 1 mm glass of (meim)(Br)Fe(III)Pc(-2) and **(B)** the 300 K absorption and MCD spectra for (meim)(Br)Fe(III)Pc(-2) recorded in DCM. ϵ for the Q_{00} transition (λ_{max}=691 nm) is 63 800 L mol^{-1} cm^{-1} at 300 K and 97 600 L mol^{-1} cm^{-1} at 77 K.

parameters obtained from spectral deconvolution were determined from calculations that assume the rigid shift approximation [25], the MCD spectra are scaled up 1.43 times so that $\Delta\epsilon$ is linear with respect to the applied magnetic field. The use of 77 K absorption spectra ensures that spectral intensity due to vibronic hot bands is minimized.

The 77 K absorption and 4 K MCD fits for the Q region (500 - 800 nm) of $Na[(CN)_2Fe(III)Pc(-2)]$ are displayed in Figure 7-9. Because of the temperature dependence in the MCD spectra, the 21 absorption bands are fit with MCD C terms. The low temperature Q region fit for (meim)(Br)Fe(III)Pc(-2) (Figure 7-10) also used 21 bands in the fit of the absorption and MCD spectral envelopes. The B region (250 - 500 nm) absorption and MCD spectral fits for $Na[(CN)_2Fe(III)Pc(-2)]$ are shown in Figure 7-11, while the fits of the B region (250 - 450 nm) for (meim)(Br)Fe(III)Pc(-2) are plotted in Figure 7-12. The absorption and MCD spectra, in Figures 7-11 and 7-12, are fit to 17 and 11 bands, respectively. The lack of systematic noise in the MCD residuals for Figures 7-9 to 7-12 suggests that the number of bands used in the fits reliably reproduce the numbers and the positions of electronic transitions that comprise the electronic spectra. The fitting parameters obtained for the Q and B regions of $Na[(CN)_2Fe(III)Pc(-2)]$ are listed in Table 7-2. Different solutions were used in the measurement of the absorption and MCD spectra for (meim)(Br)Fe(III)Pc(-2) and tables for the fitting parameters are not listed, because it is impossible to determine C_0/D_0 values from the fits.

7.3 DISCUSSION

The royal blue coloured iron(III) phthalocyanine complexes can be generated chemically [103,125,146,150] and electrochemically [35]. In his review of the electrochemical properties of metallophthalocyanines, Lever [42] lists $E_{\frac{1}{2}}$ (Fe(II)/Fe(III)) values for $L_2Fe(II)Pc(-2)$ with a wide variety of axial ligands and counterions. The

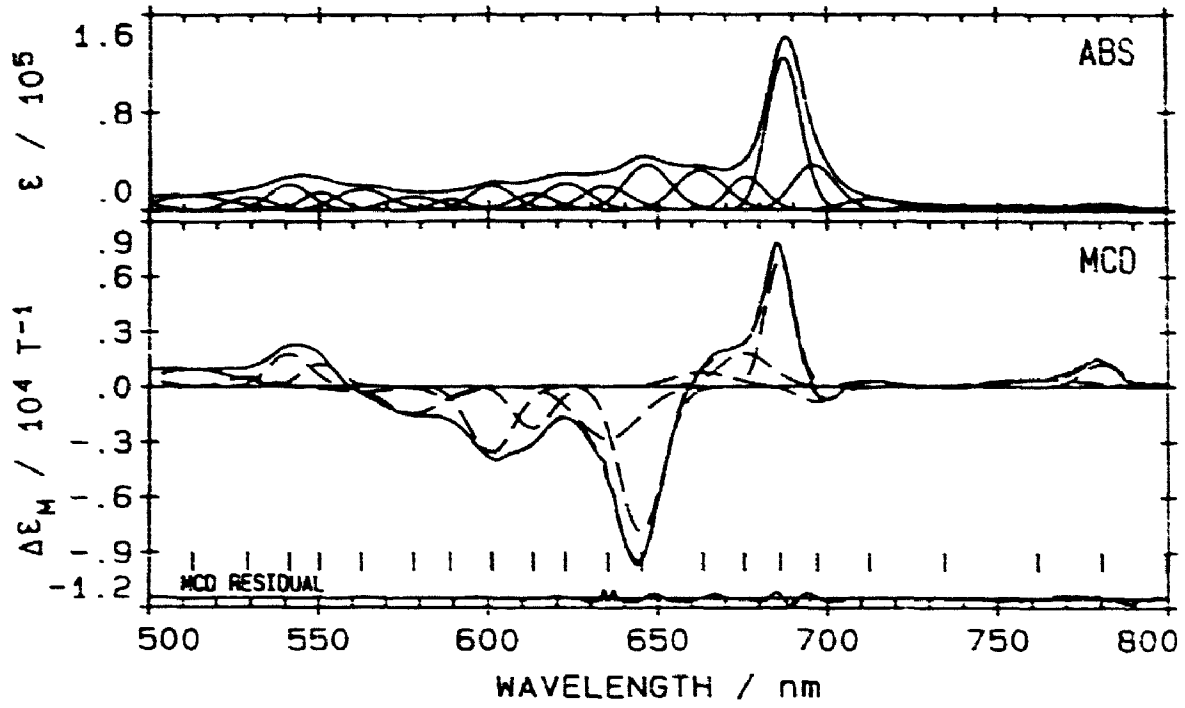

Figure 7–9 Results of a band analysis on the 77 K absorption and 4 K MCD spectra for 1 mm glasses of $Na[(CN)_2Fe(III)Pc(-2)]$ in the visible region (bands 1–24). (a) Absorption: (———) experimental data; (– – –) fitted data; (———) individual bands. (b) MCD: (———) experimental data; (– – –) fitted data; (— —) individual bands.

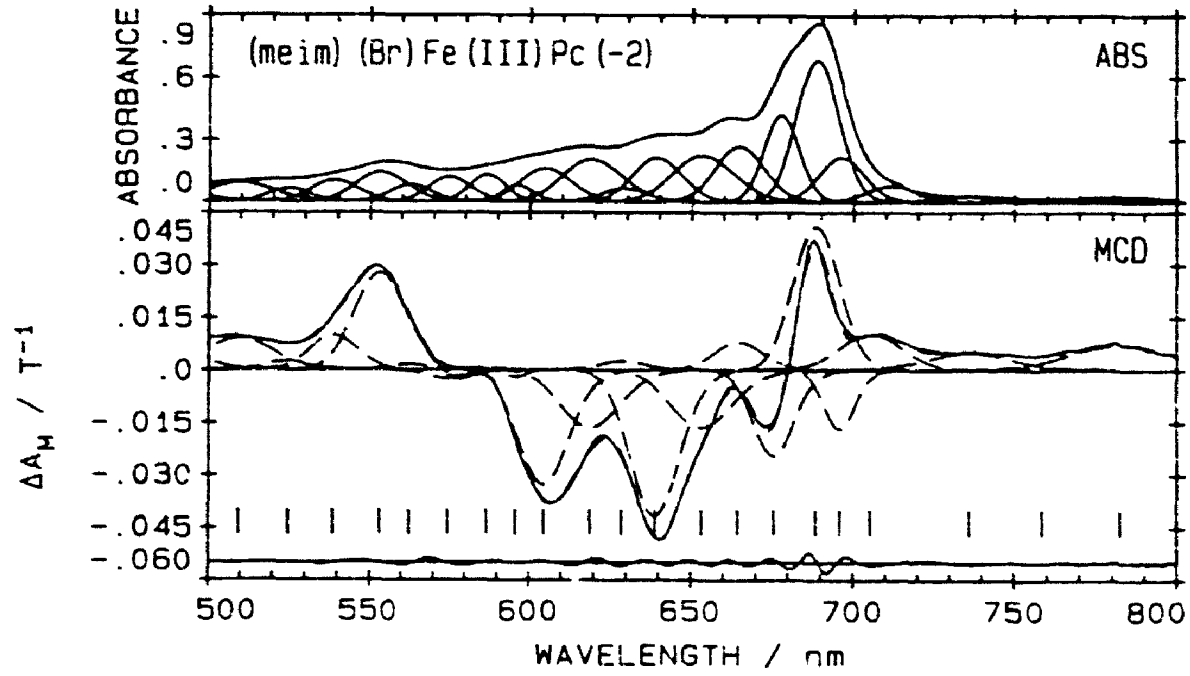

Figure 7–10 Results of a band analysis of the 77 K absorption and 4 K MCD spectra for 1 mm glasses of (meim)(Br)Fe(III)Pc(–2) in the visible region (bands 1–24). (a) Absorption: (———) experimental data; (– – –) fitted data; (———) individual bands. (b) MCD: (———) experimental data; (– – –) fitted data; (— —) individual bands.

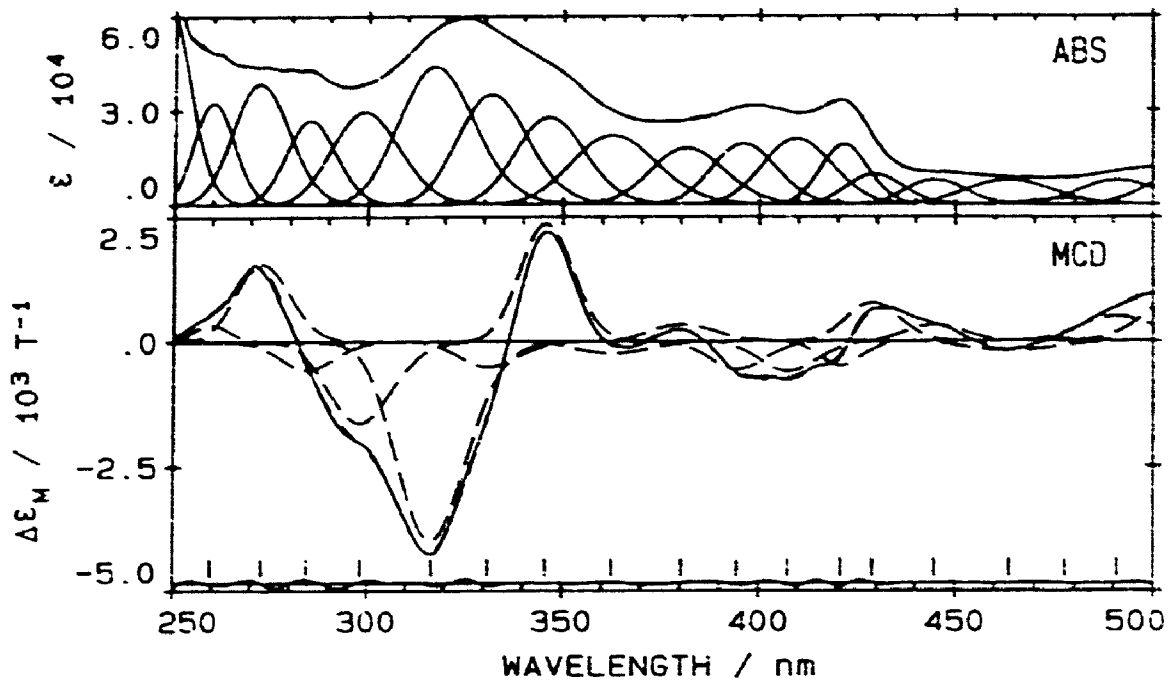

Figure 7–11 Results of a band analysis on the 77 K absorption and 4 K MCD spectra for 1 mm glasses of $Na[(CN)_2Fe(III)Pc(-2)]$ in the ultraviolet region (bands 25–44). (a) Absorption: (———) experimental data; (– – –) fitted data; (———) individual bands. (b) MCD: (———) experimental data; (– – –) fitted data; (— —) individual bands.

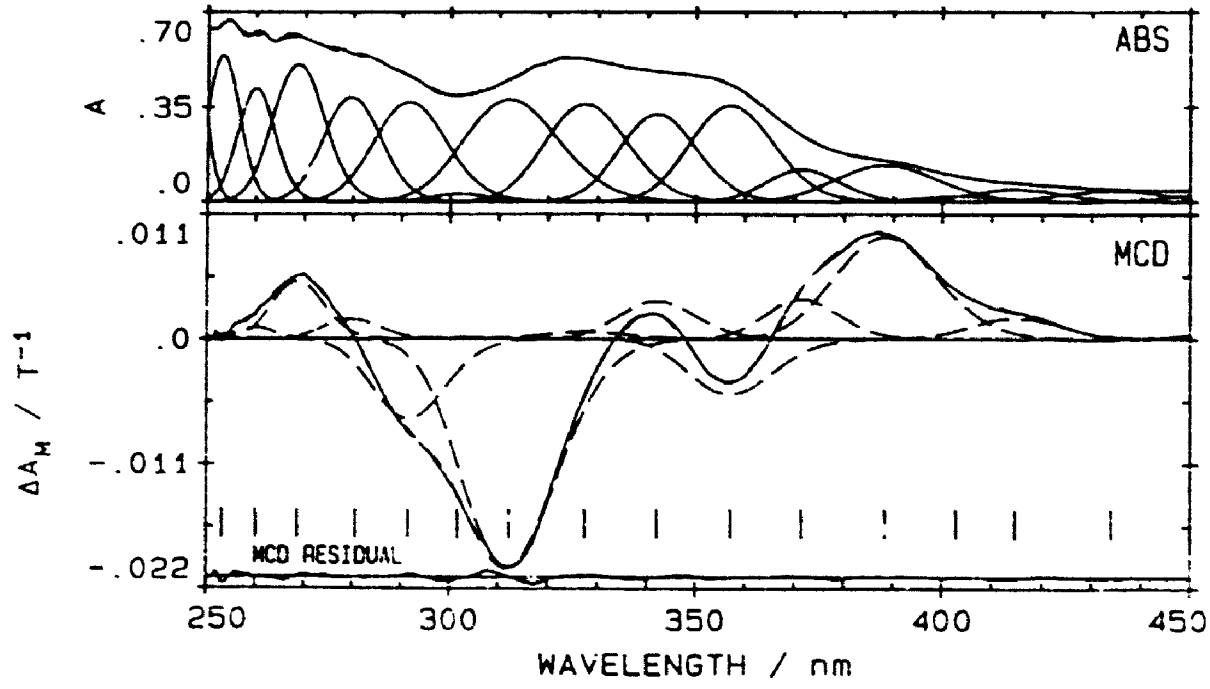

Figure 7–12 Results of a band analysis on the 77 K absorption and 4 K MCD spectra for 1 mm glasses of (meim)(Br)Fe(III)Pc(–2) in the ultraviolet region (bands 25–43). (a) Absorption: (———) experimental data; (– – –) fitted data; (———) individual bands. (b) MCD: (———) experimental data; (– – –) fitted data; (— —) individual bands.

Table 7-2
Band-Fitting Parameters[a] for Na[(CN)$_2$Fe(III)Pc(-2)] in 70:30 DCM:CB.

band #	ν /cm^{-1}	λ /nm	$\Delta\nu$ /cm^{-1}	D_0[b]	Band type	$\langle\Delta\epsilon_M\rangle_0$[c]	C_0, B_0[d] /10^{-3}	$(B_0, C_0)/D_0$
1	12508	799	240	0.147	C	3.238	21.23	0.144
2	12820	780	218	0.259	C	27.20	178.4	0.689
3	13135	761	578	0.490	C	24.41	160.0	0.327
4	13617	734	482	0.395	C	-3.197	20.96	-0.053
5	14041	712	321	0.779	C	9.808	64.31	0.083
6	14349	697	273	2.535	C	-16.16	-106.0	
7	14578	686	214	6.884	C	130.8	857.3	0.125
8	14804	675	386	1.632	C	61.86	405.6	0.249
9	15080	663	468	2.696	C	30.91	202.6	0.075
10	15505	645	361	2.929	C	-238.7	-1566.	-0.534
11	15750	635	535	1.615	C	-125.5	-823.3	-0.510
12	16069	622	436	1.799	C	-0.638	-4.181	-0.002
13	16314	613	350	0.978	C	-63.84	-418.6	-0.428
14	16641	601	420	1.587	C	-118.7	-778.6	-0.491
15	16982	589	356	0.584	C	-16.64	-109.1	-0.187
16	17298	578	578	1.156	C	-64.13	-420.6	-0.364
17	17781	562	585	1.864	C	-12.44	-81.62	-0.044
18	18179	550	429	1.141	C	38.05	249.5	0.219
19	18479	541	475	1.802	C	60.32	395.6	0.220
20	18906	529	534	1.022	C	18.89	123.8	0.121
21	19505	513	1021	2.117	C	66.45	435.7	0.206
22	20382	491	939	1.206	C	37.06	243.0	0.201
23	20939	478	832	0.411	C	-3.731	-244.6	-0.595
24	21574	464	1174	1.405	C	-13.45	-88.15	-0.063
25	22483	445	883	1.016	C	16.69	109.5	0.108
26	23313	429	869	1.224	C	37.53	246.1	0.201
27	23764	421	707	2.106	C	-19.21	-126.0	-0.060
28	24546	407	1034	3.449	C	-33.27	-218.2	-0.063
29	25349	394	1063	3.040	C	-30.77	-201.8	-0.066
30	26292	380	1325	3.356	C	22.18	145.5	0.043
31	27586	363	1621	4.975	C	-18.68	-122.6	-0.025
32	28912	346	1299	5.313	C	138.3	906.5	0.171
33	30187	331	1592	7.192	C	-35.33	-231.6	-0.032
34	31572	317	2072	10.19	C	-342.2	-2244.	-0.220
35	33534	298	2138	6.538	C	-135.7	-889.6	-0.136
36	35156	284	1967	4.577	C	-42.07	-275.9	-0.060
37	36649	273	2180	7.834	C	121.0	793.6	0.094
38	38513	260	1568	4.924	C	18.39	120.6	0.024
39	40255	248	2082	10.65	C	6.299	41.30	0.004

[a]Statistics. B region: $\lambda_{245-520\ nm}$, χ^2=48.16, $\Sigma(\Delta\epsilon)^2$=2.36×10^6. Q region: $\lambda_{470-800\ nm}$, χ^2=133.1, $\Sigma(\Delta\epsilon)^2$=8.09×10^6 [b]$D_0=\langle\epsilon\rangle_0/326.6$, where the units of D_0 (dipole strength) are D^2 (Debye units) [25]. [c]$\langle\Delta\epsilon_M\rangle_0$ is the zeroth moment of the MCD. When fitting with B and C terms the program calculates $\langle\Delta\epsilon_M\rangle_0$. [d]The Faraday term values, C_0 and B_0, are calculated directly from the moments as follows: $B_0, C_0=\langle\Delta\epsilon_M\rangle_0$.

1.0 volt variability in $E_{\frac{1}{2}}$ can be explained by studying the Nicholson-Shain (NS) plots of $L_2Fe(II)Pc(-2)$ [42,149-151]. Analysis of the NS plots indicates that metal oxidation (equation 7-1) is followed by a ligand exchange (equation 7-2). The π donor/acceptor properties of the axial ligands influences the ease of oxidation, while the ferric oxidation state is stabilized by axial ligation of a counterion.

$$L_2Fe(III)Pc(-2) \longrightarrow [L_2Fe(III)Pc(-2)]^+ + e^- \quad (7-1)$$

$$[L_2Fe(III)Pc(-2)]^+ + X^- \longrightarrow L(X)Fe(III)Pc(-2) + e^- \quad (7-2)$$

L(X)Fe(III)Pc(-2) can be obtained by chemical oxidation of $L_2Fe(II)Pc(-2)$ [103,125,146,150], and by addition of basic ligands to the intermediate spin (Cl)Fe(III)Pc(-2) complex [147,148]. The results obtained from the addition of basic ligands to intermediate spin (Cl)Fe(III)Pc(-2) (Chapter 8) agree with the electrochemical studies [42,149,150]. The negatively charged counterion (X^-) which is positioned *trans* to a basic ligand (L) stabilizes the ferric oxidation state. The absorption spectrum reported for five coordinate pyridinoiron(II) phthalocyanine [146] has a spectral envelope consistent with the III, not II oxidation state. Exchange of an axial pyridine ligand with free chloride in the chlorinated solvent results in a negative shift in the $E_{\frac{1}{2}}$ value of the Fe(II)/Fe(III) couple and a spontaneous metal oxidation.

The absorption spectrum for (py)(Cl)Fe(III)Pc(-2) [146] demonstrate the usefulness of UV-visible spectroscopy in studying the redox chemistry of iron phthalocyanine. Although there are a variety of absorption spectra reported for low spin L(X)Fe(III)Pc(-2) complexes [35,103,125,146,150], there are a very limited number of available MCD spectra. The greater resolution and detail of an MCD spectrum, compared to the absorption spectrum, makes it a better technique to probe the electronic arrangement within L(X)Fe(III)Pc(-2). With the lack of available MCD spectra, the results obtained for the isoelectronic Mn(II)Pc(-2) [23,35,152] species are useful in the analysis of the MCD spectra reported here for L(X)Fe(III)Pc(-2).

7.3.1 Assignment of the Electronic Ground State in L(X)Fe(III)Pc(−2)

Low (S=1/2) or intermediate (S=3/2) spin states are possible for the E_g ground state of the ferric ion. Analysis of low temperature, matrix isolated MCD spectra of Mn(II)Pc(−2) [152] determined that the ground state was $^4E_g(e_g{}^3b_{2g}a_{1g})$. The spin state for L(X)Fe(III)Pc(−2) may differ from intermediate spin (S=3/2) Mn(II)Pc(−2) because of the different conditions that the MCD spectra were measured under. Spectral measurements on Mn(II)Pc(−2) were performed in an argon matrix where the manganese ion is square planar, while the spectral measurements on [Fe(III)Pc(−2)]+ were performed on low temperature glasses where the ferric ion is expected to be octahedrally coordinated. The crystal structure of [PNP][$(CN)_2$Fe(III)Pc(−2)] (PNP=bis(triphenylphosphine)iminium) [119] verifies the octahedral structure for iron(III) phthalocyanine bound to axial cyanide (CN^-) ligands. The ferric ion is located in the plane of the Pc(−2) ring, with axial Fe–C and equatorial Fe–N bond distances of 1.90 Å and 1.941 Å, respectively.

The different structural arrangements in L(X)Fe(III)Pc(−2) and Mn(II)Pc(−2) will affect the location and the energies of the 3d orbitals. The influence of octahedral (O_h) and tetragonal (D_{4h}) fields on the metal 3d shell are illustrated in Figure 7–13. The positioning of the orbitals under a weak tetragonal field is the accepted order for low spin L_2Fe(II)Pc(−2) complexes [117,118,153]. The assignment of the $^4E_g(e_g{}^3b_{2g}a_{1g})$ ground state to Mn(II)Pc(−2) indicates a cross–over in the e_g and the b_{2g} orbital energies, shown in Figure 7–13, under the strong tetragonal distortion expected for a square planar complex. The ferric ion in L(X)Fe(III)Pc(−2) is expected to retain the orbital arrangement featured in Figure 7–13, due to the weak tetragonal distortion. The two lowest lying orbitally degenerate spin states available for L(X)Fe(III)Pc(−2) are $^2E_g(b_{2g}{}^2e_g{}^3)$ and $^4E_g(b_{2g}{}^2e_ga_{1g}b_{1g})$. The energy separation between the e_g, and the a_{1g} and b_{1g} orbitals is not expected to vary significantly between low spin Na_2[$(CN)_2$Fe(II)Pc(−2)] (Chapter 6) and Na[$(CN)_2$Fe(III)Pc(−2)],

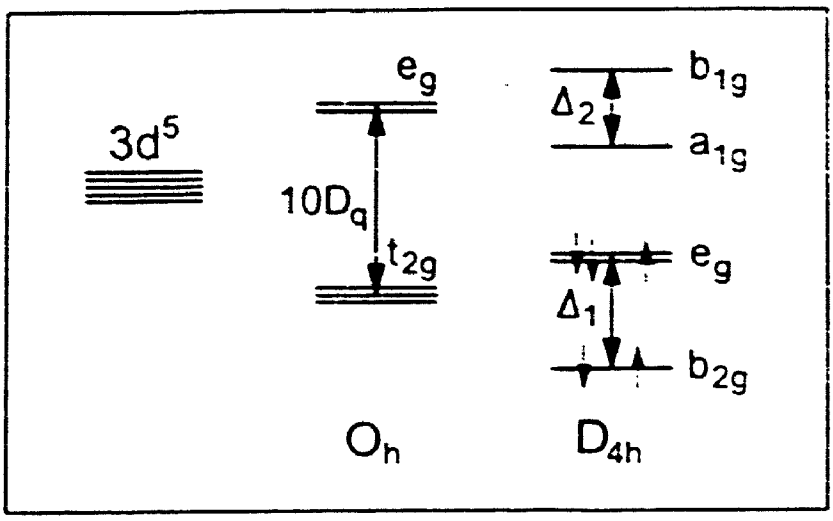

Figure 7-13 The energy level splitting for metal 3d orbitals under a ligand field with octahedral ($10D_q$) and axial (Δ_1,Δ_2) distortions.

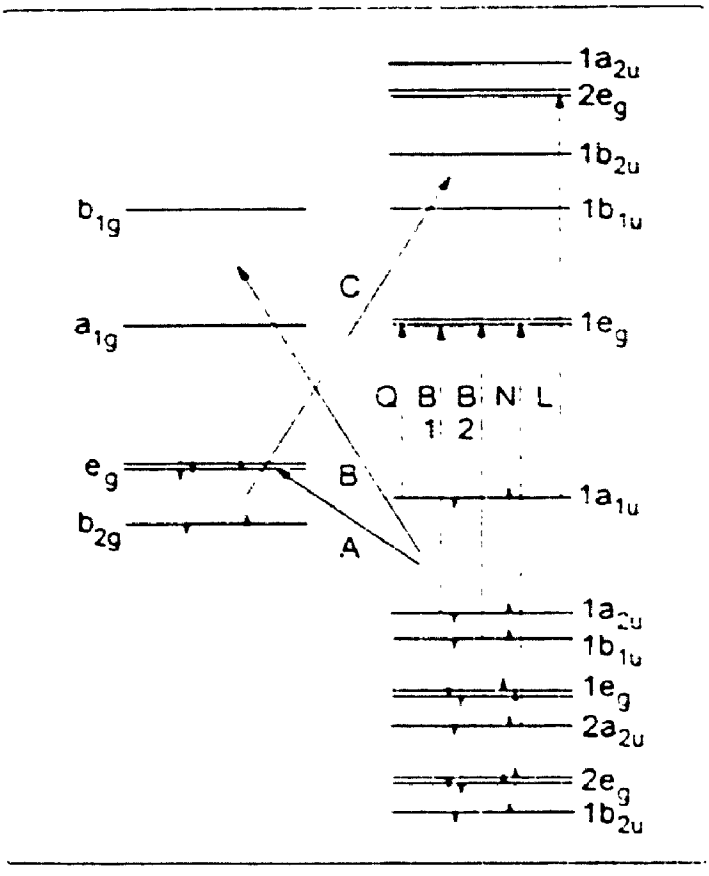

Figure 7-14 Selected molecular orbitals for the ^2E_g ground state of L(X)Fe(III)Pc(-2). The A, B and C labelled arrows represent the allowed: $a_{iu},b_{iu}(\pi) \rightarrow e_g(d)$; $a_{iu},b_{iu}(\pi) \rightarrow a_{1g},b_{1g}(d)$; and $e_g,b_{2g}(d) \rightarrow a_{2u},b_{iu}(\pi^*)$ CT transitions, respectively.

therefore the ground state is assigned as low spin $^2E_g(b_{2g}{}^2e_g{}^3)$. The g factors of 3.08 ± 0.04 for $Na[(CN)_2Fe(III)Pc(-2)]$ and 3.21 ± 0.04 for (meim)(Br)Fe(III)Pc(-2), obtained from low temperature MCD spectral analysis, and the $g_{||}$=2.03 and $g_{\perp}$=1.87 values reported for the EPR spectra of iron(III) tetracarbonylphthalocyanine [147] are consistent with a low spin (S=1/2) ^2E_g ground state.

7.3.2 Allowed Electronic Transitions for Low Spin (S=1/2) L(X)Fe(III)Pc(-2)

Figure 7-14 illustrates specific molecular orbitals of the 18-π-electron system of the phthalocyanine ring and the 3d orbitals of iron. The arrows in Figure 7-14 represent allowed transitions from the ^2E_g ground state. In addition to the five major ring based transitions, the Q, B1, B2, N and L bands, there are a significant number of allowed LMCT and MLCT transitions. The allowed charge transfer transitions, the direction of charge transfer and the transition polarization are listed in Table 7-3.

Depending on the transition polarization, two types of C terms will contribute to the MCD spectral envelopes. Figure 7-15A displays xy (E_u) polarized transitions from the degenerate ground state into nondegenerate excited states. The Q, B1, B2, N and

Table 7-3
Allowed charge transfer transition for low spin (S=1/2) L(X)Fe(III)Pc(-2)[a].

One Electron Transition	Excited State[c]	Charge Transfer	Polarization of Transition	MCD Term Expected[b]
$a_{1u}, a_{2u} \rightarrow a_{1g}, b_{1g}$	^2E_u	L → M	Z	C_B
$b_{1u}, b_{2u} \rightarrow a_{1g}, b_{1g}$	^2E_u	L → M	Z	C_B
$a_{1u} \rightarrow e_g$	$^2A_{1u}$	L → M	XY	C_A
$a_{2u} \rightarrow e_g$	$^2A_{2u}$	L → M	XY	C_A
$b_{1u} \rightarrow e_g$	$^2B_{1u}$	L → M	XY	C_A
$b_{2u} \rightarrow e_g$	$^2B_{2u}$	L → M	XY	C_A
$b_{1g} \rightarrow b_{1u}, b_{2u}$	^2E_u	M → L	Z	C_B
$e_g \rightarrow b_{1u}$	$^2A_{iu}$, $^2B_{iu}$	M → L	XY	C_A
$e_g \rightarrow b_{2u}$	$^2A_{iu}$, $^2B_{iu}$	M → L	XY	C_A

[a]The ground state electronic configuration of the iron 3d orbitals is $(b_{2g})^2(e_g)^3$ and the symmetry of the ground state is ^2E_g. [b]The subscripts A and B denote that the transitions are xy and z polarized, respectively. [c]i=1,2.

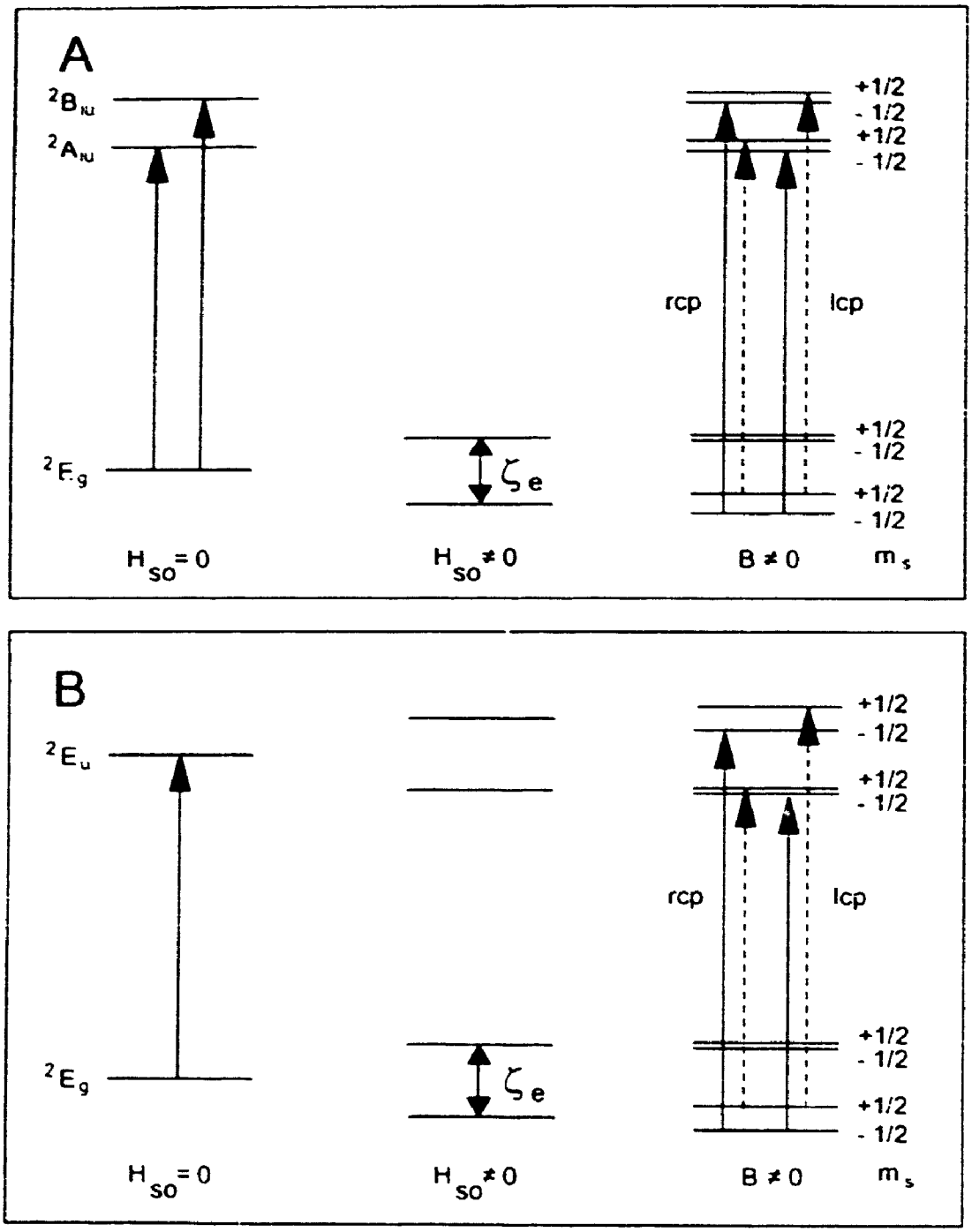

Figure 7-15 Energy level diagrams for **(A)** the $^2E_g \rightarrow {}^2A_{iu}, {}^2B_{iu}$ (i=1,2) transitions and **(B)** the $^2E_g \rightarrow {}^2E_u$ transitions. The Zeeman ($H_{so} \neq 0$) and the spin orbit (ζ_e) splittings are highly exaggerated with respect to the energy separation between electronic states. Right circularly polarized (rcp) and left circularly polarized (lcp) transitions for the lowest energy ground state Kramers doublet are plotted. The solid arrows represents the transitions expected when the MCD signal saturates, while the dashed arrows represent the additional transition that occur when the MCD signal is not saturated.

L bands, the MLCT1 and MLCT2 bands, and certain LMCT bands are xy polarized. Spin-orbit coupling (H_{so}) splits the ^2E_g ground state into two Kramers doublets. The solid arrows in Figure 7-15A, for an applied magnetic field (B≠0), represent the allowed transitions when the ground state is saturated. A single electronic transition is allowed between the ground and excited states, with the difference in the magnetic moment determining the sign (+) or (-) of the MCD signal. The MCD C terms arising from xy polarized transitions will be denoted as C_A terms, where the A subscript denotes the xy transition polarization.

Both the ground and excited states in Figure 7-15B are orbitally degenerate and the electronic transition is z (A_{2u}) polarized. Several of the LMCT and MLCT transitions listed in Table 7-3 are z polarized. Because spin-orbit coupling splits the ground and excited states into pairs of Kramers doublets, a z polarized transition will consist of individual transitions into each excited state Kramers doublet. The matrix isolation study of Mn(II)Pc(-2) [152] determined the spin-orbit coupling parameter (ζ) to be about 300 cm^{-1}. Since the Zeeman splittings are very small compared to the spin-orbit splitting, ζ approximates the energy separation between the two transitions that make up a z polarized band. The two transitions will be identified as oppositely signed MCD C terms and are labelled C_{B+} and C_{B-}, with B denoting the z polarization of the transition and the +/- labels indicating the sign of the MCD signal.

7.3.3 Assignment of the Low Temperature Absorption and MCD Spectral Fits for Na[(CN)$_2$Fe(III)Pc(-2)]

The deconvoluted fits presented in this chapter are the first such calculations on an open shell metallophthalocyanine with a degenerate ground state. The large number of bands (39) required to fit the 250 to 900 nm region of the absorption and MCD spectra for Na[(CN)$_2$Fe(III)Pc(-2)] makes the task of assigning specific bands to ring ($\pi \rightarrow \pi^*$), MLCT ($d \rightarrow \pi$) and LMCT ($\pi \rightarrow d$) transitions difficult. The spectral

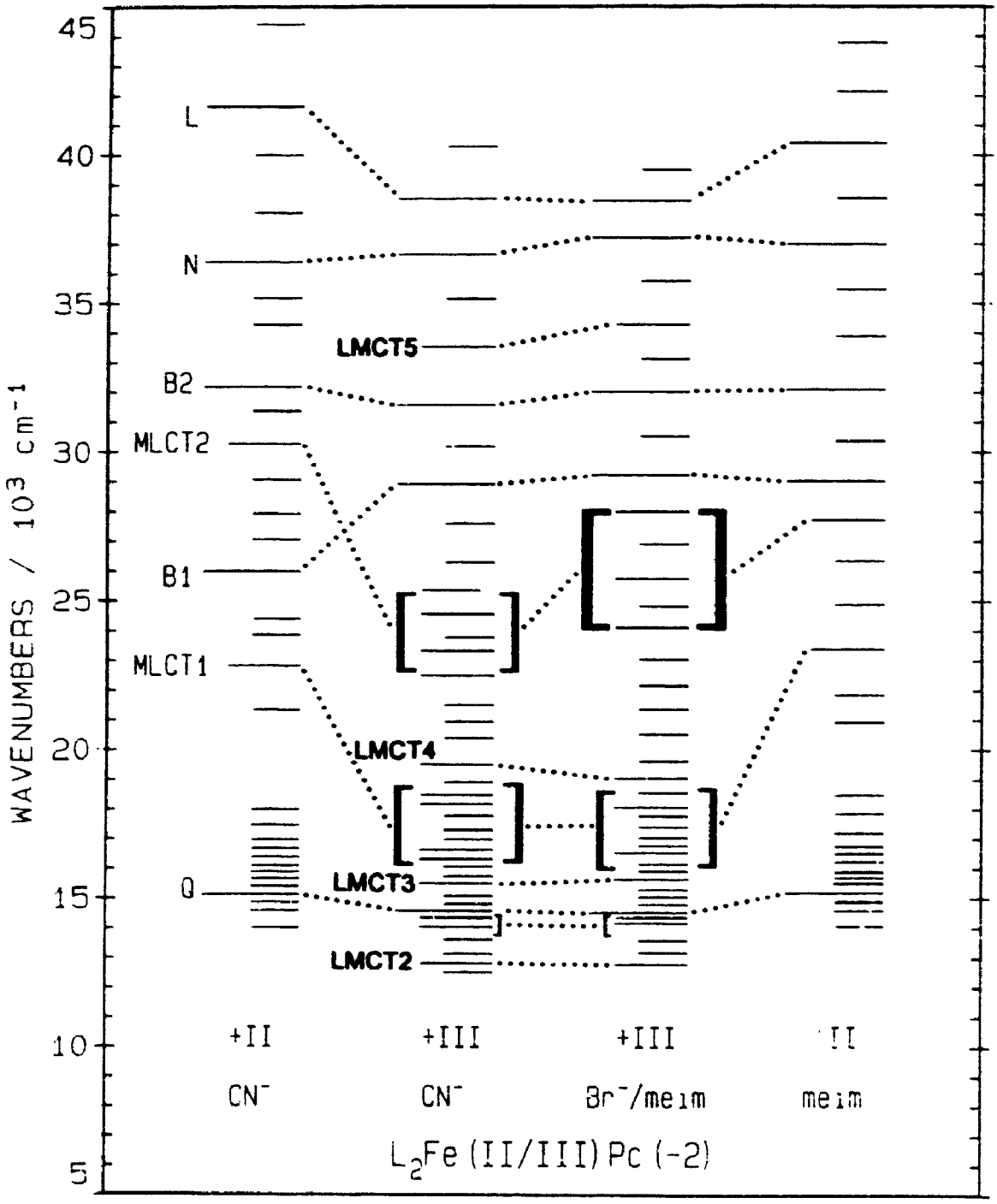

Figure 7-16 Comparison of the fitted band centre energies for $Na[(CN)_2Fe(III)Pc(-2)]$, $Na_2[(CN)_2Fe(II)Pc(-2)]$ (Chapter 6), (meim)(Br)Fe(III)Pc(-2) and $(meim)_2Fe(II)Pc(-2)$ (Chapter 6). The line lengths are: long for ring transitions, intermediate for CT transitions and small for unassigned transitions.

fits for $L_2MgPc(-2)$ [27] and $L_2Fe(II)Pc(-2)$ (Chapter 6) are invaluable in the identification of the $\pi \rightarrow \pi^*$ and the MLCT transitions. Figure 7-16 displays the fitted band centre energies for $Na_2[(CN)_2Fe(II)Pc(-2)]$ (Chapter 6) and for $Na[(CN)_2Fe(III)Pc(-2)]$. The spectral assignments for the absorption and MCD spectra of $Na[(CN)_2Fe(III)Pc(-2)]$ are summarized in Table 7-4.

7.3.3.1 The Q, B1, B2, N and L bands

The absorption band centred at 686 nm (14 578 cm^{-1}) is assigned as the Q band. The B1, B2, N and L bands are more difficult to locate because CT bands overlap and camouflage their exact locations within the spectral envelopes. The positions of these four transitions can be determined by understanding the effect of Fe(III) on the Pc(-2) π and π^* orbitals and by predicting the sign of the MCD C_A terms. The removal of an $e_g(d\pi)$ electron results in a deficiency at the iron core, which is partially compensated for by the removal of electron density from the axial CN^- and equatorial Pc(-2) ligands (Figure 7-17). The π donor/acceptor properties of Pc(-2) are chameleon-like and it is not difficult to predict a shift from π acceptor to π donor with ferrous to ferric oxidation. The spectral changes due to the withdrawal of π electron density from the Pc(-2) ring are expected to resemble those observed in phthalocyanine π-cation radicals [2,26,28,35] and those observed in $(NH_3)(CO)Fe(II)Pc(-2)$ (Chapter 6), where the strong π acceptor CO pulls electron density away from the Pc(-2) ring. Using the spectral results for $[MgPc(-1)]^{\cdot+}$ (Chapter 5) and $(NH_3)(CO)Fe(II)Pc(-2)$ (Chapter 6) as templates, the following spectral changes are expected for $Na[(CN)_2Fe(III)Pc(-2)]$: (i) the energy separation between the B1/B2 and N/L band pairs will be reduced, (ii) the changes in the energies of the B2, N and L bands will be small, and (iii) the B1 band will shift to a higher energy. These trends plus the predicted signs of the MCD bands are employed in the assignment.

For an E_g ground state, the ground and excited state symmetries determine the sign of the MCD C_A terms [25,152]. The electronic transitions with $^2A_{1u}$ (Q and L) and $^2A_{2u}$ (B1 and L) excited states have MCD C_A terms whose signs are opposite to those with $^2B_{1u}$ (B2) and $^2B_{2u}$ excited states. The (+) MCD C_A term assigned to the Q band indicates that the B1, N and L transitions will have (+) C_A terms, while the B2 band will have a (−) C_A term. The bands at 346 nm (28 912 cm^{-1}) (+), 317 nm (31 572 cm^{-1}) (−), 273 nm (36 649 cm^{-1}) (+) and 260 nm (38 513 cm^{-1}) (+) are assigned as B1, B2, N and L, respectively. This assignment is consistent with the expected changes in the transition energies following metal oxidation and with the predicted signs of the MCD C terms.

7.3.3.2 Degenerate Charge Transfer Bands

From Figure 7-14 and Table 7-3, we find that there are seven allowed charge transfer transitions that will have MCD C_A terms. Since the excited states for the $e_g(d\pi) \rightarrow 1b_{1u}(\pi^*)$ (MLCT1) and the $e_g(d\pi) \rightarrow 1b_{2u}(\pi^*)$ (MLCT2) transitions split into

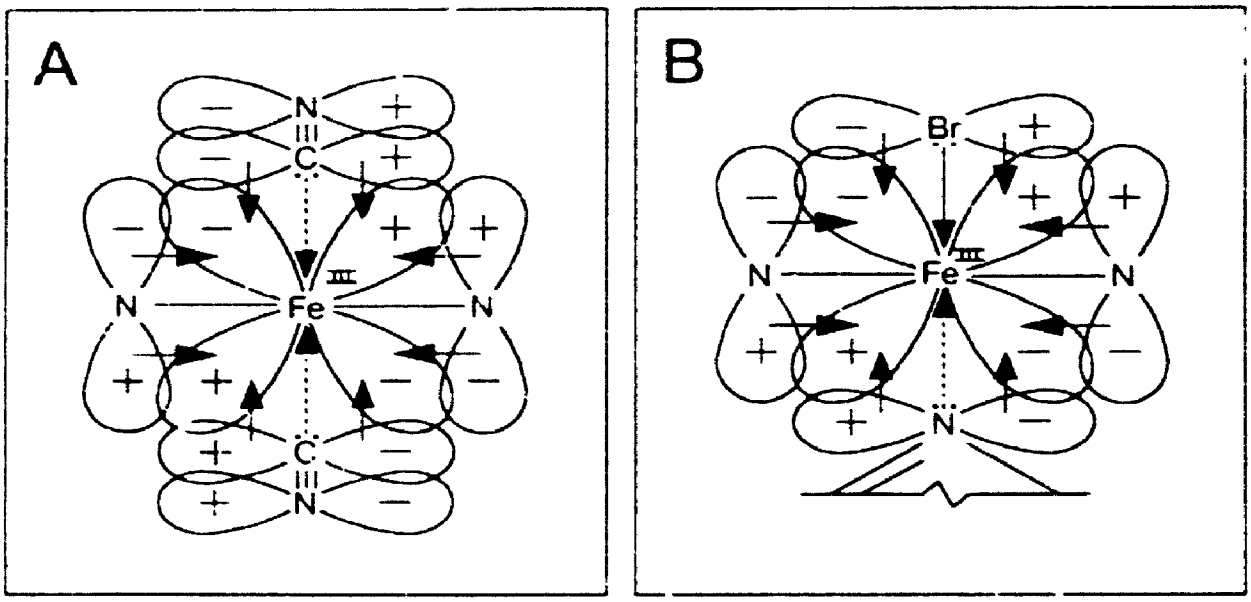

Figure 7-17 Selected overlapping iron ($d\pi$) and ligand (π and π^*) molecular orbitals in **(A)** $Na[(CN)_2Fe(III)Pc(-2)]$ and **(B)** (meim)(Br)Fe(III)Pc(−2). The arrows represent the direction of electron donation.

the four states with $^2A_{1u}$, $^2A_{2u}$, $^2B_{1u}$ and $^2B_{2u}$ symmetries [using group theory, e_g^2 breaks down into the four irreducible representations: a_{1u}, a_{2u},b_{1u}, b_{2u}], the associated MCD signal will consist of four C_A terms. The five allowed LMCT transitions $1a_{1u}(\pi) \rightarrow e_g(d\pi)$ (LMCT1), $1a_{2u}(\pi) \rightarrow e_g(d\pi)$ (LMCT2), $1b_{1u}(\pi) \rightarrow e_g(d\pi)$ (LMCT3), $2a_{2u}(\pi) \rightarrow e_g(d\pi)$ (LMCT4) and $1b_{2u}(\pi) \rightarrow e_g(d\pi)$ (LMCT5) have excited states of $^2A_{1u}$, $^2A_{2u}$, $^2B_{1u}$, $^2A_{2u}$ and $^2B_{2u}$. The expected signs of the corresponding C_A terms are: (+), (+), (−), (+) and (−), respectively.

In a study to correlate absorption spectra with the redox potentials for the Mn(II)Pc(−2) molecule [23], the $e_g(d\pi) \rightarrow 1b_{1u}(\pi^*)$ MLCT transition was predicted to be near 635 nm (15 725 cm^{-1}). To minimize any confusion over the labelling of charge transfer transitions in this chapter, we note here that our labels vary from those used by Lever et al. [23], in that they assign the parity-forbidden $e_g(d\pi) \rightarrow e_g(\pi^*)$ transition as MLCT1 and the allowed $e_g(d\pi) \rightarrow 1b_{1u}(\pi^*)$ transition as LMCT2, while in this study we assign the two allowed $e_g(d\pi) \rightarrow 1b_{1u}(\pi^*)$ and $e_g(d\pi) \rightarrow 1b_{2u}(\pi^*)$ transitions as MLCT1 and MLCT2. The four transitions at 613 nm (16 314 cm^{-1}) (−), 601 nm (16 641 cm^{-1}) (−), 550 nm (18 179 cm^{-1}) (+) and 541 nm (18 479cm^{-1}) (+), in the spectra of $Na[(CN)_2Fe(III)Pc(-2)]$, are close to the predicted energies of the LMCT1 bands in the Mn(II)Pc(−2) spectra [23,152]. The presence of two (+) and two (−) signed C_A terms is consistent with the assignment of the four bands as LMCT1. The location of the MLCT2 band, in the spectrum of $Na[(CN)_2Fe(III)Pc(-2)]$ is expected to be around 400 nm. The four MCD C_A terms at 445 nm (22 483 cm^{-1}) (+), 429 nm (23 313 cm^{-1}) (+), 407 nm (24 546 cm^{-1}) (−) and 394 nm (25 349 cm^{-1}) (−) are tentatively assigned to the LMCT2 transition.

The (+) C_A term at 780 nm (12 820 cm^{-1}) represents either the LMCT1 or the LMCT2 band. The predicted locations of the LMCT1 and LMCT2 bands in Mn(II)Pc(−2) spectra, based on redox potentials, are 911 nm (10 970 cm^{-1}) for MLCT1 and 381 nm (26 180 cm^{-1}) for LMCT2 [23]. On the basis of these results

the 780 nm band is assigned as LMCT1. This assignment is not consistent with the absorption spectrum reported for low spin iron(III) tetracarbonylphthalocyanine [147] in which two weak charge transfer bands were located at 1100 and 1200 nm. If the 780 nm band is LMCT1, then these CT bands should not be present, because we do not expect to see charge transfer bands with energies lower than the LMCT1 transition. A major difficulty in attempting to correlate spectral band positions with redox potentials is that configuration interaction, which can have a pronounced effect on the energies of electronic transitions, is ignored. The spectral results indicate that configuration interaction does have a significant influence on the energies of the MLCT transitions and the 780 nm band is reassigned as MLCT2. The location of the MLCT1 band is somewhere beyond the 900 nm spectral cutoff.

The 500 to 690 nm MCD spectral region is difficult to interpret because in addition to the Q_{00} and Q_{vib} bands, which typically extend across a 3000 cm^{-1} energy range in metallophthalocyanines, LMCT bands are also expected. Ignoring configuration interaction, the 2600 cm^{-1} gap between the B1 and B2 bands and the location of the LMCT2 band at 780 nm suggest that the LMCT3 band will overlap the Q_{vib} manifold around 650 nm (15 385 cm^{-1}). The large (-) MCD C_A term at 645 nm (15 505 cm^{-1}) is in the appropriate location, has the correct sign, and is assigned as LMCT3. The large C_0/D_0 ratio (-0.534; Table 7-2) for LMCT3 may be attributed to intensity borrowing from the Q_{vib} manifold. The LMCT4 band is expected around 520 nm and is assigned to the (+) MCD C_A term at 513 nm (19 505 cm^{-1}). The energy separation (≈13 500 cm^{-1}) between the N and C bands, based on the general location of the C band, in the vapour phase absorption spectra of various metallophthalocyanines [65], at 200 nm (50 000 cm^{-1}), approximates the energy separation between the MLCT4 and MLCT5 bands and places the MLCT5 band around 300 nm (33 333 cm^{-1}). The (-) C_A term at 298 nm (33 534 cm^{-1}) is assigned as LMCT5.

7.3.3.3 Nondegenerate Charge Transfer Bands

Although Table 7-3 lists several z polarized charge transfer transitions, only one set of C_B terms was isolated from the MCD spectrum. The two oppositely signed C terms at 697 nm (14 349 cm^{-1}) (+) and 712 nm (14 041 cm^{-1}) (−) have an energy separation of 308 cm^{-1} which matches the spin-orbit coupling parameter (ζ). These two bands are MCD C_{B+} and C_{B-} terms and based of their locations they represent either the $1a_{1u}(\pi) \rightarrow a_{1g}(d^*)$ (LMCT7) or the $1a_{1u}(\pi) \rightarrow b_{1g}(d^*)$ (LMCT8) transition. At this time, we believe that the absorption bands reported at 1100 and 1200 nm for iron(III) tetracarbonylphthalocyanine [147] are the spin-orbit split components of the LMCT7 transition. The 697 and 712 nm bands are therefore assigned as LMCT8.

7.3.4 Assignment of the Low Temperature Absorbance and MCD Spectral Fits for (meim)(Br)Fe(III)Pc(−2)

The band centre energies obtained from deconvolution of the absorption and MCD spectra for (meim)(Br)Fe(III)Pc(−2) are plotted against those obtained for $(meim)_2$Fe(II)Pc(−2) (Chapter 6), in Figure 7-16. The assignments of the bands that comprise the spectra for (meim)(Br)Fe(III)Fc(−2) are summarized in Table 7-5. The presence of single (+) and (−) C_A terms for the MLCT1 transition and the greater MCD intensity when compared to the same transition in $Na[(CN)_2Fe(III)Pc(-2)]$, indicates that the energy separation between the $^2A_{1u}$ and $^2A_{2u}$ excited states, which are (+) C_A terms, and the $^2B_{1u}$ and $^2B_{2u}$ excited states, which are (−) C_A terms, is negligible and the MCD intensities represent the sum of the respective pairs of transitions. The weakness of the MCD spectral intensity for the B1 band arises from the overlap of the hidden (−) C_A term of the MLCT2 band.

Table 7-4
Assigned transitions for the absorption and MCD spectra of $Na[(CN)_2Fe(III)Pc(-2)]$.

Band	One Electron Transition	Excited State	C Term Sign	λ /nm	ν /cm⁻¹
Q	$1a_{1u}(\pi) \rightarrow 1e_g(\pi^*)$	$^2A_{1u}$	+	686	14578
B1	$1a_{2u}(\pi) \rightarrow 1e_g(\pi^*)$	$^2A_{2u}$	+	346	28912
B2	$1b_{1u}(\pi) \rightarrow 1e_g(\pi^*)$	$^2B_{1u}$	-	317	31572
N	$2a_{2u}(\pi) \rightarrow 1e_g(\pi^*)$	$^2A_{2u}$	+	273	36649
L	$1a_{1u}(\pi) \rightarrow 2e_g(\pi^*)$	$^2A_{1u}$	+	260	38513
MLCT1	$e_g(d\pi) \rightarrow 1b_{1u}(\pi^*)$	$^2B_{iu}$	-	613	16314
		$^2B_{iu}$	-	601	16641
		$^2A_{iu}$	+	550	18179
		$^2A_{iu}$	+	541	18479
MLCT2	$e_g(d\pi) \rightarrow 1b_{2u}(\pi^*)$	$^2A_{iu}$	+	445	22483
		$^2A_{iu}$	+	429	23313
		$^2B_{iu}$	-	407	24546
		$^2B_{iu}$	-	394	25349
LMCT2	$1a_{2u}(\pi) \rightarrow e_g(d\pi)$	$^2A_{2u}$	+	780	12820
LMCT3	$1b_{1u}(\pi) \rightarrow e_g(d\pi)$	$^2B_{1u}$	-	645	15505
LMCT4	$1a_{2u}(\pi) \rightarrow e_g(d\pi)$	$^2A_{2u}$	+	513	19505
LMCT5	$1b_{2u}(\pi) \rightarrow e_g(d\pi)$	$^2B_{2u}$	-	298	33534
LMCT7	$1a_{1u}(\pi) \rightarrow b_{1g}(d)$	^2E_u	-	712	14041
			+	697	14349

Table 7-5
Assigned transitions for the absorption and MCD spectra of (meim)(Br)Fe(III)Pc(-2).

Band	One Electron Transition	Excited State	C Term Sign	λ /nm	ν /cm⁻¹
Q	$1a_{1u}(\pi) \rightarrow 1e_g(\pi^*)$	$^2A_{1u}$	+	689	14524
B1	$1a_{2u}(\pi) \rightarrow 1e_g(\pi^*)$	$^2A_{2u}$	+	342	29231
B2	$1b_{1u}(\pi) \rightarrow 1e_g(\pi^*)$	$^2B_{1u}$	-	312	32024
N	$2a_{2u}(\pi) \rightarrow 1e_g(\pi^*)$	$^2A_{2u}$	+	269	37211
L	$1a_{1u}(\pi) \rightarrow 2e_g(\pi^*)$	$^2A_{1u}$	+	260	38447
MLCT1	$e_g(d\pi) \rightarrow 1b_{1u}(\pi^*)$	$^2B_{iu}$	-	605	16542
		$^2A_{iu}$	+	553	18077
MLCT2	$e_g(d\pi) \rightarrow 1b_{2u}(\pi^*)$	$^2A_{iu}$	+	415	24109
		$^2A_{iu}$	+	388	25743
		$^2B_{iu}$	-	357	28001
LMCT2	$1a_{2u}(\pi) \rightarrow e_g(d\pi)$	$^2A_{2u}$	+	782	12783
LMCT3	$1b_{1u}(\pi) \rightarrow e_g(d\pi)$	$^2B_{1u}$	-	639	15651
LMCT4	$1a_{2u}(\pi) \rightarrow e_g(d\pi)$	$^2A_{2u}$	+	525	19057
LMCT5	$1b_{2u}(\pi) \rightarrow e_g(d\pi)$	$^2B_{2u}$	-	292	34295
LMCT7	$1a_{1u}(\pi) \rightarrow b_{1g}(d)$	^2E_u	-	705	14178
			+	696	14369

7.3.5 Comparison of the Spectral Fits for Low Spin (S=1/2) L(X)Fe(III)Pc(−2) to Those for Low Spin (S=0) L_2Fe(II)Pc(−2)

The spectral differences between L_2Fe(II)Pc(−2) and L(X)Fe(III)Pc(−2) arise from the removal of an iron $e_g(d\pi)$ electron. The change in ground state symmetry, $^1A_{1g}$ in L_2Fe(II)Pc(−2) to ^2E_g in L(X)Fe(III)Pc(−2), causes an increase in the number of allowed charge transfer bands. In addition to the new charge transfer transitions into the 3/4 filled $e_g(d\pi)$ orbitals, z polarized charge transfer transitions that are formally forbidden for the $^1A_{1g}$ ground state of L_2Fe(II)Pc(−2) gain intensity. The increase in the number of fitted bands upon metal oxidation, shown in Figure 7-16, demonstrates the increased charge transfer contribution to the spectral envelope of the L(X)Fe(III)Pc(−2) complexes.

An increase in the number of allowed charge transfer transitions is not the only difference between the spectra of L_2Fe(II)Pc(−2) and L(X)Fe(III)Pc(−2). There are also significant changes in the energies of the Q, B1, L, MLCT1 and MLCT2 bands following metal oxidation. The ferrous to ferric oxidation facilitates a change in the direction of π donation between iron and the Pc(−2) ligand. Because of the vacancy in the $e_g(d\pi)$ orbitals, iron(III) removes electron density from the phthalocyanine ring. This explains the compression of the B1/B2 band pair, which is a common feature of L(CO)Fe(II)Pc(−2) spectra where the strong π acceptor CO ligand pulls electron density away from the Pc(−2) ring. The general agreement in the energies of the $\pi \rightarrow \pi^*$ transitions, for Na[$(CN)_2$Fe(III)Pc(−2)] and (meim)(Br)Fe(III)Pc(−2), verifies that the ferric state, rather than the axial ligands, has the greatest influence on their energies.

Although the ferrous to ferric oxidation dominates the spectral changes, differences in axial ligands exert a minor influence the spectral envelopes. Since axial ligation is the only adjustable quantity, the small variation in band centre energies (Figure 7-16), especially for the MLCT2 band, is attributed to axial ligand differences. Selected π and π^* orbitals in Na[(CN)Fe(III)Pc(−2)] and (meim)(Br)Fe(III)Pc(−2) are plotted in

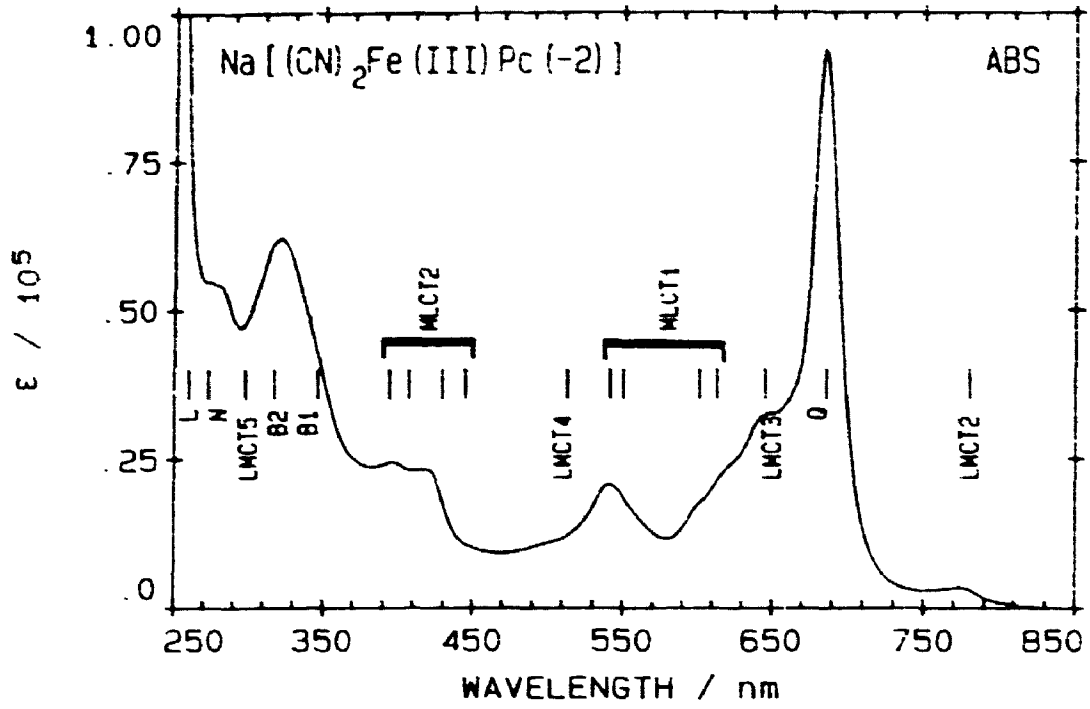

Figure 7-18 The room temperature (300 K) absorption spectra of $Na[(CN)_2Fe(III)Pc(-2)]$ in DCM. The location of the assigned $\pi \rightarrow \pi^*$, MLCT and LMCT band centres, which were obtained from deconvolution of the low temperature spectra, are represented by the labelled vertical lines.

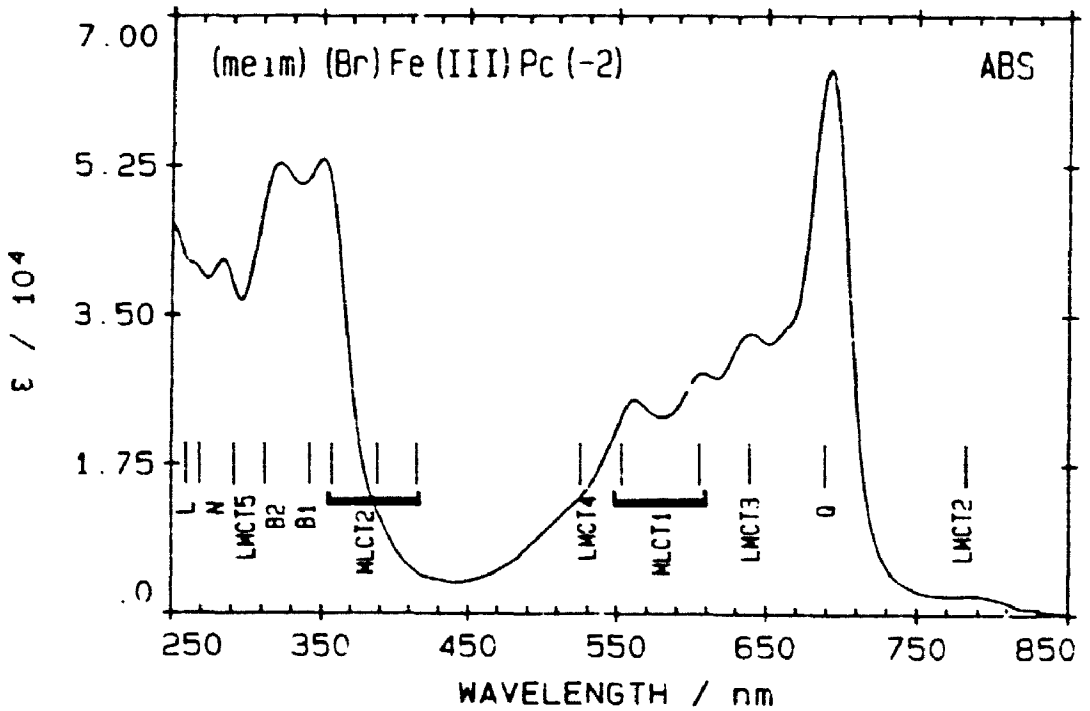

Figure 7-19 The room temperature (300 K) absorption spectra of (meim)(Br)Fe(III)Pc(-2) in DCM. The location of the assigned $\pi \rightarrow \pi^*$, MLCT and LMCT band centres, which were obtained from deconvolution of the low temperature spectra, are represented by the labelled vertical lines.

Figure 7–17. The energy separation between the MLCT2/MLCT1 and the B2/B1 band pairs for meim/Br^-, when compared to CN^-, indicates a greater axial π donation in (meim)(Br)Fe(III)Pc(−2) than in $Na[(CN)_2Fe(III)Pc(-2)]$

7.4 CONCLUSIONS

Low temperature (4 K), variable field (0 to 4 tesla) MCD spectra of metal oxidized $Na[(CN)_2Fe(III)Pc(-2)]$ and (meim)(Br)Fe(III)Pc(−2) were employed in the assignment of the ^2E_g ground state to these molecules. The average orbital g factors of 3.08 $\pm$ 0.04 for $Na[(CN)_2Fe(III)Pc(-2)]$ and 3.21 $\pm$ 0.04 for (meim)(Br)Fe(III)Pc(−2) were determined from the field dependence studies. Low temperature absorption (77 K) and MCD (4 K) spectra were subjected to spectral deconvolution calculations to determine the positions of specific $\pi \rightarrow \pi^*$, LMCT and MLCT transitions. The complete spectral analysis for $Na[(CN)_2Fe(III)Pc(-2)]$ and for (meim)(Br)Fe(III)Pc(−2) are summarized in Figures 7–18 and 7–19, respectively.

CHAPTER 8

INTERMEDIATE SPIN IRON(III) PHTHALOCYANINE

8.1 INTRODUCTION

An intriguing iron phthalocyanine (FePc) complex is formed when simple and peripherally substituted iron phthalocyanines are dissolved in non-coordinating solvents [52,125,154]. The interest in this intense green coloured complex centres on the characterization of the oxidation and spin states of the iron ion. In the literature, this complex has been assigned as intermediate spin iron(II) phthalocyanine [52], as intermediate spin iron(III) phthalocyanine [125,131,140,155] and as high spin iron(III) phthalocyanine [127,147,148]. Because it is accepted that in the solid state Fe(II)Pc(-2) is intermediate spin (S=1) [138,156,157], the first paper to report the absorption and MCD spectra of this complex assigned it as four coordinate intermediate spin iron(II) phthalocyanine [52]. A recent X-ray crystal structure [158] demonstrated that this complex is actually five coordinate square pyramidal. A study of the binding of imidazole to peripherally substituted iron phthalocyanine [147,148] assigned five coordinate chloroiron(III) octacarboxyphthalocyanine as high spin. Reported Mössbauer spectra [125,131], EPR spectra [125,127,131,147] and magnetic susceptibility measurements [125,131] agree with the assignment of the ferric oxidation state, but vary in their assignment of the spin state (high, intermediate or an admixture) of the iron phthalocyanine complex.

The relationship between the coordination number and the spin state in iron(III) phthalocyanine (low spin six cooridinate and intermediate and/or high spin five coordinate) is an interesting phenomenon. The ability to cause significant changes in the spin state, the molecular structure, and the electronic spectra of iron(III) phthalocyanine by varying the number and types of axial ligands is potentially useful in the development of artificial devices that mimic natural processes. In this chapter the

deconvolution results obtained from room temperature absorption and MCD spectra of formatoiron(III) phthalocyanine ((Fo)Fe(III)Pc(−2)) are used to assign the electronic transitions that comprise the spectral envelopes. Low temperature electron paramagnetic resonance (EPR) spectra of chloroiron(III) phthalocyanine are used to verify the oxidation and the spin state of (X)Fe(III)Pc(−2). The spectral assignment for (Fo)Fe(III)Pc(−2) is compared to the results for L_2Fe(II)Pc(−2) and L(X)Fe(III)Pc(−2) in order to study the effects of metal oxidation and axial ligand removal on these molecules spin states and electronic spectra.

8.2 RESULTS

8.2.1 Chemical Oxidation of Iron(II) Phthalocyanine

The absorption spectral changes observed during the stepwise titration of bromine (Br_2) into (NH_3)(CO)Fe(II)Pc(−2) are displayed in Figure 8−1. The lack of sharp isosbestic points indicates that more than one complex is present during the formation of (Br)Fe(III)Pc(−2). The transient that appears as the shoulder near 700 nm is located where the Q band of low spin L(X)Fe(III)Pc(−2) arises. A small amount of low spin iron(III) phthalocyanine is present during the oxidation. Ignoring the low spin component, the major changes in the spectral envelope include: (i) the Q band is blue shifted from 659 to 657 nm, (ii) a reduction in the Q band intensity, (iii) the formation of two broad, weak bands at 758 and 851 nm, (iv) a reduction in the spectral intensity between 260 and 340 nm, and (v) the formation of poorly resolved spectral intensity in the previously clear spectral window between 400 and 500 nm. The final spectrum is consistent with the absorption spectrum reported for bromoiron(III) phthalocyanine ((Br)Fe(III)Pc(−2)) [125,154].

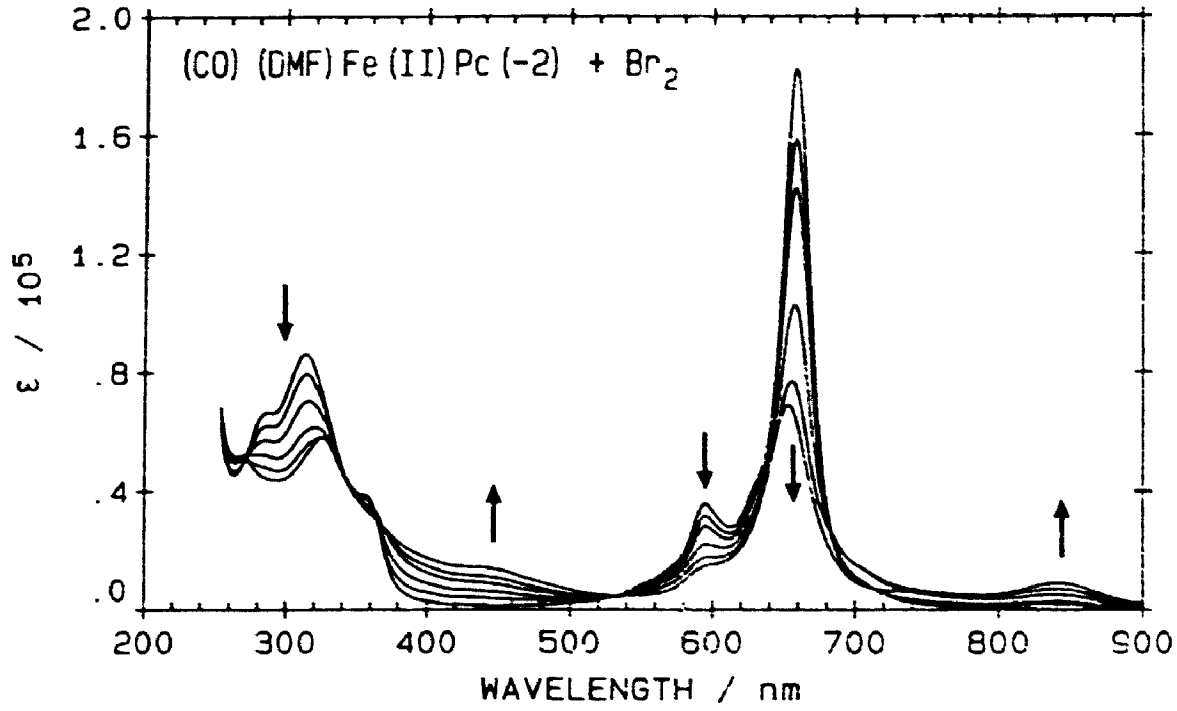

Figure 8-1 Absorption changes observed during the titration of Bromine (Br_2) into (DMA)(CO)Fe(II)Pc(-2) dissolved in 98:2 DCE:DMF. The arrows represent the spectral changes.

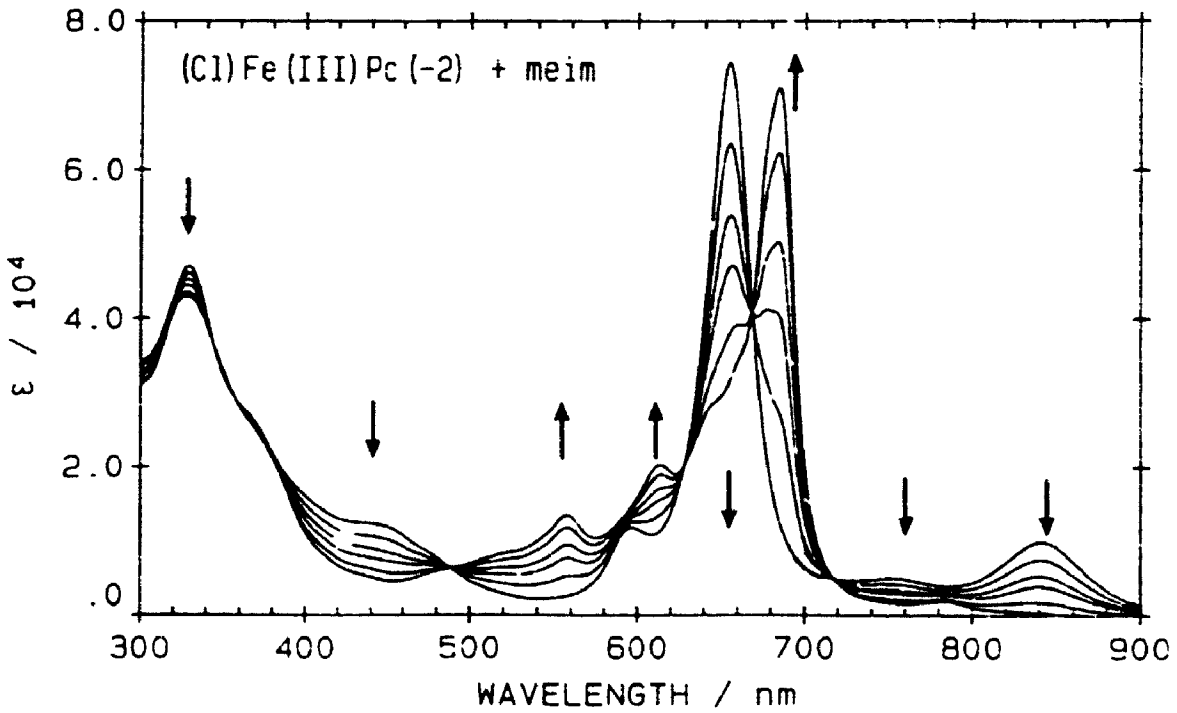

Figure 8-2 Absorption changes observed during the titration of N-methyimidazole (meim) into (Cl)Fe(III)Pc(-2) dissolved in DCB. The arrows represent the spectral changes.

8.2.2 Conversion of Intermediate Spin (S=3/2) Iron(III) Phthalocyanine to Low Spin (S=1/2) Iron(III) Phthalocyanine

Chloroiron(III) phthalocyanine ((Cl)Fe(III)Pc(−2)), which has a similar spectral envelope to the final absorption spectrum in Figure 8-1, is easily prepared by refluxing solid Fe(II)Pc(−2) in chlorinated solvents with a high boiling point. The harsh conditions are responsible for the ferrous to ferric oxidation. The results from the addition of N-methylimidazole (meim) into a solution of (Cl)Fe(III)Pc(−2) in ortho-dichlorobenzene (*o*-DCB), displayed in Figure 8-2, verifies the ferric oxidation state. As meim is titrated into the solution of (Cl)Fe(III)Pc(−2) (Figure 8-2), the absorption spectra exhibits isosbestic changes at 490, 630, 665 and 720 nm. The shape of the final absorption spectrum is typical of a low spin iron(III) phthalocyanine with: (i) weak charge transfer bands between 720 and 820 nm, (ii) the Q band at 690 nm, and (iii) a mixture of Q_{vib} and CT transitions between 450 and 680 nm. Since meim is a reducing ligand, a conversion from ferrous to ferric is unexpected upon complexation of the axial meim ligand. The absence of the 500 nm marker band, which is characteristic of ring oxidization, in the initial spectrum indicates that an internal electronic rearrangement [Fe(II)Pc(−1) → Fe(III)Pc(−2)] does not occur.

Results from the titration of hydrochloric acid (HCl) into a solution of low spin Na[(Cl)(CN)Fe(III)Pc(−2)] (Figure 8-3) also supports the ferric state in these five coordinate iron phthalocyanine complexes. Because HCl is a reducing acid, the spectral changes observed are expected to arise from either axial ligand exchange or axial ligand removal. As HCl is added, bands characteristic of low spin iron(II) phthalocyanine (Chapter 7) disappear while bands characteristic of (Cl)Fe(III)Pc(−2) form at 841, 753 and 656 nm. Sharp isosbestic points located near 480, 630, 670 and 730 nm indicate clean conversions.

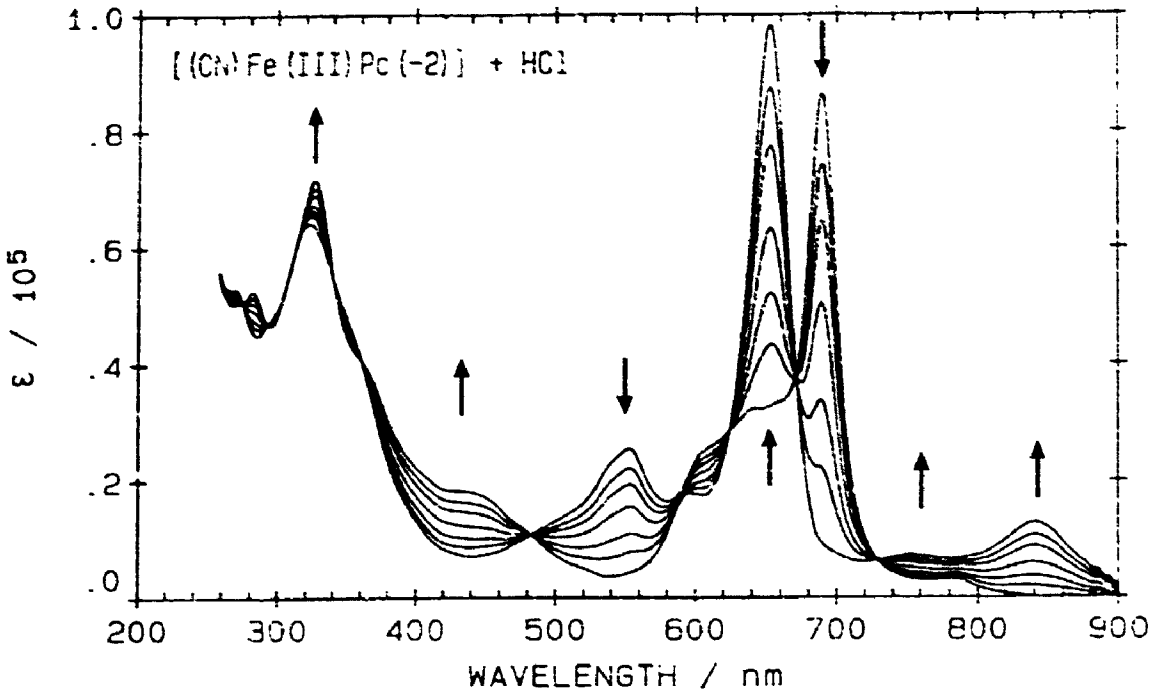

Figure 8-3 Absorption changes observed during the titration of hydrochloric acid (HCl) into Na[(CN)(Cl)Fe(III)Pc(-2)] dissolved in 98:2 DCM:DMF. The arrows represent the spectral changes.

Table 8-1
Observed maxima in the absorption spectra of the metal oxidized (X)Fe(II)Pc(-2) species in 1,2-dichlorobenzene.

(X)Fe(III)Pc(-2)	λ_{max} (nm)					
(Cl)Fe(III)Pc(-2)	841	753	656	598	330	
(Br)Fe(III)Pc(-2)	851	758	657	600	453	331
(ClO_4)Fe(III)Pc(-2)	839		652			325
(Ac)Fe(III)Pc(-2)	832		654			330
(Fo)Fe(III)Pc(-2)	842	753	656	599	446	328
(Pr)Fe(III)Pc(-2)	830		653			330
(La)Fe(III)Pc(-2)	844	755	657	599	447	330

The absorption band maxima for a series of (X)Fe(III)Pc(−2) complexes are listed in Table 8−1. Aside from a slight movement in the position of the band maxima, the shape of the spectral envelopes are consistent across the series of axial ligands.

8.2.3 Absorption and MCD Spectra

The absorption and MCD spectra of (Cl)Fe(III)Pc(−2) (Figure 8−4A) and (Fo)Fe(III)Pc(−2) (Figure 8−4B) are very distinct, when compared to the spectra of low spin L_2Fe(II)Pc(−2) (Chapter 6) and low spin L(X)Fe(III)Pc(−2) (Chapter 7). The titration results presented in Figures 8−1 to 8−3 indicate that iron is in its ferric oxidation state. Unlike the low spin iron(III) phthalocyanine complexes that were described in Chapter 7, the room temperature spectra of the (X)Fe(III)Pc(−2) complexes exhibit derivative MCD band shapes in both the Q and B regions; bands that are typical for transitions into degenerate excited states. In the 300 K MCD spectra of the low spin L(X)Fe(III)Pc(−2) complexes (Chapter 7), there is an absence of degenerate band shapes, which is to be expected for complexes with E_g ground states. The room temperature MCD spectra of (X)Fe(III)Pc(−2) indicate that the ground state for (X)Fe(III)Pc(−2) is not orbitally degenerate.

Ignoring the charge transfer regions between 400 and 500 nm, and between 700 and 900 nm, the spectra for (X)Fe(III)Pc(−2) have the appearance expected for a metalloporphyrin rather than a metallophthalocyanine. The majority of the MCD spectral intensity arises from two derivative shaped bands at 330 and 650 nm. This is similar to the dominant presence of the Q and B bands in the MCD spectra envelopes of metalloporphyrins [46]. Taking into account the different energies of the Q and B bands, the absorption and MCD spectra of (X)Fe(III)Pc(−2) are remarkably similar to the spectra of some high spin iron(III) porphyrins [159] and the spectrum of intermediate spin iron(III) tetraazaporphyrin [160].

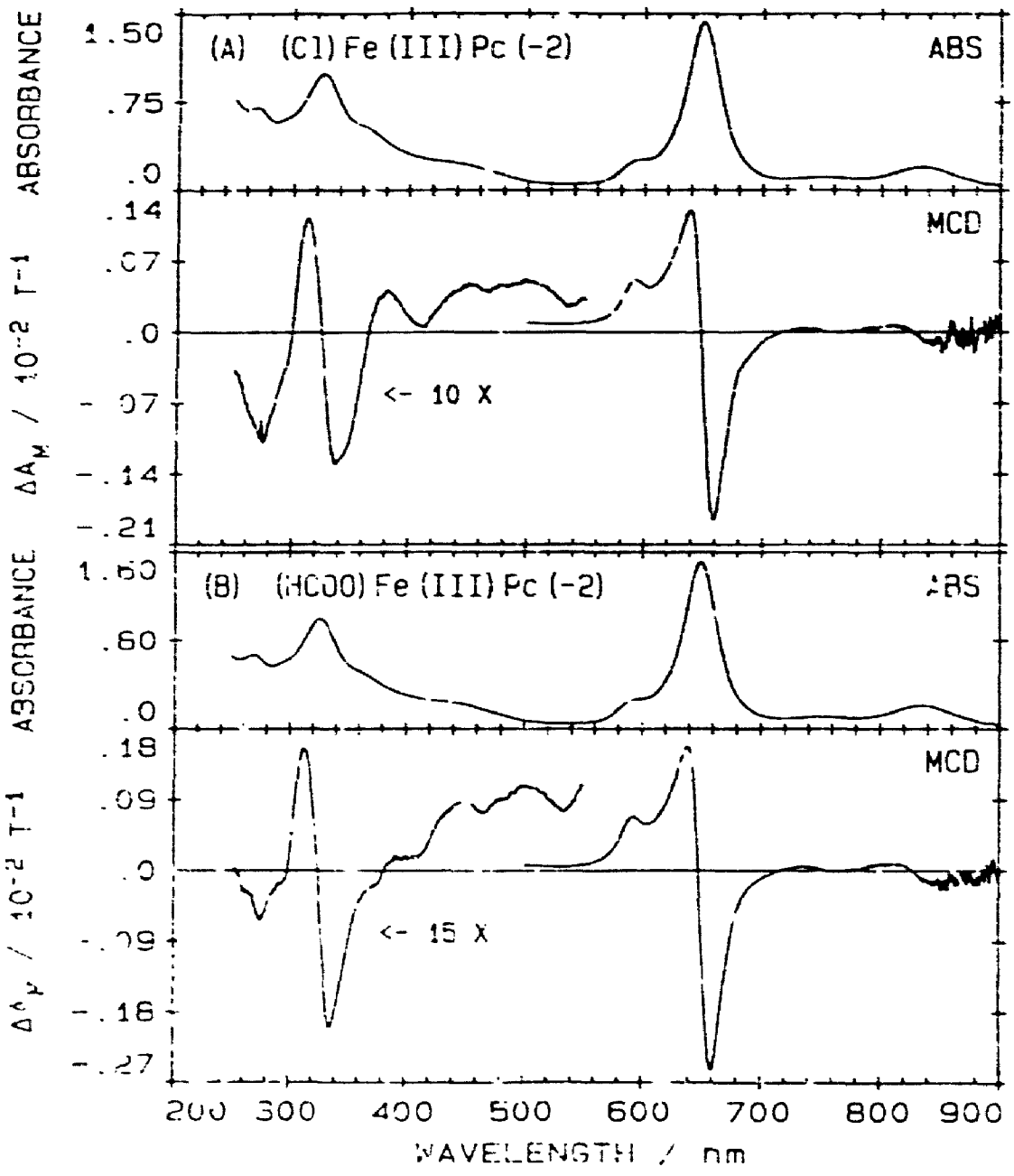

Figure 8-4 Absorption (ABS) and MCD spectra of (A) (Cl)Fe(III)Pc(-2) recorded in DCB and (B) (Formato)Fe(III)Pc(-2) recorded in DCB.

8.2.4 EPR Spectra

The low temperature (10 K) EPR spectrum of (Cl)Fe(III)Pc(−2) in a frozen solution of *o*–DCB is shown in Figure 8–5. The two EPR signals centred at 3272 and 1588 gauss have g factors of 2.074 ($g_{||}$) and 4.273 ($g_{\perp}$), respectively. Theoretical calculations on iron(III) porphyrins [161] indicate that the EPR spectra for intermediate spin complexes will have $g_{||}$ and $g_{\perp}$ values of 2 and 4, respectively. The similarity between the experimental values for (Cl)Fe(III)Pc(−2) and the predicted values for intermediate spin ferric porphyrins indicates that (Cl)Fe(III)Pc(−2) is intermediate spin. The slightly larger value for $g_{\perp}$ (4.273) may be due to a small admixture of the high spin $^6A_{2g}$ state.

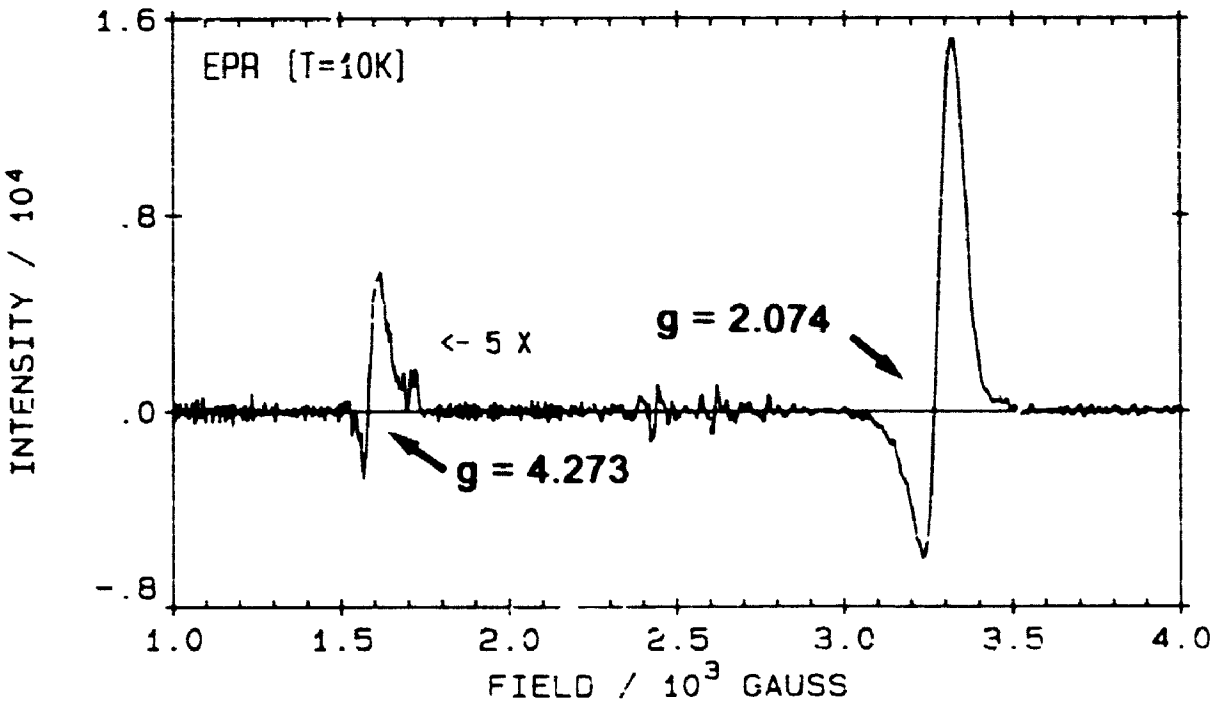

Figure 8–5 The 10 K EPR spectrum of (Cl)Fe(III)Pc(-2) dissolved in 1,2–dichlorobenzene. The values of the g factors were calculated from the absolute value of the internal standard DPPH.

8.2.5 Spectral Band Deconvolution

The derivative Gaussian shaped bands employed to fit the MCD spectra of (Fo)Fe(III)Pc(−2) are not the traditional MCD A terms. Although there is no orbital degeneracy in (Fo)Fe(III)Pc(−2), the spin degeneracy in the $^4A_{2g}$ ground state makes it impossible to exhibit "true" MCD A terms. Two temperature dependent C terms that are oppositely signed and close in energy will overlap to yield temperature dependent "pseudo" A terms (labelled as C_A terms). These C_A terms account for the fitted derivative bands in the room temperature MCD spectra.

From studies of variable temperature MCD spectra of low and high spin iron(III) porphyrins [46], it is found that the effect of varying the temperature is more pronounced for orbital degeneracy than spin degeneracy. In low spin iron(III) porphyrins, with orbitally degenerate ground states, the MCD spectral envelopes vary significantly between room and liquid helium temperatures, while in high spin iron(III) porphyrins the MCD spectral envelopes intensify between room and liquid helium temperatures, but retain their general shape. Because the spectral intensity, rather than envelope shape, is influenced by variations in the temperature and the magnetic field strength, deconvolution calculations are possible on room temperature absorption and MCD spectra.

Spectral deconvolution results for the Q (550 − 900 nm) and B (250 − 550) regions of (Fo)Fe(III)Pc(−2) are presented in Figures 8−6 and 8−7, respectively. The total number of bands required to fit the absorption spectra was 14 for the Q region and 18 for the B region. The lack of systematic noise in the MCD residuals, that are plotted at the bottom of the MCD fits, indicates that the fits are reliable. Twelve temperature dependent C_A terms and linked C_B terms were required to fit the MCD spectra from 250 to 900 nm. Three Q region (550 to 900 nm) absorption bands were fit to MCD C_A terms while nine B region (250 to 550 nm) absorption bands required MCD C_A terms. The remaining 20 absorption bands (11 in the Q region and 9 in

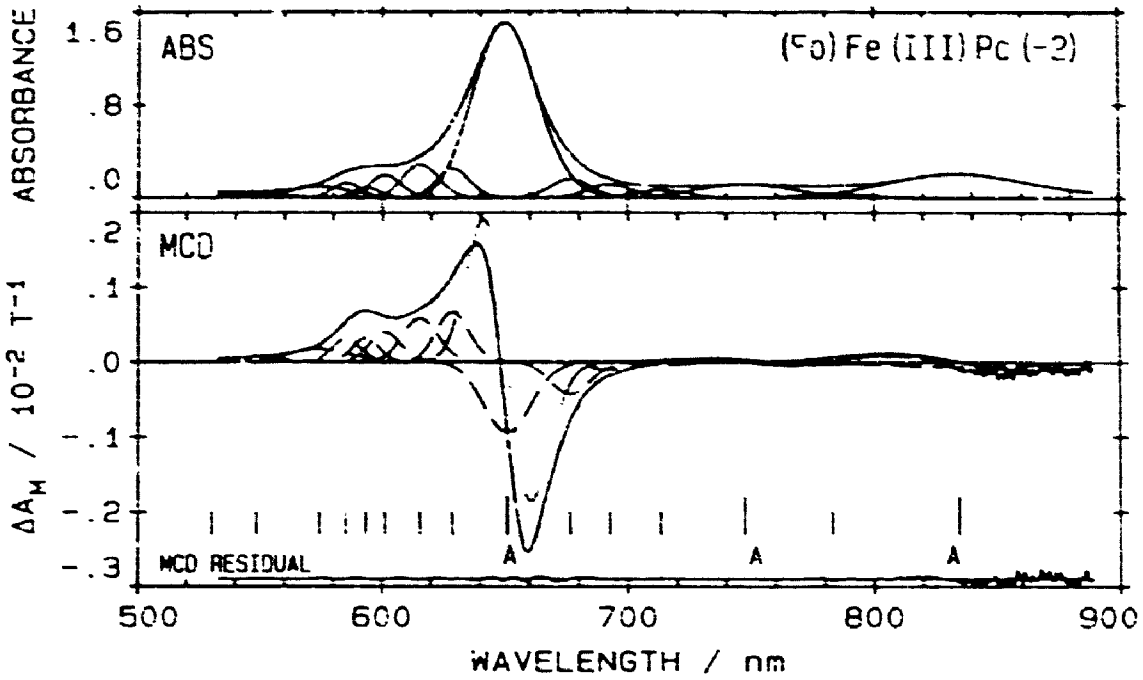

Figure 8-6 Results of band analysis of the absorption (ABS) and MCD spectra for (Fo)Fe(III)Pc(-2) in DCB in the visible region (bands 1-15). (a) Absorption: (———) experimental data; (- - -) fitted data; (———) individual bands. (b) MCD: (———) experimental data; (- - -) fitted data; (.....) A terms; (- - -) B terms. The band centres of the C_A terms are labelled "A".

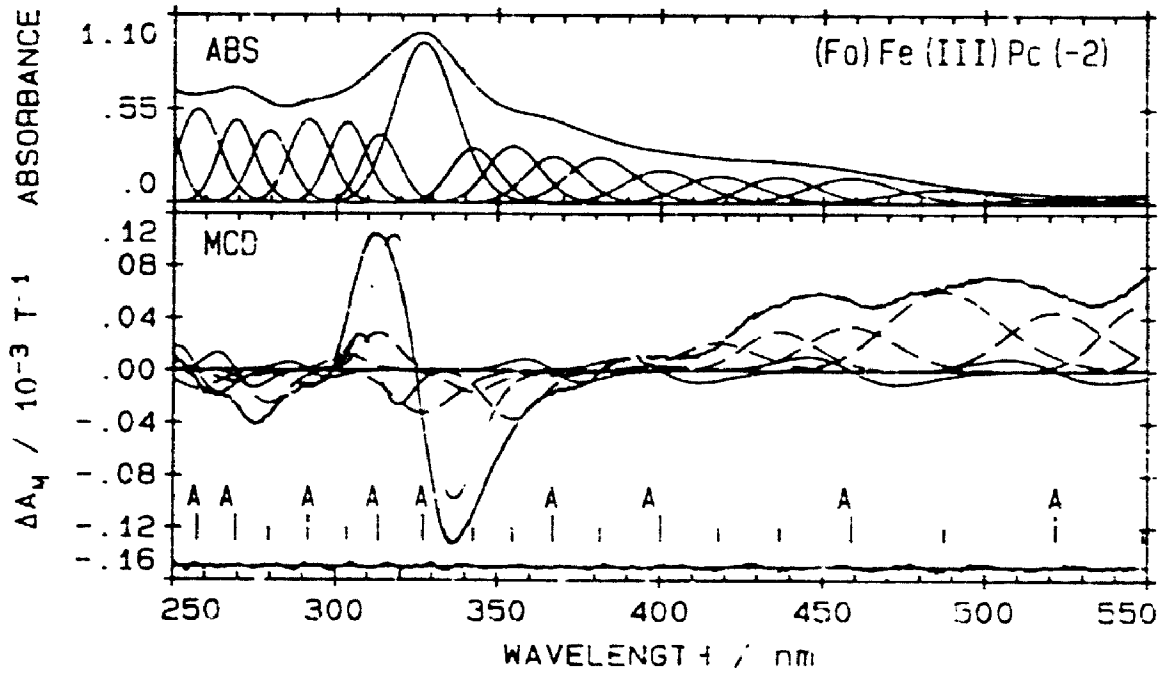

Figure 8-7 Results of band analysis of the absorption (Abs) and MCD spectra for (Fo)Fe(III)Pc(-2) in DCB in the ultraviolet region (bands 16-35). (a) Absorption: (———) experimental data; (- - -) fitted data. (———) individual bands. (b) MCD: (———) experimental data; (- - -) fitted data; (.....) A terms; (- - -) B terms. The band centres of the C_A terms are labelled "A".

Table 8-2A
Band-fitting parameters[a] for a 1,4-dichlorobutane solution of (Fo)Fe(III)Pc(-2)[f] in the Q band (900 - 550 nm) region.

band no.	ν cm^{-1}	λ nm	$\Delta\nu$ cm^{-1}	D_0/C^b (10^{-5})	band type[g]	$\langle\Delta A_M\rangle_n{}^c$ (10^{-5})	$B_0(A_1)/C^d$ (10^{-7})	$B_0(A_1)/D_0{}^e$ (10^{-3})	μ^e
1	11985	834	995	5.647	A	716.7	470.0	832.3	0.78
					B	-0.535	-0.351	-0.622	
2	12770	783	515	0.486	B	-0.028	-0.018	-0.370	
3	13377	748	840	2.404	A	173.8	114.0	474.2	0.44
					B	0.159	0.105	0.437	
4	14020	713	464	0.737	B	-0.137	-0.090	-1.221	
5	14439	693	439	1.164	B	-0.339	-0.222	-1.907	
6	14784	676	414	1.502	B	-1.298	-0.851	-5.666	
7	15362	651	532	22.56	A	2595.	1701.	754.0	0.70
					B	-3.454	-2.265	-1.004	
8	15904	629	403	2.110	B	1.802	1.182	5.602	
9	16245	616	479	2.577	B	1.726	1.132	4.393	
10	16634	610	420	1.647	B	1.078	0.707	4.293	
11	16855	593	353	0.615	B	0.722	0.473	7.691	
12	17085	585	392	0.975	B	0.758	0.497	5.097	
13	17410	574	863	1.621	B	0.921	0.604	3.726	
14	18227	549	967	0.536	B	0.259	0.170	3.172	

[a]Statistics are as follows. Q-region: $\lambda_{550-850nm}$, $\chi^2=2.49\times10^{-5}$, $\Sigma(\Delta A)^2=4.42\times10^{-7}$. [b]$D_0=\langle A\rangle_0/326.6$ where the units of D_0 (dipole strength) are D^2 (D: Debye units); Nyokong, T. N., Ph.D. Thesis, The University of Western Ontario, London, Canada, 1986, p 537. [c]$\langle\Delta A_M\rangle_1$ is the first moment and $\langle\Delta A_M\rangle_0$ is the zeroth moment of the MCD. When fitting with an A term, the program calculates $\langle\Delta A_M\rangle_1$; therefore n=1 in the table. When fitting with a B term, the program calculates $\langle\Delta A_M\rangle_0$; therefore n=0 in the table. The Faraday term values A_1 and B_0 are calculated directly from the moments as follows: $A_1=\langle\Delta A_M\rangle_1/152.5$ and $B_0=\langle\Delta A_M\rangle_0/152.5$. [d]The units of A_1 are D^2, and the units of B_0 are D^2/cm^{-2}; see TNN Thesis, p 537. A_1 data are printed above B_0 data when both A and B terms are used. [e]μ=magnetic moments in units of Bohr magnetons, μ_B, calculated as $2(\langle A_1/D_0\rangle \times 0.4669)$ [f]The concentration (C) of (Fo)Fe(III)Pc(-2) is not known. [g]With the spin degeneracy of the ground state, the A labels refer to overlapping, oppositely signed MCD C terms, while the B labels refer to single MCD C terms.

Table 8-2B
Band-fitting parameters[a] for a 1,4-dichlorobutane solution of (Fo)Fe(III)Pc(-2)[f] in the B band (550 - 240 nm) region.

band no.	ν cm^{-1}	λ nm	$\Delta\nu$ cm^{-1}	D_0/C[b] (10^{-5})	band type[g]	$\langle\Delta A_M\rangle_n$[c] (10^{-5})	$B_0(A_1)/C$[d] (10^{-7})	$B_0(A_1)/D_0$ (10^{-3})	μ[e]
1	19171	522	1299	0.732	A	60.03	39.36	537.7	0.50
					B	0.327	0.214	2.923	
2	20514	487	1735	2.315	B	0.552	0.362	1.564	
3	21800	459	1537	3.480	A	86.53	56.74	163.0	0.15
					B	0.257	0.169	0.486	
4	22896	437	1364	3.042	B	0.192	0.126	0.414	
5	23925	418	1609	3.536	B	0.152	0.100	0.283	
6	24985	400	1691	4.295	A	80.52	52.80	122.9	0.11
					B	0.025	0.017	0.040	
7	26215	381	1696	5.661	B	-0.008	-0.005	-0.009	
8	27254	367	1487	4.859	A	53.65	35.18	72.40	0.07
					B	-0.021	-0.014	-0.029	
9	28193	355	1502	5.838	B	-0.210	-0.138	-0.236	
10	29194	343	1450	5.228	B	-0.087	-0.057	-0.109	
11	30565	327	2068	20.76	A	1050.	688.7	331.7	0.31
					B	-0.236	-0.154	-0.074	
12	31907	313	1391	5.681	A	121.5	79.66	140.2	0.13
					B	0.135	0.089	0.157	
13	32955	303	1513	7.093	B	0.058	0.038	0.053	
14	34282	292	1715	8.022	A	383.3	25.13	31.33	0.03
					B	-0.060	-0.039	-0.049	
15	35776	280	1750	6.734	B	-0.132	-0.086	-0.128	
16	37139	269	1818	7.747	A	90.32	59.23	76.46	0.07
					B	-0.046	-0.030	-0.039	
17	38814	258	2241	10.34	A	172.2	112.9	109.2	0.10
					B	-0.086	-0.057	-0.055	
18	40679	246	1901	8.895	B	-0.031	-0.021	-0.023	

[a]Statistics are as follows. B-region: $\lambda_{240.55nm}$, $\chi^2=1.49\times10^{-6}$, $\Sigma(\Delta A)^2=2.97\times10^{-9}$. [b]$D_0 = \langle A\rangle_0/326.6$ where the units of D_0 (dipole strength) are D^2 (D: Debye units); Nyokong, T. N., Ph.D. Thesis, The University of Western Ontario, London, Canada, 1986, p 537. [c]$\langle\Delta A_M\rangle_1$ is the first moment and $\langle\Delta A_M\rangle_0$ is the zeroth moment of the MCD. When fitting with an A term, the program calculates $\langle\Delta A_M\rangle_1$; therefore n=1 in the table. When fitting with a B term, the program calculates $\langle\Delta A_M\rangle_0$; therefore n=0 in the table. The Faraday term values A_1 and B_0 are calculated directly from the moments as follows: $A_1=\langle\Delta A_M\rangle_1/152.5$ and $B_0=\langle\Delta A_M\rangle_0/152.5$. [d]The units of A_1 are D^2, and the units of B_0 are D^2/cm^{-2}; see TNN Thesis, p 537. A_1 data are printed above B_0 data when both A and B terms are used. [e]μ=magnetic moments in units of Bohr magnetons, μ_β, calculated as $2(\langle A_1/D_0\rangle \times 0.4669)$ [f]The concentration (C) of (Fo)Fe(III)Pc(-2) is not known. With the spin degeneracy of the ground state, the A labels refer to overlapping, oppositely signed MCD C terms, while the B labels refer to single MCD C terms.

the B region) were fit to B terms in the MCD spectra. The fitting parameters obtained from the absorption and MCD spectral fits for (Fo)Fe(III)Pc(-2) are listed in Tables 8-2A and 8-2B.

8.3 DISCUSSION

The square pyramidal iron(III) phthalocyanine complexes have been known since the pioneering studies of Linstead [14-16,33,162]. The first prepared complex was chloroiron(III) phthalocyanine ((Cl)Fe(III)Pc(-2)), which was prepared by heating iron(II) phthalocyanine in hydrochloric acid [162]. Studies that focused on the reaction of HCl with Fe(II)Pc(-2) [61] indicated that a chloride ion was bound axially while the Pc(-2) ring was protonated at an aza-bridging nitrogen. The electronic spectra of this complex was shown to have the split Q band expected for a D_{2h} MPc [1,34]. In recent years, it has been shown that (Cl)Fe(III)Pc(-2) could be formed without the use of HCl and without the accompanying complication of ring protonation [61]. The first absorption and MCD spectra of the unprotonated (Cl)Fe(III)Pc(-2) complex were reported by Stillman and Thomson [52]. Published absorption and MCD spectra for chloroiron(III) octacarboxyphthalocyanine [147] reproduced the distinctive spectral envelopes present in unsubstituted (Cl)Fe(III)Pc(-2). The only other published spectra are the absorption spectra for the halogenated (X)Fe(III)Pc(-2) complexes (X = F, Cl, Br and I) [125,154]. The questionable quality of the absorption spectra, due to the presence of trace amounts of low spin L(X)Fe(III)Pc(-2), makes it difficult to probe the axial ligand effect on transition energies. Our ability to produce high quality absorption and MCD spectra and to accurately analyse the spectra using computer aided deconvolution has facilitated this study of the (X)Fe(III)Pc(-2) complexes.

8.3.1 The Spin State of Chloroiron(III) Phthalocyanine

Because of the limited number of published electronic spectra for (X)Fe(III)Pc(-2)

[52,125,154], the published spectra of five coordinate iron(III) porphyrins [159,160] are useful in understanding the five coordinate iron(III) phthalocyanine complexes. The tetraazaporphyrins are expected to exhibit similar physical properties when compared to phthalocyanines, since both molecules have exactly the same arrangement of heteroatoms in their 18-π-electron systems, with the tetraazaporphyrins lacking only the four peripherally fused benzene rings. Since the order of the $1a_{1u}(\pi)$ and $1a_{2u}(\pi)$ orbitals changes from porphyrins to phthalocyanines due to the presence of the four aza-bridging nitrogens, it is not unexpected that the absorption spectrum of intermediate spin iron(III) tetraazaporphyrin [160] resembles the absorption spectra of (X)Fe(III)Pc(-2).

The EPR spectrum recorded at 77 K for chloroiron(III) octaethyltetraazaporphyrin ((Cl)Fe(III)OETAP(-2)) [160] exhibits g factors of 3.98 and 1.99 as expected for an intermediate spin (S=3/2) ground state. The $g_{\perp}$ value of 3.98 for (Cl)Fe(III)OETAP(-2) [160] is smaller than the one reported here for (Cl)Fe(III)Pc(-2) ($g_{\perp}$=4.273). A powdered sample of (Cl)Fe(III)Pc(-2) at 78 K yielded a EPR $g_{\perp}$=4.67 [131] which prompted the authors to assign the complex to an admixed (S=3/2+5/2) ground state. Our $g_{\perp}$ value for (Cl)Fe(III)Pc(-2) is consistent with a small admixture of the S=5/2 state into the S=3/2 state. Since the spin state of ferrous phthalocyanine in solution is S=0 [117,118,153] and in solid is S=1 [138,156,157] the difference in the $g_{\perp}$ value can be attributed to the physical differences between the two samples.

Comparison of the spectral results for (Cl)Fe(III)Pc(-2) and (Cl)Fe(III)OETAP(-2) to those for chloroiron(III) etioporphyrin I [159], chloroiron(III) porphyrins containing substituted CF_3 groups [159], and chloroiron(III) protoporphyrin-IX [163] shows that there is distinct resemblance in the absorption and MCD spectra while there is a distinct difference in the spin states. The majority of the non-low spin (S≠1/2) iron(III) porphyrins have EPR spectra that are characteristic of the high spin complexes [161]. The differences in the spin states, between the (Cl)Fe(III)Pc(-2) and

(Cl)Fe(III)OETAP(−2) complexes and the iron(III) porphyrins, is partially explained in terms of the size of the "hole" in the macrocycle. The smaller size of the "hole" in tetraazaporhyrin and phthalocyanine, compared to the porphyrins, results in stronger ligand field interaction with iron. The increased ligand field strength together with the smaller displacement of the iron from the plane of the four pyrollic nitrogens in phthalocyanine and octaethyltetraazaporphyrin compared to protoporphyrin−IX results in a larger splitting of the 3d orbitals. The displacement of iron out of the plane of the macrocycle is known to increase with the occupancy of the ferric $d_{x^2-y^2}$ (b_{1g}) orbital [164], due to a repulsive interaction with electrons on the pyrollic nitrogens. Typical 0.39 to 0.62 Å displacements are observed [158,160,163] for high spin five coordinate iron(III) porphyrins. The 0.30 Å displacement in (Cl)Fe(III)Pc(−2) [158] is smaller, but close to the known range of iron displacements for high spin iron(III) porphyrins [163]. This result supports the assignment of the spin state in (Cl)Fe(III)Pc(−2) as an admixture (S=3/2+5/2).

8.3.2 Allowed Electronic Transitions for Intermediate Spin (S=3/2) (X)Fe(III)Pc(−2)

The energy level diagram in Figure 8−8 illustrates the effect of octahedral (O_h) and tetragonal (D_{4h} and C_{4v}) fields on the energies of the iron 3d orbitals. This figure demonstrates how the displacement of iron out of the Pc(−2) ring as a result of a reduction in symmetry from $D_{4h} \rightarrow C_{4v}$ reduction in symmetry pulls the $e_g(d\pi)$ and $a_{1g}(d)$ orbitals closer together to facilitate the preferred $(b_{2g}^2)(e_g^2)(a_{1g})$ electronic arrangement. Under D_{4h} symmetry, the ground state of (X)Fe(III)Pc(−2) splits apart into four, $^4A_{1g}$, $^4A_{2g}$, $^4B_{1g}$ and B_{2g}, states with the $^4A_{2g}$ state the lowest in energy [131,152,161].

Displayed in Figure 8−9 are selected molecular orbitals and allowed transitions for the $^4A_{2g}$ ground state. With the partial vacancy in the metal $e_g(d\pi)$ orbital the $a_{iu}(\pi), b_{iu}(\pi) \rightarrow e_g(d\pi)$ (i=1,2) LMCT transitions, to orbitally degenerate ^4E_u excited

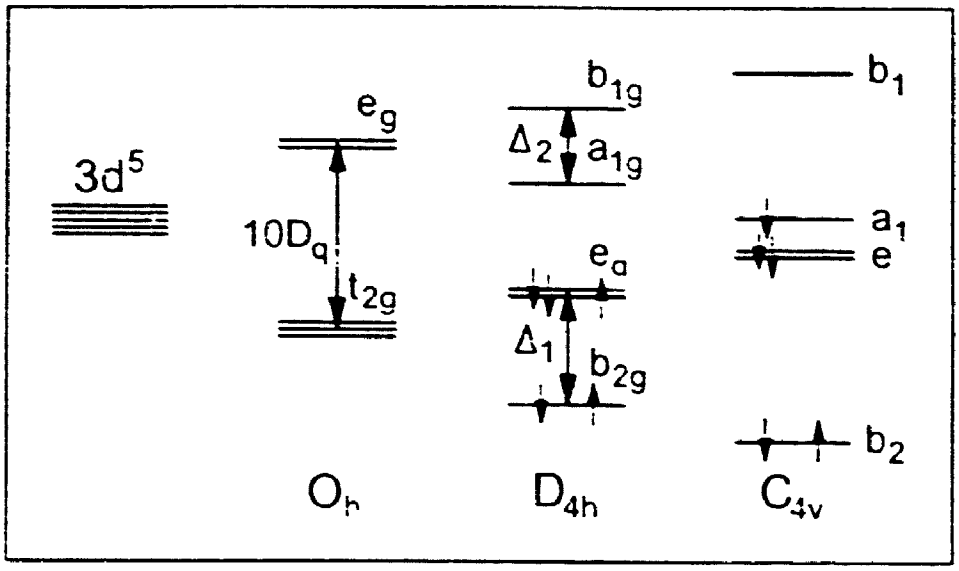

Figure 8–8 The energy level splitting for metal 3d orbitals under a ligand field with octahedral ($10D_q$) and axial (Δ_1,Δ_2) distortions.

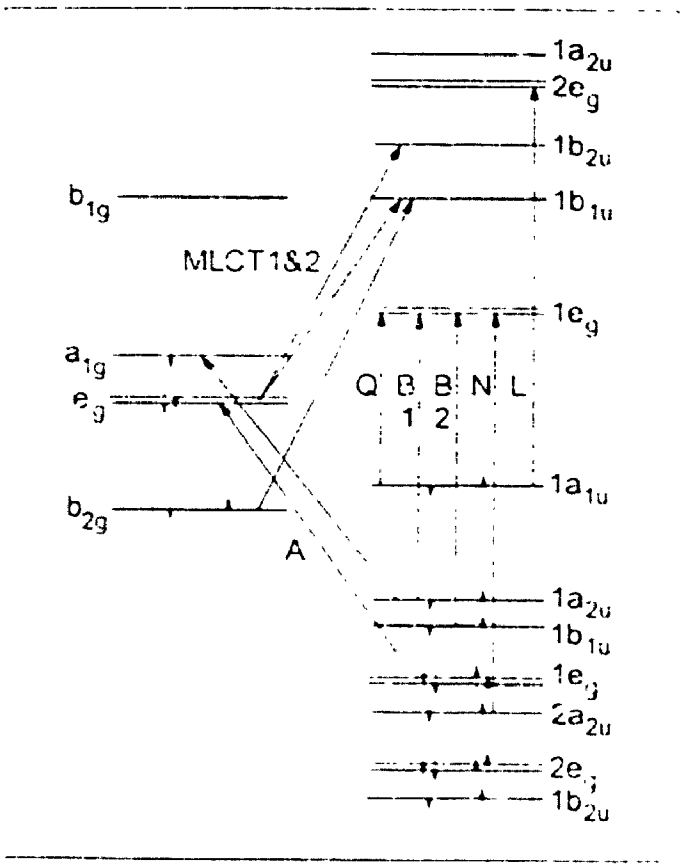

Figure 8–9 Selected molecular orbitals and allowed electronic transitions for the intermediate spin $^4A_{2u}$ ground state of (X)Fe(III)Pc(−2). The arrow labelled A represents the allowed degenerate LMCT transitions.

states, are allowed. The LMCT bands are expected to complicate the electronic spectrum of the Pc(−2) ring. The allowed charge transfer transitions, the direction of charge transfer and the expected MCD terms are listed in Table 8−3. Since the ground state is spin degenerate, the traditional MCD A and B terms are replaced by the corresponding C_A and C_B terms.

Figure 8−10 is presented in order to illustrate the complexity of the $^4A_{2g} \rightarrow {}^4E_u$ transition and to show the origin of the MCD C_A terms. In the absence of an applied magnetic field, zero field splitting (2D=20 cm^{-1}) [161] of the ground state results in approximately 91% occupancy of the ground ($M_S=\pm 1/2$) Kramers doublet. Spin orbit coupling splits the ^4E_g excited state into four equally spaced ($\zeta/3$=100 cm^{-1}) Kramers doublets [152]. The allowed right and left circularly polarized transitions, under an applied magnetic field (B≠0), are shown in Figure 8−10. Focusing on the four allowed transitions out of the lowest energy doublet (the solid and dashed arrows), if the spectral band widths are significantly larger than the Zeeman and spin orbit splittings then adding the spectral intensity from the four transitions together yields a derivative shaped MCD band, which is typical for C_A terms. The spectral intensity from transitions out of the higher energy doublet (the dotted arrows), which is approximately 9% occupied, broaden the absorption band and appear as weak high energy positive and low energy negative shoulders on the derivative bands in the MCD spectrum.

The components of the nondegenerate $^4A_{2g} \rightarrow {}^4A_{1u}$ transition will give rise to C_B terms in the MCD spectrum. In the absence of orbital degeneracy, there are four allowed electronic transitions, two for each Kramers doublet, which have identical transition energies. Since the four bands have identical energies, the resultant MCD C_B term appears as a single signed band with an intensity equal to the sum of the intensities of the four transitions.

Unlike low spin L(X)Fe(III)Pc(−2) (Chapter 6), low temperature MCD spectra are

Table 8-3
Allowed charge transfer transition for intermediate spin (S=3/2) Iron(III) Phthalocyanine[a].

One Electron Transition	Excited State	Charge Transfer	Polarization of Transition	MCD Term Expected[b]
$a_{1u}, a_{2u} \rightarrow e_g$	^4E_u	L → M	XY	C_A
$b_{1u}, b_{2u} \rightarrow e_g$	^4E_u	L → M	XY	C_B
$a_{2u} \rightarrow a_{1g}$	$^4A_{1u}$	L → M	Z	C_B
$b_{2u} \rightarrow b_{1g}$	$^4A_{1u}$	L → M	Z	C_B
$e_g \rightarrow b_{1u}, b_{2u}$	^4E_u	M → L	XY	C_A
$b_{2g} \rightarrow b_{1u}$	$^4A_{1u}$	M → L	Z	C_B

[a]The ground state electronic configuration of the iron 3d orbitals is $(b_{2g})^2(e_g)^2(a_{1g})^1$ and the ground state symmetry is $^4A_{2g}$. [b]The subscripts A and B denote that the transitions are xy and z polarized.

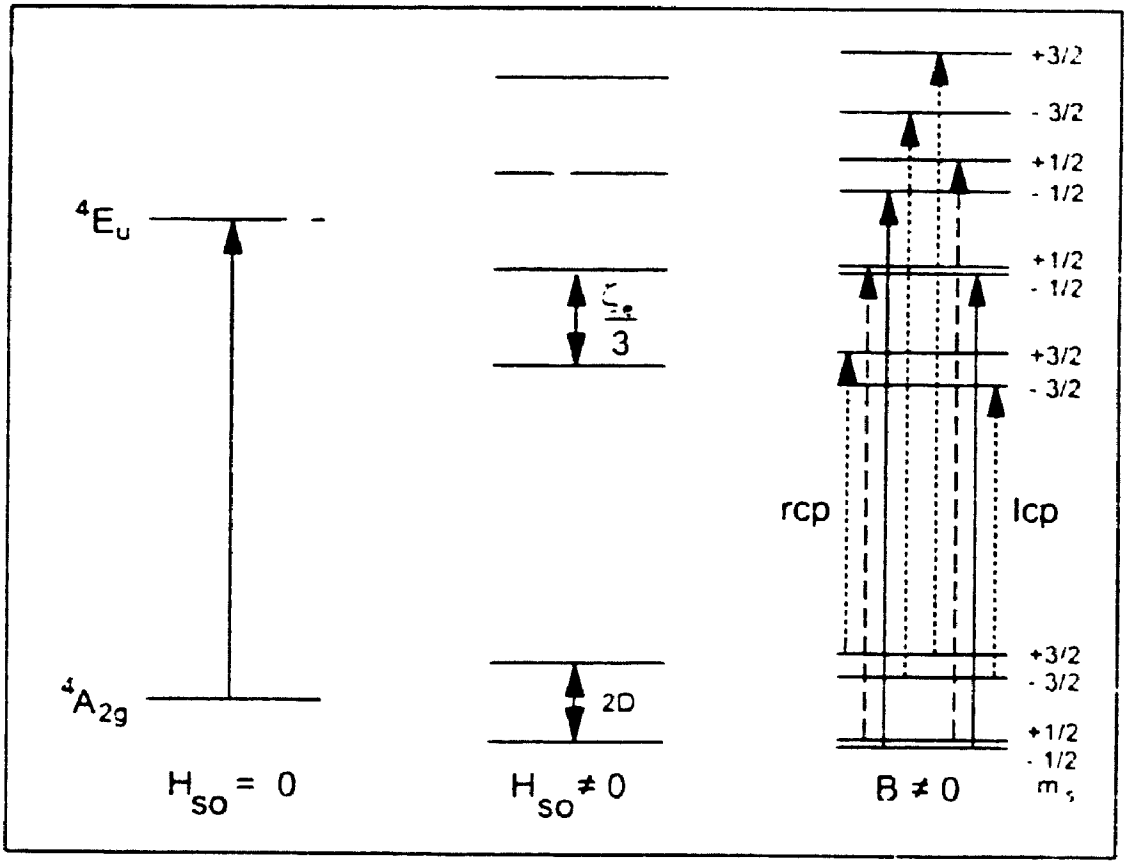

Figure 8-10 Energy level diagram for the $^4A_{2g} \rightarrow {}^4E_g$ electronic transition. The zero field (2D), spin orbit (ζ_e), and Zeeman splittings are highly exaggerated with respect to the energy separation between electronic states. Right circularly polarized (rcp) and left circularly polarized (lcp) transitions are plotted, with the solid and dashed arrows representing transitions from the low energy Kramers doublet, and the dotted arrows representing transitions from the high energy Kramers doublet.

not essential in the analysis of intermediate spin (X)Fe(III)Pc(−2) complexes. Saturation of the $^4A_{2g}$ ground state will enhance the MCD signal due to significant increases in the intensity of the C_A and C_B terms, but the general shape of the spectral envelope is not expected to change from room to liquid helium temperatures.

8.3.3 Assignment of the Fitted Absorption and MCD Spectra of Formatoiron(III) Phthalocyanine

In the electronic spectra of iron(III) phthalocyanines, degenerate transitions present at wavelengths higher than the Q band are attributed to MLCT. Since we assign the intense absorption band at 651 nm (15 362 cm^{-1}) as Q, the two degenerate bands at 834 nm (11 985 cm^{-1}) and 748 nm (13 377 cm^{-1}) are LMCT transitions. The energy separation ($\Delta\nu$=1392 cm^{-1}) between the 834 and 748 nm bands is a close match to the energy separation between the B1 ($1a_{2u}(\pi) \rightarrow 1e_g(\pi^*)$) and B2 ($1a_{1u}(\pi) \rightarrow 1e_g(\pi^*)$) bands in L_2Fe(II)Pc(−2), thus the 834 nm band is assigned to the $1a_{2u}(\pi) \rightarrow e_g(d\pi)$ (LMCT2) transition and the 748 nm band is assigned to the $1b_{1u}(\pi) \rightarrow e_g(d\pi)$ (LMCT3) transition. We have decided to reserve the LMCT1 label for the $1a_{1u}(\pi) \rightarrow e_g(d\pi)$ transition which is expected beyond the low energy (900 nm) spectral cutoff. The 1342 cm^{-1} gap between the two bands at 327 nm (30 565 cm^{-1}) and 313 nm (31 907 cm^{-1}) is comparable to the energy separation (1392 cm^{-1}) of the LMCT1 and LMCT2 bands, therefore these two bands are assigned as B1 and B2, respectively. The band at 522 nm (19 171 cm^{-1}) is assigned to the $2a_{2u}(\pi) \rightarrow e_g(d\pi)$ (LMCT4) transition. The 5794 cm^{-1} separation between the LMCT3 and LMCT4 bands matches up best to the 5232 cm^{-1} separation between the B2 (313 nm) and 269 nm (37 139 cm^{-1}) bands. Because the N and LMCT4 bands arise from common occupied orbitals, the 269 nm band is assigned to the N transition. The L band has very small variations in its energy with respect to metal or ligand oxidation, therefore the 258 nm (38 814 cm^{-1}) band is assigned as the L band. Of

the four remaining unassigned degenerate transitions, the two at 459 nm (21 800 cm^{-1}) and 400 nm (24 985 cm^{-1}) are in the spectral region where the two MLCT transitions are expected and are assigned as MLCT1 ($e_g(d\pi) \rightarrow 1b_{1u}(\pi^*)$) and MLCT2 ($e_g(d\pi) \rightarrow 1b_{2u}(\pi^*)$). The 292 nm (34 282 cm^{-1}) band is assigned to the $1b_{2u}(\pi) \rightarrow e_g(d\pi)$ (MLCT5) transition. The separation (12 482 cm^{-1}) of the LMCT4 and LMCT5 transtions approximates the expected separation of the L and C transitions and verifies that the LMCT5 and C bands arise from a common occupied orbital. The final MCD C_A term at 367 nm (27 254 cm^{-1}) is assigned to the $1e_g(\pi) \rightarrow a_{1g}(d)$ transition. Although this transition is forbidden under D_{4h} symmetry, (Fo)Fe(III)Pc(−2) actually exhibits C_{4v} symmetry under which the transition is allowed.

8.3.4 Comparison of the Deconvolution Results for (Fo)Fe(III)Pc(−2), $(NH_3)_2$Fe(II)Pc(−2), (NH_3)(CO)Fe(II)Pc(−2) and Na[$(CN)_2$Fe(III)Pc(−2)]

The energy level diagram presented in Figure 8−11 compares the deconvolution results for (Fo)Fe(III)Pc(−2) with those for $(NH_3)_2$Fe(II)Pc(−2) (Chapter 6), (NH_3)(CO)Fe(II)Pc(−2) (Chapter 6) and Na[$(CN)_2$Fe(III)Pc(−2)] (Chapter 7). In this study of the spectral properties of intermediate spin (Fo)Fe(III)Pc(−2), we need to focus on the influence of the oxidation and spin state. Figure 8−11 will be usefull in understanding these effects. The major spectral changes following metal oxidation are: (i) the presence of degenerate LMCT bands, (ii) the red shift in the energies of the MLCT1 and MLCT2 bands, and (iii) the compression of the MLCT1/MLCT2, B1/B2, and N/L band pairs, and have been discusses extensively in Chapter 7. The spectral changes from low (S=1/2) to intermediate (S=3/2) spin Fe(III)Pc(−2) are: (i) a blue shift in the the Q, B1, B2, N and L band energies, (ii) a red shift in the MLCT2−5 band energies, (iii) a blue shift in the MLCT1 and MLCT2 band energies, and (iv) a further compression of the MLCT1/MLCT2, B1/B2 and N/L band pairs. These results indicate that factors other than the oxidation state of iron influence the spectra

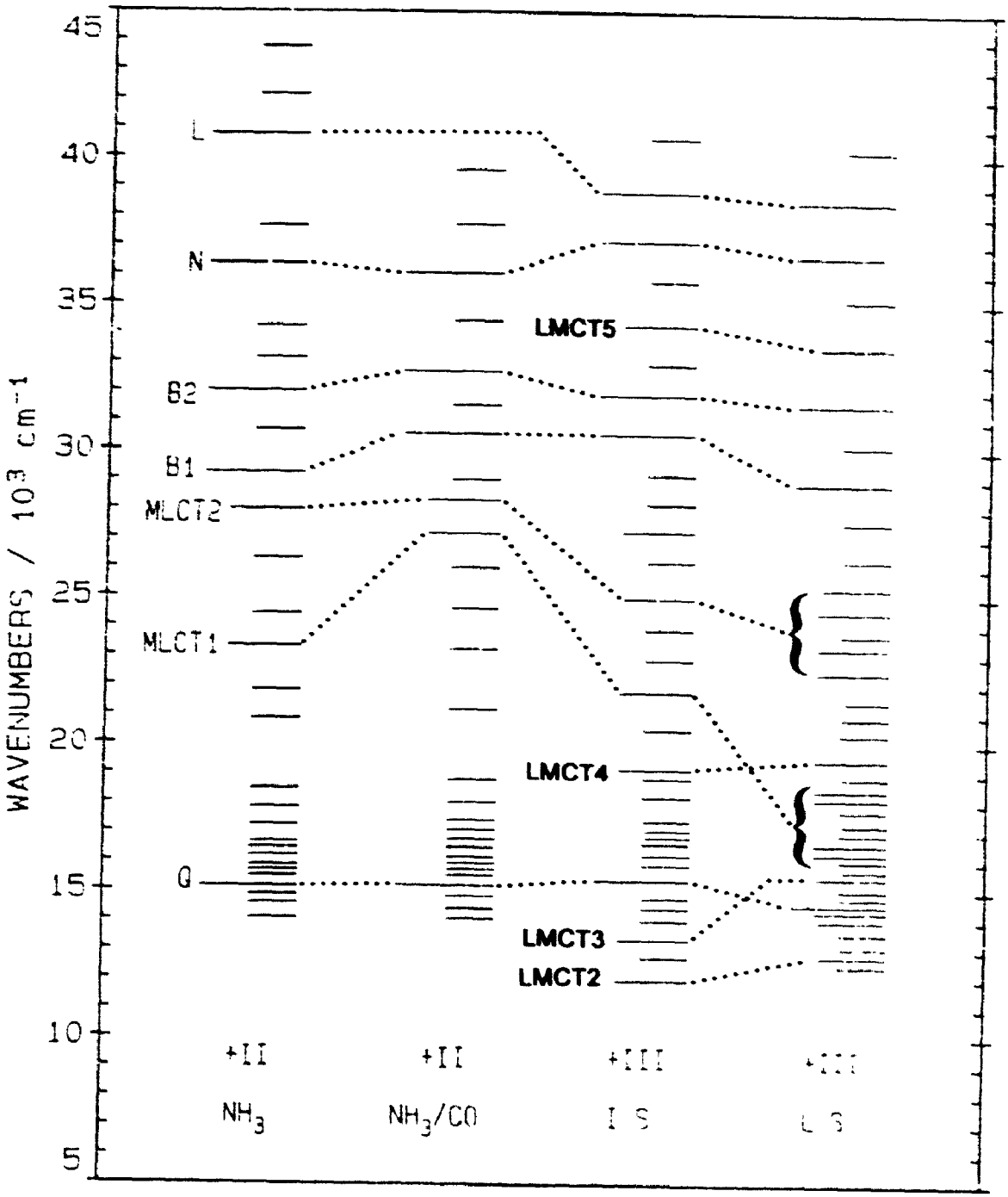

Figure 8-11 Comparison of the fitted band centre energies for $(NH_3)_2Fe(II)Pc(-2)$ (Chapter 6), $(NH_3)(CO)Fe(II)Pc(-2)$ (Chapter 6), $(Fo)Fe(III)Pc(-2)$ and $Na[(CN)_2Fe(III)Pc(-2)]$ (Chapter 7). The line lengths are: long for degenerate ring transitions, intermediate for degenerate CT transitions and small for nondegenerate transitions.

of the intermediate spin (S=3/2) (X)Fe(III)Pc(−2) complexes.

Changes in the axial ligands and the molecular structures may account for the differences between low (S=1/2) and intermediate (S=3/2) spin Fe(III)Pc(−2). The overlap of selected π orbitals in (Cl)Fe(III)Pc(−2) and (meim)(Br)Fe(III)Pc(−2) is plotted in Figure 8–12. The two halogen ligands (chloride and bromide) and the N–methylimidazole ligand are expected to donate σ and π electron density to iron(III). The halogen ligands are weaker σ donors and stronger π donors compared to N–methylimidazole, which is a strong σ donor and either a weak π donor or a weak π acceptor. Because the σ and π donor strengths of the axial chloride, bromide and formate ligands are comparble (their respective (X)Fe(III)Pc(−2) complexes have virtually identical absorption spectra), these ligands cannot be responsible for the spectral differences. The variation in the MLCT and LMCT transition energies for $Na[(CN)_2Fe(III)Pc(-2)]$ and (meim)(Br)Fe(III)Pc(−2) (Chapter 7) is not large enough to attribute the spectral differences to the presence or absence of a second axial ligand.

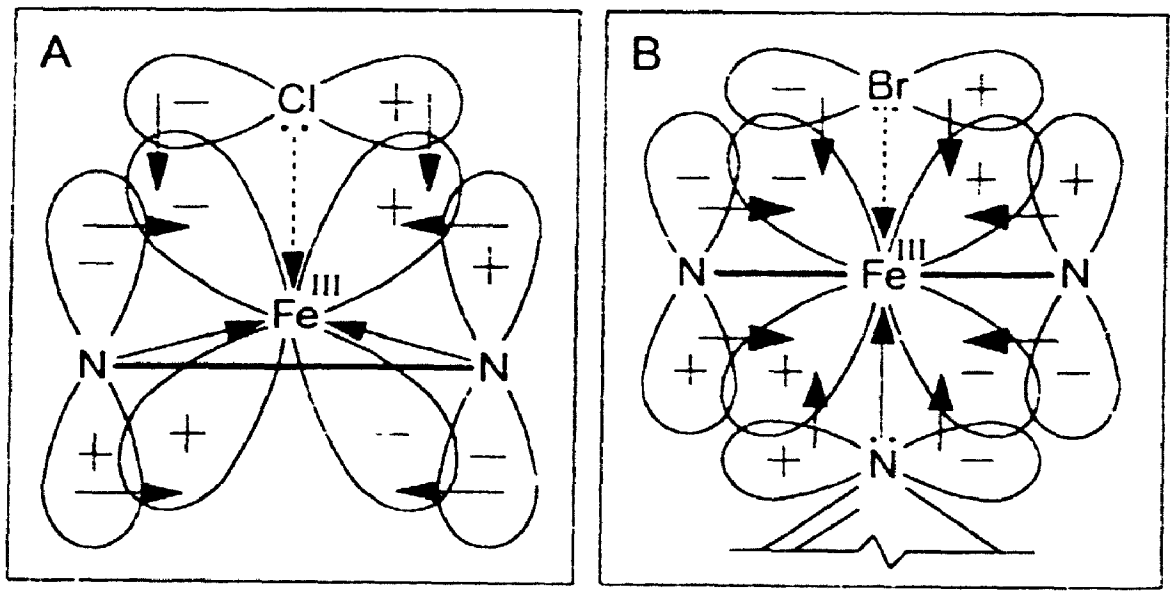

Figure 8–12 Selected overlapping axial and equatorial π and π^* molecular orbitals in **(A)** (Cl)Fe(III)Pc(−2) and **(B)** (meim)(Br)Fe(III)Pc(−2). The arrows represent the direction of electron donation.

Unless a *trans* effect is occurring in L(X)Fe(III)Pc(−2), the axial ligands are not responsible for the spectral differences between low and intermediate spin Fe(III)Pc(−2).

The structural differences between (Fo)Fe(III)Pc(−2), five coordinate with iron displaced out the plane of the Pc(−2) ring, and $Na[(CN)_2Fe(III)Pc(-2)]$, six coordinate with iron in the plane of the phthalocyanine ring, may be the major factor that accounts for the spectral differences between low and intermediate spin iron(III) phthalocyanines. The large (0.30 Å) displacement of the ferric ion out of the plane of the phthalocyanine ring in (Cl)Fe(III)Pc(−2) will reduce the equatorial $d\pi-p\pi$ orbital overlap and the electron withdrawing power of the 3/4 filled $e_g(d\pi)$ orbitals on the equatorial π-system. This explains the energy shifts in the LMCT (red shift) and MLCT (blue shift) bands from low to intermediate spin Fe(III)Pc(−2) and why the energies of the Q, B1, B2, N and L band in (Fo)Fe(III)Pc(−2) approach the values reported for $L_2MgPc(-2)$ where magnesium is chromophorically silent [27].

8.4 CONCLUSIONS

10 K EPR measurements indicate that chloroiron(III) phthalocyanine has an intermediate spin (S=3/2) ground state with a small admixture of the high spin (S=5/2) state. Deconvolution of the spectral data for formatoiron(III) phthalocyanine located twelve electronic transitions with orbitally degenerate excited states in the absorption and MCD spectra. Pure Pc(−2) ring transitions were located at 651 (Q), 327 (B1), 313 (B2), 269 (N) and 258 nm (L). The bands at 834, 748, 522, and 292 nm are assigned as LMCT transitions that arise from Pc(−2) ring orbitals that are common with the B1, B2, N and C transitions, respectively, into the half filled iron $e_g(d\pi)$ orbital. The band at 367 nm is assigned as a LMCT that is parity forbidden $[1e_g(\pi) \rightarrow a_{1g}(d)]$ under D_{4h} symmetry, but allowed $[1e(\pi) \rightarrow a_1(d)]$ under the C_{4v} symmetry of (Fo)Fe(III)Pc(−2). MLCT transitions are assigned to the bands at 459 (MLCT1) and 400 nm (MLCT2).

CHAPTER 9

LOW SPIN IRON(III) PHTHALOCYANINE π-CATION RADICAL

9.1 INTRODUCTION

Ring oxidized and reduced phthalocyanines are useful model compounds in the study of naturally occurring porphyrin radical complexes such as the magnesium chlorin π-cation radical which is present in the early stages of photosynthesis [165] and the catalase, peroxidase and cytochrome P450 classes of heme enzymes [84,91,93,166,167]. More often than not, porphyrin π-cation radicals dimerize readily in solution and spectral techniques such as electron paramagnetic resonance (EPR) are unable to discern any information from the dimers. Although ring oxidized magnesium and zinc phthalocyanine are known to be present in solution as a mixture of monomer and dimer [26-28,35,37], we have been able to obtain the spectra of pure monomers and dimers [ ]. The benefits of studying metallophthalocyanines rather than metalloporphyrins are: (i) the ring transitions are spread out over a greater spectral region in MPc complexes [1,2] and thus they are easier to isolate, and (ii) the highest occupied molecular orbital in ring oxidized MPc(-1) is known to be the $1a_{1u}(\pi)$ orbital [1,2,21,28]. For several porphyrin π-cation radicals there is a continuing debate on whether the two highest occupied ($1a_{2u}(\pi)$ and $1a_{1u}(\pi)$) molecular orbitals change positions upon ring oxidation [82-84] and the analysis of the spectral data of the phthalocyanine π-cation radicals is potentially useful in resolving this debate.

Since the heme enzymes are also prone to oxidation at the metal centres (one half of the postulated two electron oxidation in horseradish peroxidase compound I is the oxidation of iron from III to IV [167]), then an ideal MPc model should have a transition metal core, with an extensive redox chemistry itself. In this chapter, the deconvolution results obtained from the low temperature absorption (77 K) and MCD (4 K) spectra of $Cl_2Fe(III)Pc(-1)$ are used to assign the $\pi \rightarrow \pi$, $\pi \rightarrow \pi^*$, and charge

transfer (CT) transitions that comprise the spectral envelopes. The low temperature electron paramagnetic resonance (EPR) spectrum of $Cl_2Fe(III)Pc(-1)$ is used to determine the spin of the ground state. Field dependent studies of the low temperature MCD spectra are used to determine the orbital g factor and the orbital degeneracy of the ground state.

9.2 RESULTS

9.2.1 Absorption and MCD Spectra of $Cl_2Fe(III)Pc(-1)$

Figure 9-1 illustrates the room (300 K) and the low (77/4 K) temperature absorption and MCD spectra for a ring oxidized iron(III) phthalocyanine ($Cl_2Fe(III)Pc(-1)$). $Cl_2Fe(III)Pc(-1)$ was prepared by oxidizing a solution of (meim)(Cl)Fe(III)Pc(-2) with elemental chlorine (Cl_2). The medium intensity, broad absorption band at 516 nm in Figure 9-1 marks the site of oxidation as the ring [2,35,37,70,71,103]. The presence of a single sharp absorption band between 650 and 900 nm indicates that $Cl_2Fe(III)Pc(-1)$ is present in solution as either a monomer or dimer, but not as a mixture. The absorption maximum for this band ranges from 792 to 824 nm, depending of the axial ligand (X) in the $X_2Fe(III)Pc(-1)$ complexes (Table 9-1), and lines up with the 825 nm Q band in monomeric MgPc(-1) [28] and ZnPc(-1) [26,35].

Table 9-1
Observed maxima in the absorption spectra of the metal and ring oxidized $X_2Fe(III)Pc(-1)$ species in DCM.

$X_2Fe(III)Pc(-1)$	λ_{max} (nm)					
$(Cl)_2Fe(III)Pc(-1)$	792			516	432	323
$(NO_3)_2Fe(III)Pc(-1)$	800	773		517	402	319
$(CN)_2Fe(III)Pc(-1)$	795	757	701	520	323	
$(ClO_4)_2Fe(III)Pc(-1)$	824	719		526	319	

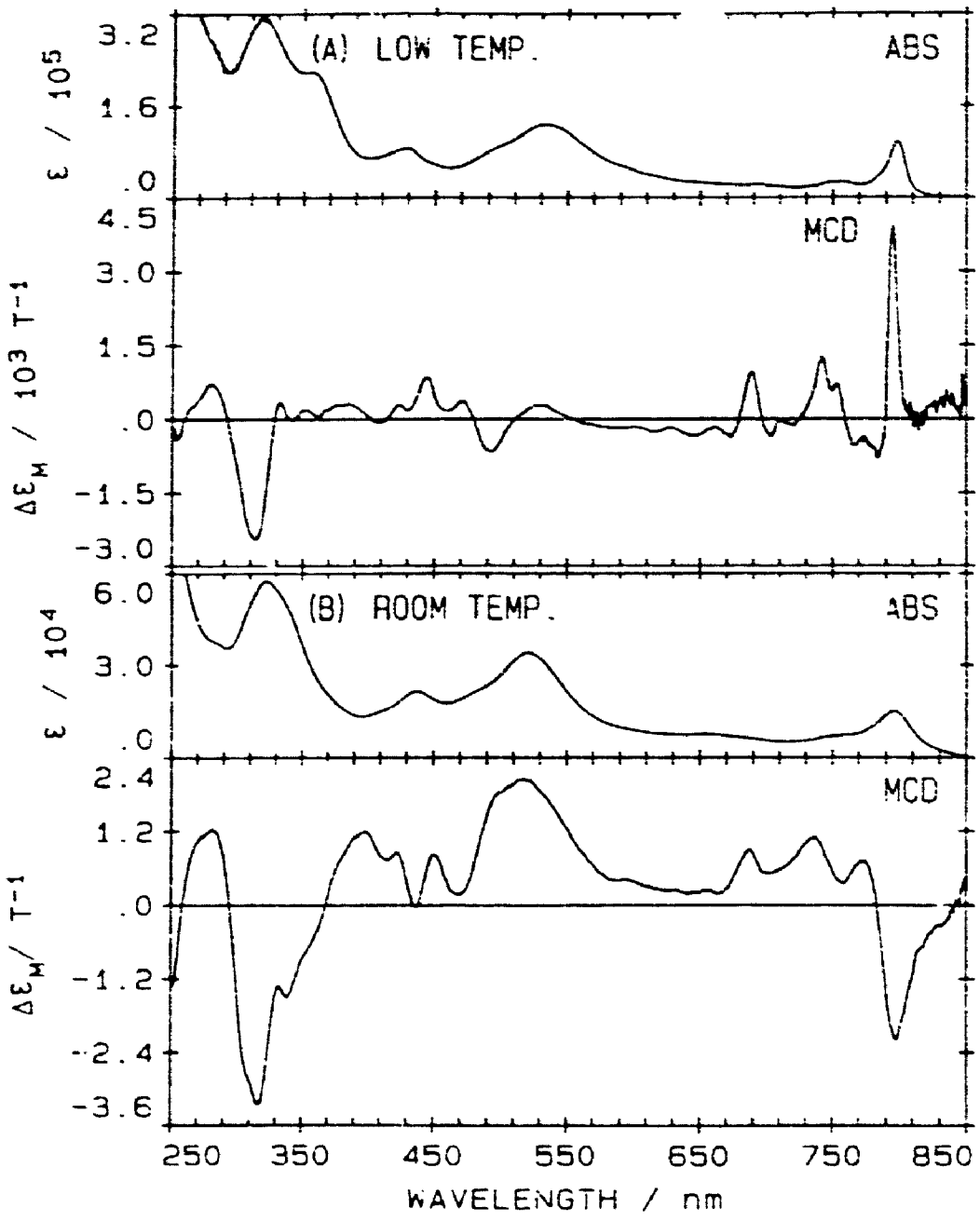

Figure 9-1 (A) 77 K absorption (ABS) and 4 K MCD spectra for a 1 mm DCM:CB glass of $Cl_2Fe(III)Pc(-1)$ (B) 300 K absorption and MCD spectra for $Cl_2Fe(III)Pc(-1)$ recorded in DCM.

9.2.2 Variable Field MCD Spectra of Cl_2Fe(III)Pc(-1)

The 2.8 K MCD spectra of Cl_2Fe(III)Pc(-1) measured at magnetic field strengths ranging from 0 to 4 tesla are plotted in Figure 9-2. The changes in the positive (+) MCD spectral intensity (ΔA) at 690, 740, and 795 nm are plotted against the applied magnetic field in the inset in Figure 9-2. The deviation from linearity in the inset in Figure 9-2 and the eventual saturation of the MCD signal at high magnetic fields in Figure 9-2 confirms that the ground state in Cl_2Fe(III)Pc(-1) is orbitally degenerate.

9.2.3 Determination of the Orbital g_{av} Factor

Plots of $\ln((K+\Delta A)/(K-\Delta A))$ versus $\beta B/kT$ and ΔA versus $\beta B/kT$ for Cl_2Fe(III)Pc(-1) are displayed in Figure 9-3. The values for ΔA and K are determined from the local maximum at 795 nm. Since the spectral envelope is saturated at 4 tesla (Figure 9-2), the value for K (0.032 at 795 nm) is recorded directly from the plot. Although K is a known quantity, the linear plot in Figure 9-3A is easier to analyse than the exponential plot in Figure 9-3B and was used to determine g_{av}. The least squares optimization, the results are plotted in Figure 9-3A, yielded a value of 4.66 $\pm$ 0.05 for g_{av}. The agreement between the experimental points and the fitted straight lines (Figure 9-3A) and the fitted exponential curves (Figure 9-3B) provide strong support for the linear fits.

9.2.4 Low Temperature EPR Spectra of Cl_2Fe(III)Pc(-1)

The 10 K electron paramagnetic resonance (EPR) spectrum of Cl_2Fe(III)Pc(-1) is shown in Figure 9-4. The region from 2000 to 3200 gauss has been omitted because it is devoid of spectral intensity. The general shape of the EPR spectrum is indicative of a triplet (S=1) spin state [168]. The most intense EPR band is centred at 1591 gauss (g=4.2670), has a band width of 30 gauss, and represents the forbidden ($\Delta M_S=\pm 2$) transition. The EPR spectral intensity from 3200 to 3600 gauss

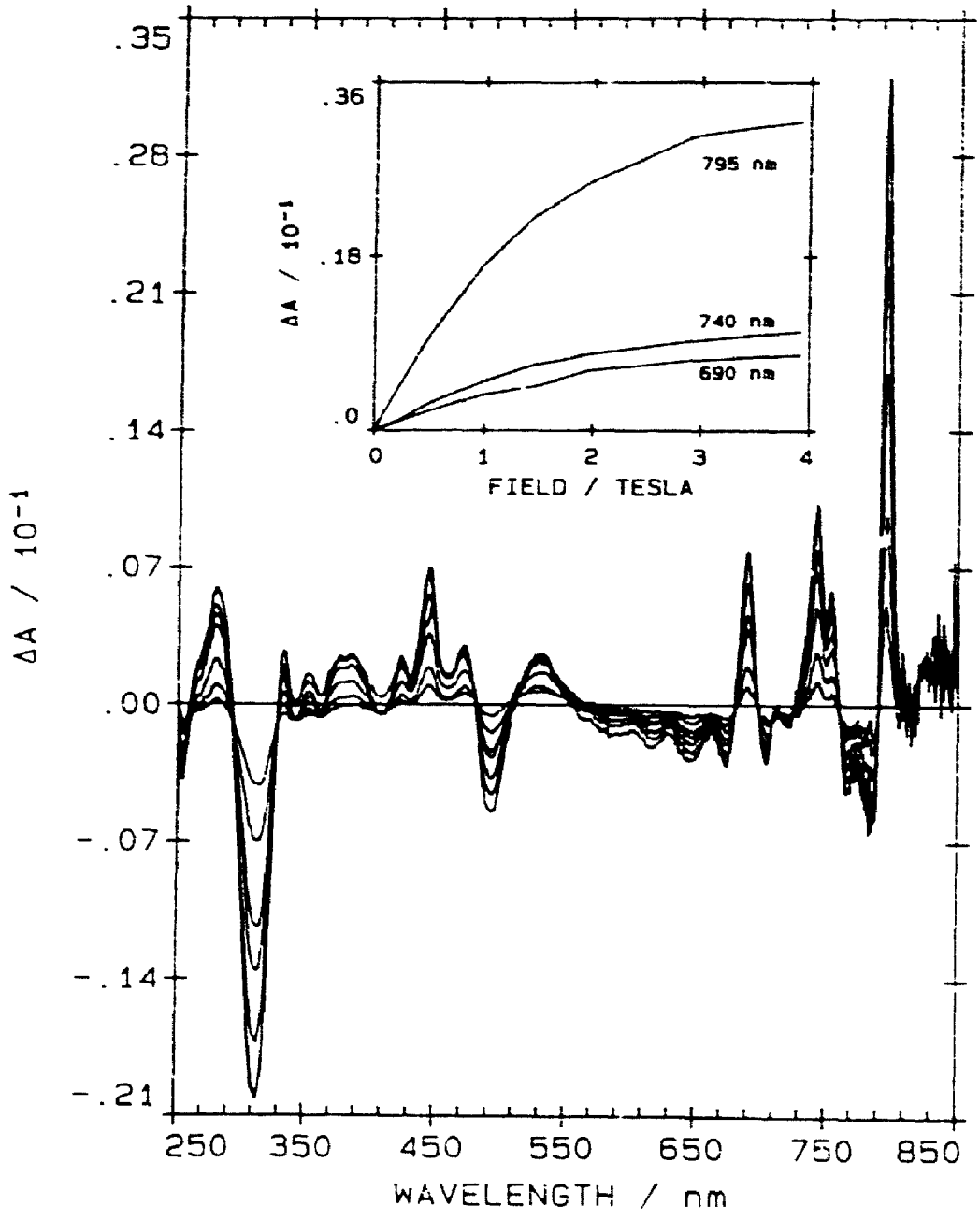

Figure 9-2 MCD spectral changes observed for a 1 mm DCM:CB glass of $Cl_2Fe(III)Pc(-1)$, at 2.8 K, when the magnetic field is varied between 0 and 4.0 Tesla. The inset displays the change in the spectral intensity at three wavelengths).

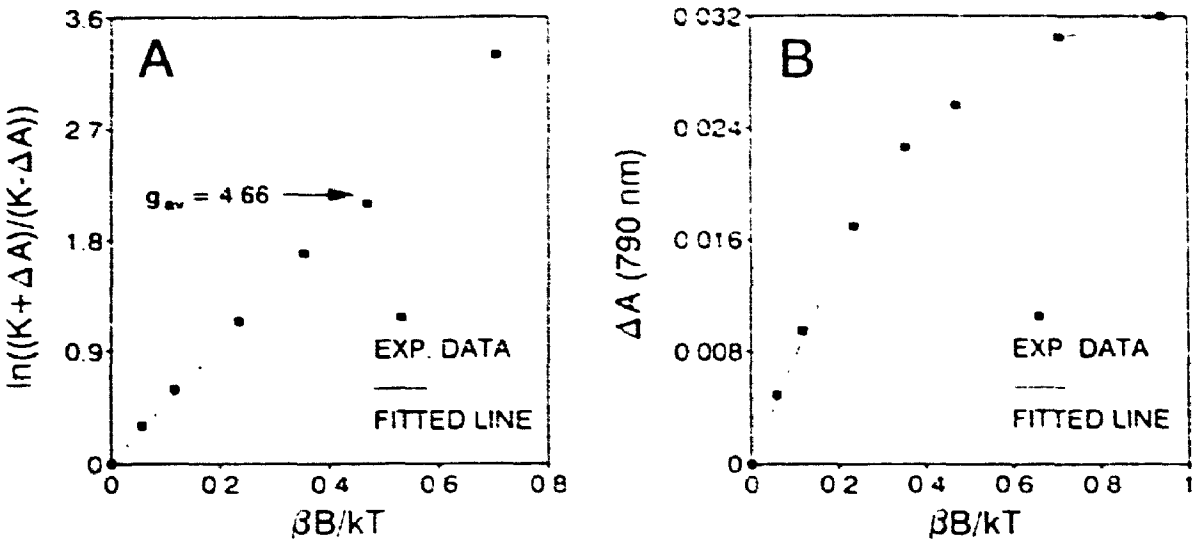

Figure 9-3 Experimental and predicted plots of: **(A)** $\ln[(K+\Delta A)/(K-\Delta A)]$ vs. $\beta B/kT$, and **(B)** ΔA vs. $\beta B/kT$ obtained from the low temperature (2.8 K), variable field MCD spectra of $Cl_2Fe(III)Pc(-1)$. ΔA and K represent the 795 nm spectral and saturation intensities, respectively.

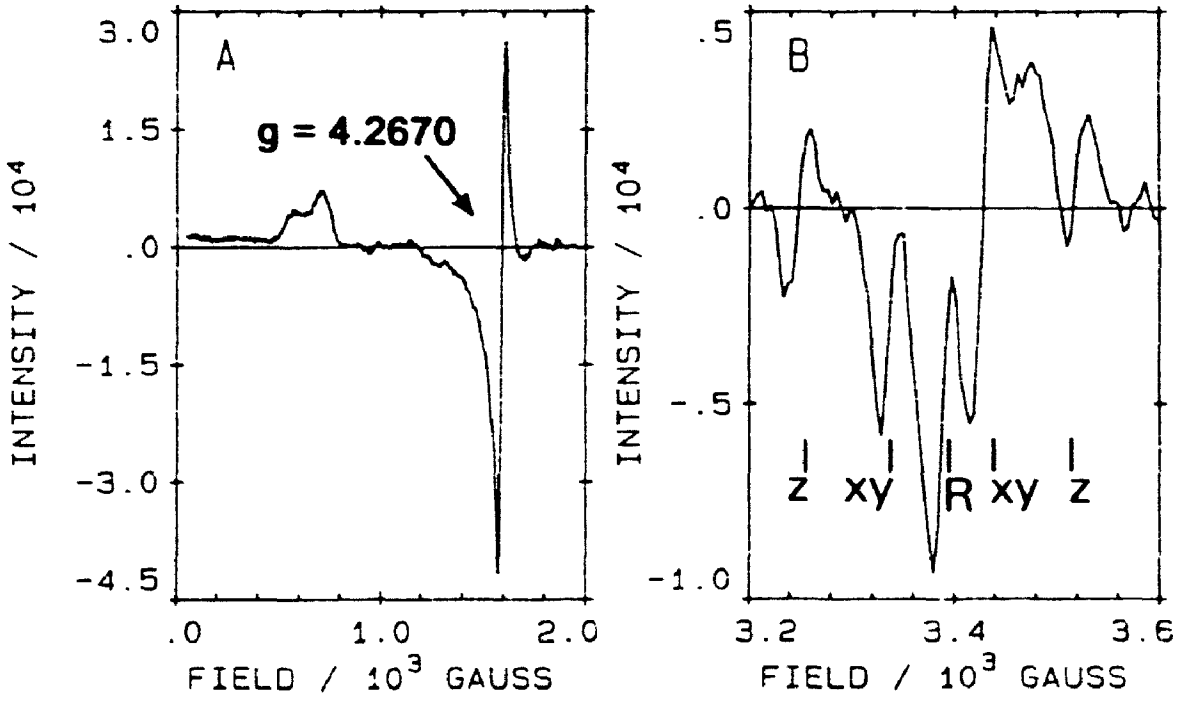

Figure 9-4 The 10 K EPR spectra for $Cl_2Fe(III)Pc(-1)$ recorded in *o*-DCB. The absolute value of the g factors were calculated from the signal of a DPPH standard.

(Figure 9–4B) is dominated by the allowed ($\Delta M_S=\pm 1$) transition for a molecule with D_{4h} symmetry [168]. Of the five bands present in this region, the middle band (labelled R), which is centred near the free electron value (g=2.0023), is an artifact that appears in the triplet (S=1) spectrum [168]. The two bands labelled xy, which overlap the artifact band represent the $\Delta M_S=\pm 1$ transitions along the degenerate x,y molecular axes. The two z labelled bands at the edges of Figure 9–4B are $\Delta M_S=\pm 1$ transitions along the molecular z axis.

9.2.5 Spectral Band Deconvolution Calculations

Results from the spectral deconvolution of the 77 K absorption and 4 K MCD spectra of $Cl_2Fe(III)Pc(-1)$ are displayed in Figures 9–5 and 9–6. Since the analysis of Figures 9–1 and 9–2 demonstrates that $Cl_2Fe(III)Pc(-1)$ has an orbitally degenerate ground state, the absorption and MCD spectra shown in Figures 9–5 and 9–6, have been fit to Gaussian bands. The Q region (Figure 9–5) was fit to 20 bands, while the B region (Figure 9–6) was fit to 22 bands. The MCD residuals verify the reliability of the spectral fits. The fitting parameters obtained for the Q and B regions have been summarized in Tables 9–2A and 9–2B.

9.3 DISCUSSION

Following the precedent of the concerted two electron (metal plus ring) oxidation in HRP I [167], it is possible that $[Fe(III)Pc(-2)]^+$ could be oxidized directly to $[Fe(IV)Pc(-1)]^{\cdot+++}$. Magnetic susceptibility measurements, oxidation titrations, and elemental analysis on thionyl chloride oxidized Fe(II)Pc(−2) [128] indicate that oxidation of the ring and metal results in the formation of the stable $Cl_2Fe(III)Pc(-1)$. The only other high quality electronic spectrum reported for an iron(III) phthalocyanine π–cation radical is the absorption spectrum of $(CN)(CF_3CO_2)Fe(III)Pc(-1)$ [103]. With this limited spectral database for $X_2Fe(III)Pc(-1)$ complexes, very little is known about:

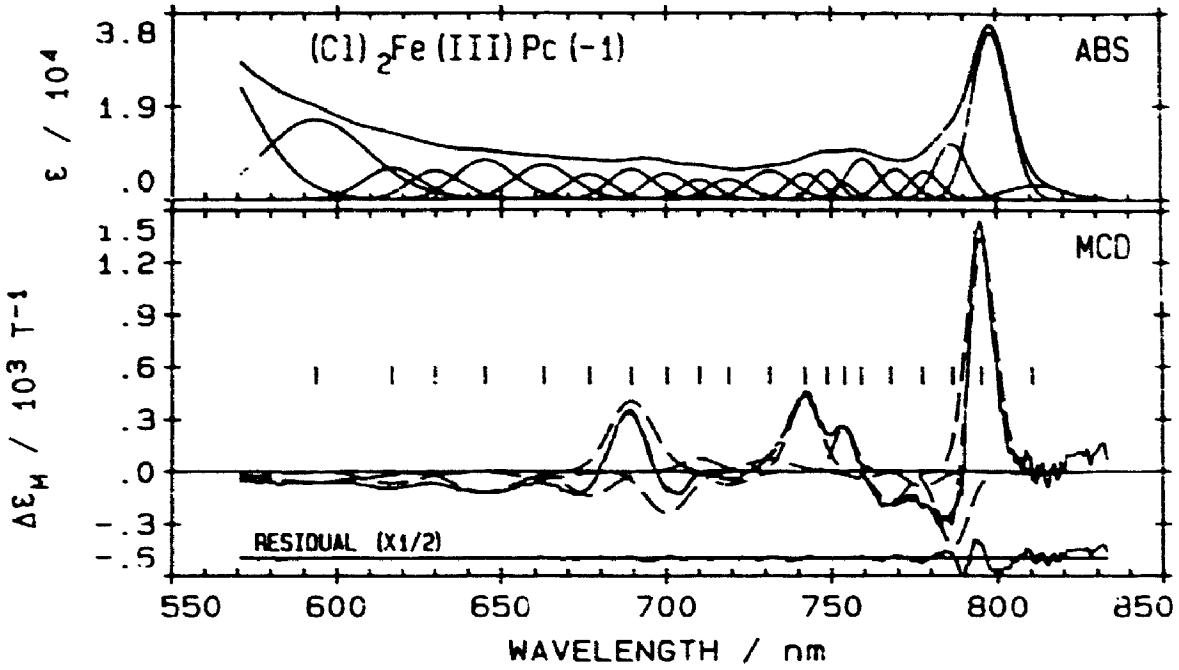

Figure 9–5 Results of a band analysis on the 77 K absorption (ABS) and 4 K MCD spectra for a 1 mm DCM:CB glass of $Cl_2Fe(III)Pc(-1)$ in the visible region (bands 1–21). (a) Absorption: (———) experimental data; (– – –) fitted data; (———) individual bands. (b) MCD: (———) experimental data; (– – –) fitted data; (– – –) individual bands.

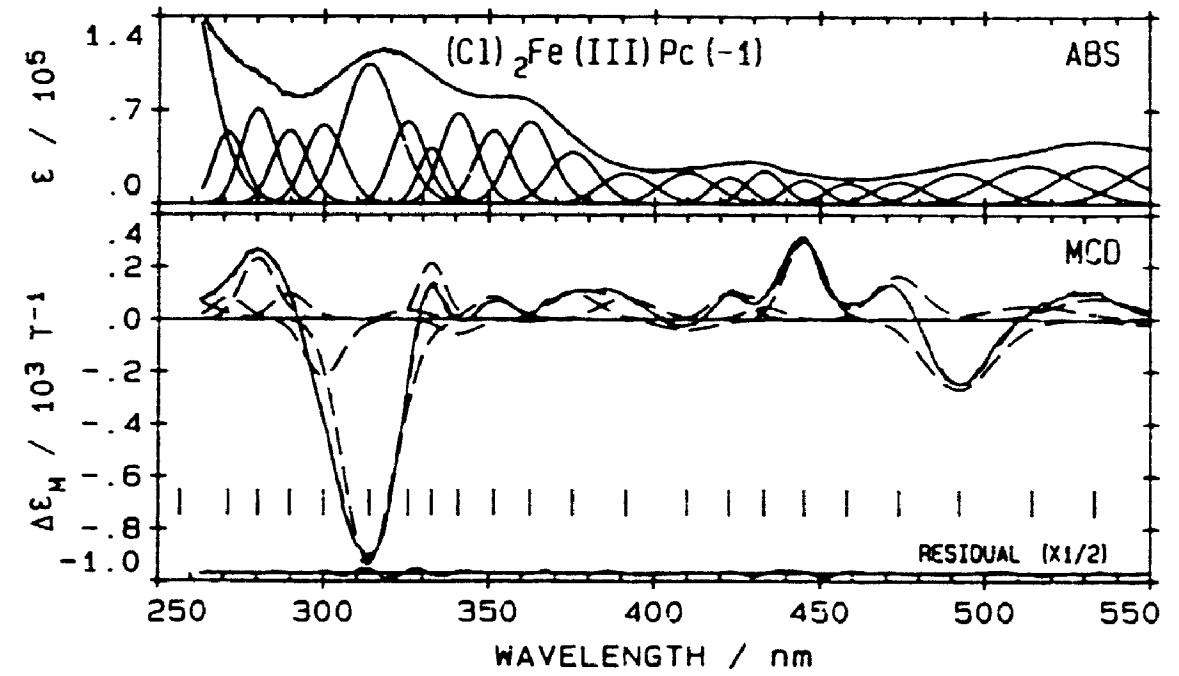

Figure 9–6 Results of a band analysis on the 77 K absorption (ABS) and 4 K MCD spectra for a 1 mmm DCM:CB glass of $Cl_2Fe(III)Pc(-1)$ in the ultraviolet region (bands 21–43). (a) Absorption: (———) experimental data; (– – –) fitted data; (———) individual bands. (b) MCD: (———) experimental data; (– – –) fitted data; (– – –) individual bands.

Table 9-2A

Band-Fitting Parameters[a] for a 70:30 DCM:CB glass of $Cl_2Fe(III)Pc(-1)$ in the Q Band (850 - 550 nm) Region.

band #	ν /cm^{-1}	λ /nm	$\Delta\nu$ /cm^{-1}	D_0[b]	Band type	$\langle\Delta\epsilon_M\rangle_0$[c]	C_0, B_0[d] /10^{-3}	$(B_0, C_0)/D_0$ /10^{-3}
1	12318	812	325	0.242	C	-0.991	-6.501	-26.86
2	12576	795	162	1.843	C	41.16	269.9	146.4
3	12713	787	170	0.545	C	-13.74	-90.07	-165.2
4	12861	778	176	0.254	C	-2.896	-18.99	-74.76
5	13025	768	173	0.304	C	-5.912	-38.77	-127.5
6	13175	759	182	0.403	C	-1.264	-8.170	-20.27
7	13264	754	130	0.108	C	6.157	40.38	373.9
8	13358	749	152	0.242	C	0.167	1.096	4.529
9	13478	742	195	0.268	C	14.50	95.07	354.7
10	13673	731	286	0.413	C	3.599	23.60	57.14
11	13906	719	268	0.259	C	-3.462	-22.71	-87.68
12	14082	710	244	0.227	C	3.088	20.25	89.21
13	14281	700	301	0.366	C	-12.03	-78.85	-215.4
14	14506	689	332	0.464	C	22.12	145.1	312.7
15	14781	677	337	0.385	C	-7.693	-50.46	-131.1
16	15092	663	461	0.704	C	-2.840	-18.62	-26.45
17	15504	645	500	0.844	C	-9.164	-60.09	-71.20
18	15877	630	462	0.561	C	-1.172	-7.686	-13.70
19	16217	617	540	0.701	C	-5.357	-35.12	-50.10
20	16844	594	1040	3.277	C	-8.598	-56.37	-17.20
21	17897	559	1114	6.554	C	-7.617	-49.94	-7.620
22	18032	555	1003	5.674	C	-2.849	-18.68	-3.292

[a]Statistics. Q region: $\lambda_{550-820\ nm}$, χ^2=117.0, $\Sigma(\Delta\epsilon)^2$=1.79×10^5. [b]$D_0=\langle\epsilon\rangle_0/326.6$, where the units of D_0 (dipole strength) are D^2 (Debye units) [25]. [c]$\langle\Delta\epsilon_M\rangle_0$ is the zeroth moment of the MCD. When fitting with C terms the program calculates $\langle\Delta\epsilon_M\rangle_0$. [d]The Faraday C_0 term is calculated directly from the moments as follows: $C_0=\langle\Delta\epsilon_M\rangle_0$.

Table 9-2B

Band-Fitting Parameters[a] for a 70:30 DCM:CB glass of $Cl_2Fe(III)Pc(-1)$ in the B Band (550 – 250 nm) Region.

band #	ν /cm^{-1}	λ /nm	$\Delta\nu$ /cm^{-1}	D_0[b]	Band type	$\langle\Delta\epsilon_M\rangle_0$[c]	C_0, B_0[d] /10^{-3}	$(B_0, C_0)/D_0$ /10^{-3}
1	18766	533	990	4.983	C	10.31	67.57	13.56
2	19452	514	1157	5.579	C	7.261	47.61	8.534
3	20318	492	1004	3.781	C	-31.53	-206.8	-54.69
4	21106	474	801	2.083	C	14.99	98.27	47.18
5	21820	458	718	1.712	C	0.131	0.862	0.504
6	22458	445	675	1.797	C	21.40	140.3	78.07
7	23082	433	702	2.453	C	3.274	21.47	8.753
8	23654	423	733	2.030	C	7.321	48.02	23.66
9	24398	410	1118	3.571	C	-4.459	-29.25	-8.191
10	25548	391	1215	3.619	C	9.247	60.65	16.76
11	26655	375	1179	5.583	C	11.04	72.38	12.96
12	27598	362	1158	8.363	C	-0.896	-5.879	-0.703
13	28449	352	1065	6.681	C	7.778	50.99	7.632
14	29334	341	1110	8.357	C	-5.205	-34.13	-4.084
15	30050	333	871	3.937	C	14.85	97.38	24.73
16	30719	326	1183	7.736	C	3.151	20.66	2.671
17	31860	314	1920	20.51	C	-132.4	-868.3	-42.33
18	33339	300	1498	8.623	C	-23.34	-153.1	-17.75
19	34514	290	1457	7.566	C	9.713	63.69	8.418
20	35677	280	1542	10.02	C	24.01	157.4	15.71
21	36852	271	1509	7.153	C	8.179	53.64	7.499
22	38953	257	3034	4.570	C	15.98	104.8	6.558

[a]Statistics. B region: $\lambda_{250\text{-}550\ nm}$, χ^2=30.6, $\Sigma(\Delta\epsilon)^2$=1.33×10^5. [b]$D_0=\langle\epsilon\rangle_0/326.6$, where the units of D_0 (dipole strength) are D^2 (Debye units) [25]. [c]$\langle\Delta\epsilon_M\rangle_0$ is the zeroth moment of the MCD. When fitting with C terms the program calculates $\langle\Delta\epsilon_M\rangle_0$. [d]The Faraday C_0 term is calculated directly from the moments as follows: $C_0=\langle\Delta\epsilon_M\rangle_0$.

(i) the location of ring and CT transitions in the electronic spectrum, (ii) the orbital degeneracy of the ground state, (iii) the spin (low, intermediate or high) of the ferric ion, and (iv) the aggregation following ring oxidation.

9.3.1 Monomeric $Cl_2Fe(III)Pc(-1)$

The assignment of the (+) MCD band at 795 nm (12 576 cm^{-1}) as Q (Figure 9-5), the saturation of the 2.8 K and 3.92 tesla MCD spectrum (Figure 9-2) and the presence of the spin forbidden ($\Delta M_S=\pm 2$) EPR transition (Figure 9-4) indicate that $Cl_2Fe(III)Pc(-1)$ is monomeric. The location of the Q band at ~795 nm for $Cl_2Fe(III)Pc(-1)$ is within the range of known values for monomeric $[MPc(-1)]^{\cdot +}$ [2,28,35,37,70,71,103]. Saturation of the MCD signal and the calculated g_{av} of 4.66 $\pm$ 0.05 indicate a significant spin-orbital contribution to the ground state. A cofacial $[Fe(III)Pc(-1)]_2^{++}$ dimer is not expected to exhibit EPR spectral intensity, which has been demonstrated for $[LMgPc(-1)]_2^{++}$ (Chapter 5). The presence of the $\Delta M_S=\pm 2$ EPR transition at g=4.267 is consistent with the triplet (S=1) ground spin state expected for monomeric $Cl_2Fe(III)Pc(-1)$.

9.3.2 Allowed Electronic Transitions in Low Spin $Cl_2Fe(III)Pc(-1)$

The ground state of $Cl_2Fe(III)Pc(-1)$ is identified as low spin ^3F_u, from the EPR and MCD spectral results. Selected molecular orbitals and allowed electronic transitions for the ^3E_u ground state are plotted in Figure 9-7. In addition to the allowed $\pi \rightarrow \pi^*$ and CT transitions, low lying $\pi \rightarrow \pi$ transitions are expected. The allowed CT transitions, their excited states, and their transition polarizations are shown in Table 9-3.

Since the ground state in $Cl_2Fe(III)Pc(-1)$ is orbitally degenerate, the MCD spectrum will be dominated by two types of C terms. The MCD C_A term is xy polarized and results from the $^3E_u \rightarrow {}^3A_{iu}, {}^3B_{iu}$ (i=1,2) transitions shown in

Table 9–3
Allowed Charge Transfer Transition for Low Spin (S=1) $X_2Fe(III)Pc(-1)$[a]

One Electron Transition	Excited State[c]	Charge Transfer	Polarization of Transition	MCD Term Expected[b]
$a_{1u}, a_{2u} \rightarrow a_{1g}, b_{1g}$	^3E_g	L → M	Z	C_B
$b_{1u}, b_{2u} \rightarrow a_{1g}, b_{1g}$	^3E_g	L → M	Z	C_B
$a_{1u} \rightarrow e_g$	$^3A_{1g}$	L → M	XY	C_A
$a_{2u} \rightarrow e_g$	$^3A_{2g}$	L → M	XY	C_A
$b_{1u} \rightarrow e_g$	$^3B_{1g}$	L → M	XY	C_A
$b_{2u} \rightarrow e_g$	$^3B_{2g}$	L → M	XY	C_A
$b_{1g} \rightarrow b_{1u}, b_{2u}$	^3E_g	M → L	Z	C_B
$e_g \rightarrow b_{1u}$	$^3A_{ig}, {}^3B_{ig}$	M → L	XY	C_A
$e_g \rightarrow b_{2u}$	$^3A_{ig}, {}^3B_{ig}$	M → L	XY	C_A

[a]The ground state configuration of the iron 3d orbitals is $(b_{2g})^2(e_g)^3$ and the ground state symmetry is ^3E_u. [b]The subscripts A and B denote that the transitions are xy and z polarized, repectively. [c]i=1,2.

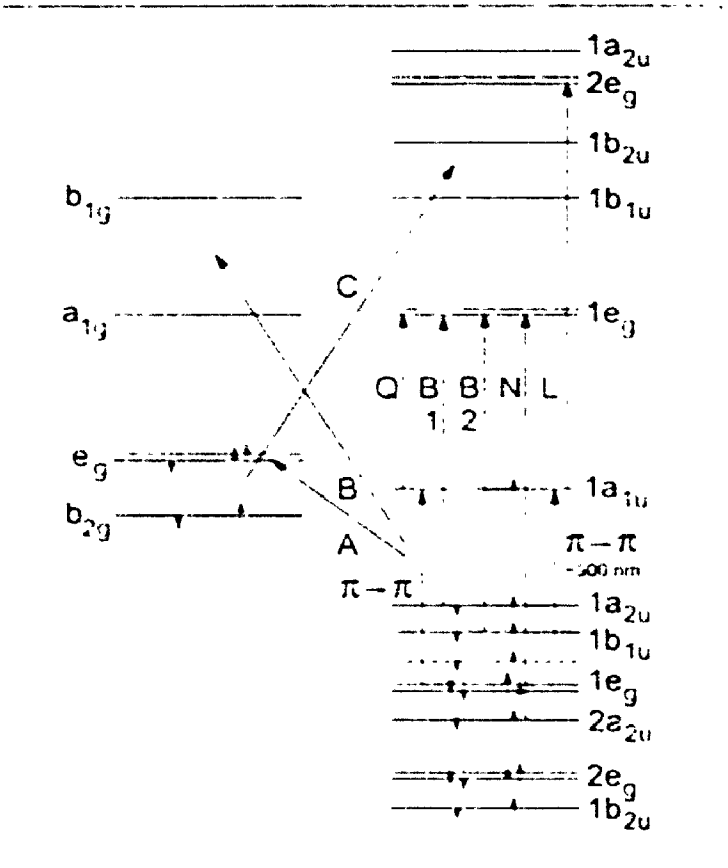

Figure 9–7 Selected molecular orbitals and allowed electronic transitions for the ^3E_u ground state of $X_2Fe(III)Pc(-1)$. The arrows labelled A, B and C represent the allowed $a_{iu}(\pi), b_{iu}(\pi) \rightarrow e_g(d\pi)$, $a_{iu}(\pi), b_{iu}(\pi) \rightarrow a_{1g}(d), b_{1g}(d)$ and $e_g(d\pi), b_{2g}(d) \rightarrow a_{2u}(\pi^*), b_{iu}(\pi^*)$ (i=1,2) CT transitions, respectively.

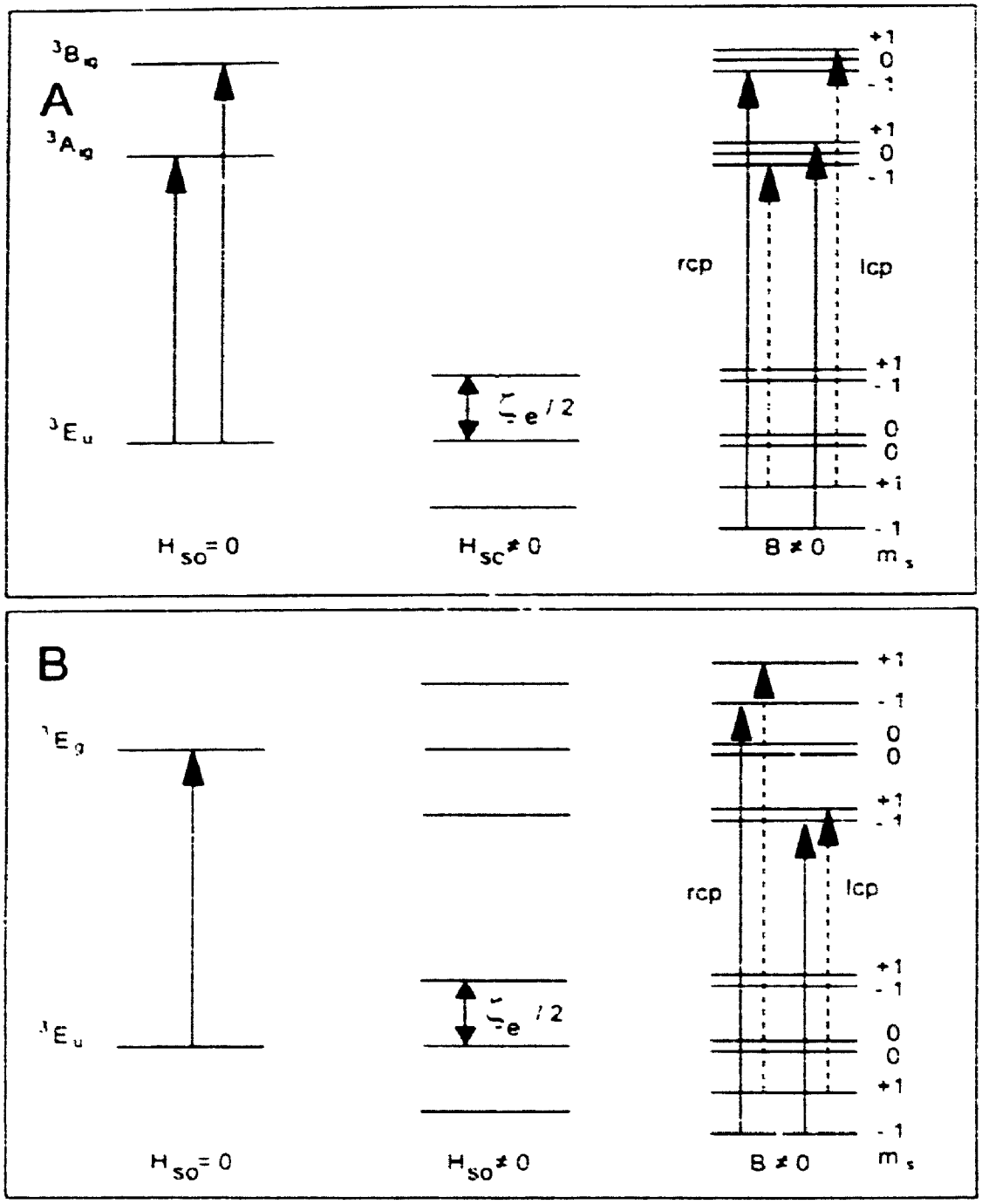

Figure 9-8 Energy level diagrams for (A) the $^3E_u \rightarrow {}^3A_{ig}, {}^3B_{ig}$ (i=1,2) and (B) the $^3E_u \rightarrow {}^3E_g$ transitions. The Zeeman and the spin orbit (ζ_e) splittings are highly exaggerated with respect to the energy separation between electronic states. Right circularly polarized (rcp) and left circularly polarized (lcp) transitions from the lowest energy Kramers doublet are plotted. The solid arrows represent transitions from the low energy Zeeman spit component of the doublet, while the dotted arrows represents transition from the higher energy component.

Figure 9-8A. The xy polarized transitions, shown as solid arrows in Figure 9-8A, will appear in the MCD spectra as individual C_A terms, with either (+) or (−) intensities. The second MCD term is the C_B term which arises from the z polarized $^3E_u \rightarrow {}^3E_g$ transition shown in Figure 9-8B. This transition has an A term shape in the MCD spectrum, which arises from two oppositely signed C terms separated by the spin-orbit coupling energy (ζ_e).

9.3.3 Assignment of the Spectral Fits for Cl_2Fe(III)Pc(−1)

The spectral assignments in previous chapters are part of a continuing process that utilizes the results from simple systems to analyse the more complicated systems. Three examples that exemplify this process are: (i) MgPc(−2) fits used to isolate $\pi \rightarrow \pi^*$ transitions from $\pi \rightarrow \pi$ transitions in MgPc(−1), (ii) MgPc(−2) fits used to isolate $\pi \rightarrow \pi^*$ transitions from CT transitions in low spin L_2Fe(II)Pc(−2), and (iii) low spin L_2Fe(II)Pc(−2) fits used to isolate LMCT transitions from MLCT transitions in low and intermediate spin [Fe(III)Pc(−2)]$^+$. This work progresses one further step in the assignment of the Cl_2Fe(III)Pc(−1) spectra which are comprised of $\pi \rightarrow \pi^*$, $\pi \rightarrow \pi$, MLCT, and LMCT transitions. The spectral fits of monomeric [MgPc(−1)]$\cdot^+$ (Chapter 5), intermediate spin (Fo)Fe(III)Pc(−2) (Chapter 8), low spin Na[$(CN)_2$Fe(II)Pc(−2)] (Chapter 7) and Cl_2Fe(III)Pc(−1) are plotted in Figure 9-9. The [MgPc(−1)]$\cdot^+$ fit provides the general location of the low lying $\pi \rightarrow \pi$ transitions, while the (Fo)Fe(III)Pc(−2) and the Na[$(CN)_2$Fe(III)Pc(−2)] fits outline the general location of MLCT and LMCT transitions.

9.3.3.1 The Q, B1, B2, N and L Bands

The spectral fits for MgPc (Chapters 4-5) and FePc (Chapters 6-8) indicate that varying the axial ligands, changing between the ferric and ferric oxidation states, and oxidizing the phthalocyanine ring have little effect on the B2, N and L band energies,

but cause wide variances in the Q and B1 band energies. Both effects have to be taken into account as we assign these bands in the absorption and MCD spectra of $Cl_2Fe(III)Pc(-1)$. It is also noted that the assignment of the (+) MCD C_A term at 795 nm as Q requires the B1, B2, N and L band to have (+), (–), (+), and (+) C_A terms. The bands at 314 nm (31 860 cm^{-1}) (–), 280 nm (35 677 cm^{-1}) (+) and 257 nm (38 953 cm^{-1}) (+) are assigned as B2, N and L, respectively. Utilizing the location of the Q and B1 bands, at 828 and 387 nm ,respectively, for $[MgPc(-1)]^{\cdot +}$ and positioning the Q band at 795 nm for $Cl_2Fe(III)Pc(-1)$, results in the assignment of the B1 band to the transition at 375 nm (26 655 cm^{-1}).

9.3.3.2 Low Lying $\pi \rightarrow \pi$ Transitions

The spectral fits of monomeric and dimeric MgPc(–1) (Chapter 5) demonstrated the presence of two ring based $\pi \rightarrow \pi$ transitions between 400 and 550 nm. The broad absorption band located near 500 nm is the familiar ring oxidation "marker" band and is a z polarized transition, while the higher energy band is xy polarized. The bands at 445 nm (22 458 cm^{-1}) (+) and 533 nm (18 766 cm^{-1}) (+) are assigned as the xy and z polarized transitions, respectively. Because of its broadness, the 533 nm band is assigned as the $\pi \rightarrow \pi$ marker band, but its MCD signature is not consistent with a z polarized ($^3E_u \rightarrow {}^3E_g$) transition. This transition should appear in the MCD as a derivative shaped band arising from two oppositely signed C terms, not the single (+) MCD C term observed. Two possibilities that explain this discrepancy are. (i) the transition is actually xy polarized, and (ii) the transition is z polarized, but is obscured by an intense overlapping xy polarized transition. Since the MCD results for MgPc(–1) [28] and ZnPc(–1) [35,37] provide irrefutable evidence that this transition is z polarized, then the two C_B terms must be present under an overlapping intense C_A term. The 445 nm band is assigned to the $1e_g(\pi) \rightarrow 1a_{1u}(\pi)$ transition because the (+) MCD C_A term is expected for the transition to the $^3A_{2g}$ excited

state, and because the decrease in this band's energy, from $[MgPc(-1)]^{\cdot +}$ (Figure 9-9) to $Cl_2Fe(III)Pc(-1)$, is consistent with the decrease in the 533 nm "marker" band energy and the increase in the Q band energy.

9.3.3.3 Charge Transfer Bands

Following ring oxidation, the only "new" CT band arises from the z polarized $b_{2g}(d) \rightarrow 1a_{1u}(\pi)$ transition. This band is expected on the red side of the Q band and the spectral results for $Cl_2Fe(III)Pc(-1)$ indicate that it appears beyond the 900 nm spectral cutoff. The electron vacancy in the $1a_{1u}(\pi)$ orbital yield this additional MLCT, but the triplet spin of the ^3E_u ground state results in a previously allowed LMCT transition becoming formally forbidden. The $1a_{1u}(\pi) \rightarrow e_g(d\pi)$ transition is spin forbidden and the LMCT1 band will either be absent or a very weak band in the electronic spectra of $Cl_2Fe(III)Pc(-1)$. These examples are the only differences between the allowed CT transitions in low spin L(X)Fe(III)Pc(-2) and low spin $Cl_2Fe(III)Pc(-1)$

The excited states of the MLCT1 and MLCT2 transitions are composed of the four nondegenerate ($^3A_{1g}$, $^3A_{2g}$, $^3B_{1g}$, and $^3B_{2g}$) states. As with low spin L(X)Fe(III)Pc(-2), these bands appear in the low temperature MCD spectrum as pairs of oppositely signed C_A terms. The four bands at 742 nm (13 478 cm^{-1}) (+), 754 nm (13 264 cm^{-1}) (+), 768 nm (13 025 cm^{-1}) (-), and 787 nm (12 713 cm^{-1}) (-) are assigned to MLCT1. The 410 nm (24 398 cm^{-1}) (-), 423 nm (23 654 cm^{-1}) (+), and 433 nm (23 082 cm^{-1}) (+) bands are assigned to MLCT2. The fourth (-) C_A term, for MLCT2, is obscured by intense (+) C terms. The red shifts in MLCT band energies following ring oxidation are consistent with the observed red shifts in the Q and B1 band energies following ring oxidation.

The excited states of the LMCT2 ($1a_{2u}(\pi) \rightarrow e_g(d\pi)$), LMCT3 ($1b_{1u}(\pi) \rightarrow e_g(d\pi)$), LMCT4 ($1a_{2u}(\pi) \rightarrow e_g(d\pi)$), and LMCT5 ($1b_{2u}(\pi) \rightarrow e_g(d\pi)$) transitions are $^3A_{2g}$,

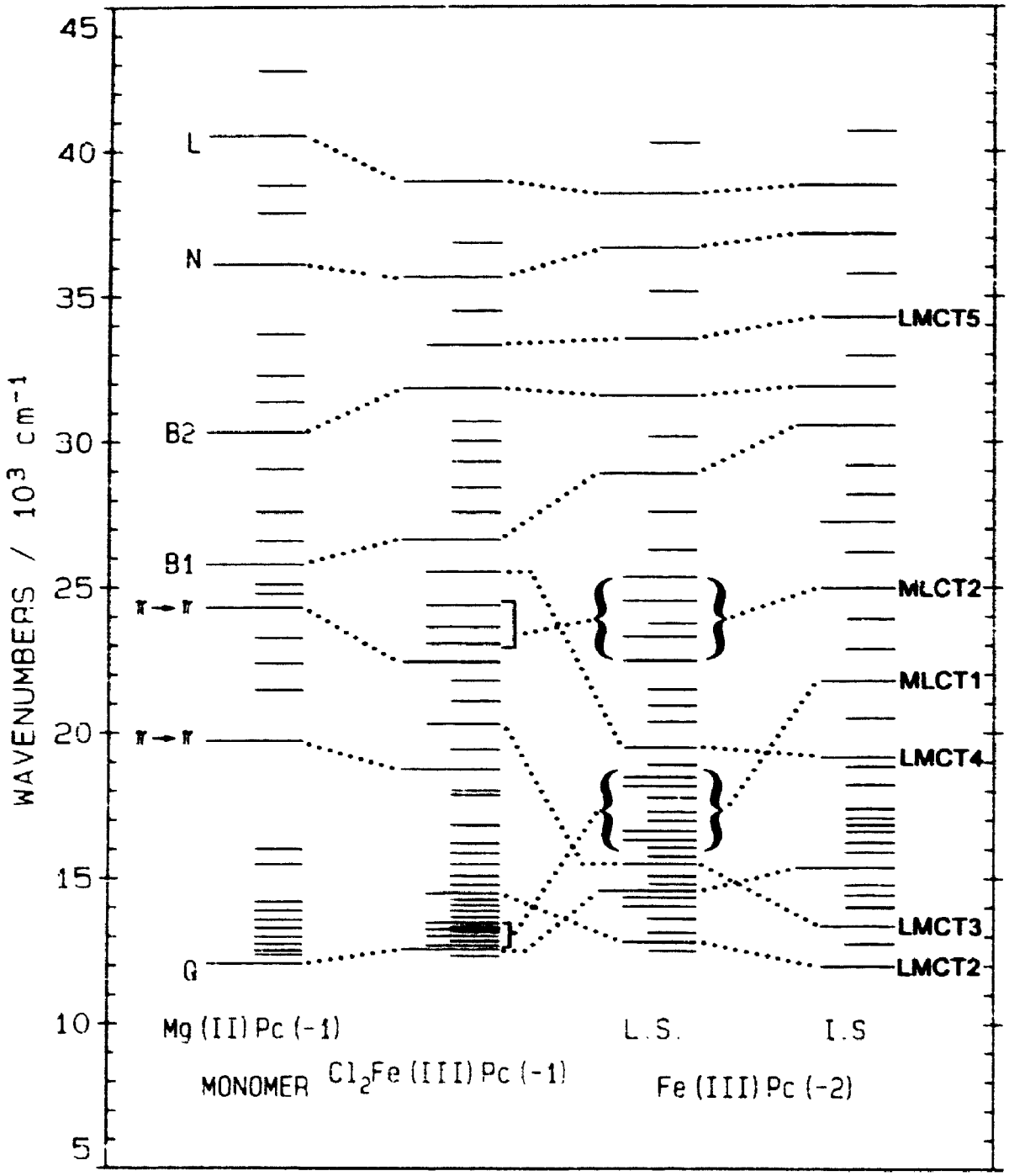

Figure 9-9 Comparison of the fitted band centre energies for $[(im)_nMgPc(-1)]^{+}$ (monomer; Chapter 5), $Cl_2Fe(III)Pc(-1)$, (Cl)Fe(III)Pc(-2) (Chapter 8) and $Na[(CN)_2Fe(III)Pc(-2)]$ (Chapter 7). The lengths of the plotted lines are used to discriminate between the types of transitions, with the long lines representing ring ($\pi \rightarrow \pi$ and $\pi \rightarrow \pi^*$) transitions, the intermediate lines representing CT transitions and the small lines representing unassigned transitions.

$^3B_{1g}$, $^3A_{2g}$, and $^3B_{2g}$, respectively. From 900 to 250 nm, the four transitions will appear in the MCD spectrum with a sequence of (+) (−) (+) (−) C_A terms. The transitions at 689 nm (14 506 cm^{-1}) (+), 492 nm (20 318 cm^{-1}) (−), 391 nm (25 548 cm^{-1}) (+), and 300 nm (33 339 cm^{-1}) are assigned as LMCT2–5.

9.3.4 Comparison between the Deconvolution Data For MgPc(−1), Cl_2Fe(III)Pc(−1) and L(X)Fe(III)Pc(−2)

Several interesting trends are observed from the four spectral fits in Figure 9–9. These are: (i) the energies of the Q and B1 bands shift in the same direction, (ii) the energies of the two $\pi \rightarrow \pi$ bands shift in the opposite direction to shifts in the Q and B1 band energies, (iii) the LMCT band energies increase with the removal of electrons from the phthalocyanine ring, (iv) the MLCT band energies decrease with the removal of electrons from the phthalocyanine ring, (v) there is no systematic variation in the higher energy ($\nu > 30\ 000\ cm^{-1}$) bands, and (vi) the energy separation between the LMCT2/LMCT3, MLCT1/MLCT2, and B1/B2 band pairs increases with the removal of electrons from the phthalocyanine ring. Because the Q and B1 bands are known to arise from transitions into mixed states [21], it is not unexpected that variations in their energies are in the same direction. The band energy shifts, listed in examples (ii) to (iv), suggest an increase in the $e_g(d\pi)$ and $1a_{1u}(\pi)$ orbital energies with the removal of electrons from these orbitals. If the energy of the $1a_{1u}(\pi)$ orbital in Figure 9–7 increases, then a decrease, or red shift, in the energies of the Q state (and B1, since it is coupled with the Q) is expected together with an increase in the energies of the $\pi \rightarrow \pi$ bands. An increase in the $e_g(d\pi)$ orbital energy (Figure 9–7) will cause a decrease in the MLCT transition energies and an increase in the LMCT transition energies. The lack of systematic variation in the high energy ring and CT transfer transitions suggests that oxidation effects are most pronounced for the bands whose ground or excited state molecular orbitals are either oxidized or couple into

Table 9–4
Assigned transitions for low spin (S=1) $Cl_2Fe(III)Pc(-1)$[a].

Band	One Electron Transition	Excited State[b]	C Term Sign	λ /nm	ν /cm⁻¹
Q	$1a_{1u}(\pi)\rightarrow 1e_g(\pi^*)$	$^3A_{1g}$	+	7[illegible]5	12 576
B1	$1a_{2u}(\pi)\rightarrow 1e_g(\pi^*)$	$^3A_{2g}$	+	3[illegible]5	26 655
B2	$1b_{1u}(\pi)\rightarrow 1e_g(\pi^*)$	$^3B_{1g}$	-	314	31 860
N	$2a_{2u}(\pi)\rightarrow 1e_g(\pi^*)$	$^3A_{2g}$	+	280	35 677
L	$1a_{1u}(\pi)\rightarrow 2e_g(\pi^*)$	$^3A_{1g}$	+	257	38 953
π→π	$1e_g(\pi)\rightarrow 1a_{1u}(\pi)$	$^3A_{2g}$	+	445	22 458
π→π	??????$\rightarrow 1a_{1u}(\pi)$	^3E_g	+	533	18 766
MLCT1	$e_g(d\pi)\rightarrow 1b_{1u}(\pi^*)$	$^3B_{1g}$	-	787	12 713
		$^3B_{1g}$	-	768	13 025
		$^3A_{1g}$	+	754	13 264
		$^3A_{1g}$	+	742	13 478
MLCT2	$e_g(d\pi)\rightarrow 1b_{2u}(\pi^*)$	$^3A_{1g}$	+	433	23 082
		$^3A_{1g}$	+	423	23 654
		$^3B_{1g}$	-	410	24 398
LMCT2	$1a_{2u}(\pi)\rightarrow e_g(d\pi)$	$^3A_{2g}$	+	689	14 506
LMCT3	$1b_{1u}(\pi)\rightarrow e_g(d\pi)$	$^3B_{1g}$	-	492	20 318
LMCT4	$1a_{2u}(\pi)\rightarrow e_g(d\pi)$	$^3A_{2g}$	+	391	25 548
LMCT5	$1b_{2u}(\pi)\rightarrow e_g(d\pi)$	$^3B_{2g}$	-	300	33 339

[a]The ground state configuration of the iron 3d orbitals is $(b_{2g})^2(e_g)^3$ and the symmetry of the ground state is ^3E_u. [b]i=1,2.

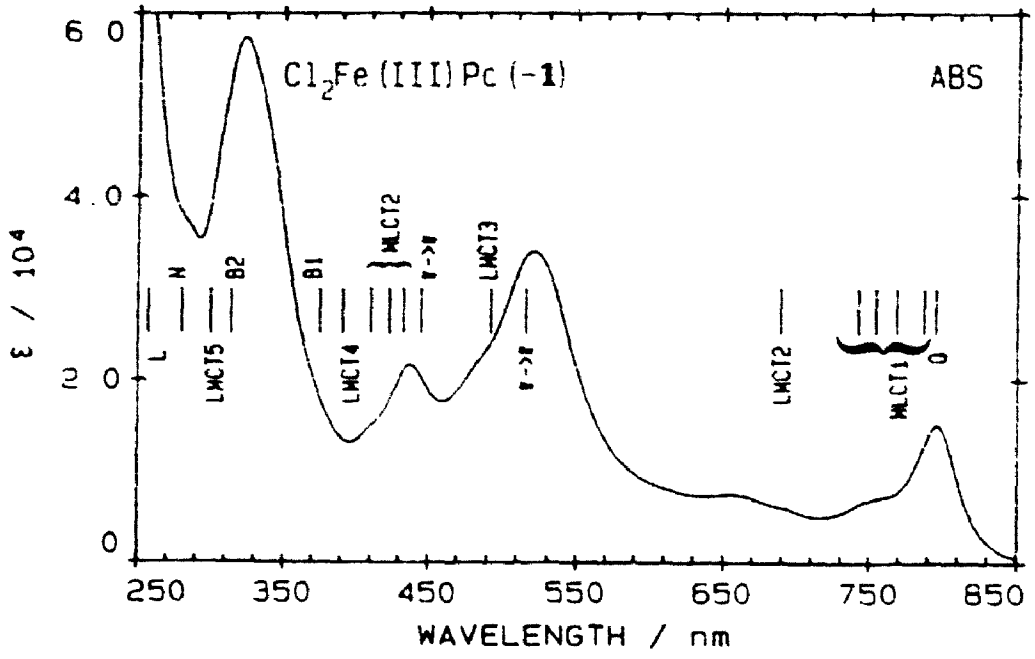

Figure 9–10 The room temperature (300 K) absorption spectra of $Cl_2Fe(III)Pc(-1)$ in DCM. The location of the assigned $\pi \rightarrow \pi$, $\pi \rightarrow \pi^*$, MLCT and LMCT band centres, which were obtained from deconvolution of the low temperature spectra, are represented by the labelled vertical lines.

oxidized orbitals. The increased energy separation for the three pairs of bands (B1/B2, MLCT1/MLCT2, LMCT2/LMCT3) upon ring oxidation is consistent with the results described in Chapters 7 and 8, and is directly related to the removal of electron density from the phthalocyanine ring.

9.4 CONCLUSIONS

The presence of a single Q band at 795 nm in the absorption spectrum of $Cl_2Fe(III)Pc(-1)$ indicates that it is a pure monomer. The low temperature EPR spectrum recorded for $Cl_2Fe(III)Pc(-1)$ is consistent with a triplet (S=1) spin state. The EPR spectrum is dominated by the spin forbidden ($\Delta M_S=\pm 2$) band at g=4.2670 (the bandwidth is 30 gauss) and the two pairs of weak bands between 3200 and 3600 gauss represent spin transitions along the anisotropic xy and z axis. An average orbital g factor of 4.66 $\pm$ 0.05 was obtained from the low temperature MCD spectra of $Cl_2Fe(III)Pc(-1)$. The MCD and EPR spectral results were used to assign the ground state in $Cl_2Fe(III)Pc(-1)$ as ^3E_u. Table 9-4 and Figure 9-10 summarize the analysis of the low temperature absorption and MCD spectra for $Cl_2Fe(III)Pc(-1)$.

CHAPTER 10

GENERAL CONCLUSIONS

The major focus of this thesis is a spectroscopic study of the oxidation chemistry of metallophthalocyanines and the assignment of the state–state transitions that comprise the electronic spectra. Peripherally substituted magnesium and zinc phthalocyanine–N–isologs ($MgPcN_4$, $ZnPcN_4$); and magnesium phthalocyanine, iron phthalocyanine, and their oxidation products were studied using the techniques of ultraviolet–visible absorption, magnetic circular dichroism (MCD) and electronic paramagnetic resonance (EPR) spectroscopy.

Summary

Metallophthalocyanine–N–Isologs

Deconvolution results for the absorption and MCD spectra of $MPcN_4(-2)$ (M = Zn, Mg) illustrate the effect of peripheral substitution on the inner 18–π–electron system. The large zero–field splitting ($\Delta E \approx 250\ cm^{-1}$) of the Q_x and Q_y bands in $MPcN_4(-2)$ arises from the asymmetric arrangement of the fused pyridine rings and the resulting reduction in symmetry ($D_{4h} \rightarrow D_{2h}$) of the inner 18–$\pi$–electron system.

Magnesium Phthalocyanine

Oxidation of MgPc(−2) is possible using chemical, electrochemical and photochemical methods. Through the measurement of low temperature absorption and EPR spectra, solutions of MgPc(−1) are shown to be equilibrium mixtures of monomer and dimer. Pure monomer and dimer absorption and MCD spectra are obtained and subjected to spectral deconvolution. In addition to the five major ring transitions (Q, B1, B2, N and L) present for neutral and ring oxidized magnesium phthalocyanine,

two bands arising from $\pi \rightarrow \pi$ transitions into the oxidized $1a_{1u}(\pi)$ orbital are isolated in the monomer and the dimer spectra. The 500 nm $\pi \rightarrow \pi$ transition is the customary marker band for ring oxidation.

Iron Phthalocyanine

The more interesting and difficult molecule to study is iron phthalocyanine (FePc). Analysis of the absorption and MCD spectra for various low spin $L_2Fe(II)Pc(-2)$ complexes isolates two degenerate $[e_g(d\pi) \rightarrow 1b_{1u}(\pi), 1b_{2u}(\pi)]$ MLCT transitions within the spectral "window" of MgPc(−2), which are present in all neutral and oxidized iron phthalocyanine complexes. The π donor/π acceptor strengths of the axial ligands have a pronounced influence on the energies of the ring and charge transfer transitions. An inductive effect utilizing the iron(III) $e_g(d\pi)$ orbitals as an electron conduit to remove (or add) electron density from (or to) the phthalocyanine ring to strong (or from weak) π acceptor axial ligands explains the differences in the electronic spectra of the various $L_2Fe(II)Pc$ (−2) complexes.

Oxidation of Fe(II)Pc(−2) occurs first at the iron centre (ferrous to ferric) then at the phthalocyanine ring. The hole introduced into the $e_g(d\pi)$ molecular orbital, upon metal oxidation, results in the presence of several degenerate LMCT $[a_{iu}(\pi), b_{iu}(\pi) \rightarrow e_g(d\pi);\ i=1,2]$ transitions in the absorption and MCD spectra. The number of axial ligands in iron(III) phthalocyanines is directly related to the spin state of the molecule. Low temperature EPR and MCD spectra indicate that five coordinate (one axial ligand) (X)Fe(III)Pc(−2) is intermediate spin (S=3/2; $^4A_{2g}$ ground state), while six coordinate (two axial ligands) L(X)Fe(III)Pc(−2) is low spin (S=1/2; ^2E_g ground state). Spectral fits of the low and intermediate spin $[Fe(III)Pc(-2)]^+$ complexes are used to assign degenerate $\pi \rightarrow \pi^*$, MLCT and LMCT transitions.

Iron(III) phthalocyanine π−cation radical is a pure monomer, as demonstrated by the triplet (S=1) low temperature EPR spectrum, and has an orbitally degenerate (^3E_u)

ground state. The spectral analysis for low spin $Cl_2Fe(III)Pc(-2)$ allows the assignment of $\pi \rightarrow \pi^*$, $\pi \rightarrow \pi$, MLCT, and LMCT transitions to its absorption and MCD spectra.

Significance

The results presented in this study allow us to characterize the transitions that comprise the electronic spectra of neutral and oxidized magnesium and iron phthalocyanine. The fits of the absorption and MCD spectra of these metallophthalocyanines not only adds to the general knowledge about phthalocyanines, but the fitting parameters reported here are invaluable to theoretical chemists attempting to refine their calculations. Since the current interest in the phthalocyanines appears focused on their redox chemistry, the spectra recorded both during and after metal (iron phthalocyanine only) and ring oxidation (both magnesium and iron phthalocyanine) allow us the opportunity to study the changes in the energies of the ground and excited states upon oxidation. The extra bands appearing in the electronic spectra due to the holes in the oxidized iron $e_g(d\pi)$ and phthalocyanine $a_{1u}(\pi)$ orbitals serve as additional probes of the orbital arrangement within the metallophthalocyanine molecule.

The spectral results for low and intermediate spin iron(III) phthalocyanine demonstrate the interesting axial ligand chemistry of iron pthalocyanine. The removal of an axial ligand in iron(III) phthalocyanine is followed by a conversion from low (S=1/2) to intermediate spin (S=3/2) and a displacement of iron out of the plane of the phthalocyanine ring. The absorption and MCD spectral envelopes are quite different for the low and intermediate spin complexes. Although deconvolution results for these two Fe(III)Pc(-2) complexes are important to theoreticians, the most interesting aspects of these results are the changes in spin state and structure of iron(III) phthalocyanine following the addition or removal of axial ligands, which can be followed in the electronic spectra. The interconversion between low and

intermediate spin iron(III) phthalocyanines is an ideal molecular system for researchers attempting to develop molecular electronic devices.

APPENDIX

The Quality of the Metallophthalocyanine Spectra

Since the reported spectra were measured on metallophthalocyanine complexes which were present in solution at concentrations of about 10^{-5} mol L^{-1}, the purity of the prepared complexes can affect the quality of the spectra. The mass spectra fragmentation patterns of the purified metallophthalocyanines were used to ensure that there was no chemical modification of the phthalocyanine ring. Absorption spectra were measured on at least three samples (each sample was prepared from a different group of starting materials) of each MPc complex. The ability to accurately reproduce the absorption spectra in three samples was used to verify the quality of the samples and the spectra. When literature spectra were available they were compared to our measured spectra as a final check of the purity.

Nomenclature

The term neutral phthalocyanine is employed when the net charge on the metallophthalocyanine (MPc) molecule is zero. In a neutral metallophthalocyanine the metal is in the +2 oxidation state and the phthalocyanine ring in the −2 oxidation state. The naming of the ring oxidized complexes (the phthalocyanine ring is oxidized to its −1 oxidation state) as metallophthalocyanine π−cation radicals takes into account the presence of an unpaired π electron on the phthalocyanine ring and the net positive charge on the metallophthalocyanine ($[M(II)Pc(-1)]^+$) molecule.

Significant Digits in Wavenumber Values

Although the values for wavenumbers are only correct to $\pm$ 50 cm^{-1}, they are reported with an additional (unsignificant) digit to ensure that there is no rounding off error when wavenumbers are converted to wavelengths.

REFERENCES

1. Stillman, M.J.; Nyokong, T. In *Phthalocyanines: Properties and Applications;* Leznoff, C.C., Lever, A.B.P., Eds., VCH Publications: New York, 1989; pp 133-209.
2. Stillman, M.J. In *Phthalocyanines: Principles and Applications;* Leznoff, C.C., Lever, A.B.P., Eds., VCH Publications: New York, in press.
3. Bartholomew, C.R. Ph.D. Theis, Univerisy of Strathclyde, United Kingdom, **1987**.
4. Darwent, J.R.; Douglas, P.; Harriman, A.; Porter, G.; Richoux, M.C. *Cooord. Chem. Rev.* **1982**, *44*, 83-125.
5. Elliot, C.M.; Hershenhart, E.J. *J. Am. Chem. Soc.* **1982**, *104*, 7519-7526.
6. Spikes, J. D. *Photochem. Photobiol.* **1986**, *43*, 691.
7. Palmer, S.M.; Stanton, J.L; Martinsen, J.; Ogawa, M.Y.; Heuer, W.B.; Van Wallendael, S.E.; Hoffman, B.M.; Ibers, J.A. *Mol. Cryst. Liq. Cryst.* **1985**, *125*, 1-11.
8. Yamakado, H.; Yakushi, K.; Kosugi, N.; Kuroda, H.; Kawamoto, A.; Tanaka, J.; Sugano, T.; Kinoshita, M.; Hino, S. *Bull. Chem.Soc. Jpn.* **1989**, *62*, 2267-2272.
9. Almeida, M.; Kanatzidis, M.G.; Tonge, L.M.; Marks, T.J.; Marcy, H.O.; McCarthy, W.J.; Kannewurf, C.R. *Solid State Commun.* **1987**, *63*, 457-461.
10. Hoffman, B.M.; Ibers, J.A. *Acc. Chem. Res.* **1983**, *16*, 15-21.
11. Marks, T.J. *Science* **1985**, *227*, 881-889.
12. Kasuga, K.; Tsutsui, M. *Coord. Chem. Rev.* **1980**, *32*, 67-95.
13. Dandridge, A.E.; Drescher, H.A.; Thomas, J. (to Scottish Dyes Ltd.), British Patent 322,169 **1929**.
14. Linstead, R.P. *J. Chem. Soc.* **1936**, 1195-1209.
15. Dent, C.E.; Linstead, R.P.; Lowe, A.R. *J. Am. Chem. Soc.* **1934**, 1033-1039.
16. Linstead, R.P.; Robertson, J.M. *J. Chem. Soc.* **1936**, 1195-1209.
17. Robertson, J.M. *J. Chem. Soc.* **1935**, 615-621.
18. Robertson, J.M.; Woodward, I. *J. Chem. Soc.* **1937**, 219-230.
19. Robertson, J.M.; Woodward, I. *J. Chem. Soc.* **1940**, 36-48.
20. Moser, F.H.; Thomas, A.L *The Phthalocyanines*; CRC Press: Boca Raton, Fl., 1983.
21. Gouterman, M. In *The Porphyrins*. Vol. III, Part A, *Physical Chemistry*;

Dolphin, D., Ed.; Academic Press: New York, 1989, 1–165

22. Lever, A.B.P.; Licoccia, S.; Magnell, K.; Minor, P.C.; Ramaswany, B.S. *Adv. Chem. Ser.* **1982**, *201*, 237–252.

23. Lever, A.B.P.; Pickens, S.R.; Minor, P.C.; Licoccia, S.; Ramaswany, B. S.; Magnell, K. *J. Am. Chem. Soc.* **1981**, *103*, 6800–6806.

24. Barth, G.; Dawson, J.H.; Dolinger, P.M.; Linder, R.E.; Bunnenberg, E.; Djerassi, C. *Anal. Biochem.* **1975**, *65*, 100–108.

25. Piepho, S.B.; Schatz, P.N. *Group Theory in Spectroscopy, with Applications to Magnetic Circular Dichroism*; John Wiley and Sons, **1983**.

26. Nyokong, T.; Gasyna, Z.; Stillman, M.J. *Inorg. Chem.* **1987**, *26*, 1087–1095.

27. Ough, E.A.; Nyokong, T.; Creber, K.A.M.; Stillman, M.J. *Inorg. Chem.* **1988**, *27*, 2725–2732.

28. Ough, E.A.; Gasyna, Z.; Stillman, M.J. *Inorg. Chem.* **1991**, *30*, 2301–2310.

29. Schaffer, A.M.; Gouterman, M.; Davidson, E.R. *Theoret. Chim. Acta* **1973**, *30*, 9–30.

30. Schaffer, A.M.; Gouterman, M. *Theoret. Chim Acta* **1972**, *25*, 62.

31. Mack, J.; Stillman, M.J. To be published.

32. Orti, E.; Bredas, J.L.; Clarisse, C. *J. Chem. Phys.* **1990**, *92*, 1228–1234.

33. Linstead, R.P.; Lowe, A.R. *J. Chem. Soc.* **1934**, 1022.

34. Martin, K.A.M., M.Sc. Thesis, The University of Western Ontario, London, Ontario, Canada, **1979**.

35. Nyokong, T.N.; Ph.D. Thesis, The University of Western Ontario, London, Ontario, Canada, **1986**.

36. Nyokong, T.; Stillman, M.J. *J. Autom. Chem.* **1986**, *8*, 122–133.

37. Nyokong, T.; Gasyna, Z.; Stillman, M.J. *Inorg. Chem.* **1987**, *26*, 548–553.

38. Gasyna, Z.; Browett, W.R.; Nyokong, T.; Kitchenham, R.; Stillman, M.J. *Chemom. Intell. Lab. Syst.* **1989**, *5*, 233–246.

39 Mack, J.; Stillman, M.J. To be published.

40. Browett, W.R.; Stillman, M.J. *Comput. Chem.* **1987**, *11*, 241–250.

41. Browett, W.R.; Stillman, M.J. *Comput. Chem.* **1987**, *11*, 73–82.

42. Lever, A.B.P.; Mileeva, E.R.; Speier, G. In *Phthalocyanines: Principles and Applications;* Leznoff, C.C., Lever, A.B.P., Eds., VCH Publications: New York, in press.

43. Nevin, W.A.; Liu, W.; Melnik, M.; Lever, A.B.P. *J. Electrochem.* **1986**, *213*, 217–234.

44. Lever, A.B.P.; Hempstead, M.R.; Leznoff, C.C.; Liu, W.; Melnik, M.; Nevin, W.A.; Seymour, P. *Pure Appl. Chem.* **1986**, *58*, 1467–1476.

45. Martin, K.A.; Stillman, M.J. *Can. J. Chem.* **1979**, *57*, 1211.

46. Sharonov, Y.A. *Soviet Scientific Reviews*. Section D, Vol. 10(3), *Physicochemical Biology Reviews*; Skulachev, V.P., Ed., Harwood Academic Publishers, **1991**.

47. Yokote, M; Fukumatsu, F. *Koka (Industrial Chemistry)* **1958**, *61*, 994–996.

48. Fukada, N. *Nika (Japanese Journal of Chemistry)* **1957**, *78*, 1348–1351.

49. Yokote, M.; Shibamiya, F.; Shoji, S. *Koka (Industrial Chemistry)* **1964**, *67*, 166–168.

50. Yokote, M.; Shibamiya, F. *Koka (Industrial Chemistry)* **1959**, *62*, 224.

51. Yokote, M.; Shibamiya, F.; Yokomizo, H. *Yugokyo* **1969**, *29*, 340–344.

52. Stillman, M.J.; Thomson, A.J. *J Chem. Soc., Faraday Trans. II* **1974**, *70*, 790–804.

53. Nyokong, T.; Stillman, M.J *Unpublished*.

54. Stephens, P.J.; Suetaak, W.; Schatz, P.N.; *J. Chem. Phys.* **1966**, *44*, 4595–4602.

55. Wohrle, D.; Schmidt, v. *J. Chem. Soc., Dalton Trans.* **1988**, 549.

56. Kobayashi, N.: Lever, A.B.P. *J. Am. Chem. Soc.* **1987**, *109*, 7433.

57. Radzki, S.; Mack, J.; Stillman, M.J. *New. J. Chem.* **1992**, *16*, 583–589.

58. Dawson, J.H.; Dooley, D.M. In *Iron Porphyrins*, Part 3; Lever, A.B.P., Gray, Eds., VCH Publishers: New York, 1988.

59. Cotton, F.A.; *Chemical Applications of Group Theory*, Wiley Interscience, **1971**.

60. Yang, C.H.; Chang, C. *J. Chem. Soc. Dalton Trans.* **1982**, 2539–2540.

61. Jones, J.G.; Twigg, M.V. *J. Chem. Soc. (A)* **1970**, 1546–1550.

62. Schatz, P.N.; McCafferty, A.J. *J. Chem. Soc. Quart. Rev.* **1969**, *23*, 552.

63. Stephens, P.J. *Chem. Phys. Letters* **1968**, *2*, 241.

64. Stephens, P.J. *J. Chem. Phys.* **1970**, *52*, 3489.

65. Edwards, L.; Gouterman, M. *J. Mol. Spec.* **1970**, *33*, 292–310.

66. Minor, P.C.; Lever, A.B.P.; Gouterman, M. *Inorg. Chem.* **1985**, *24*, 1894.

67. Hollebone, B.R.; Stillman, M.J. *J. Chem. Soc. Faraday Trans. II* **1977**, *74*, 2107.

68. Nyokong, T.; Gasyna, Z.; Stillman, M.J. *ACS Symposium Series* **1986**, *321*, Ch. 21, 309–327.

69. Prasad, D.R.; Ferraudi, G. *J. Phys. Chem.* **1984**, *88*, 1670.

70. Homborg, H. *Z. Anorg. Allg. Chem.* **1983**, *507*, 35–50.

71. Homborg, H.; Kalz, W. *Z. Naturforsch* **1978**, *33b*, 1067–1071.

72. Linder, R.E; Rowlands, J.R.; Hush, N.S. *Mol. Phys.* **1971**, *21*, 417–437.

73. Kahl, J.L.; Faulkner, L.R.; Dwarakanath, K.; Tachikawa, H. *J. Am. Chem. Soc.* **1986**, *108*, 5434.

74. Gradyushko, A.T.; Sevchenko, A.N.; Solovyov, K.N.; Tsvirko, M.P. *Photochm. Photobio.* **1970**, *11*, 387.

75. Gagne, R.R.; Koval, C.A.; Lisensky, G.C. *Inorg. Chem.* **1980**, *19*, 2854.

76. Bard, A.J.; Faulkner, L.R. *Electrochemical Methods, Fundamentals and Applications*, J. Wiley and Sons, **1980**.

77. Lever, A.B.P.; Licoccia, S.; Magnell, K.; Minor, P.C.; Ramaswamy, B.C. In *Electrochemical and Spectrochemical Studies of Biological Redox Components; Advances in Chemistry, Vol 201*, American Chemical Society: Washington, DC, **1982**, p. 237.

78. Felton, R.H. In *The Porphyrins*, Vol V, Dolphin, D., Ed., Academic Press: New York, **1978**, pp 53–115.

79. Stillman, M.J.; Thomson, A.J. *J. Chem. Soc., Faraday Trans. II* **1974**, *70*, 805.

80. Nyokong, T.; Gasyna, Z.; Stillman, M.J. *Inorg. Chim. Acta.* **1986**, *112*, 11–15.

81. Barth, G.; Linder, E.B.; Djerassi, C. *J. Chem. Soc., Perkin II* **1974**, 1706.

82. Browett, W.R.; Stillman, M.J. *Inorg. Chim. Acta.* **1981**, *49*, 69–77.

83. Gasyna, Z.; Browett, W.R.; Stillman, M.J. *Inorg. Chem* **1988**, *22*, 4619–4622.

84. Browett, W.R.; Stillman, M.J. *Biochim. Biophys. Acta* **1981**, *660*, 1–7.

85. Clack, D.W.; Yandle, J.R. *Inorg. Chem.* **1972**, *11*, 1738–1742.

86. Clack, D.W.; Hush, N.S.; Woolsey, I.S. *Inorg. Chim. Acta* **1976**, *19*, 129–132.

87. Backer, M.; Jacquot, P.; Sauvage, F.X.; Vlierberge, B.; Lepoutre, G. *J. Chim. Phys.* **1987**, *84*, 429–431.

88. Ohtani, H.; Kobayashi, T.; Ohno, T.; Kato, S.; Tanno, T.; Yamada, A. *J. Phys. Chem.* **1984**, *88*, 4431–4435.

89. Gasyna, Z; Kobayashi, N.; Stillman, M.J. *J. Chem. Soc., Dalton Trans.* **1989**, 2397–2405.

90. Browett, W.R.; Gasyna, Z.; Stillman, M.J. *J. Am. Chem. Soc.* **1988**, *110*,

3633–3640.

91. Gasyna, Z.; Browett, W.R.; Stillman, M.J. *Biochemistry* **1988**, *27*, 2503–2509.

92. Browett, W.R.; Gasyna, Z.; Stillman, M.J. *Biochem. Biophys. Rres. Commun.* **19983**, *112*, 515–520.

93. Browett, W.R.; Stillman, M.J. *Biochem. Biophys. Acta* **1980**, *623*, 21–31.

94. Gasyna, Z.; Browett, W.R.; Stillman, M.J. *ACS Symp. Ser.* **1986**, *321*, 298–308.

95. Gasyna, Z.; Stillman, M.J. *Inorg. Chem.* **1990**, *29*, 5101–5109.

96. Gasyna, Z.; Browett, W.R.; Stillman, M.J. *Inorg. Chem.* **1984**, *23*, 382–384.

97. Gasyna, Z.; Browett, W.R.; Stillman, M.J. *Inorg. Chem.* **1985**, *24*, 2440–2447.

98. Dolphin, D. *Isr. J. Chem.* **1981**, *21*, 67–71.

99. Dolphin, D.; James, B.R.; Murray, A.L.; Thornback, J.R. *Can. J. Chem.* **1980**, *58*, 1125–1132.

100. Jones, J.G.; Twigg, M.V. *Inorg. Chem.* **1970**, *6*, 245–247.

101. Van Vlierberge, B.; Ferrausi, G. *Inorg. Chem.* **1987**, *26*, 337–340.

102. Ferraudi, G.J.; Prasad, D.R. *J. Chem Soc., Dalton Trans.* **1980**, 2137–2140.

103. Kalz, W.; Homborg, H.; Kuppers, H.; Kennedy, B.J.; Murray, K.S. *Z. Naturforsch* **1984**, *39B*, 1478.

104. Minor, P.C.; Gouterman, M.; Lever, A.B.P. *Inorg. Chem.* **1985**, *24*, 1894–1900.

105. Hollebone, B.R.; Stillman, M.J. *Chem. Phys. Lett.* **1974**, *29*, 284–286.

106. Collamati, I.; Ercolani, C.; Rossi, G. *Inorg. Nucl. Chem. Letters* **1976**, *12*, 799–802.

107. Ercolani, C.; Gardini, M.; Monacelli, F.; Pennesim G.; Rossi, G. *Inorg. Chem.* **1983**, *22*, 2584–2589.

108. Stynes, D.V.; James, B.R. *J. Am. Chem. Soc.* **1974**, *95*, 2733–2738.

109. Calderazzo, F.; Papmaloni, G.; Vitali, D.; Pelizzi, G.; Collamati, I.; Frediani, S.; Serra, A.M. *J. Organomet. Chem.* **1980**, *191*, 217–242.

110. Calderazzo, F.; Frediani, S.; James, B.R.; Pampaloni, G.; Reimer, K.J.; Sams, J.R.; Serra, A.M.; Vitalli, D. *Inorg. Chem.* **1982**, *21*, 2302–2306.

111. James, B.R.; Reimer, K.J.; Wong, T.C.T. *J. Am. Chem. Soc.* **1977**, *99*, 4815.

112. Calderazzo, F.; Vitalli, D.; Pampaloni, G.; Collamati, I. *J. Chem. Soc., Chem. Commun.* **1979**, 221.

113. Furuya, N.; Yoshiba, H. *J. Electroanal. Chem.* **1989**, *263*, 171–174.

114. Stynes, D.V. *J. Am. Chem. Soc.* **1974**, *96*, 5942–5943.

115. Stynes, D.V. *Inorg. Chem.* **1977**, *16*, 1170–1173.

116. Jones, J.G.; Twigg, M.V. *Inorg. Chem.* **1977**, *16*, 1170–1173.

117. Jones, J.G.; Twigg, M.V. *Inorg. Chem.* **1969**, *8*, 2120–2123.

118. Sweigart, D.W. *J. Chem. Soc., Dalton Trans.* **1976**, 1476–1477.

119. Küppers, H.; Kalz, W.; Homborg, H. *Acta. Crys., Sect. C: Cryst. Struct. Commun.* **1985**, *C41*, 1420–1423.

120. Calderazzo, F.; Pampaloni, G.; Vitali, D.; Collamati, I.; Dessy, G.; Fares, V. *J. Chem. Soc., Dalton Trans.* **1980**, 1965–1968.

121. Ercolani, C.; Monacelli, F.; Dzugan, S.; Goedken, V.L.; Pennesi, G.; Rossi, G. *J. Chem. Soc., Dalton Trans.* **1991**, 1309–1315.

122. Ohya, T.; Takeda, J.; Kobayashi, N.; Sato, M. *Inorg. Chem.* **1990**, *29*, 3734–3737.

123. Kobayashi, N.; Konami, H.; Ohya, T.; Sato, M.; Shirai, H. *Makromol. Chem., Rapid Commun.* **1989**, *10*, 1–4.

124. Kennedy, B.J.; Murray, K.S.; Homborg, H.; Kalz, W. *Inorg. Chim. Acta* **1987**, *134*, 19–21.

125. Kennedy, B.J.; Murray, K.S.; Zwack, P.R.; Homborg, H.; Kalz, W. *Inorg. Chem.* **1986**, *25*, 2539–2545.

126. Dickens, L.L.; Fanning, J.C. *Inorg. Nucl. Chem Lett.* **1976**, *12*, 1–5.

127. Kobayashi, N.; Shirai, H.; Hojo, N. *J. Chem. Soc., Dalton Trans.* **1984**, 2107–2110.

128. Myers, J.F.; Rayner Canham, G.W.; Lever, A.B.P. *Inorg. Chem.* **1975**, *24*, 461–468.

129. Ouédraogo, G.V.; More, C.; Richard, Y.; Benlian, D. *Inorg. Chem.* **1981**, *20*, 4387–4393.

130. Ogoshi, H.; Sugimoto, H.; Watanabe, E.; Yoshida, Z.; Maeda, Y.; Sakai, H. *Bull. Chem. Soc. Jpn.* **1981**, *54*, 3414–3419.

131. Kennedy, B.J.; Brain, G.; Murray, K.S. *Inorg. Chim. Acta* **1984**, *81*, L29–L31.

132. Frampton, C.S.; Silver, J. *Inorg. Chim. Acta* **1985**, *96*, 187–191.

133. Kennedy, B.J.; Murray, K.S.; Zwack, P.R.; Homborg, H.; Kalz, W. *Inorg. Chem.* **1985**, *24*, 3302–3305.

134. Ohya, J.; Kobayashi, N.; Sato, M. *Inorg. Chem.* **1987**, *26*, 2506–2509.

135. Ercolani, C.; Paoletti, A.M.; Pennesi, G.; Rossi, G. *J. Chem. Soc., Dalton Trans.* **1991**, 1317–1321.

136. Dale, B.W. *Mol. Phys.* **1974**, *28*, 503–511.

137. Grenoble, D.C.; Drickamer, H.G. *J. Chem. Phys.* **1971**, *55*, 1624–1633.

138. Dale, B.W.; Williams, R.J.P.; Edwards, P.R.; Johnson, C.E. *J. Chem. Phys.* **1968**, *49*, 3445–3449.

139. Dezsi, I.; Balazs, A.; Molnar, B.; Gorobchenko, V.D.; Lukashevich, I.I. *J. Inorg. Nucl. Chem.* **1969**, *312*, 1661–1666.

140. Hudson, A.; Whitfield, H.J. *Inorg. Chem.* **1967**, *6*, 1120–1123.

141. Mack, J.; Kirby, S.; Ough, E.A.; Stillman, M.J. *Inorg. Chem.* **1992**, *31*, 1717–1719.

142. Jones, J.G.; Twigg, M.V. *Inorg. Chim. Acta* **1974**, *10*, 103–104.

143. Kadish, K.M.; Bottomley, L.A.; Cheng, J.S. *J. Am. Chem. Soc.* **1978**, *100*, 2731–2737.

144. Dale, B.W.; Williams, R.J.P.; Edwards, P.R.; Johnson, C.E. *Trans. Faraday Soc.* **1968**, *64*, 620.

145. McHugh, A.J.; Gouterman, M.; Weiss, C. *Theoret. Chim. Acta* **1972**, *24*, 346.

146. Stymne, B.; Sauvage, F.X.; Wettermark, G. *Spectrochim. Acta* **1980**, *36A*, 397–402.

147. Kobayashi, N.; Koshiyama, M.; Funayama, K.; Osa, T.; Shirai, H.; Hanabusa, K. *J. Chem. Soc, Chem. Commun.* **1983**, 913–914.

148. Kobayashi, N.; Funayama, K.; Koshiyama, M.; Osa, T.; Shirai, H.; Hanabusa, K. *J. Chem. Soc, Chem. Commun.* **1983**, 915–916.

149. Lever, A.B.P.; Minor, P.C.; Wilshire, J.P. *Inorg. Chem.* **1981**, *20*, 2550.

150. Lever, A.B.P.; Wilshire, J.P. *Inorg. Chem.* **1978**, *17*, 1145–1151.

151. Nicholson, R.S.; Shain, I *Anal. Chem.* **1964**, *36*, 706.

152. Williamson, B.E.; VanCott, T.C.; Boyle, M.E.; Misener, G.C.; Stillman, M.J.; Schatz, P.N. *J. Am. Chem. Soc.* **1992**, *114*, 2412–2419.

153. Watkins, J.J.; Balch, A L. *Inorg. Chem.* **1975**, *14*, 2720–2723.

154. Kalz, W.; Homborg, H. *Z. Naturforsh., B: Anorg. Chem., Org. Chem.* **1983**, *38B*, 470–483.

155. Taube, H.; Drevs, H.; Fluck, E.; Kuhn, P.; Braunch, K.F. *Z. Anorg. Allgem. Chem.* **1969**, *364*, 297.

156. Dale, B.W.; Williams, R.J.P.; Johnson, C.E.; Thorp, T.L. *J. Chem. Phys.*

1968, *49*, 3441–3444.

157. Barraclough, C.G.; Martin, R.L.; Mitra, S.; Sherwood, R.C. *J. Chem. Phys.* **1970**, *53*, 1643–1648.

158. Palmer, S.M.; Stanton, J.L.; Jaggi, N.K.; Hoffman, B.M.; Ibers, J.A.; Schwartz, L.H. *Inorg. Chem.* **1985**, *24*, 2040–2046.

159. Yoshimura, T.; Toi, H.; Inaba, S.; Ogoshi, H. *Inorg. Chem.* **1991**, *30*, 4315–4321

160. Fitzgerald, J.P.; Haggerty, B.S.; Rheingold, A.L.; May, L.; Brewer, G.A. *Inorg. Chem.* **1992**, *31*, 2006–2013.

161. Palmer, G. In *The Porphyrins*. Vol. IV, Part B, *Physical Chemistry*; Dolphin, D., Ed.; Academic Press: New York, **1989**, 313–353.

162. Barrett, P.A.; Frye, D.A.; Linstead, R.P. *J. Chem. Soc.* **1938**, 1157

163. Koenig, D. *Acta Crystallogr.* **1965**, *18*, 663–673.

164. Scheidt, W.; Reed, C. *Chem. Rev.* **1981**, *81*, 543–555.

165. Davis, M.S.; Forman, A.; Fajer, J. *Proc. Natl. Acad. Sci. U.S.A.* **1979**, *76*, 4170–4174.

166. O'Brien, P.J. *Pharm. Theoret.* **1978**, *42*, 517–536.

167. Dolphin, D.; Muljiani, Z.; Rousseau, K.; Borg, D.C.; Fajer, J.; Felton, R.H. *Ann. New York Acad. Sci* **1973**, *206*, 177.

168. van der Waals, J.H.; van Dorp, W.G.; Schaafsma, T.J. In *The Porphyrins*. Vol. IV, Part B, *Physical Chemistry*; Dolphin, D., Ed.; Academic Press: New York, **1989**, 257–312.